The Influence of Microstructural Components on the Formability of Aluminium Alloy Sheets

Michael Langille

Communauté
UNIVERSITÉ Grenoble Alpes

THÈSE

Pour obtenir le grade de

DOCTEUR DE LA COMMUNAUTE UNIVERSITE GRENOBLE ALPES

Spécialité : **Matériaux, Mécanique, Génie civil, Electrochimie**

Arrêté ministériel : 25 mai 2016

Présentée par

Michael Langille

Thèse dirigée par **Alexis DESCHAMPS** et codirigée par **Frédéric DE GEUSER**

préparée au sein du **Laboratoire des Sciences et Ingénierie des Matériaux et des Procédés (SIMaP)**
dans **l'école Doctorale Ingénierie – Matériaux, Mécanique Energétique Environnement Procédés Production (I-MEP2)**

Influence des constituants microstructuraux sur la formabilité des tôles en alliages d'aluminium

Thèse soutenue publiquement le **5 juin 2019**,
devant le jury composé de :

Pr. Joël Bonneville
Professeur à l'université de Poitiers (Rapporteur)
Pr. Aude Simar
Professeure à l'université catholique de Louvain, Belgique (Rapporteur)
Pr. Michel Perez
Professeur à l'INSA Lyon (Président)
Dr. Gilles Guiglionda
Ingénieur de recherche à Constellium (Invité)
Pr. Alexis Deschamps
Professeur à Grenoble-INP (Directeur de thèse)
Dr. Frédéric De Geuser
Chargé de recherche au SIMAP (Co-encadrant)
Pr. Bradley Diak
Associate Professor at Queen's University, Canada (Co-encadrant)

Acknowledgements

I have many people to thank for their involvement in making this thesis possible. I will start with my supervisors: Alexis Deshchamps, Frédéric De Geuser, Bradley Diak, and Gilles Guiglionda. Each of you have contributed in a unique and special way to this work, and have always been there for me professionally and personally. I will be forever greatful for all of your guidance, patience, and many discussions that we had over the past three and a half years.

Next, I would like to thank my interns, Devang Sejani for assisting in hardness testing, and Sami Meddeb for his work on atom probe tomography. I would like to thank Pr. Guillaume Parry for his guidance and assistance in completing the finite element modelling used in this thesis.

I would also like to thank Dr. Shigeo Saimoto, one of my previous professors. He taught me how to properly do research, to think for myself and how to create a pathway to understanding from the experimental results. I owe Dr. Saimoto my sincerest gratitude for his patience and mentorship over the last 5 years and I would not be where I am today without him.

J'aimerai bien de remercie tous les autres professeurs, doctorants et stagiaires qui m'ont aidé à apprendre le français (et la science aussi). Vous m'avez appris plus que la langue mais aussi la vie à la française et l'importance de l'apéro. Je vous souhaite la force de finir vos thèses même si ça prend super longtemps !!!

Aussi, je dois remercier tous l'équipe de jjb au Martial Gym. Vous m'avez appris comment rester tranquille même quand il y a beaucoup de stresse dans ma vie. Vous étiez une famille pour moi pendant cette thèse et vous m'avez donné un endroit où je peux être moi-même, merci.

I also must thank someone who I found during my time in Grenoble. I will never forget how you helped me get through this, especially the final few months. Thank you.

I would like to thank my family and friends from back home. Despite being over 6000 km away from home, they were always there when I needed it most and were always willing to listen. I could not have completed this without you.

Finally, I need to thank my past self for deciding to do this. I can't believe it's finally over but here we are!

Table of Contents

Acknowledgements 1

Résumé étendu 7

INTRODUCTION 7

MÉTHODES ET MATÉRIELS 8

i) Formation des amas lors du vieillissement naturel et du pré-vieillissement des alliages Al-Mg-Si-Cu 9

ii) Asymétrie dans les tests de sensibilité de la vitesse de déformation : méthodes et analyses 11

iii) Effets de la composition et du traitement des alliages sur les propriétés mécaniques des alliages Al-Mg-Si-Cu 14

iv) Essai de sensibilité de la vitesse de déformation à basse température : profil thermique des obstacles 16

v) Analyse de la striction dans les alliages d'aluminium durcissant par vieillissement : effets de la sensibilité de la vitesse de déformation et de l'écrouissage 20

CONCLUSIONS 24

1 Introduction 27

1.1 Thesis approach 27

1.1.1 Formation of clusters during natural and pre-ageing of Al-Mg-Si-Cu alloys 28

1.1.2 Asymmetry in strain rate sensitivity testing: methods and analyses 28

1.1.3 Effects of alloy composition and processing on the mechanical properties of Al-Mg-Si-Cu alloys 28

1.1.4 Characterization of thermally activated dislocation glide in naturally aged Al-Mg-Si-Cu Alloys: what it tells us about clusters 29

1.1.5 An analysis of necking formation in age-hardenable aluminium alloys: the effect of strain rate sensitivity 29

1.2 References 29

2 Literature Review 31

2.1 Microstructure effects 31

2.1.1 Solutes and clusters 32

2.1.2 Precipitates 32

2.1.3 Dispersoids 33

2.1.4 Grain Size 33

2.1.5 Texture 34

2.2 Plastic flow 34

2.2.1 Yielding 34

2.2.2 Strain hardening 35

2.3 Strain rate sensitivity 37

2.4 Formability 40
2.5 Effects of processing on obstacle formation 40
2.5.1 Effects of natural ageing 41
2.5.2 Effects of pre-ageing 41
2.5.3 Effects of artificial ageing 41
2.6 Effects of composition on obstacle formation 42
2.6.1 Effects of Cu additions 42
2.6.2 Effects of Si additions 42
2.6.3 Effects of Mg addition 43
2.7 Conclusions 43
2.8 References 43
3 Materials and experimental methodology 53
3.1 Alloy compositions and heat treatments 53
3.2 Microstructure characterization 54
3.2.1 Hardness testing 54
3.2.2 Differential scanning calorimetry 55
3.2.3 Atom probe tomography 57
3.3 Mechanical characterization 58
3.3.1 Tensile testing 58
3.3.2 Strain rate sensitivity testing 59
3.3.3 Low-temperature testing 60
3.4 References 62
4 Formation of clusters during natural and pre-ageing of Al-Mg-Si-Cu alloys 65
Abstract 66
1.0 Introduction 67
2.0 Background 67
3.0 Materials and methods 68
4.0 Experimental Results and Analysis 70
4.1 Effects of Cu addition with 0.9 at% Si 70
4.2 Effects of Si additions with 0.1 at% Cu 73
4.3 Effects of composition on hardness 74
4.4 Effects of composition on kinetics 76
4.5 Results Summary 77
5.0 Discussion 78
5.1 Natural Ageing 78

5.2 Pre-Ageing 78
5.3 Artificial Ageing 79
6.0 Conclusions 80
7.0 Acknowledgements 80
8.0 References 81
5 Effect of Si on the strain rate sensitivity of naturally aged Al-Mg-Si-Cu alloys 86
Abstract 87
1.0 Introduction 88
2.0 Background 89
3.0 Experimental Details 90
4.0 Results and Analysis 90
4.1 Microstructure and constant strain rate properties 90
4.2 Strain rate sensitivity 92
4.3 Strain rate sensitivity results 93
5.0 Discussion 96
6.0 Conclusions 100
7.0 References 101
6 Influence of composition on the material properties in Al-Mg-Si-Cu alloys 106
Abstract 107
1.0 Introduction 108
2.0 Background 108
3.0 Materials and Methods 111
4.0 Results and analysis 112
4.1 NA1m 118
4.2 sNA1m 118
4.3 sNA1w 118
5.0 Discussion 119
5.1 Effects on mechanical properties 119
5.2 Effects on constitutive parameters 120
6.0 Conclusions 121
7.0 References 121
7 Characterization of Thermally Activated Dislocation Glide in Naturally Aged Al-Mg-Si-Cu Alloys: What it tells us about clusters 127
Abstract 128
1.0 Introduction 129
2.0 Background and Theory 129

3.0 Methods and Materials 133
4.0 Results and Discussion 134
4.1 Yield strength dependence on temperature 134
4.2 Haasen plot representation 135
4.3 T4 clusters compared to saturated solid solution state at 78 K 139
4.4 Dislocation-dislocation interactions in the alloys at larger strains 143
5.0 Conclusions 144
6.0 References 145
8 An analysis of necking formation in Al-Mg-Si-Cu alloys: the effect of strain rate sensitivity 148
Abstract 149
1.0 Introduction 150
2.0 Background and Model Design 150
3.0 Methods and Materials 153
4.0 Model implementation: parametric study on the effects of m_{uc} and m_{dc} 156
5.0 Application of the model to experimental data 163
6.0 Discussion 166
6.1 Neck localization, stabilization, and propagation 167
6.2 ULDL: $m_{uc} = m_{dc} = 0$ 167
6.3 UHDL: m_{uc} 0.05; $m_{dc} = 0$ 167
6.4 ULDH: $m_{uc} = 0$; $m_{dc} = 0.05$ 168
6.5 UHDH: $m_{uc} = m_{dc} = 0.05$ 168
7.0 Conclusions 168
8.0 References 169
9 Discussion, conclusions and perspectives 171
9.1 Discussion 171
9.1.1 Solute additions and processing on the mechanical properties 171
9.1.2 Strain rate sensitivity testing and asymmetry 176
9.1.3 Connection of the mechanical properties to failure properties 178
9.2 Conclusions 179
9.3 Perspectives 180
Appendices 182
Appendix 1 – Supplementary plots 182
Appendix 1.1 – Hardness plots 182
Appendix 1.2 – DSC thermographs 183

Appendix 1.3 – sNA1w mechanical data 185
Appendix 1.4 – Haasen plot information 186
1.5 The yield strength for the AQ samples at 78K in the three conditions 192
Appendix 2 – Temperature dependent shear modulus of aluminium 193

Résumé étendu

INTRODUCTION

Au fur et à mesure que la demande pour la production de véhicules de tourisme à faibles émissions de carbone et à haut rendement énergétique augmente, la demande d'alliages d'aluminium légers pour remplacer les composants existants en acier, le plus souvent sous la forme de peaux et de composants extérieurs, augmente également. Comme de nombreuses recherches l'ont montré, les alliages d'aluminium de la série 6000, dont les principaux éléments d'alliage sont principalement le magnésium (Mg), le silicium (Si) et le cuivre (Cu), ont démontré une résistance à la corrosion et une qualité de surface adéquates pour les portes, toits et capots de voitures. Cependant, à mesure que les concepteurs automobiles recherchent des formes extérieures (et des profils) de plus en plus complexes, la quantité de déformation plastique nécessaire pour que les tôles en alliage d'aluminium soient correctement embouties dans leur forme finale augmente constamment. Malheureusement, la plupart des alliages actuels n'ont pas une ductilité suffisante, ou plus précisément une aptitude au formage, pour permettre le formage de ces pièces à déformation élevée sans présenter de fissures. Il est entendu qu'une grande capacité d'écrouissage et une sensibilité élevée à la vitesse de déformation permettent une plus grande déformation avant la rupture du matériau, mais la compréhension complète des interactions entre la composition de l'alliage, le traitement, les propriétés des matériaux et, finalement, la formabilité reste difficile à cerner. Les procédés standards de traitement des tôles d'alliages pour applications automobiles consistent en la mise en solution, un traitement de stabilisation (vieillissement naturel ou pré-vieillissement), le formage, la peinture, et enfin la cuisson de la peinture qui s'accompagne d'un durcissement du composant final. Les effets de la composition sur la réponse à la cuisson de la peinture et sur la formation de la microstructure ont été bien étudiés mais les effets des traitements de stabilisation sur la formabilité ultérieure sont beaucoup moins bien compris. Ainsi, le but de cette thèse est de mieux comprendre et de relier la composition des alliages de neuf (9) alliages Al-Mg-Si(-Cu) par différentes voies de traitement thermique aux propriétés mécaniques résultantes et à leur influence sur la ductilité et, idéalement, la formabilité de la tôle en aluminium.

La thèse est divisée en cinq parties principales qui suivent l'introduction, l'analyse bibliographique et les sections sur la méthodologie. Les sections sont les suivantes :

i) Formation d'amas au cours du vieillissement naturel et du pré-vieillissement des alliages Al-Mg-Si-Cu
ii) Asymétrie dans les tests de sensibilité de la vitesse de déformation : méthodes et analyses
iii) Effets de la composition et du traitement des alliages sur les propriétés mécaniques des alliages Al-Mg-Si-Cu
iv) Essais de sensibilité de la vitesse de déformation à basse température : profil thermique des obstacles
v) Analyse de la striction, dans les alliages d'aluminium : effets de la sensibilité de la vitesse de déformation et du durcissement d'écrouissage

Chaque chapitre est conçu pour utiliser l'information recueillie dans le chapitre précédent afin de fournir une meilleure base pour la compréhension de chacun des phénomènes étudiés dans chaque section. Ce résumé étendu permettra au lecteur de comprendre le travail effectué pour

cette thèse et de comprendre les principaux résultats de chaque article et les parties critiques de chaque discussion.

MÉTHODES ET MATÉRIELS

Les neuf alliages Al-Mg-Si(-Cu) choisis pour ces travaux ont été fournis par le Constellium Technology Centre (C-TEC) situé à Voreppe, France. La composition de ces alliages est indiquée ci-dessous dans le tableau 1. Le rapport Mg + Cu/Si est représenté sur la figure 1 et comparé aux alliages d'aluminium courants de la série 6000. La conception des compositions des alliages était telle qu'il serait possible de tester les effets de :

a) Additions de cuivre à 0,9 at % Si (C0S0, C2S0 et C8S0)
b) Additions de cuivre à 1,3 at % Si (C0S3, C2S3, C5S3 et C8S3)
c) Additions de Si à 0,1 at % Cu (C2S0, C2S1 et C2S3)
d) Additions de Si à 0,3 at % Cu et 0,4 at % Mg (C8S0 et C8S3)
e) Additions de Mg à 0,9 à Si et 0,3 at % Cu (C8S0 et C8S0M)

Sample Name	Si	Cu	Mg
C0S0	0.895	0.008	0.404
C2S0	0.896	0.089	0.381
C8S0	0.879	0.333	0.379
C8S0M	0.899	0.337	0.557
C2S1	1.069	0.087	0.372
C0S3	1.299	0.004	0.387
C2S3	1.262	0.088	0.400
C5S3	1.284	0.218	0.372
C8S3	1.324	0.329	0.385

Tableau 1: Concentrations nominales de chacune des teneurs en alliages pour les neuf alliages testés dans ce travail en (en at %). Les éléments mineurs tels que Fe, Ti, Ni, etc. se trouvent dans le corps principal de la thèse.

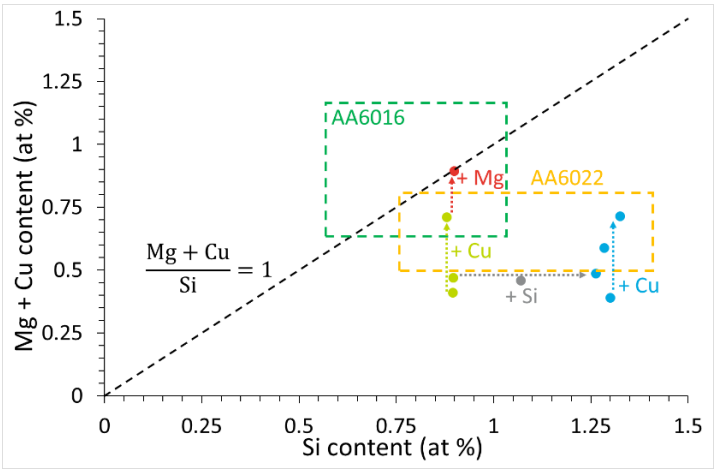

Figure 1: *Représentation graphique des teneurs en Cu et en Mg comparées aux teneurs en Si des neuf alliages Al-Mg-Si-Cu testés dans ce travail. La ligne pointillée noire indique un rapport de 1:1 (Mg + Cu) à Si. Les flèches pointillées vertes et bleues indiquent les additions de Cu à Si constant, la flèche pointillée rouge indique l'addition de Mg à Cu et Si constants, tandis que la flèche grise indique l'addition de Si à Cu et Mg constants. Deux alliages courants, AA6016 et AA6022, sont présentés à titre de comparaison.*

En raison des exigences industrielles et des pratiques actuelles entourant la production de tôles en alliage d'aluminium pour les applications automobiles, les échantillons ont été testés dans un état stabilisé par pré-vieillissement, vieillissement naturel ou une combinaison des deux. Les programmes exacts de traitement thermique effectués sur les alliages sont illustrés à la figure 2 ci-dessous.

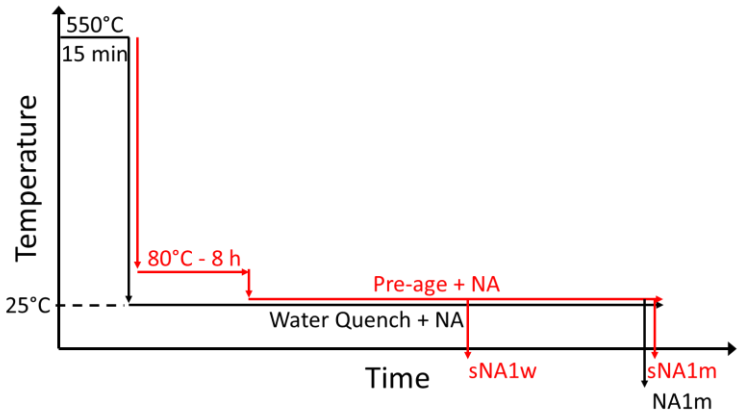

Figure 2: *Illustration des programmes de traitement thermique effectués sur les neuf alliages Al-Mg-Si-Cu résultant des conditions i) sNA1w, ii) sNA1m, et iii) NA1m.*

En effet, lors de la production de composants extérieurs automobiles, les tôles sont produites en usine et expédiées aux constructeurs automobiles, ce qui entraîne inévitablement la formation d'amas.

i) Formation des amas lors du vieillissement naturel et du pré-vieillissement des alliages Al-Mg-Si-Cu

Pour les alliages d'aluminium de la série Al-Mg-Si, lors des processus de vieillissement à basse température (vieillissement naturel ou pré-vieillissement), deux distributions différentes d'amas sont formées avec un rapport Mg/Si inférieur ou supérieur à l'unité, respectivement. En formant des amas avant les processus ultérieurs de vieillissement artificiel, la barrière énergétique pour la formation de précipités peut être réduite si la stœchiométrie des amas est plus proche de celle des précipités de premier ordre, β'' ayant une stœchiométrie de Mg_5Si_6. En raison de l'effet négatif du vieillissement naturel, c'est-à-dire qu'un vieillissement prolongé de l'alliage immédiatement après la trempe provoquerait une diminution du durcissement lors de la cuisson des peintures, les fabricants ont commencé à mettre en œuvre le procédé de pré-revenu (PA) avant le vieillissement naturel (NA). Séparément, l'ajout de Cu a également augmenté le rapport (Mg + Cu)/Si dans les amas qui se forment à température ambiante et avant le vieillissement, réduisant ainsi l'effet négatif du vieillissement naturel. Il est donc important de mieux comprendre l'effet des divers ajouts d'éléments d'alliage sur l'évolution de la dureté pendant le vieillissement naturel NA et pendant le vieillissement naturel secondaire qui suit le pré-revenu (sNA), comme le montrent les figures 3a et 3b, respectivement.

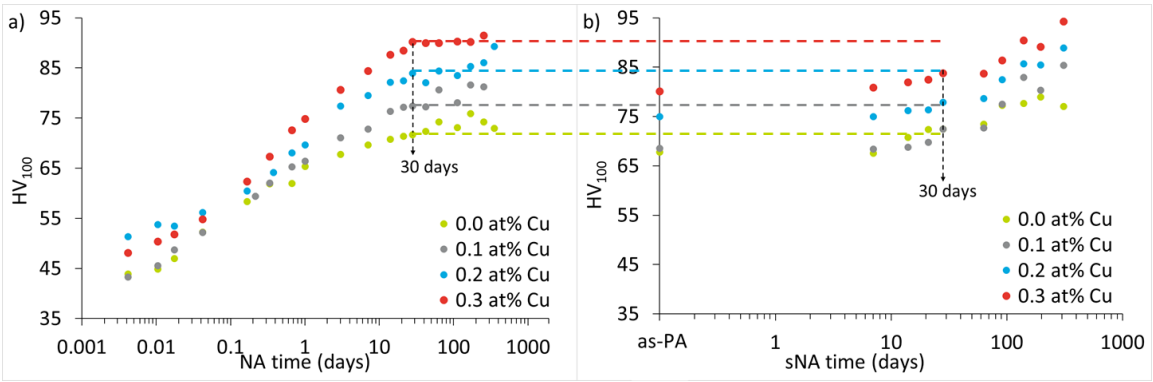

Figure 3: *Les courbes de dureté montrant les effets des additions de Cu à 0,4 % Mg et 1,3 % Si pour* ***a)*** *la trempe à l'eau avec vieillissement naturel, et* ***b)*** *le pré-vieillissement à 80 °C pendant 8 heures avec vieillissement naturel secondaire. La dureté de chaque alliage après 30 jours de NA ou de sNA est reliée aux lignes pointillées de couleur correspondante.*

Le concept de la présence de deux types d'amas différents dans le système d'alliage Al-Mg-Si(-Cu) n'est pas identifiable à partir des essais de dureté, mais ces essais peuvent éclairer l'évolution générale de la résistance mécanique et de la fraction du soluté qui se regroupe dans les amas au cours du temps. A partir de l'état trempé (WQ) (figure 3a), la dureté initiale augmente avec la teneur en Cu, ce qui s'étend sur toute la durée du processus jusqu'à 30 jours de NA. Il en va de même en ce qui concerne la dureté après pré-revenu pour laquelle les additions de Cu augmentent la dureté initiale et augmentent simultanément le temps d'incubation avant que l'augmentation de dureté ne reprenne. Après 30 jours de sNA, les mêmes tendances se retrouvent avec une augmentation de la dureté coïncidant avec une augmentation de la teneur en Cu. Il est intéressant de noter que les duretés après 30 jours NA et sNA ne sont pas égales pour chacun des alliages, la dureté NA étant toujours égale ou supérieure à la dureté sNA. Les additions de cuivre font augmenter la différence entre la dureté NA et la dureté sNA. Pour délimiter les différences entre les types d'amas qui se forment au cours des deux processus, des thermographes de calorimétrie différentielle à balayage (DSC) pour les échantillons dans les états NA1m (vieillissement naturel 1 mois) et as-PA (après pré-revenu) ont été réalisés, comme le montrent les figures 4a et 4b ci-dessous, respectivement, pour déterminer l'évolution de l'intensité maximale de dissolution en fonction de la teneur en Cu.

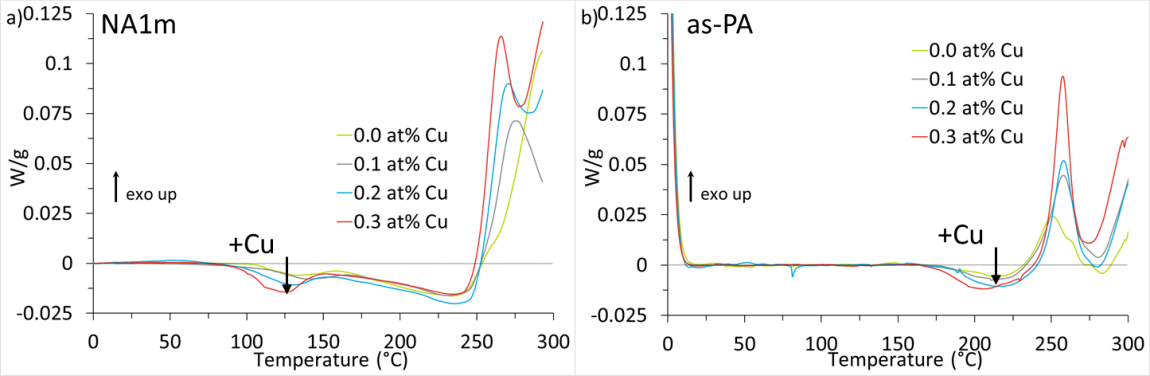

Figure 4: *Thermographes DSC montrant les effets des additions de Cu pour des échantillons contenant 1,3 at % Si et 0,4 à Mg dans les conditions* ***a)*** *NA1m et* ***b)*** *de pré-vieillissement.*

Les thermographes DSC montrent l'effet des additions de Cu sur le comportement de dissolution des amas formés pendant NA et PA. La figure 4a montre un pic de dissolution dépendant du Cu, centré à 125 °C, dont l'intensité augmente avec la teneur en Cu. Le deuxième pic de dissolution (ayant son pic à 235 °C) ne présente pas de dépendance au Cu et a une augmentation très progressive à partir de 150 °C. L'intensité totale de dissolution augmente avec la teneur en Cu et est en corrélation directe avec une augmentation de la dureté. Dans la figure 4b, il n'y a pas de premier pic de dissolution et les thermographes DSC ne montrent aucun comportement de mise en amas ou de dissolution avant 175 °C. Le pic de dissolution à 210 °C a une dépendance mineure en Cu, son intensité augmentant légèrement avec la teneur en Cu. Comme l'intensité de dissolution totale est considérablement inférieure à celle de la condition NA1m, elle correspond à la dureté relativement plus faible de la condition as-PA par rapport à la dureté NA1m. Par ailleurs, l'inversion de l'effet négatif du vieillissement naturel dans le système de la série 6000 est éliminée par l'ajout de Cu à la figure 4a, l'augmentation de Cu faisant passer la température du pic de précipitation de 300 °C (sans Cu) à 265 °C (0,3 % Cu). Par ailleurs, l'introduction du pré-revenu avant le vieillissement artificiel réduit également l'effet négatif du vieillissement naturel, de sorte que dans la figure 4b, le pic de précipitation reste à 250 °C, indépendamment de la teneur en Cu, à une température nettement inférieure à celles de l'état NA1m.

ii) Asymétrie dans les tests de sensibilité de la vitesse de déformation : méthodes et analyses

Après avoir obtenu une compréhension générale des effets des ajouts de composition et du traitement sur la formation des amas et leur dureté correspondante, l'accent a été mis sur l'évaluation de la sensibilité de la vitesse de déformation des alliages afin de saisir et de déterminer un des paramètres critiques contrôlant la formabilité des alliages d'aluminium. La définition de la sensibilité de la vitesse de déformation de fait en termes d'évolution du volume d'activation inverse avec l'augmentation de la contrainte. Le volume d'activation peut être considéré comme la surface balayée par une dislocation entre les deux positions metastables de dislocations (avant et après) de l'activation thermique des obstacles contrôlant la déformation dans un matériau, multipliée par le vecteur du Burger, b. Le volume d'activation est directement lié à la taille, d, et la distribution ou l'espacement, l, des obstacles dans le matériau.

$$\frac{1}{V'} = \frac{1}{kT}\frac{\partial \sigma}{\partial \ln \dot{\epsilon}}\Big|_{T,\Sigma} = bdl$$

$$S = \frac{1}{T}\frac{\partial \sigma}{\sigma\, \partial \ln \dot{\epsilon}} = \frac{1}{T}\frac{\partial \ln \sigma}{\partial \ln \dot{\epsilon}} = k/V'$$

Où T est la température absolue, Σ, est la structure, σ, l'état de contrainte actuel, et $\dot{\epsilon}$, la vitesse de déformation. Dans le cas de la déformation plastique des alliages durcissables par vieillissement, les obstacles initiaux présents dans le matériau sont les amas, étant soit plus (interception positive) soit moins (interception négative) thermiquement activables que les dislocations. Au fur et à mesure que la déformation plastique progresse et que la densité des dislocations augmente, cela réduit leur espacement et finit par entraîner un changement de l'obstacle contrôlant la vitesse de déplacement des dislocations, entraînant un changement dans la sensibilité de la vitesse de déformation. La présentation typique de la sensibilité du taux de déformation est de tracer le volume d'activation inverse, $\frac{1}{T}\frac{\Delta \sigma}{\Delta \ln \dot{\epsilon}}$ versus $\sigma - \sigma_{0.2\%}$ dans ce qui est connu comme le diagramme de Haasen. Pour les matériaux purs où les dislocations sont les seuls obstacles présents et contrôlent la limite d'élasticité du matériau, la courbe de Haasen a une intersection de zéro. En ayant deux espèces différentes d'obstacles présents dans le matériau, des amas supposés constants tout au long de la déformation, et des dislocations qui augmentent en densité, on s'attendrait à ce que le diagramme de Haasen se manifeste en deux sections séparées, une première partie étant caractéristique des amas et la seconde étant liée aux dislocations. De plus, il est possible d'effectuer des tests de sensibilité de la vitesse de déformation soit en augmentant (ci-après dénommés " changements ascendants "), soit en diminuant (ci-après dénommés " changements descendants ") la vitesse de déformation de base. On a constaté qu'il y avait une différence dans la sensibilité de la vitesse de déformation des alliages de la série 6000 entre les variations du changement ascendant et les variations du changement descendant. L'une des composantes les plus importantes de cette thèse est la méthode précise utilisée pour effectuer les mesures de sensibilité de la vitesse de déformation. Ceci a été obtenu en utilisant ce que l'on appelle la méthode de compensation, selon laquelle, lors d'un changement de vitesse, la rigidité de la machine de traction change et provoque une perturbation sur l'échantillon à tester. La méthode de compensation tient compte de ce changement de rigidité, de sorte que le temps nécessaire pour effectuer le changement de vitesse est considérablement réduit, ce qui augmente la précision de la mesure et réduit les effets de la déformation ultérieure sur le changement de contrainte final. En raison de la nature de la rigidité de la machine, la compensation est plus importante lors des essais de changement du changement descendant lorsque la rigidité de la

machine diminue, plutôt que lors des essais de changement du changement ascendant lorsque la rigidité de la machine augmente. Les figures 5a et 5b, respectivement, illustrent un exemple de test de changement du changement descendant non compensé et compensé de façon idéale.

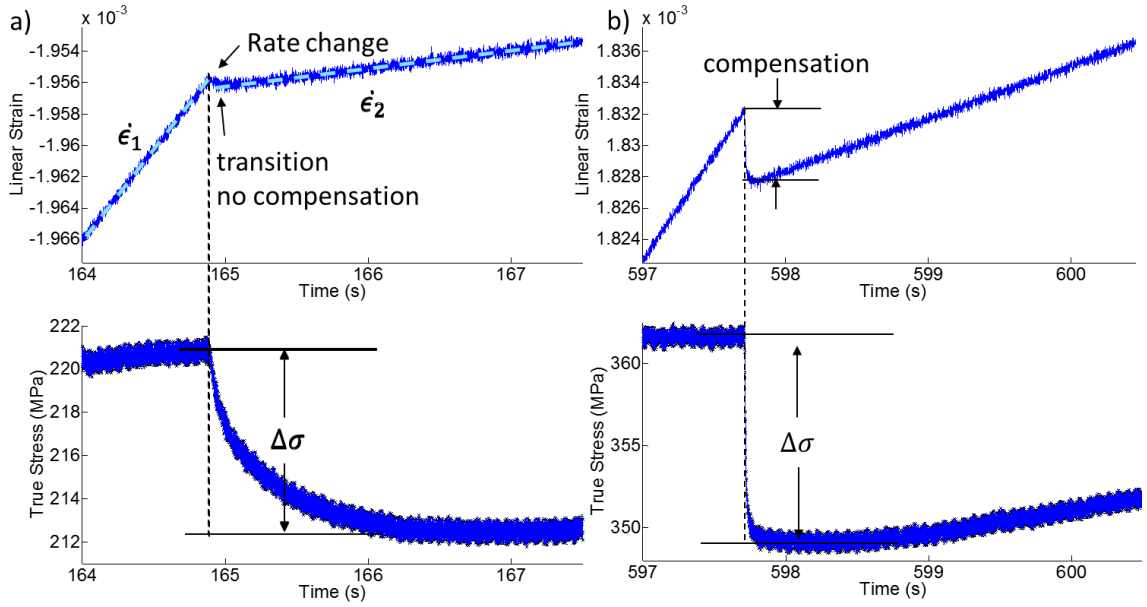

Figure 5: *La dépendance temporelle du contrôle de la déformation réelle (en haut) et de la réponse à la contrainte réelle (en bas) avec un changement de vitesse de déformation pour un échantillon d'essai avec* ***a)*** *aucune compensation (méthode traditionnelle), et* ***b)*** *une compensation idéale. Notez la relaxation des contraintes sur une plus longue période pour atteindre une contrainte minimale dans l'essai non compensé par rapport à l'essai compensé.*

Il est évident que le rôle de la compensation diminue non seulement le temps nécessaire pour obtenir la contrainte minimale, mais réduit également la production de dislocations subséquente et le durcissement qui se produit entre le moment du changement de vitesse et le minimum dans la figure 5a. Ce durcissement diminuerait inévitablement le changement de contrainte apparent dû au changement de taux et entraînerait une augmentation apparente du volume d'activation (valeur inférieure sur la courbe de Haasen). Pour illustrer les différences entre les changements du changement ascendant et du changement descendant, la figure 6 présente un exemple de diagramme de Haasen réalisé dans le cadre de ce travail.

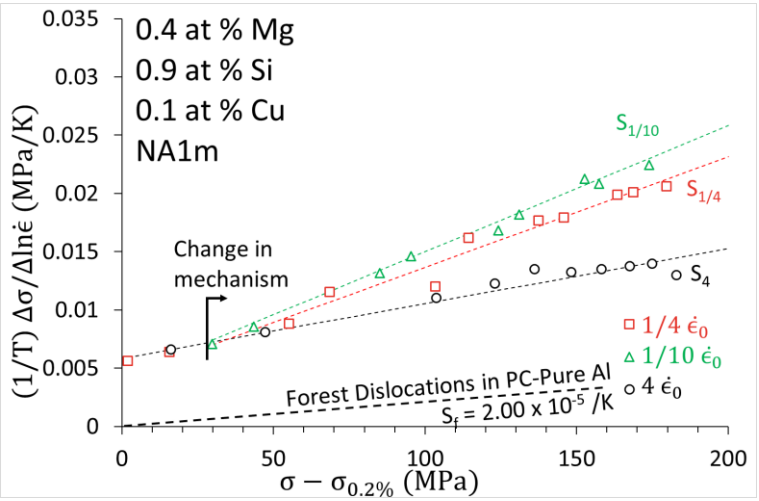

Figure 6: *Le diagramme de Haasen montrant les différences entre les tests de sensibilité de la vitesse de déformation $S_{1/4}$ (rouge), $S_{1/10}$ (vert) et S_4 (noir) pour l'échantillon C2S0 dans la condition NA1m. Noter l'écart important entre les tests de changement (S_4) et les deux tests de changement ($S_{1/4}$ et $S_{1/10}$) qui sont identiques et qui dévient après environ 40 MPa d'écrouissage ; cette transition est marquée par la flèche noire. La sensibilité de la vitesse de déformation pour les dislocations de la forêt dans l'aluminium polycristalline pur est présentée à des fins de comparaison.*

D'après la figure 6, il est évident qu'il y a une distinction dans le volume d'activation inverse apparent lorsqu'on effectue des tests de changement du changement ascendant et des tests de

changement du changement descendant ¼ et 1/10. Immédiatement après la limite d'élasticité, le volume d'activation inverse est identique pour les tests de changement du changement ascendant et du changement descendant, car on présume que les obstacles au contrôle de la vitesse sont dus aux amas formés pendant le traitement thermique du NA1m. Toutefois, après un écrouissage suffisant (40 MPa), les deux essais commencent à diverger, ce qui suggère un changement dans le mécanisme de déformation entre les essais de variation vers le haut et vers le bas, la sensibilité de la vitesse de déformation des essais descendants étant supérieure. On soupçonne que la différence de volume d'activation inverse entre les essais du changement ascendant et du changement descendant est due à la restauration des produits de dislocation qui contribuent à la contrainte d'écoulement mais qui sont facilement restaurés pendant le processus de changement de vitesse à la température ambiante. Par ailleurs, il est possible de déterminer les effets des ajouts de Si sur la sensibilité de la vitesse de déformation des alliages à l'état NA1m, la courbe de Haasen présentée à la figure 7.

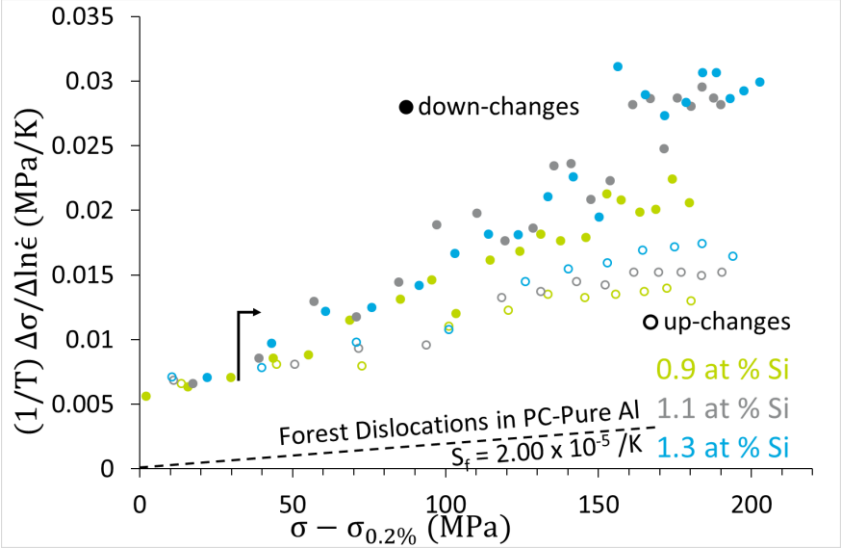

Figure 7: *Le diagramme de Haasen illustrant les effets du Si sur l'évolution du volume d'activation inverse pendant le durcissement sous contrainte. Les down-changes ¼ et 1/10 (symboles fermés) ne sont pas identifiés séparément dans ce graphique mais sont différenciés des up-changes (symboles ouverts). Il est clair que le volume d'activation inverse du rendement à environ 40 MPa est similaire pour tous les alliages, indépendamment de la direction du changement de vitesse.*

On peut observer dans la figure 7 que le volume initial d'activation inverse ne change pas de façon significative avec l'ajout de Si, ni entre les tests de changement du changement ascendant et du changement descendant. Les différences entre les tests de variation vers le haut et vers le bas apparaissent après 40 MPa d'écrouissage (marqués par la flèche noire), les tests de variation vers le bas ayant une augmentation marquée de la sensibilité de la vitesse de déformation. Au fur et à mesure que la déformation progresse, on peut constater que les ajouts de Si augmentent le volume d'activation inverse dans les tests de changement du changement ascendant et du changement descendant, ainsi que la sensibilité de la vitesse de déformation. On a constaté que la différence entre les sensibilités de la vitesse de déformation vers le bas et vers le haut augmentait avec la teneur en Si, ce qui suggère que la composante de annihilation contribuant à l'augmentation du volume d'activation inverse est directement liée à la quantité de Si présente dans l'alliage. Deux hypothèses sont faites à cet égard : Les ajouts de Si augmentent le nombre de produits de dislocations récupérables fabriqués ou les ajouts de Si facilitent l'annihilation des produits de dislocations récupérables.

iii) Effets de la composition et du traitement des alliages sur les propriétés mécaniques des alliages Al-Mg-Si-Cu

Disposant désormais d'une méthode fiable pour déterminer la sensibilité de la vitesse de déformation pour les variations ascendantes et descendantes, l'attention se porte maintenant sur les effets de la composition et du traitement des alliages sur les autres propriétés mécaniques des alliages. Dans ce travail, les courbes contrainte-déformation ont été ajustées à l'aide d'une relation constitutive en deux étapes ayant une forme de Hollomon

$$\sigma = \sigma_0 + K_{mi}\epsilon^{n_i} = \sigma_0 + K_i\epsilon^{n_i}\dot{\epsilon}^m$$

Où σ_0 est la limite proportionnelle, étant commune aux deux courbes, K_{mi}, le facteur pré-exponentiel, n_i, l'exposant de durcissement sous contrainte, et m, la sensibilité de la vitesse de déformation. La sensibilité de la vitesse de déformation a deux options ; m_{dc} quand la vitesse diminue et m_{uc}, quand la vitesse augment. Puisque l'ajustement est séparé en deux régions séparées, l'ajustement total se compose de 5 paramètres ; un commun σ_0, K_{m1} et n_1, et K_{m2} et n_2. L'équation peut être convertie pour incorporer les paramètres de sensibilité de la vitesse de déformation grâce à $K_i = K_{mi}/\dot{\epsilon}^m$ qui peut ensuite être utilisée comme équation constitutive pour la modélisation par éléments finis en fonction de la vitesse de déformation. Étant donné que cette thèse porte surtout sur le comportement des alliages à forte déformation et pendant la striction, les valeurs pour la deuxième moitié de l'ajustement seront présentées avec les données $\sigma_{0.2\%}$. Les différences dues aux additions de solutés sur les valeurs de $\sigma_{0.2\%}$, n_2, et m_{uc} et m_{dc} sont montrées dans les figures 8-10 pour les conditions a) NA1m et b) sNA1m, respectivement.

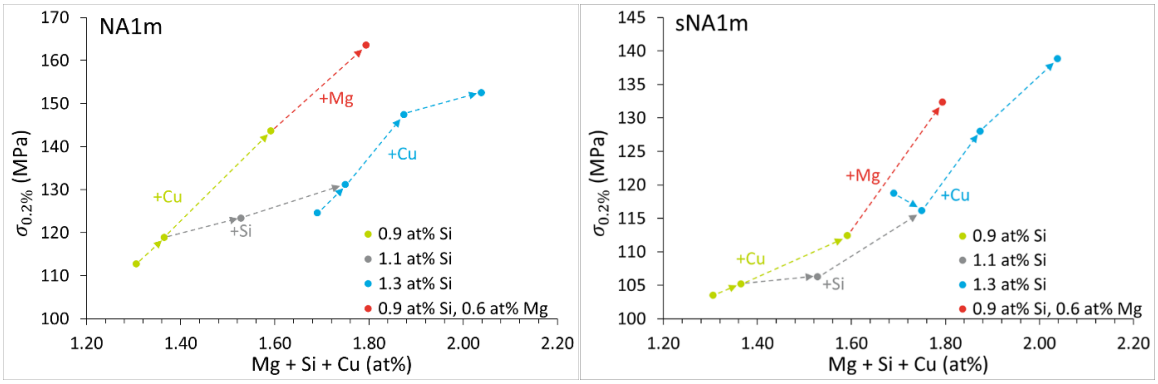

Figure 8: *L'évolution de la limite d'élasticité de 0,2 % avec la teneur totale en solutés dans les conditions* ***a)*** *NA1m et* ***b)*** *sNA1m. Pour plus de clarté, les effets des additions de Cu à 0,9 et 1,3 at % Si sont reliés par des flèches en pointillés verts et bleus, respectivement. Les effets des additions de Si à 0,2 % Cu et 0,4 % Mg sont liés aux flèches en pointillés gris. Les effets de l'addition de Mg à 0,9 % Si et 0,3 % Cu sont reliés par des flèches en pointillés rouges.*

Comme décrit précédemment, les différences entre les effets de la composition sur le comportement d'écrouissage du système Al-Mg-Si-Cu dépendent directement du processus de traitement thermique effectué et des types d'amas formés. Dans l'état NA1m, il a été démontré que les additions de Cu jouent un rôle important dans l'augmentation de l'intensité du pic de dissolution à basse température (voir Figure 4a) par rapport aux effets des additions de Si qui ne jouent pas un rôle important. Ceci se traduit par une réduction significative des effets de renforcement du Si par rapport au Mg et au Cu. La situation change dans le cas de la condition sNA1m (PA avec 1 mois de sNA) où le renforcement total dû aux additions de solutés semble être similaire pour toutes les espèces de solutés. Ceci est en corrélation avec les augmentations plus faibles de l'intensité du pic de dissolution après pré-revenu (figure 4b) pour Cu et Si. Il est à noter que Mg semble conserver son rôle d'agent durcissant relativement plus fort que les autres espèces de solutés.

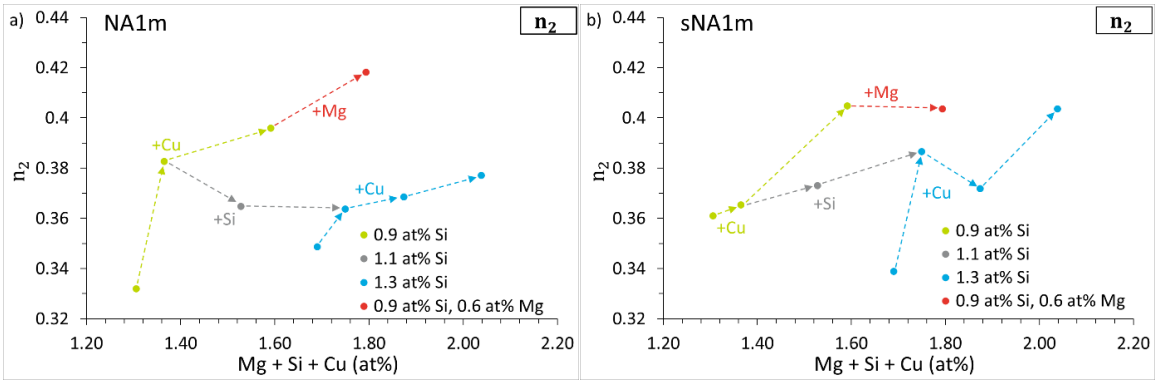

Figure 9: *L'évolution du taux de durcissement par écrouissage n_2 avec la teneur totale en solutés dans les conditions* ***a)*** *NA1m et* ***b)*** *sNA1m. Pour plus de clarté, les effets des additions de Cu à 0,9 et 1,3 at % Si sont reliés par des flèches en pointillés verts et bleus, respectivement. Les effets des additions de Si à 0,2 % Cu et 0,4 % Mg sont liés aux flèches en pointillés gris. Les effets de l'addition de Mg à 0,9 % Si et 0,3 % Cu sont reliés par des flèches en pointillés rouges.*

Les effets des additions de solutés sur l'exposant de durcissement par déformation dépendent du traitement thermique effectué, chaque élément d'alliage sera discuté et des explications possibles seront présentées. On suppose que dans l'état NA1m, il y a rétention de Mg en solution solide puisqu'il y a encore un durcissement substantiel dans la courbe de dureté NA pour l'échantillon à haute teneur en Mg et qu'il a été démontré que Mg en solution augmente le taux d'écrouissage des alliages d'aluminium. Ceci contraste avec la condition sNA1m où il y a une élimination plus complète de Mg de la solution solide, comme en témoigne non seulement la courbe de $\sigma_{0.2\%}$ dans la condition de sNA mais aussi son effet sur l'augmentation de la limite d'élasticité dans la figure 8b. Le résultat serait que l'absence d'atomes de Mg restant en solution enlèverait l'effet positif sur le taux d'écrouissage, tel qu'observé. En ce qui concerne les ajouts de Si, dans l'état NA1m, il a été démontré que les ajouts de Si augmentent la cinétique NA de telle sorte qu'après 1 mois de NA, il y a une réduction de Si libre en solution réduisant le durcissement sous contrainte malgré la présence de Si supplémentaire dans l'alliage et son rôle mineur d'augmentation de la limite élastique indiqué sur la figure 8a. Dans l'état sNA1m, c'est l'inverse qui se produit : le Si supplémentaire se joint moins aux amas de sorte qu'il y a un excès de Si en solution, ce qui entraîne un comportement accru d'écrouissage. En gardant à l'esprit l'idée d'un soluté libre en solution augmentant le durcissement par écrouissage, l'ajout de Cu au système à 0,9 % de Si a une augmentation plus positive par rapport à 1,3 % de Si, probablement due à l'augmentation de la cinétique de NA trouvée dans le système à 1,3 % de Si réduisant la quantité totale de Cu libre en solution. Dans l'état sNA1m, les effets des additions de Cu sont encore positifs alors que les différences entre les additions de Cu à 0,9 et 1,3 at % Si disparaissent.

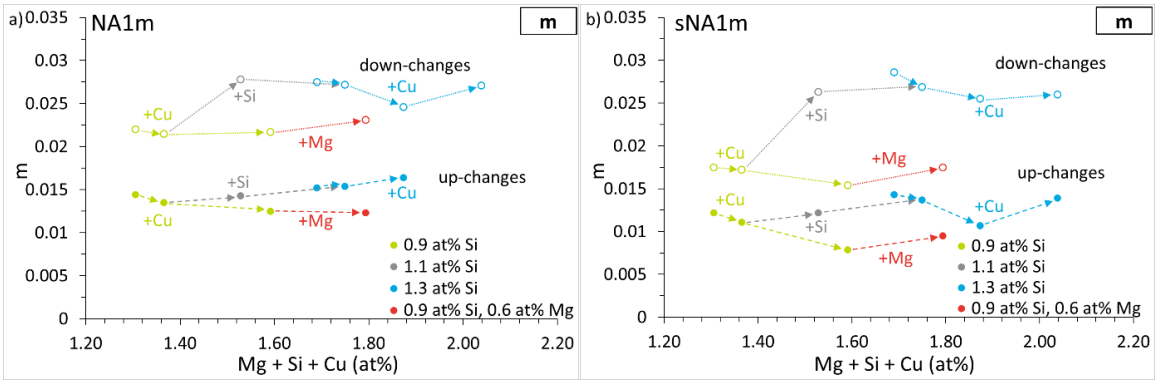

Figure 10: *L'évolution des sensibilités de la vitesse de déformation des m_{uc} (cercles fermés) et des m_{dc} (cercles ouverts) avec la teneur totale en solutés dans les conditions* ***a)*** *NA1m et* ***b)*** *sNA1m. Pour plus de clarté, les effets des additions de Cu à 0,9 et 1,3 at % Si sont reliés par des flèches en pointillés verts et bleus, respectivement. Les effets des additions de Si à 0,2 % Cu et 0,4 % Mg sont liés aux flèches en pointillés gris. Les effets de l'addition de Mg à 0,9 % Si et 0,3 % Cu sont reliés par des flèches en pointillés rouges.*

Enfin, les différences entre les additions de soluté sur les m_{uc} et le m_{dc} sont moins importantes que les propriétés précédentes où les additions de Si ont un effet positif sur les deux paramètres de sensibilité de la vitesse de déformation dans les deux conditions de traitement thermique. Dans l'état NA1m, à 0,9 % de Si, les additions de Cu résultent en une légère diminution de la m_{uc} tandis qu'à 1,3 % de Si, il y a une augmentation nette. Cet écart est probablement attribuable à l'élimination accrue du Cu libre de la solution en raison de l'accélération de la cinétique causée par l'ajout de Si. Dans l'état sNA1m, à 0,9 % en % de Si, les additions de Cu provoquent une forte diminution de la m_{uc} couplée à un pic de de mise en amas observable dans le thermographe DSC as-PA où la présence de soluté libre est généralement caractérisée par une diminution ou une contribution négative à la sensibilité de la vitesse de déformation lorsque cet effet est réduit dans le cas 1,3 % en Si. Les ajouts de magnésium entraînent une très légère augmentation du m_{uc} et du m_{dc} dans l'état sNA1m probablement dû à l'incorporation du soluté dans les amas. Dans l'état NA1m, les ajouts de Mg ont une petite contribution négative à la m_{uc} probablement due à la rétention de Mg libre en solution qui augmente le taux de d'écrouissage alors qu'il y a un très petit effet positif dans le m_{dc}.

iv) Essai de sensibilité de la vitesse de déformation à basse température : profil thermique des obstacles

Une autre méthode de caractérisation des amas et des obstacles au contrôle de la déformation est la variation de l'énergie thermique disponible dans le système lors d'expériences de sensibilité de la vitesse de déformation. Compte tenu de l'équation générale de la vitesse de déformation

$$\dot{\epsilon} = \dot{\epsilon}_0 \exp\left(\frac{\Delta G(\sigma)}{kT}\right)$$

Où $\dot{\epsilon}$ est la vitesse de déformation imposé, $\dot{\epsilon}_0$ est la vitesse de déformation de base, $\Delta G(\sigma)$, l'énergie d'activation en fonction de la contrainte, k, la constante de Boltzmann et T, la température en absolu, en modifiant la température de test, il est possible de modifier la quantité d'énergie thermique, kT, disponible pour le système. Ce changement de l'énergie thermique disponible entraîne une modification du volume d'activation à mesure que les nouvelles positions stables des dislocations sont modifiées. Comme nous l'avons montré précédemment, un changement de la vitesse de déformation appliquée, $\Delta \ln \dot{\epsilon}$, induit une modification de la contrainte, $\Delta\sigma$, de sorte que la contrainte du matériau peut être liée au volume d'activation inverse, $1/V'$ comme suit

$$\frac{1}{V'} = \frac{1}{kT}\frac{\Delta\sigma}{\Delta \ln \dot{\epsilon}}\Big|_{T,\Sigma} = \frac{1}{bdl}$$

Ce qui peut alors être lié à la sensibilité de la vitesse de déformation

$$S = \frac{1}{T}\frac{\Delta\sigma}{\sigma\,\Delta \ln \dot{\epsilon}} = \frac{1}{T}\frac{\Delta \ln \sigma}{\Delta \ln \dot{\epsilon}} = k/V'$$

Cependant, en utilisant l'équation de Taylor $(\sigma - \sigma_{0.2\%})/M = \alpha\mu b/l$ il est possible de directement résoudre la distance d'activation d_1 en déterminant la sensibilité du taux de déformation de la région dominée par les amas S_1, de telle sorte que

$$d_1 = \frac{k}{S_1 \alpha \mu(T) b^2}$$

Où α est la résistance à l'obstacle et μ(T), le module de cisaillement dépendant de la température. Il est également possible de déterminer la zone d'activation, $a' = d_1 l$, de manière à pouvoir inclure à la fois une mesure indirecte de la taille des amas, d_1, et leur distribution (ou espacement), l. En effectuant les mesures de sensibilité de la vitesse de déformation à différentes températures, il est possible de déterminer les profils d'obstacles à travers les variations de d_1, et/ou les effets de la distribution des obstacles. Un schéma montrant le profil thermique d'un exemple d'obstacle est illustré ci-dessous à la figure 11.

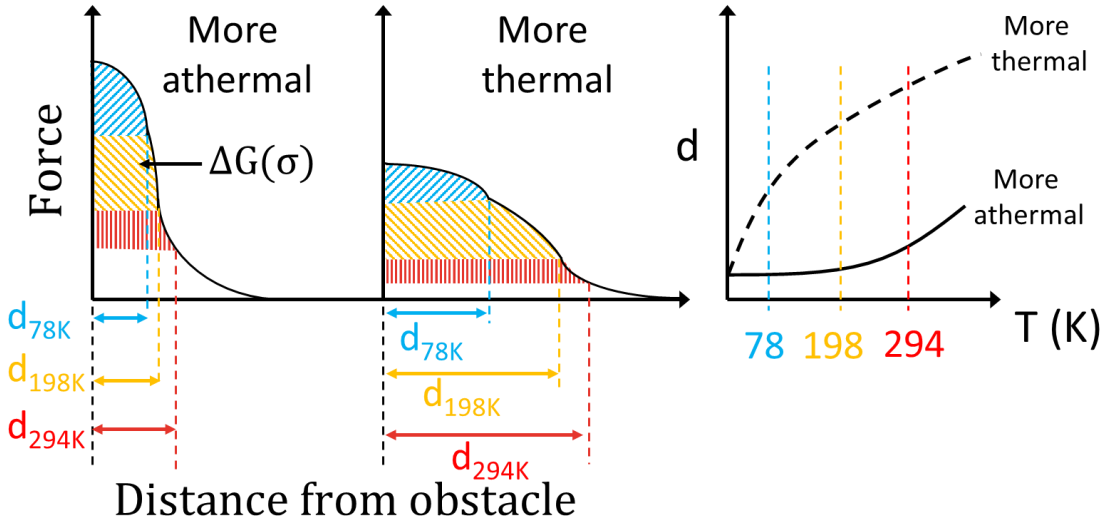

Figure 11: *Schéma de profil force-distance montrant les effets de la température sur l'évolution de la distance d'activation, d, à 78 (bleu), 198 (jaune) et 294 K (rouge). Il est à noter que les énergies thermiques sont additives de sorte qu'à 294 K, les trois régions colorées sont incluses dans le terme kT. La forme du profil dépend strictement du type d'obstacles présents et le schéma ci-dessus montre le profil d'un obstacle de type plus athermique (amas ou précipité) versus un obstacle plus thermique (atome de soluté). Ces valeurs peuvent ensuite être tracées sur un diagramme de distance d'activation en fonction de la température (illustré à droite) pour observer comment elles changent avec la température.*

Afin de générer et de commencer à comprendre la forme des obstacles présents dans l'alliage, des mesures de sensibilité de la vitesse de déformation ont été effectuées à 78, 198 et 294 K pour les neuf alliages dans les trois conditions expérimentales. La figure 12 montre la courbe de Haasen pour un seul alliage (C2S1) à l'état NA1m aux trois températures.

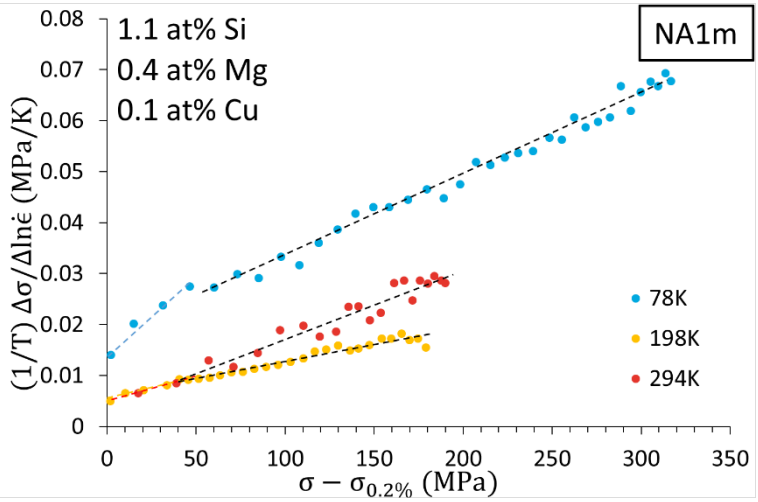

Figure 12: *Diagramme de Haasen montrant l'évolution du volume d'activation inverse avec écrouissage à 78 (bleu), 198 (jaune) et 294 K (rouge) pour l'échantillon C2S1 dans la condition NA1m. La pente S_1 est indiquée par une ligne pointillée de la couleur correspondante, tandis que la grande pente de déformation, S, est indiquée par une ligne pointillée noire. Notez que S_1 pour les essais à 198 et 294 K sont presque identiques, ce qui suggère qu'il n'y a pas de changement significatif dans la distance d'activation avec la température.*

Au fur et à mesure que la température d'essai change, il y a un changement clair à la fois dans l'interception, qui représente la densité des obstacles, et dans la pente S_1, qui représente leur capacité relative à subir une activation thermique. A 198 et 294 K, S_1 ne semble pas changer, et l'interception suggère que les obstacles se comportent de manière très similaire à ces deux températures. Si l'on compare S_1 à S à 294 K, la sensibilité du taux de déformation augmente de façon significative en raison de l'annihilation des produits de dislocation récupérables produits pendant la déformation, comme on l'a vu précédemment dans les différences observées entre les essais de variation du changement ascendant et du changement descendant. A 198 K, il n'y a presque pas de différence entre S_1 et S, ce qui suggère que les obstacles se comportent de la même manière que les dislocations et que l'énergie thermique est insuffisante pour permettre l'annihilation des produits d'interaction des dislocations produits pendant les changements descendant. 78 K, l'interception et S_1 augmentent, ce qui suggère que la densité des obstacles en cours d'activation augmente et que leur distance d'activation diminue. Par comparaison, S est significativement inférieur à S_1, ce qui indique que la distance d'activation des obstacles est beaucoup plus petite, de sorte que les dislocations doivent être beaucoup plus proches des obstacles avant l'activation thermique que les dislocations. Pour les effets de chaque élément d'alliage, il est possible de tracer le profil distance-température et de le comparer à celui des dislocations à chaque température. Pour des raisons d'espace, les exemples d'additions de Mg et de Si à 0,3 % at % Cu seront montrés pour les conditions AQ, sNA1m, et NA1m. Celles-ci sont illustrées ensemble à la figure 13.

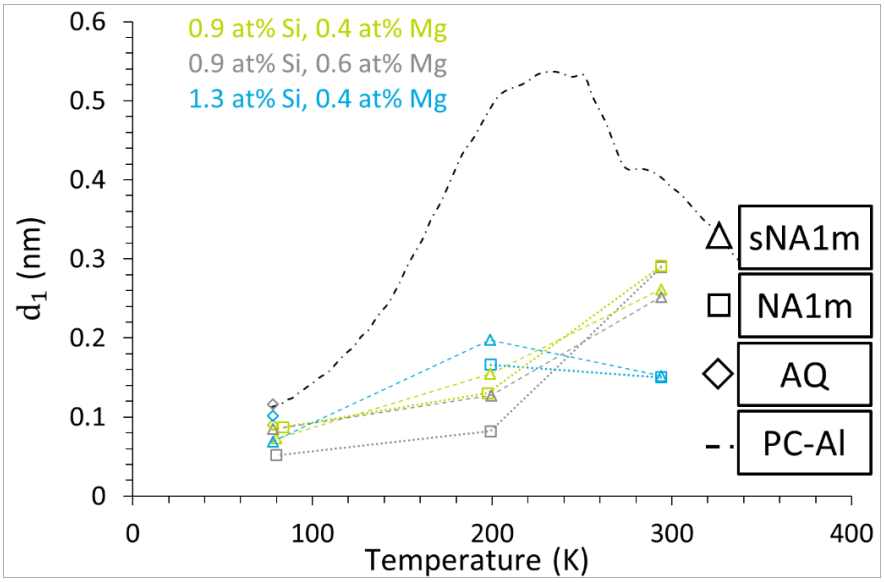

Figure 13: *L'évolution de la distance d'activation avec la température montrant les effets des ajouts de Mg (gris) et de Si (bleu) par rapport à l'alliage de base (vert), tous ayant 0,3 at% Cu. Les conditions sNA1m (triangle), NA1m (carré) et AQ (diamant) sont comparées à l'aluminium polycristalline pur (ligne pointillée noire) pour servir de référence.*

Comme on l'a montré précédemment pour l'alliage C2S1 à l'état NA1m, la sensibilité de la vitesse de déformation S_1 était la plus élevée à 78 K, ce qui donne le plus petit d_1, les mêmes tendances que pour tous les alliages et conditions. Pour chacun des alliages, la condition AQ a un d_1 le plus proche de la ligne de dislocation, car c'est la condition la plus proche d'une solution solide, ce qui donne la plus grande distance d'activation, les atomes solutés étant des obstacles très faibles et l'interaction soluté-dislocation étant dominée par le champ de contrainte local. Pour tous les alliages, la condition NA1m a une distance d'activation plus petite que la condition sNA1m, indépendamment de la température d'essai, ce qui suggère que les amas formés dans la condition NA1m sont plus forts ou plus gros. Ceci est confirmé par le fait que la limite d'élasticité $\sigma_{0.2\%}$ est plus élevée pour les alliages à l'état NA1m que pour les alliages à l'état sNA1m. A 78 K, il est difficile de discerner quel alliage a le plus petit et le plus grand d_1 mais à 198 K, cela devient plus simple, l'alliage riche en magnésium ayant la plus petite distance d'activation, et l'alliage riche en silicium, la plus grande. Il est intéressant de noter que d_1 de l'alliage riche en silicium ne change pas de façon significative entre 198 et 294 K, ce qui suggère que ces amas sont de nature plus athermique (voir figure 11), peut-être parce qu'ils sont plus gros, car il y a une élimination plus complète du soluté de la solution solide avec le Si ajouté, voir le graphique de dureté NA de la figure 3a. L'alliage de base (vert dans figure 13) et l'alliage de magnésium ajouté présentent tous deux une forte augmentation de la distance d'activation, ce qui suggère que ces amas sont de nature plus thermique et qu'il peut y avoir une composante du soluté qui contribue à la plus grande distance d'activation suggérée par le durcissement continu présenté par ces alliages même après 30 jours de NA et sNA. Il semblerait que s'il reste une partie du soluté en solution, il y a une plus grande rétention du soluté dans la condition NA1m car ces distances d'activation sont plus grandes que dans la condition sNA1m. Enfin, pour tous les alliages à des températures supérieures à 78 K, les obstacles formés lors des traitements thermiques sont considérablement plus forts que les dislocations, ayant des distances d'activation bien inférieures à celles du PC-Al. Le début de la restauration peut être observé sur la ligne PC-Al, avec un début à 210 K où la distance d'activation commence à diminuer.

v) Analyse de la striction dans les alliages d'aluminium durcissant par vieillissement : effets de la sensibilité de la vitesse de déformation et de l'écrouissage

La dernière composante de cette thèse consistait à appliquer la relation constitutive à la modélisation par éléments finis afin de mieux comprendre les effets du durcissement par déformation et de la sensibilité de la vitesse de déformation à la fois du changement ascendant et du changement descendant sur la formation et la propagation de la striction. En général, l'apparition d'une striction diffuse est dictée par le critère de Considère selon lequel une fois que le taux de durcissement par déformation, $d\sigma/d\epsilon$ diminue en dessous de la contrainte d'écoulement, σ, la localisation de la déformation aura lieu. Cependant, comme la relation constitutive dictant la contrainte d'écoulement est donnée par une relation de Hollomon modifiée, $\sigma = \sigma_0 + K\epsilon^n\dot{\epsilon}^m$, le critère de Considère devient légèrement plus complexe et s'exprime comme suit

$$\frac{d\sigma}{d\epsilon} = \frac{K\epsilon^n\dot{\epsilon}^m}{\epsilon}\left(n + m\frac{\partial \ln \dot{\epsilon}}{\partial \ln \epsilon}\right) = \sigma_0 + K\epsilon^n\dot{\epsilon}^m$$

L'effet intéressant est que lors d'une déformation uniforme, le terme $\frac{\partial \ln \dot{\epsilon}}{\partial \ln \epsilon}$ est nul de sorte que le critère général Considère est rétabli. Cependant, lors de la formation d'une striction diffuse, $\frac{\partial \ln \dot{\epsilon}}{\partial \ln \epsilon}$ devient non nul de sorte qu'il y a un effet de la sensibilité de la vitesse de déformation. La figure 14 montre le schéma d'un essai de traction conduit au-delà du critère de Considère de sorte qu'il existe un profil de vitesse de déformation non uniforme et identifie les régions intérieures et extérieures à la striction où la vitesse de déformation locale est supérieure et inférieure à la vitesse de déformation appliquée, respectivement. Des études approfondies ont été réalisées sur les effets de la sensibilité de la vitesse de déformation sur le comportement d'allongement post-uniforme des matériaux, ce qui permet, en augmentant la sensibilité de la vitesse de déformation, soit de stabiliser la striction diffuse, soit de permettre sa propagation, ce qui est le cas par exemple dans les matériaux super-plastiques. Cependant, en raison de la nature délicate de la mesure précise de la sensibilité de la vitesse de déformation vers le bas, seule la sensibilité de la vitesse de déformation vers le haut est généralement utilisée pour la région à l'intérieur de la zone de striction où la vitesse de déformation a augmenté alors que peu ou pas d'attention a été placée sur la région externe à cette zone.

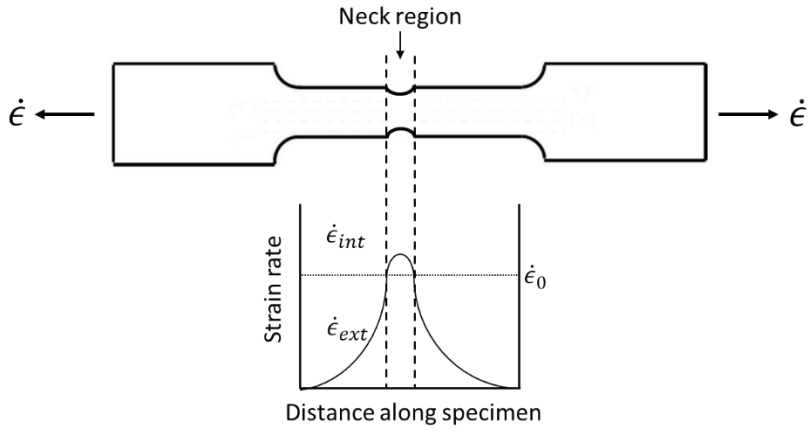

Figure 14: *Schéma montrant la distribution de la vitesse de déformation le long de la longueur de la jauge, à la fois à l'intérieur du col, avec $\dot{\epsilon}_{int} > \dot{\epsilon}_0$, et à l'extérieur du col, avec $\dot{\epsilon}_{ext} < \dot{\epsilon}_0$, où $\dot{\epsilon}_0$ est la vitesse de déformation de base. Dans l'exigence d'avoir une distribution continue de la déformation et du taux de déformation, il y aura inévitablement une distance, $d_{\dot{\epsilon}_0}$, où la vitesse de déformation actuel est la vitesse de déformation de base.*

Comme le montre le schéma ci-dessus, en se déplaçant le long de la distance de l'échantillon de traction, il existe trois régions : a) une région intérieure du col, ayant une vitesse de déformation $\dot{\epsilon}_{int}$ étant contrôlée par m_{uc}, b) une région extérieure du col, ayant une vitesse de

déformation $\dot{\epsilon}_{ext}$ étant contrôlée par m_{dc}, et c) une région de transition ayant la vitesse de déformation de base, $\dot{\epsilon}_0$.

$$\sigma_{uc} = \sigma_0 + K_{uc}\dot{\epsilon}^{m_{uc}}\epsilon^n \quad \text{(a)}$$
$$\sigma_{dc} = \sigma_0 + K_{dc}\dot{\epsilon}^{m_{dc}}\epsilon^n \quad \text{(b)}$$

En raison des vitesses de déformation uniques et locales, l'intérieur du cou sera contrôlé par l'équation (a) et l'extérieur par l'équation (b), ces équations étant à la base de la relation de Considère dans leurs régions respectives. Comme on l'a vu précédemment, le m_{dc} est supérieur au m_{uc}, de sorte qu'une diminution de la vitesse de déformation à l'extérieur du cou peut entraîner une diminution plus importante de la contrainte d'écoulement que l'augmentation due à la vitesse de déformation locale accrue sur l'intérieur du cou. L'interaction entre ces deux régions peut permettre de mieux comprendre l'adaptation des matériaux par l'intermédiaire des deux sensibilités de la vitesse de déformation afin de retarder l'apparition d'une striction localisée. Nous avons réalisé une étude paramétrique pour faire varier les valeurs de m_{uc} et m_{dc} à 0 ou 0,05 avec deux exposants de durcissement d'écrouissage différents, afin de mieux comprendre les effets des sensibilités de la vitesse de déformation sur la formation, la propagation, la stabilisation et la localisation d'une striction générée artificiellement. Les modèles ont été déformés jusqu'à ce que la région uniforme du modèle obtienne la déformation répondant au critère de Considère, 0.265 pour les paramètres n = 0.375 et 0.281 pour les paramètres n = 0.400, respectivement. Le modèle a été exécuté en utilisant Abacus/CAE 6.14.3 en utilisant la relation constitutive susmentionnée avec une vitesse de déformation de base imposé, $\dot{\epsilon}_0 = 5x10^{-4}\,s^{-1}$, identique aux vitesses de déformation de base des expériences de sensibilité de la vitesse de déformation. Pour des informations plus détaillées sur les conditions du modèle et sur le maillage, voir le chapitre 8 dans le corps de la thèse. Un exemple de distribution de la déformation et de la vitesse de déformation d'un échantillon jusqu'à la limite de l'allongement uniforme sont illustrées à la figure 15 ci-dessous.

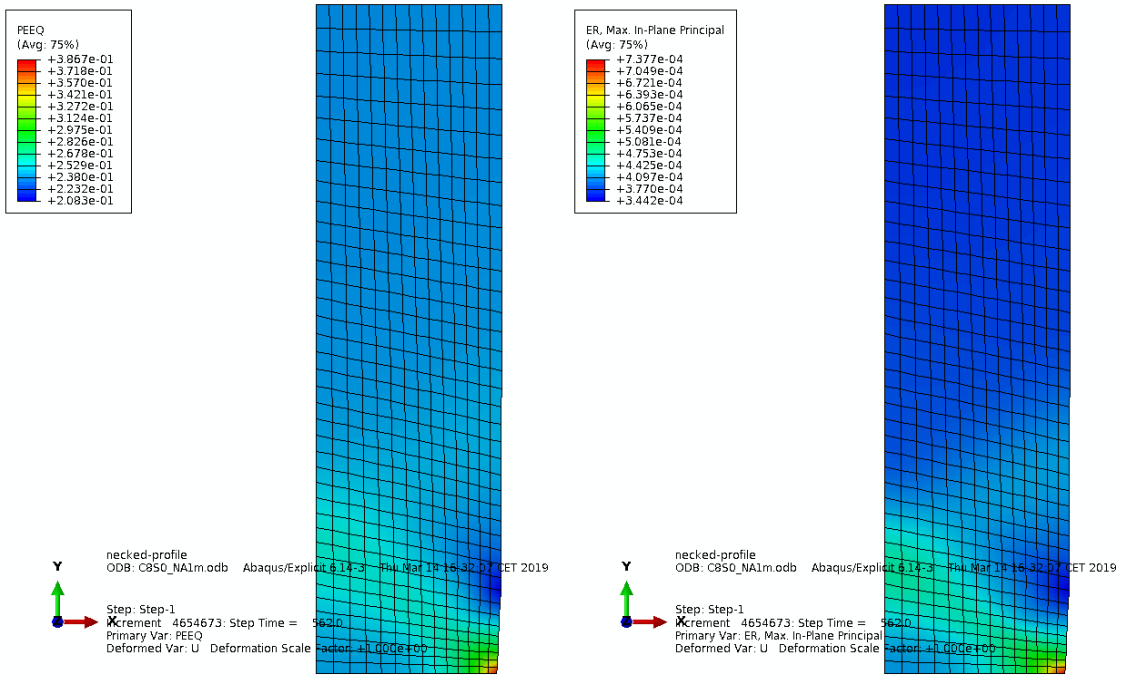

Figure 15: *Les distributions* ***a)*** *de déformation et* ***b)*** *de vitesse de déformation de l'échantillon après avoir été déformées à ϵ_D = 0.241 (dans la région uniforme). Il est clair que la déformation et la vitesse de déformation les plus élevées se*

situent au centre du cou et diminuent jusqu'à un minimum à la limite du cou artificiel, mais ce minimum est bien inférieur à la vitesse de déformation imposée de 5 x 10^{-4} s^{-1} et est dû à l'insertion du cou artificiel.

On voit clairement qu'il y a une région ayant à la fois une grande déformation et une grande concentration de vitesse de déformation qui se trouve au centre du cou. La déformation et la vitesse de déformation diminuent en s'éloignant (le long de l'axe des y) du cou jusqu'à atteindre une distance minimale de 1.5 mm ; l'emplacement de l'apparition du cou artificiel. Les figures 16 et 17 montrent les profils de déformation de sortie et les profils de distance de vitesse de déformation, respectivement, pour les 4 paramétriques ayant un exposant d'écrouissage de 0.375 après avoir été déformés en ϵ_D de 0.265.

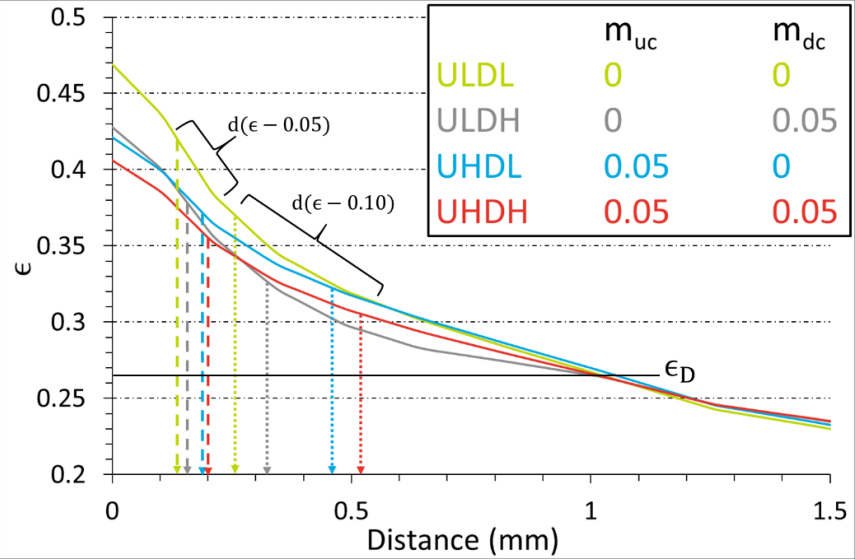

Figure 16: *L'évolution de la déformation prédite par FEM en fonction de la distance du centre du cou artificiel pour les échantillons paramétriques ULDL (vert), ULDH (gris), UHDL (bleu) et UHDH (rouge). Les lignes pointillées verticales sont les lignes $d_{0.05}$ et les lignes pointillées sont les lignes $d_{0.10}$. Ces lignes aident à illustrer l'évolution générale de la distribution de la déformation le long du cou formé.*

Les effets de la m_{uc} et de la m_{dc} sont facilement perceptibles dans l'évolution de la distribution des déformations à partir du centre du cou. L'augmentation de m_{uc} ou de m_{dc} a une forte influence sur la diminution de la contrainte au centre du cou, tandis que la combinaison de l'augmentation de la m_{uc} et de m_{dc} à l'unisson entraîne une diminution supplémentaire. Comme il est important de comprendre non seulement la déformation au centre du cou mais aussi la distribution de la déformation, la distance pour une chute de 0.05 et 0.10, $d_{0.05}$ et $d_{0.10}$, respectivement, est indiquée. Il n'est pas surprenant que les paramètres ULDL donnent la distribution de déformation la plus radicale car il n'y a pas d'effet de $m\frac{\partial \ln \dot{\epsilon}}{\partial \ln \epsilon}$ car m est nul, de sorte que lors de la formation d'un col diffus, il n'y a pas de durcissement supplémentaire dû à la vitesse de déformation. Ceci est en contraste avec le fait que $\frac{\partial \ln \dot{\epsilon}}{\partial \ln \epsilon}$ soit négatif entraîne une chute de contrainte en dehors du cou de sorte que le critère de Considère est rempli en dehors du cou et aussi à l'intérieur parce que la m_{uc} est nul. La situation est inversée pour les paramètres UHDL : $\frac{\partial \ln \dot{\epsilon}}{\partial \ln \epsilon}$ est positif à l'intérieur du cou et nul à l'extérieur du cou, de sorte que le durcissement supplémentaire causé par m_{uc} fait que le critère Considère n'est pas respecté à l'intérieur du cou en raison du durcissement accru mais est toujours respecté à l'extérieur du cou, entraînant la propagation du cou. Ces effets sont plus apparents dans les distances $d_{0.10}$, de sorte que l'effet de m_{uc} sur la délocalisation de la déformation à l'intérieur du cou est supérieur à celui de m_{dc}. Enfin, dans le cas où m_{uc} et m_{dc} sont tous deux augmentés comme dans le cas de l'UHDH, les effets du durcissement local à l'intérieur du cou et de la chute de contrainte dans les régions extérieures entraînent la délocalisation et la propagation du cou et donnent les plus faibles concentrations de déformation dans et autour du cou.

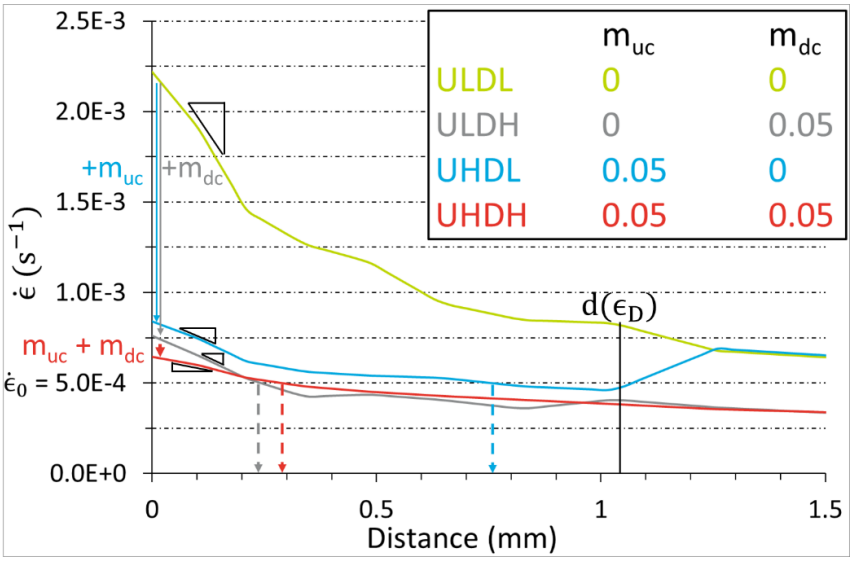

Figure 17: *L'évolution du taux de déformation avec la distance du centre du cou artificiel dans le FEM pour les échantillons paramétriques ULDL (vert), ULDH (gris), UHDL (bleu) et UHDH (rouge). Les lignes pointillées verticales en b) sont les distances requises pour obtenir la vitesse de déformation de base, $d_{\dot{\epsilon}_0}$. Les triangles montrent la pente de l'indicateur de déformation avec la distance près du centre du cou pour faciliter la comparaison entre les échantillons.*

Comme la même méthode a été employée pour les effets de la m_{uc} et du m_{dc} sur la distribution de la vitesse de déformation autour de la striction, il est possible de comprendre l'évolution de celle-ci par accumulation de la déformation. Il est clair que m_{uc} et la m_{dc} agissent individuellement, et à l'unisson, pour limiter l'augmentation de la vitesse de déformation au centre du cou, bien que leur effet composé soit moins important qu'une augmentation individuelle, par rapport au cas des ULDL. Les paramètres UHDL entraînent une diminution de la vitesse de déformation à une distance inférieure à d_{ϵ_D}, ce qui fait que la vitesse de déformation augmente en dehors de cette région. Cette augmentation à grande distance entraîne une accumulation de la contrainte à distance du centre du col et indique que m_{uc} agit en prolongeant la durée de la striction diffuse avant une transition vers une striction localisée. L'évolution des vitesses de déformation pour UHDL est légèrement inférieure à celle pour ULDH et fournit des preuves supplémentaires de stabilisation du cou. Bien que la vitesse de déformation du col de l'ULDH soit inférieure à celle de l'UHDL, la distribution de la vitesse de déformation autour du centre du col est plus abrupte, de sorte que la partie du col sensible à la vitesse (située à l'extérieur de $d_{\dot{\epsilon}_0}$) est considérablement réduite et indique que le col est plus localisé. Enfin, l'augmentation de m_{uc} et de m_{dc} dans le cas de UHDH entraîne non seulement une réduction de la vitesse de déformation au centre du cou, mais aussi une réduction significative de la distribution de la vitesse de déformation sur la longueur de l'échantillon. Cela se reflète dans le profil de déformation où il n'y a pas de grande différence dans la distribution de la déformation le long de la longueur de l'échantillon, ce qui indique clairement la lenteur de la formation d'un col diffus qui finira par se localiser en cas de sur contrainte importante.

En général, on peut dire qu'il est plus avantageux d'augmenter à la fois m_{uc} et m_{dc} pour permettre à la fois la stabilisation et la propagation du col après la fin de l'allongement uniforme. L'effet durcissant de m_{uc} semble être plus important que l'effet adoucissant de m_{dc}. On peut dire que la plus grande partie de la propagation du col (augmentant la vitesse de déformation à l'extérieur du col) est contrôlée par m_{uc} tandis que les propriétés de localisation du col sont dues au comportement adoucissant extérieur causé par m_{dc}. La délocalisation et la propagation du col ne sont probablement possibles que lorsque m_{uc} et m_{dc} sont très élevés, comme c'est le cas pour les matériaux super-plastiques. Bien qu'ils ne soient pas montrés ici, les effets de l'augmentation de

l'exposant d'écrouissage entraînent une diminution des effets de m_{uc} et de m_{dc} en raison de la résistance accrue de l'échantillon en déplaçant le début du col diffus vers des déformations plus élevées (et des forces supérieures) de sorte que le durcissement ou le ramollissement ajouté sur le col intérieur et extérieur, respectivement, induisent une variation d'une fraction inférieure de la résistance totale du matériau. Cela est dû au fait que la partie du critère de Considère contrôlant le composant de durcissement par déformation après le col, $n + m\frac{\partial \ln \dot{\epsilon}}{\partial \ln \epsilon}$, nécessite une augmentation ou une diminution plus importante du taux de déformation local pour produire un effet équivalent à une valeur n inférieure. Par ailleurs, l'augmentation de m_{uc} ou de m_{dc} aurait le même effet que l'augmentation ou la diminution du taux de déformation, mais avant l'apparition d'un col local.

CONCLUSIONS

Les conclusions suivantes peuvent être tirées à l'issue de ces travaux :

- Les types d'amas formées pendant NA et PA ne sont pas les mêmes
    - Pendant NA, Cu et Mg ont une forte influence sur la formation des amas capables de se dissoudre à basse température. Les ajouts de Si n'augmentent pas de façon significative la formation de ces amas, mais ils contribuent à réduire davantage leur température de dissolution.
    - Au cours du pré-revenu, un seul type d'amas semble se former, il se dissout à des températures supérieures à celles qui se sont formés au cours du NA. Les additions de Cu, Mg et Si semblent toutes augmenter l'intensité de dissolution des amas. Il a été démontré que le PA limite l'effet négatif du vieillissement naturel souvent observé dans les alliages Al-Mg-Si-Cu.
- Il y a une grande différence entre les volumes d'activation inverse et les sensibilités de la vitesse de déformation en variation ascendante (plus petits) et en variation descendante (plus grands). L'utilisation de la méthode de compensation pendant les essais fait partie intégrante de l'obtention de mesures précises et fiables, en particulier pendant les essais descendants.
- L'expression des additions de Cu, Mg et Si sur les propriétés mécaniques obtenues dans la série 6000 dépend directement du traitement thermique effectué.
    - En présence de NA, Cu et Mg ont une influence nettement plus grande que Si sur l'augmentation de la limite d'élasticité.
    - Pendant le PA, tous les éléments d'alliages contribuent de manière égale à l'augmentation de la limite d'élasticité.
    - L'ajout de Si augmente à la fois la sensibilité de la vitesse de déformation en variation ascendante et descendante, indépendamment du traitement thermique. Les ajouts de Cu et de Mg n'ont pas tendance à affecter celle-ci.
- Il est possible de déterminer le profil d'interaction amas-dislocation en effectuant des mesures de sensibilité de la vitesse de déformation à différentes températures.
    - La distance d'activation des alliages à l'état sNA1m est généralement inférieure à celle de l'état NA1m, ce qui suggère une élimination plus complète du soluté de la matrice.
    - Il a été démontré que l'ajout de Si réduit la distance d'activation à la température ambiante, ce qui suggère une élimination plus complète du soluté de la matrice, comme l'indiquent les courbes de dureté NA et sNA.
- Il a été démontré que l'augmentation de la m_{uc} et de m_{dc} ensemble réduisait l'intensité de la vitesse de déformation au centre du col de striction en conjonction avec la vitesse de

déformation et la distribution de la déformation sur toute la longueur du col. La distance entre le centre du col et la vitesse de déformation de base s'est avérée insuffisante pour définir la taille du col, mais elle joue un rôle important dans la compréhension de l'évolution de celui-ci.

- La majeure partie de l'allongement post-striction est déterminée par le paramètre m_{uc} en raison de l'effet très localisé de l'augmentation de la vitesse de déformation à l'intérieur du col.
- Le composant m_{dc} n'agit que sur les régions extérieures au col, étant de taille beaucoup plus importante de sorte que son effet est effectivement "dilué".
- Dans l'étude de l'échantillon, la distance par rapport à la vitesse de déformation de base est contrôlée initialement par le gradient de déformation et ensuite par l'intensité de la vitesse de déformation au centre du col.

1 Introduction

The environmental regulations surrounding the reduction of fuel emissions in transport have driven the necessity for improving automotive fuel efficiency [1], specifically in passenger vehicles. The objective of reducing the emissions can be undertaken by many methods; improved engine performance, enhanced filtering systems, and weight reduction, which has been the focus of most automotive manufacturers (AMs). Switching from higher density, stronger, more ductile steels to lighter, less ductile and formable aluminium alloys has been shown to be a suitable method for reducing fuel consumption through weight reduction. However, the most cost-effective sheet aluminium alloys used for body-in-white (BIW) applications, the 6000-series, still display a lack of formability to meet design requirements imposed during forming whereby cracking occurs at sharp bends [2]. The current alloys used are AA6111 (USA) and AA6016 (EU) both of which have sufficient strength, corrosion resistance, and surface finish but lack the formability demands of suppliers [3], [4]. As such, there is a strong demand to understand the influence of the composition and heat treatments in order to optimize the formability of this alloys series such that sharper bends and/or reduced sheet thicknesses may be implemented allowing for improved aesthetics and reduced vehicle weight.

The 6000-series alloys of aluminium used in BIW applications are based on the ternary Al-Mg-Si system with the option of Cu additions. Similar to the 2000-series (Al-Cu) and 7000-series (Al-Zn) alloys, the 6000-series are age-hardenable alloys indicating that they may harden over time. Solute atoms (Mg, Si, and Cu) diffuse to form metastable obstacles (known as clusters and precipitates, depending on their size, stoichiometry, stability, etc) which influence the plastic deformation response of the automotive sheets during forming, and strengthen the material after final heat treatment. Conventionally, the alloys used for BIW applications are cast at a certain composition, hot-rolled to reduce the thickness, solutionized, and finally, cold-rolled to a final gauge. They may undergo an independent recrystallization step, or may be recrystallized at the same time as a final solution treatment, used to revert any precipitates formed during previous processes to a “random” solid solution. The final step prior to shipment to automotive manufacturers is either to ship the sheet directly, or to apply a stabilization treatment (pre-ageing) to reduce the formation of clusters during the shipping process. Once received, the AMs cut the sheet to size, and stamp the component into its desired shape (door, roof, hood, etc), and is then painted. The now painted BIW component passes through a paint-drying process, known as the paint-bake (PB) cycle, equivalent to 20 minutes at 185°C [3], used to both cure the paint and simultaneously strengthen the alloy by forming precipitates. The effects of composition and heat treatment on the forming response of the sheet into its final shape is the process that must be improved and more thoroughly understood.

1.1 Thesis approach

The basis of understanding the influence of composition on the formability of 6000-series aluminium alloys requires connecting the different length-scales involved from atomic to millimeter. The microstructure state prior to the forming operation is characterized by the distribution of solutes into clusters, whose characteristics are very elusive, due to the lack of specific crystallography, defined interfaces with the aluminium matrix, and the characteristic composition. However, different characterization techniques such as atom probe tomography (APT), differential scanning calorimetry (DSC), and Vickers micro-hardness testing (VH) can be used to obtain complementary information on the state of clustering as a function of processing parameters and alloy composition. The use of tensile and strain rate sensitivity (SRS) tests allows

capturing the mechanical properties linked to the formability behaviour. Connecting these observed mechanical properties and corresponding analyses, to the microstructure observations and implementation into finite element modeling (FEM) should allow for a more complete understanding of the role played by each solute species and heat treatments on the formability of 6000-series aluminium alloys.

The main objective of this research project is to explore the connection between the composition and the formability of 6000-series aluminium alloys, coupled with the state of clustering through two common heat treatment processes, namely natural ageing and pre-ageing. For this purpose, the influence of Cu, Si, and Mg on the formability are independently studied through systematic variations of the alloy composition in an attempt to isolate and understand the relative contributions of each alloying element to the mechanical properties and formability in this alloy series. A total of nine alloys have been studied. The thesis will be separated into chapters based on a bottom-up approach whereby each section will rely upon the previous, beginning with the effects of composition and heat treatments on the microstructure, to aid in developing the overall comprehension on the factors influencing formability. Each chapter after the literature review and methodology contained within the thesis may be treated as a stand-alone publication. Following the presentation of the papers, there will be a general discussion, conclusion, and perspectives in order to connect the themes of each of the papers into the general framework of this thesis. A summary of the papers contained within this thesis are presented below:

1.1.1 Formation of clusters during natural and pre-ageing of Al-Mg-Si-Cu alloys

Complimentary microstructure characterization by differentially scanning calorimetry and Vickers hardness testing are used to understand the formation of clusters during natural and pre-ageing processes as well as the subsequent artificial ageing responses. The effect of alloy composition will be related to the types and thermal stability of the clusters that form, along with the evolution of their kinetics through both direct natural ageing, and pre-ageing with secondary natural ageing processes. Differences between these two kinetic sequences will be discussed. Furthermore, the compositional effects on the subsequent artificial ageing kinetics and paint bake response in the alloys will be presented and discussed.

1.1.2 Asymmetry in strain rate sensitivity testing: methods and analyses

Conventionally, strain rate sensitivity (SRS) testing is performed using an instantaneous increase in the strain rate (up-change) which is important for understanding the stress-state at the interior of necking where the local strain rate increases. The testing apparatus used in this work allowed also for applying a decrease in the applied strain rate (down-change) whereby an asymmetry between down-change and up-change SRS tests within the Haasen plot is shown after a certain degree of plastic deformation. Possible origins of this asymmetry are discussed and analysis methods are developed and tested in order to connect the effects of Si content to the SRS asymmetry. The asymmetry is suspected to be due to sub-micron recoverable dislocations generated during deformation as the up-change and down-change tests only show asymmetry after a certain flow stress.

1.1.3 Effects of alloy composition and processing on the mechanical properties of Al-Mg-Si-Cu alloys

The mechanical properties of the nine 6000-series aluminium alloys having various Mg, Si, and Cu contents are examined through both tensile and strain rate sensitivity tests for the two heat treatment conditions, namely water quenched and naturally aged, and pre-aged followed by secondary natural ageing. The changes in the yield stress, strain hardening rate and capacity,

uniform and post-uniform elongations, as well as constitutive parameters are connected to the types of clusters formed by the two heat treatment schedules with varying solute contents. These properties are related back to the observations made in the DSC thermograms and the specific cluster dissolution intensity and thermal stability to explain the different observed phenomena.

1.1.4 Characterization of thermally activated dislocation glide in naturally aged Al-Mg-Si-Cu Alloys: what it tells us about clusters

By changing the testing temperature during both tensile and strain rate sensitivity tests, the amount of thermal energy within the system is adjusted. The reduction in thermal energy available to the system results in the suppression of high-energy processes (such as dislocation recovery, point defect diffusion, etc) which inevitably changes the deformation behaviour of the tested alloys. Each of the nine alloys have been tested in three heat treatment conditions, at three different temperatures, with each displaying two domains of strain rate sensitivity, S_1 (directly after yielding) relating to the initial obstacle (cluster) behaviour and a large-strain strain rate sensitivity, S. The evolution of these parameters with both temperature and alloy composition are discussed and compared to the values of pure polycrystalline aluminium in order to detail the effects of alloying on the strain rate sensitivities in Al-Mg-Si(-Cu) alloys. The changes in yield stress, activation volume and distance, and derived obstacle force-distance profiles are determined and discussed in terms of the changes in microstructure.

1.1.5 An analysis of necking formation in age-hardenable aluminium alloys: the effect of strain rate sensitivity

The initial understanding of increasing the strain rate sensitivity (SRS) leading to an improved formability through delaying the onset of localized necking is conventionally tied to the increased strain rate observed within the diffuse neck. This work has evidenced an asymmetry between the SRS measured during increasing and decreasing strain rate jumps, namely the decreasing SRS is larger than that of the increasing SRS. The result is that the same (but opposite) change in the local strain rate will result in a greater decrease in stress due to the decreased local strain rate compared to the relative increase in stress caused by the local increase in strain rate. The influence of this phenomenon on the development of a diffuse neck is tested through the finite element modelling of the neck evolution during a tensile test using a specific constitutive law whose parameters depend on sign of the strain rate evolution.

1.2 References

[1] V. Mickunaitis, A. Pikunas, and I. Mackoit, “REDUCING FUEL CONSUMPTION AND CO2 EMISSION IN MOTOR CARS,” *Transport*, vol. XXII, no. 3, pp. 160–163, 2007.

[2] J. Hecht and A. Hoffmann, “Audi Ultra Strategy - Lightweight Design Technologies in Competition,” presented at the Proceedings of the Materialien im Karosseriebau Automotive Circle International, Bad Nauheim, Germany, 2013.

[3] J. Hirsch, “Recent development in aluminium for automotive applications,” *Trans. Nonferrous Met. Soc. China*, vol. 24, no. 7, pp. 1995–2002, Jul. 2014.

[4] J. Hirsch, “Automotive trends in aluminium-The European perspective,” in *Materials Forum*, 2004, vol. 28, pp. 15–23.

2 Literature Review

The purpose of age-hardenable aluminium alloys is to produce a material that can be heat treated in order to increase its yield strength by the formation of obstacles to dislocation motion. There are three main families of age-hardenable aluminium alloys, designated by the Aluminium Association as the AA2xxx (Al-Cu), AA6xxx (Al-Mg-Si), and AA7xxx (Al-Zn-Mg) series. Other solutes and alloying elements may be added to each of these series but the main hardening species are those listed. The AA6xxx series is an ideal candidate for the automotive industry having adequate strength, good corrosion resistance and although it has good formability, it is less than that found in automotive steels. The weight reductions realized by switching from steels to the AA6xxx series exist but are not optimized as thicker gauges must be used to provide sufficient formability [1].

The formability of aluminium alloys depends on the microstructure at different length scales (grain size, texture, composition, dispersoids, clusters) and the resulting mechanical properties, namely yield stress, strain hardening and strain rate sensitivity, and related macroscopic properties such as ultimate tensile strength, elongation to failure, post-necking strain. The complex interplay between the microstructural features on dislocation production, multiplication, and recovery results in the influence of composition on the formability. This necessitates that a hierarchal approach be taken in order to connect the alloy composition, to the microstructure formed, to its resulting mechanical properties which finally influence the overall formability of the sheet metal. Thus, systematic studies of varying levels of Mg, Si, and Cu, must be performed and tested in a variety of ways in order to isolate the effects of each alloying element on the various mechanical properties that influence formability. Connecting each of these hierarchal length scales is not simple and a thorough understanding of both the microstructure features and the mechanical properties is essential.

2.1 Microstructure effects

The material properties of aluminium alloys are the expressions of the microstructural components contained within and the type of deformation mode applied; uniaxial tension, biaxial tension, creep, etc. Age-hardenable aluminium alloys, such as the AA6xxx series, contain many microstructure features such as solute atoms, clusters, precipitates, dispersoids, and grain boundaries. Each of these components can affect one (or more) of the mechanical properties and interact with the complex interplay of dislocation production and annihilation during plastic deformation. The main microstructural features that will be examined in this work are those of free solutes and clusters which act as dislocation obstacles.

The formation of each of these features depends on the composition [2]–[8], and ageing treatments [9]–[12] defined by temperature and time. The cause of the formation of solute clusters and precipitates is the reduction in Gibbs free energy of the system, ΔG which is driven by the time-dependent organization of random solutes from the solid solution due to the initial solution heat treatment (SHT). In the AA6xxx series alloys, the main solute components that are changed during heat treatments are Mg, Si, and Cu (if contained), whereby Al-Mg-Si(-Cu) complexes will form during the heat treatments to form metastable phases. The precipitation sequence in the Al-Mg-Si(-Cu) system follows

$$\text{SSSS} \rightarrow \text{solute clusters} \rightarrow \text{pre-}\beta'' \rightarrow \beta'' \rightarrow \beta', \text{U1, U2, C, L, B}', \text{Q}' \rightarrow \beta, \text{Q, Si}$$

Where SSSS is the super-saturated solid solution occurring directly after the SHT and solute clusters having varying compositions. The current understanding of the formation of these complexes are presented in the following sections.

2.1.1 Solutes and clusters

The distribution of alloying elements contained within the aluminium matrix of age-hardenable aluminium alloys is directly based on the phase diagram of the system in question. The initial SHT is assumed to dissolve all solutes within the material (as dictated by the phase diagram) whereby upon a reduction in temperature, the solutes remain "trapped" in a high-energy state (that of a random solid solution) until sufficient time and energy (temperature) is provided to permit the diffusion of hardening species to change the solute distribution. Well before the formation of precipitates, the presence of clusters takes place, defined as non-random groups of solutes, distributed on the solvent crystal lattice, without a set composition or crystal structure. Individual clusters can be defined e.g. in atom probe volumes from criteria on solute separation. However, clusters are inevitably present in any structural state, including in a random solid solution. Thus, a "clustered state" means a microstructural state comprising a higher density of clusters than a random state, and/or clusters richer in solute. An alternative description of clustering has been used in the literature as fluctuations of the local solute concentration, in an analogy to the unmixing of solutes during spinodal decomposition [13]. In the AA6xxx series of alloys, two cluster types have been distinguished; type i and type ii depending on the temperature of formation being below or above 70°C, respectively [2]. These will be discussed later.

Since the solutes present within aluminium alloys are substitutional, certain phenomena may be observed during plastic flow such as Portevin-Le Châtelier (PLC) [14], solute drag or dynamic strain-ageing (DSA) [15]–[19], which are typically associated with a negative strain rate sensitivity (nSRS) [20], [21] or a decrease in the SRS. The presence of these deformation phenomena are related to the dynamic interaction of dislocations and free solutes or solute clusters that may form during the arrest time of dislocation motion. Depending on the concentration of solutes and the deformation rate, these effects may vary in terms of critical strain or stress before they are triggered [22], [23]. Besides, the presence of solute atoms within aluminium alloys are typically characterized by an increased strain hardening rate, which has been frequently associated with a decrease of dislocation recovery during deformation [16], [24].

When clusters form within these alloys, they become obstacles to plastic deformation and thereby increase the strength of the alloy [25]–[27]. Their subsequent interaction with dislocations will be dependent on their size and mechanical stability [28], [29]. Clusters being of the same crystal nature as the matrix and of low solute concentration, they are shearable in nature. As a result, the strengthening contribution of the obstacles will be closely related to the specific cluster strength as shown by de Vaucorbeil et al. [28]. Their influence on strain hardening is more complex as it can be both negative (due to cluster shearing and increased dynamic recovery because of lower solute content) or positive (due to a dynamic evolution of the clusters during straining).

2.1.2 Precipitates

The formation of precipitates within age-hardenable aluminium alloys has been studied in detail. Although there are many types of precipitates that can form within AA6xxx series alloys such as β'', β', β, Q', Q, L, etc, [3], [4], [30]–[32] it is the size and number density of the precipitates that will largely dictate their influence on mechanical behaviour. See Figures 2-1a and 2-1b for examples of precipitates in AA6063 formed through heat treatments at two different temperatures.

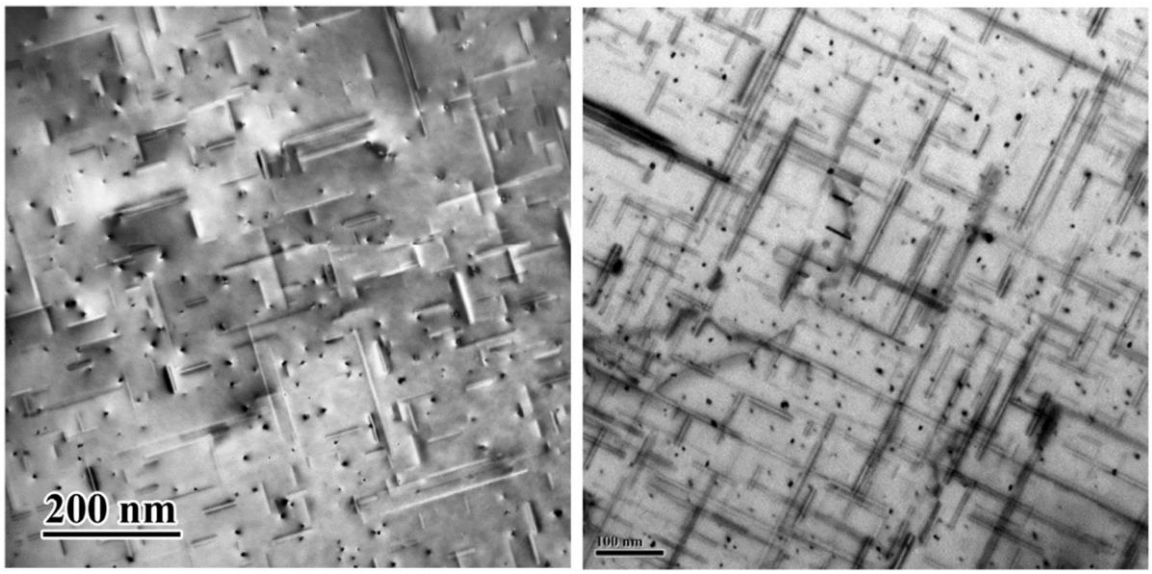

Figure 2-1: a) *Bright-field TEM observations of the β'' precipitates formed at optimum aged AA6063 (5h at 180 °C) shown to occur along the {100} directions taken from [33] and* ***b)*** *Bright-field TEM observations of the same AA6063 alloy from a) but aged now for 45 minutes at 230 °C showing larger precipitates along the {100] plane, likely β' or Q', taken from [34].*

The precipitates may either be shearable or unshearable (see Figure 2-2 below for an example of precipitate shearing after yield), which will change the observed strain hardening behaviour and the types of dislocations generated during plastic flow [35]. For the L, Q' precipitates, which contain Cu [3], [30], [31] this transition occurs when the diameter is between 2.5 and 3.0 nm [36]. The deformation behaviour of shearable precipitates follows that of a banded structure whereby once dislocations shear through a precipitate along the glide plane in a successive manner forming dislocation braids [33], [37]. Once they have grown to become unshearable, the dislocation-precipitate interactions is that of bypassing and the formation of Orowan loops [35], [36] or punched out prismatic loop stacks [38] resulting in a more homogeneous dislocation distribution, promoting recovery and yielding a decrease in the strain hardening rate coupled with a decreased strain hardening capacity [36].

2.1.3 Dispersoids

Dispersoids within aluminium alloys are formed during the casting of the ingot and aid in the hot-rolling process that reduces the thickness of the material. These particles are typically 2 – 10 µm in size, composed of $Al_xFe_y(Mn_z)$ and do not dissolve during the SHT due to their thermal stability. These large particles are unshearable and thus result in the formation of geometrically necessary dislocations (GNDs) within the material during plastic flow [38], [39]. The resulting strain hardening behaviour may be linear [40] as the generated dislocations pile-up at high energy grain boundaries, although dynamic recovery inevitably decreases the strain hardening capacity rapidly. In the event that there is a large friction stress within the matrix, dislocations may "pivot" or flow around the dispersoids requiring less energy to produce strain resulting in a parabolic strain hardening behaviour [40].

2.1.4 Grain Size

In pure, polycrystalline materials, the grain size is the upper boundary for dislocation slip distance [41], [42] while in engineering alloys, the presence of other obstacles of smaller length scales (such as dispersoids, precipitates, or clusters) will inevitably be the limiting factor for dislocation slip.

The grain boundaries are also areas of high solubility [43] for solute atoms such that enhanced precipitation (known as grain boundary precipitation) may occur. It has been previously determined that a grain size of 50 µm or less [44] is ideal for reducing grain size effects on the formability of sheet aluminium having a gauge of 1 mm, that is sheets should be 20 grains or more in thickness.

2.1.5 Texture

The texture of a material manifests itself by many ways, in particular in the form of the Lankford constant, or R-value [45], whereby a greater R-value promotes greater formability [46]. Having a strong cube texture promotes a more uniform plastic flow when materials are loaded in the balanced biaxial condition leading to a greater stretch formability [47], [48]. There are additional effects that influence the formability of materials such as latent hardening [49], [50] whereby the interaction of secondary slip systems due to a principle stress in the minor direction results in an enhanced level of hardening. Additionally, the differences in strain hardening between the two principle directions can cause additional strain accumulation in the direction with lower strain hardening resulting in a "wandering" balanced biaxial loading pathway [51], [52].

2.2 Plastic flow

The study of plastic flow in metallic materials began with the pioneering work of Friedel [53], Ashby, [39], Seeger [54]–[58] with extensions being made by strain hardening in single crystals by Nabarro et al. [59], [60]. These authors based much of their work on the original descriptions of dislocations within materials by Frank [61] and Nye [62]. The initial theories only described the dislocation production, recovery, and interactions [56], and then described the inhomogeneities in the deformation distribution within multi-phase materials due to the presence of harder, secondary phases. The presence of secondary phases manifest effects on the initiation and evolution of plastic flow within crystalline metals. In order to effectively study the plastic flow of metals and materials, the method of tensile testing is mostly employed, whereby a sample of a given geometry (see Chapter 3.3) is placed inside a machine which attempts to maintain a constant strain (or displacement) rate and determines the force required to maintain the applied rate. The most common representation of this data is in the form of stress-strain curves which may take one of the following forms: engineering stress-engineering strain (s-e), true stress-true strain ($\sigma - \epsilon$), or true stress-true plastic strain ($\sigma - \epsilon_p$). In this work, the true stress-true plastic strain representation will be used.

The concepts of yield, strain hardening, strain rate sensitivity, and finally formability will be discussed in order to help understand the compositional and heat treatment effects on the mechanical properties of the AA6xxx series alloys.

2.2.1 Yielding

The yielding behaviour of age-hardenable aluminium alloys is dictated by the presence of obstacles: solutes, clusters, precipitates, grain boundaries, and/or dislocations. In classical theory, the yield stress, $\sigma_{0.2\%}$, of the material has contributions due to many components: the intrinsic stress, σ_0, solute strengthening, σ_{ss}, clusters/precipitate strengthening, σ_p, grain boundary strengthening, σ_{gb}, and dislocation strengthening, σ_d [27], [63].

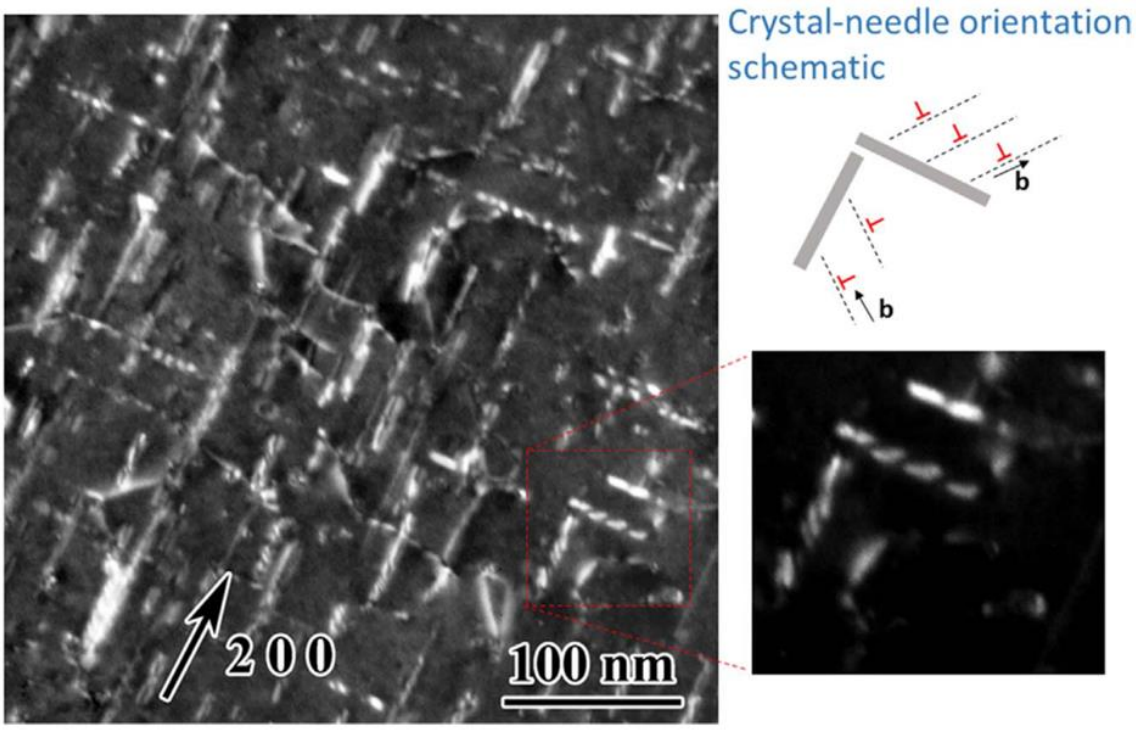

Figure 2-2: *The shearing of precipitates in AA6063 determined from weak-beam dark-field TEM observations of a deformed microstructure. The sample in questions was aged for 45 minutes at 230 ℃. The inset shows the shearing of precipitates formed along the {100} with slip taking place along the {111} creating a ± 45° slip relative to the precipitates. Taken from [33]*

This 0.2% yield point is generally used as it is a reliable measure for when plastic flow has been initiated and the first set of dislocations either nucleate or shear/bypass the primary obstacles (as shown in Figure 2-2) present in the alloy. In the case where the density of weak obstacles is large with respect to the stronger ones, a linear summation may be assumed such that

$$\sigma_{0.2\%} = \sigma_0 + \sigma_{ss} + \sigma_p + \sigma_{gb} + \sigma_d$$

Which holds true for the yielding of the material where the σ_d contributions would be due to any pre-deformation of the material and σ_{gb} effects would only manifest if the grain size is sufficiently small whereby the Hall-Petch effect is observed [64], [65]. The form of this relationship changes when the flow stress is considered whereby the dislocation contribution evolves and will eventually dominate as dislocation multiplication (and recovery) takes place. This is known as strain hardening and will be covered in the following section.

2.2.2 Strain hardening

The strain hardening behaviour of materials is governed by the production, interaction, storage, and recovery of mechanically produced dislocations during plastic flow (after yield). In conventional testing methods, such as tensile or formability tests, strain hardening is conventionally separated in four (4) stages. Each stage denotes a certain type of dislocation behaviour with those pertaining to single crystal deformation using Roman numerals while those pertaining to polycrystalline materials using Arabic numerals. The general characteristics of the monocrystalline behaviour will be described but not in great detail. Separately, certain stages depend on sample geometry (with respect to the microstructure) while others depend on temperature resulting in the appearance of some stages at lower test temperatures. These stages

of strain hardening are shown below in Figures 2-3a and 2-3b, for the typical stress-strain curves and the common Kocks-Mecking plots, for single and polycrystalline materials, respectively.

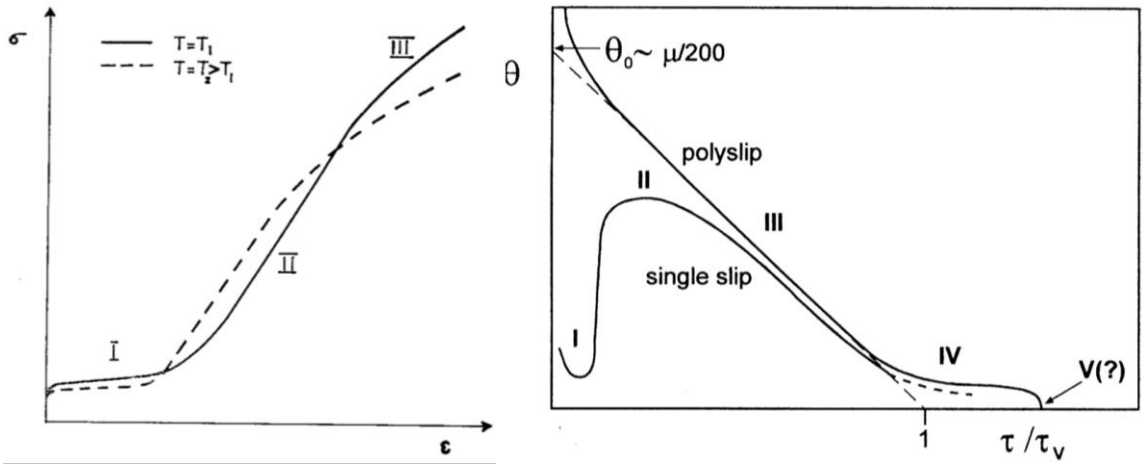

Figure 2-3: a) *A schematic true stress-true plastic strain curve showing the deformation behaviour of an fcc material at lower (solid line) and higher temperatures (dashed line) denoting the different stages of strain hardening taken from [56].* ***b)*** *A Kocks-Mecking plot ($\Theta = d\tau/d\gamma$ versus τ) schematic showing the different stages of strain hardening for single crystals (single slip) and poly-crystals (polyslip) taken from [66].*

- Stage I

Stage I of strain hardening is commonly referred to as "easy-glide". This region is only observed in pure single crystals where the dislocation density is very low [59]. The rate of strain hardening in this stage is very low and is highly sensitive to the crystal orientation. The as-grown dislocations within the material are able to move along their glide-plane at very low stresses due to the lack of dislocation obstacles present. Stage I is a nearly flat region of the stress-strain curve occurring directly after yielding (the elastic region) as shown in Figure 2-3a and 2-3b single slip.

- Stage II (2)

Stage II (2) of strain hardening is dominated by the production and build-up of dislocations within the material and is characterized by a constant strain hardening rate; or a constant slope in the stress-strain curve [59]. There is a large production of edge dislocations which may pile-up at boundaries of high dislocation density [59]. Due to the orientation dependencies and necessity of having a relatively low-obstacle density condition, stage II is almost never observed at room temperature testing of polycrystalline materials as shown in Figure 2-3a. Since stage II is a geometric-based strain hardening evolution, there is not a significant temperature dependence on its rate, as shown in Figure 2-3a. In single crystals this region follows a parabolic hardening law whereby $\sigma^2 \propto \epsilon$ with the hardening rate monotonically decreasing with increasing strain. In polycrystals, the type of dislocations produced and the relationship between stress and strain may be between linear and parabolic such that $\sigma^n \propto \epsilon$, where n, the strain hardening exponent, is between 1 (linear) and 2 (parabolic) hardening. The nature of the strain hardening relation depends on the primary obstacles interacting with the dislocations which may take the from of dislocation-dispersoid (see Chapter 2.1.3) [38], [39], dislocation-shearable/non-shearable precipitates (see Chapter 2.1.2) [36], dislocation-cluster (see Chapter 2.1.1), and dislocation-dislocation interactions. Depending on the type of interaction, three key parameters will be effected; the strain hardening rate, the rate of dislocation recovery (being most effected in stage 3), and the distribution of slip [36]. In general, geometrically necessary dislocations (GNDs) produced by dispersoids or non-shearable precipitates result in an initially linear hardening

response [40] if the friction stress within the material is sufficiently low, allowing for the accumulation of GNDs at grain boundaries and other strong obstacles. If the friction stress is sufficiently high within the material, there may be a transition to rotational flow [40] of these GNDs resulting in a parabolic hardening relation. For smaller obstacles such as precipitates, the two domains exist of being shearable or non-shearable resulting in the strain hardening to be more like a pure metal generating shear loops or generating geometrically necessary prismatic loops (GNPLs), respectively [36], [39].

- Stage III (3)

Stage III (3) is typically onset due to the occurrence of cross-slip which is a thermally activated process and triggers dynamic recovery, thereby reducing the strain hardening rate from dislocation storage (see the slope of the two curves in Figure 2-3a). The result is that a change of testing temperature will result in large changes in recovery due to dislocation arrangement, thermal activation and if present, solute mobility, and thus in strain hardening within stage 3 of deformation. In the presence of shearable precipitates or clusters, the strain hardening response is similar to that of pure metals but with an influence of these on both the production rate of dislocations and their recovery. The mechanical stability of the precipitates is assumed to be greater than that of the clusters such that it is possible for clusters to be mechanically dissolved during deformation [27], [67]. Poole et al. [36] and Jobba et al. [24] have shown that an increased presence of solutes impedes the dynamic recovery of dislocations in aluminium resulting in an increased strain hardening rate resulting in a net increase in the total dislocation density of the alloys throughout deformation, assuming the production rate is maintained.

- Stage IV (4)

The onset of stage IV (4) strain hardening begins at very large flow stresses (and strains) and is marked by a deviation from the monotonically decreasing strain hardening rate of stage 3. If this stage is prolonged, it may exhibit a small but constant hardening rate which occurs due to the steady-state production and recovery of dislocations (see Figure 2-3b). Due to its dependence on dislocation recovery, it is expected that stage 4 will have a large thermal component to its onset, rate and duration.

2.3 Strain rate sensitivity

Strain rate sensitivity (SRS) experiments are used to examine the reversible component of deformation during plastic flow, in other words the portion of the activation energy dislocations require in order to overcome (bypass, shear) obstacles within the material [68]–[71]. In their original experiments to determine the reversible component of the activation energy, Cottrell and Stokes [72] used variable temperature experiments to change the thermal energy available in the system and observed the change in the flow stress response. The alternative approach to this original method has been developed extensively by Basinski [73], Nabarro, [71], Saimoto [74], [77]–[79], Picu [20], [70], [77]–[79], McCormick [80]–[82], and Curtin [83] for a variety of materials. It consists of changing the active strain rate of deformation and determining the change in required stress to maintain the newly imposed strain rate. The basis of the thermodynamic SRS, S, begins with the rate equation for plasticity of

$$\dot{\epsilon} = \dot{\epsilon}_0 \exp\left(-\frac{\Delta G(\sigma)}{kT}\right)$$

where $\dot{\epsilon}$ is the strain rate, $\dot{\epsilon}_0$, the base strain rate, $\Delta G(\sigma)$, the stress-dependent apparent activation energy, k, the Boltzmann constant, and T, the absolute testing temperature. To determine the activation energy required to overcome the obstacles present within the material, the strain rate equation is differentiated with respect to stress at constant temperature T and structure, Σ, yielding

$$\left.\frac{\partial \ln \dot{\epsilon}}{\partial \sigma}\right|_{\Sigma,T} = \frac{\partial \ln \dot{\epsilon_0}}{\partial \sigma} - \frac{1}{kT}\frac{\partial \Delta G(\sigma)}{\partial \sigma}$$

Where $\frac{1}{kT}\frac{\partial \Delta G(\sigma)}{\partial \sigma}$ is the apparent activation energy, where the apparent activation volume is found as

$$\frac{1}{V'} = \frac{1}{kT}\left.\frac{\partial \sigma}{\partial \ln \dot{\epsilon}}\right|_{T,\Sigma}$$

Such that $\Delta G = V'\sigma$ to give the relationship between the apparent activation energy and apparent activation volume. The apparent activation volume is the total volume of material swept or overcome by the dislocations between the two metastable dislocation configurations (before and after activation). Typically, a plot of $\frac{1}{T}\frac{\Delta\sigma}{\Delta \ln \dot{\epsilon}}$ versus $\sigma - \sigma_{0.2\%}$, known as the Haasen plot [84] in the literature, is used to represent the change in the apparent activation volume during plastic flow. The initial apparent activation volume is therefore given by the intercept of the Haasen plot as $k/V' = (1/T)\,\partial\sigma/\partial \ln \dot{\epsilon}$. For the case of pure polycrystalline aluminium, the intercept of the Haasen plot is zero. The evolution of the inverse activation volume with stress is known as the thermodynamic strain rate sensitivity, S, and is the slope of the Haasen plot, found as

$$S = \frac{1}{T}\frac{\partial \sigma}{\sigma\, \partial \ln \dot{\epsilon}} = k/\sigma V'$$

Where the engineering SRS parameter, m, can be determined as $m = ST$. Alternatively, the instantaneous engineering SRS, m_i, can be calculated as

$$m_i = \left.\frac{\Delta \ln \sigma}{\Delta \ln \dot{\epsilon}}\right|_{T,\Sigma}$$

Which can be combined with the Hollomon equation (see Chapter 2.4) to model the stress-strain curve. For pure aluminium, the slope of the Haasen plot does not change throughout deformation and is characterized by the dislocation forest line of S_f, but this is not the case with alloys. Within the age-hardenable alloys, provided the alloy has been adequately annealed (ie: not a large retained dislocation density) the initial rate-controlling obstacles begin as solutes, clusters/precipitates. As deformation progresses and the dislocation density increases, the total contribution of obstacles to the flow stress evolves. Assuming a linear summation model, the relative contribution of obstacles to the total flow stress [63], [85] is given by

$$\sigma = \sigma_0 + \sigma_{ss} + \sigma_p + \sigma_d$$

Such that the dislocation density generated linearly adds to the total flow stress. In general, $\sigma_0, \sigma_{ss}, \text{and } \sigma_p$, make up the yield stress of the alloy and if the above equation is substituted into the determination of S, the total SRS [86] will be comprised as follows

$$S = \frac{1}{T}\frac{\partial\left(\sigma_{ss} + \sigma_p + \sigma_d\right)}{\sigma\, \partial \ln \dot{\epsilon}} = S_{ss} + S_p + S_d$$

Where S_{ss} is the thermodynamic SRS due to retained solutes, S_p is that due to clusters or precipitates, and S_d (or S_f) are those due to dislocations. Since directly after yield the major obstacles within the alloy are solutes or clusters / precipitates, S will be comprised solely of S_{ss} and S_p. After sufficient plastic deformation once the dislocation density becomes dominant, the total SRS will become that of dislocations as they become the new rate controlling obstacles.

When addressing the effects of temperature on the apparent activation volume, the change of the kT parameter (thermal energy available to the system) influences the calculation of ΔG and thus the apparent activation distance prior to the thermal activation of the rate controlling obstacles. If at yield and directly after, the rate controlling obstacles are assumed to be clusters or precipitates, an obstacle formed during the heat treatment process and not through plastic deformation, then an existing dislocation must overcome their energy barrier to permit plastic flow. Since S is the evolution of the inverse activation volume, V', defined as the product of b, the the burgers vector, d, the apparent activation distance of the dislocation overcoming the rate controlling obstacle, and l, the dislocation segment spacing between successive obstacles, it is possible to isolate and determine the relationship between S and the apparent activation distance, d, using the Taylor equation, $(\sigma - \sigma_{0.2\%})/M = \tau = \alpha\mu b/l$, given by

$$S = \frac{k}{(\sigma - \sigma_{0.2\%})bd}\frac{\sigma - \sigma_{0.2\%}}{M\alpha\mu b} = \frac{k}{M\alpha\mu b^2 d}$$

Whereby d can be determined directly from the thermodynamic strain rate sensitivity. The initial rate controlling obstacles in the alloys are clusters or solutes as the initial dislocation density is low. It is then possible to determine the force-distance interaction between dislocations and the initial rate controlling obstacles and its evolution with temperature to give information related to the size and density of the these obstacles. An example of two different rate controlling obstacle types (one more athermal and one more thermal) are represented below in Figure 2-4. It shows schematically the effect of temperature on the evolution of the apparent activation distance derived from the strain rate sensitivity directly after yield.

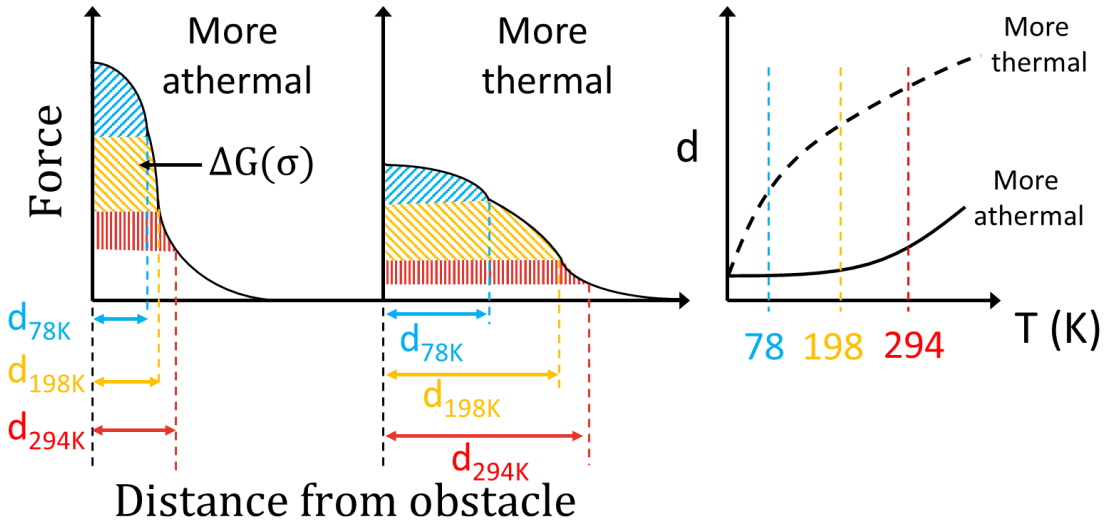

Figure 2-4: *The determination of the force-distance profile of obstacles to gain insight into their size via changes in temperature. The apparent activation distance, d, is determined directly from the initial strain rate sensitivity after yielding.*

Although rather crude, this schematic illustrates the different types of apparent activation distance versus temperature possible and how they would theoretically evolve for precipitates (more athermal obstacles) and clusters or solutes (more thermal obstacles). These activation distances may then in turn be related to the physical obstacle size at yield and if applicable, a transition from being thermally visible to becoming thermally invisible if sufficient thermal energy is present.

2.4 Formability

Although a complex subject, the formability of aluminium alloys has been related to the strain hardening and SRS at high flow stresses (high strains) whereby increased strain hardening and SRS properties result in enhanced formability [87]. The formation of necking within sheet metals is related to the geometric instabilities which develop due to the increasing stress-state, σ, and decreasing strain hardening rate, $d\sigma/d\epsilon$, resulting in the Considère criterion being met [88]. If a constitutive relation based on the Hollomon relation [87] is assumed

$$\sigma - \sigma_0 = K\epsilon^n \dot{\epsilon}^m$$

Where σ is the flow stress, σ_0 is the yield stress, K, the pre-exponential constant, and ϵ, the current plastic strain. Differentiating the Hollomon relation to yield the Considère criterion results in

$$\frac{d\sigma}{d\epsilon} = \frac{K\epsilon^n \dot{\epsilon}^m}{\epsilon}\left(n + m\frac{\partial \ln \dot{\epsilon}}{\partial \ln \epsilon}\right) = \sigma$$

Which results in both an *n* and *m* dependence. However, the dependence on *m* only takes place upon the incipient neck that is only related to *n*. Once the incipient (diffuse) neck forms, there become local changes in the strain rate such that $m\,\partial \ln \dot{\epsilon}\,/\partial \ln \epsilon$ becomes non-zero. Within the neck interior, the local strain rate changes such that $\ln \dot{\epsilon}\,/\partial \ln \epsilon$ becomes positive, and having a positive *m*-value will result in an increase in the apparent strain hardening. The contrary is true outside of the neck region, whereby $\ln \dot{\epsilon}\,/\partial \ln \epsilon$ is negative and having a positive *m*-value will result in a decrease in the apparent strain hardening, or work-softening. The result is that the diffuse neck may be stabilized or propagate to delay the formation of a local neck which renders the sample unsuitable for use.

2.5 Effects of processing on obstacle formation

The three different core methods of obstacle formation will be considered due to the three different heat treatments typically executed during industrial production; natural ageing (NA) at room temperature, pre-ageing (PA) at medium temperatures, and artificial ageing (AA) at the paint bake temperature (185 °C) with focus placed on the NA and PA processes. It has been widely found that in a majority of Al-Mg-Si alloys, NA for prolonged durations resulted in a diminished paint bake (PB) response, resulting in the material being too soft [89], [90]. As such, PA treatments have been proposed to stabilize the material and improve the PB response after prolonged NA [91]–[95].

As shown by Esmaeili and Lloyd [96] and Zhen et al. [97], [98] through differential scanning calorimetry (DSC) on as-quenched solutionized samples, the existence of two low-temperature exothermic peaks suggest that two cluster types can form at temperatures below the PB temperature. The two cluster types i and ii form at temperatures below and above 70°C, respectively [10], [98] such that NA and PA will ideally form the two unique cluster types, where type i is a detriment to the PB response [99]. Separately, De Geuser et al. [100] have used atom probe tomography (APT) to determine the differences in pair-correlation function of Si-Si, Mg-Mg

and Mg-Si clusters during both NA and PA, finding that two different types of cluster types form during the two respective processes.

2.5.1 Effects of natural ageing

The NA process in AA6xxx series alloys begins directly after quenching to room temperature whereby a sufficient equilibrium vacancy concentration coupled with the mobility of Si, Cu, and Mg in Al allow for rapid diffusion of these solutes. Werinos et al. [8] have extensively studied the stages of natural ageing directly after the quenching process originally conceived by Banhart [101], [102] in the Al-Mg-Si(-Cu) system and the evolution of clusters (type i) over time. Five critical stages to cluster formation were identified:

1) Interaction of quenched-in excess vacancies with solute atoms based on solute-vacancy binding energies [103].
2) Rapid diffusion of Si to Si-vacancy complexes due to the high diffusivity of Si in Al [104] and locally strained areas due to the smaller atomic size of Si compared to Al [105].
3) Formation of both vacancy-free and vacancy-containing Si clusters resulting in rapid hardening with Mg incorporation into the vacancy-free Si clusters from positive Si-Mg binding energy [106].
4) Incorporation of Mg (or Cu) into the Si-rich clusters formed during stage 2 and 3 resulting in slower hardening.
5) Cluster coarsening and/or depletion of the solute available for clustering causing minimal additional hardening.

These systematic processes are supported by atom probe tomography (APT) work performed by Fallah et al. [105] which showed that the initial clusters formed during NA begin as Si-rich which undergo subsequent Mg-enrichment and coarsening. The study by De Geuser et al. [100] supports this claim showing that Mg-Mg clusters appear to dissolve during NA allowing for the Mg-enrichment of the Si-Si clusters that formed.

2.5.2 Effects of pre-ageing

Unlike the NA clusters that form, the PA clusters form at temperatures above 70°C and are that of cluster type ii [10], [98]. These clusters that form during the PA treatment have been found to contain a greater Mg/Si ratio or to be Mg-rich compared to the base alloy composition [10], [107], which strongly suggests that Mg plays a large role in their formation. The goal of PA is both to partially stabilize the microstructure [5] and to produce clusters closer in Mg/Si ratio to the precipitates formed during the PB heat treatment (β'') in order to reduce the free energy barrier and improve the PB response [91], [92]. The subsequent NA response after the PA treatment has been studied by [10] but its effects on the mechanical properties remains unknown. It was suggested by Kim et al. [5], [6] that during NA after PA, cluster type i may form independently from those formed during the PA treatment while this was contested by Aruga et al. [10] suggesting that Si-aggregation to the type ii clusters is preferred.

2.5.3 Effects of artificial ageing

The purpose of AA is to increase the strength of the AA6xxx series alloys in order to improve dent resistance after the PB cycle. During the AA process, lower-energy obstacles form having a more defined crystal structure and stoichiometry than the clusters formed during PA and NA. Although AA processes follow a general nucleation, growth and coarsening sequence, the AA process never reaches the peak-age condition due to the requirements of AMs and the implementation of the PB cycle spanning only 20 minutes. Thus, it is most important to optimize the short ageing time

response of the alloys to enhance hardness increase during the PB treatment. It has been shown that if the clusters (or nuclei) that exist in the alloy after the PA or NA treatment are close in stoichiometric ratio to the precipitates that will form, the activation barrier to precipitation will be reduced and their formation will be more favourable [11], [91], [92], [108].

2.6 Effects of composition on obstacle formation

Due to the initial concerns of material strength, the effects of composition in the Al-Mg-Si(-Cu) alloys focused primarily on the age-hardening response of these alloys [109]–[111] whereby enhancing the precipitation volume fraction was found to improve the overall strength of the alloys. Subsequently, as the overall strength of the materials improved, focus was turned to processing routes commonly used and the solute effects on the natural ageing, pre-ageing, and age-hardening kinetics and responses [30], [89], [112], [113]. The current methods focus on the effects of these intermediate obstacles formed during natural and pre-ageing and their effect on the mechanical properties. Extensive work has been recently undertaken by Zhong et al. [114]–[117] to study the influence of Mg/Si ratios and Cu additions on the mechanical properties and formability of AA6xxx series aluminium alloys. This work largely expanded on the earlier studies of Hirth et al. [118] and Sachdev [119] which focused primarily on the compositional effects using a single processing route on formability rather than multiple processing protocols.

2.6.1 Effects of Cu additions

The addition of Cu to Al-Mg-Si(-Cu) alloys has been shown to increase the Cu content in clusters formed during NA and PA processes. Cu has been demonstrated to have an effect similar to Mg whereby the (Mg + Cu)/Si ratio of clusters is usually considered and Cu tends to increase this ratio [5], [6], [120]. According to Werinos et al. [8], [121], directly after quenching, Cu increases the incubation time prior to subsequent hardening due to the positive Cu solute-vacancy binding energy [103] reducing the rapid diffusivity of Si at early ageing times to form Si-vacancy complexes. Since Cu acts in a similar manner to Mg, it is primarily involved in the later-stage clustering (or Cu/Mg-enrichment phase) of the early-stage Si-rich clusters formed during NA hence primarily partaking in increasing cluster size [102], [122]. Finally, Cu additions have been shown to reduce the negative naturally ageing effect of artificial ageing by assisting in changing the stoichiometry of NA clusters to that similar to β'' reducing the energy barrier to their formation in a similar means to the PA process increasing the Mg/Si ratio of the clusters formed [110], [111]. Furthermore, as during NA and AA, Cu tends to increase cluster or precipitate size, it plays a critical role on providing additional strengthening to alloys during deformation.

2.6.2 Effects of Si additions

Adding Si to Al-Mg-Si(-Cu) alloys increases its contribution to clustering and precipitation depending on the total (Mg + Cu)/Si ratio of the alloys. The clustering pathways during NA have shown Si clustering to take place directly after quenching due to its rapid diffusivity in Al [101], [102]. Supported by work by Werinos et al. [121], Si additions during NA will decrease the initial incubation time prior to the alloy experiencing significant hardening, acting in an opposite manner to Cu. The addition of Si will also increase the early stage clustering kinetics via an increase in the number of pre-clusters through formation of Si-vacancy complexes and their transition into Si-rich clusters [105], [122], [123]. With an enhanced cluster number density decreasing the diffusion distances, the later-stage Mg (or Cu) enrichment of the clusters will accelerate. It can thus be surmised that Si additions increase the total NA clustering kinetics but due to an increase in the total Si content of the alloy [101], the (Mg + Cu)/Si ratio of the clusters that form during NA will decrease which in turn can enhance the negative natural ageing effect prior to artificial ageing. Depending on the total alloy composition, Mg (or Cu) are typically the limiting solutes in this alloy

system, thus Si additions should not play a major role in enhancing the precipitation strengthening of the alloys. Finally, in the PA process, Si additions should not have a major effect on the cluster number density as the clusters that form are Mg/Cu-rich [107]. In subsequent NA, it would be expected that Si agglomeration to the Mg/Cu-rich clusters should take place and with an increase in Si content [10], [11], the growth of the PA clusters should be accelerated due to Si rapid diffusivity in Al.

2.6.3 Effects of Mg addition

Mg additions into Al-Mg-Si(-Cu) alloys have a similar effect to Cu whereby they contribute significantly to the formation of clusters and precipitates during NA or AA, respectively. During NA, Mg additions increase the incubation time prior to appreciable hardening, possibly due to their positive binding energy with vacancies in Al [103], although the sign of this interaction is still subject to debate. Since Mg solutes play a major role in cluster growth during stage 3 and 4 of NA, their addition will tend to extend the duration of the later stages of NA through the slow enrichment of the locally strained Si-rich clusters where if additional Mg is present, longer times are required to deplete the free Mg-vacancy pairs remaining in solution. The typical result is an increase is NA cluster size and transition to more Mg-rich clusters at very long NA times [89], [90] reducing the negative natural ageing effect on the subsequent AA process. In direct AA, Mg additions increase the total amount of solute contributing to β'' formation increasing the number density and/or volume fraction of the precipitates formed resulting in a net increase in peak hardness and total strength. Concerning the PA processes, Mg additions enhance the number density of PA clusters as there is an improved availability of Mg to form Mg/Cu-rich clusters.

2.7 Conclusions

The influence on composition on the formability of AA6xxx series alloys follows a hierarchal assembly where each stage must be thoroughly characterized and understood such that the mechanical expression of the microstructure may be properly understood. This general hierarchal sequence follows the composition-structure-strength/ductility-formability order whereby the higher-order mechanical expression is a manifestation of the lower-order behaviour. Through systematic studies and probing the microstructure using DSC, APT, SAXS, and hardness testing, the connection between composition and microstructure may be realized for different heat treatments. Using tensile and SRS tests for the different heat treatments, the connections between structure and strength/ductility may be studied. Finally, using finite element modelling that utilizes both the strain hardening and SRS properties of the alloys, the extension of strength/ductility to the formability may be better understood.

2.8 References

[1] J. Hirsch, “Recent development in aluminium for automotive applications,” *Trans. Nonferrous Met. Soc. China*, vol. 24, no. 7, pp. 1995–2002, Jul. 2014.

[2] Y. Takaki, T. Masuda, E. Kobayashi, and T. Sato, “Effects of Natural Aging on Bake Hardening Behavior of Al-Mg-Si Alloys with Multi-Step Aging Process,” *Mater. Trans.*, vol. 55, no. 8, pp. 1257–1265, 2014.

[3] Y. Weng, Z. Jia, L. Ding, Y. Pan, Y. Liu, and Q. Liu, “Effect of Ag and Cu additions on natural aging and precipitation hardening behavior in Al-Mg-Si alloys,” *J. Alloys Compd.*, vol. 695, pp. 2444–2452, Feb. 2017.

[4] S. Esmaeili, X. Wang, D. J. Lloyd, and W. J. Poole, “On the precipitation-hardening behavior of the Al-Mg-Si-Cu alloy AA6111,” *Metall. Mater. Trans. A*, vol. 34, no. 3, pp. 751–763, 2003.

[5] J. Kim, E. Kobayashi, and T. Sato, “Effects of Cu addition on behavior of nanoclusters during multi-step aging in Al-Mg-Si alloys,” *Mater. Trans.*, vol. 52, no. 5, pp. 906–913, 2011.

[6] J. H. Kim and T. Sato, “Effects of Cu Addition on Nanocluster Formation and Two-Step Aging Behaviors of Al–Mg–Si Alloys,” *J. Nanosci. Nanotechnol.*, vol. 11, no. 2, pp. 1319–1322, Feb. 2011.

[7] S. Kim, J. Kim, H. Tezuka, E. Kobayashi, and T. Sato, “Formation behavior of nanoclusters in Al–Mg–Si alloys with different Mg and Si concentration,” *Mater. Trans.*, vol. 54, no. 3, pp. 297–303, 2013.

[8] M. Werinos, H. Antrekowitsch, T. Ebner, R. Prillhofer, P. J. Uggowitzer, and S. Pogatscher, “Hardening of Al–Mg–Si alloys: Effect of trace elements and prolonged natural aging,” *Mater. Des.*, vol. 107, pp. 257–268, Oct. 2016.

[9] S. Wenner, C. D. Marioara, S. J. Andersen, and R. Holmestad, “Effect of room temperature storage time on precipitation in Al–Mg–Si (–Cu) alloys with different Mg/Si ratios,” *Int. J. Mater. Res.*, vol. 103, no. 8, pp. 948–954, 2012.

[10] Y. Aruga, M. Kozuka, Y. Takaki, and T. Sato, “Effects of natural aging after pre-aging on clustering and bake-hardening behavior in an Al–Mg–Si alloy,” *Scr. Mater.*, vol. 116, pp. 82–86, Apr. 2016.

[11] Y. Aruga, M. Kozuka, Y. Takaki, and T. Sato, “Formation and reversion of clusters during natural aging and subsequent artificial aging in an Al–Mg–Si alloy,” *Mater. Sci. Eng. A*, vol. 631, pp. 86–96, Apr. 2015.

[12] S. Pogatscher *et al.*, “Process-controlled suppression of natural aging in an Al–Mg–Si alloy,” *Scr. Mater.*, vol. 89, pp. 53–56, Oct. 2014.

[13] R. Ivanov, “Solute clustering in multi-component aluminium alloys,” Université Grenoble Alpes.

[14] J. Guillot and J. Grilhe, “PHENOMENE PORTEVIN-LE CHATELIER DANS LES ALLIAGES Al-M2 A HAUTES TEMPERATURES, EN FONCTION DE LA CONCENTRATION,” *Acta Met.*, vol. 20, pp. 291–295, 1972.

[15] R. B. Sills and W. Cai, “Solute drag on perfect and extended dislocations,” *Philos. Mag.*, vol. 96, no. 10, pp. 895–921, Apr. 2016.

[16] M. A. Soare and W. A. Curtin, “Solute strengthening of both mobile and forest dislocations: The origin of dynamic strain aging in fcc metals,” *Acta Mater.*, vol. 56, no. 15, pp. 4046–4061, Sep. 2008.

[17] P. P. Gillis and J. J. Gilman, “Dynamical Dislocation Theory of Crystal Plasticity. II. Easy Glide and Strain Hardening,” *J. Appl. Phys.*, vol. 36, no. 11, p. 3380, 1965.

[18] J. G. Morris, “Dynamic strain aging in aluminum alloys,” *Mater. Sci. Eng.*, vol. 13, no. 2, pp. 101–108, 1974.

[19] S. Saimoto, J. Cooley, H. Larsen, and C. Scholler, “Kinetic analysis of dynamic point defect pinning in aluminium initiated by strain rate changes,” *Philos. Mag.*, vol. 89, no. 10, pp. 853–868, Apr. 2009.

[20] R. C. Picu, “A mechanism for the negative strain-rate sensitivity of dilute solid solutions,” *Acta Mater.*, vol. 52, no. 12, pp. 3447–3458, Jul. 2004.

[21] S. Gupta, A. J. Beaudoin, and J. Chevy, “Strain rate jump induced negative strain rate sensitivity (NSRS) in aluminum alloy 2024: Experiments and constitutive modeling,” *Mater. Sci. Eng. A*, vol. 683, pp. 143–152, Jan. 2017.

[22] R. A. Mulford and U. F. Kocks, “NEW OBSERVATIONS ON THE MECHANISMS OF DYNAMIC STRAIN AGING AND OF JERKY FLOW,” *Acta Metall.*, vol. 27, pp. 1125–1134, 1979.

[23] R. A. Mulford, “ANALYSIS OF STRENGTHENING MECHANISMS IN ALLOYS BY MEANS OF THERMAL-ACTIVATION THEORY?,” *Acta Metall.*, vol. 27, pp. 1115–1124, 1979.

[24] M. Jobba, R. K. Mishra, and M. Niewczas, “Flow stress and work-hardening behaviour of Al–Mg binary alloys,” *Int. J. Plast.*, vol. 65, pp. 43–60, Feb. 2015.

[25] M. J. Starink, “A model for co-clusters and their strengthening in Al–Cu–Mg based alloys: a comparison with experimental data,” *Int. J. Mater. Res.*, vol. 103, no. 8, pp. 942–947, 2012.

[26] M. J. Starink, P. Wang, I. Sinclair, and P. J. Gregson, “Microstrucure and strengthening of Al–Li–Cu–Mg alloys and mmcs: I. Analysis and modelling of microstructural changes,” *Acta Mater.*, vol. 47, no. 14, pp. 3841–3853, 1999.

[27] M. J. Starink and S. C. Wang, “The thermodynamics of and strengthening due to co-clusters: General theory and application to the case of Al–Cu–Mg alloys,” *Acta Mater.*, vol. 57, no. 8, pp. 2376–2389, May 2009.

[28] A. de Vaucorbeil, C. W. Sinclair, and W. J. Poole, “Dislocation glide through non-randomly distributed point obstacles,” *Philos. Mag.*, vol. 93, no. 27, pp. 3664–3679, Sep. 2013.

[29] A. J. E. Foreman and M. J. Makin, “Dislocation movement through random arrays of obstacles,” *Can. J. Phys.*, vol. 45, no. 2, pp. 511–517, 1967.

[30] L. Ding, Z. Jia, Z. Zhang, R. E. Sanders, Q. Liu, and G. Yang, “The natural aging and precipitation hardening behaviour of Al-Mg-Si-Cu alloys with different Mg/Si ratios and Cu additions,” *Mater. Sci. Eng. A*, vol. 627, pp. 119–126, Mar. 2015.

[31] K. Teichmann *et al.*, “HRTEM study of the effect of deformation on the early precipitation behaviour in an AA6060 Al–Mg–Si alloy,” *Philos. Mag.*, vol. 91, no. 28, pp. 3744–3754, Oct. 2011.

[32] S. Esmaeili, D. Vaumousse, M. W. Zandbergen, W. J. Poole, A. Cerezo, and D. J. Lloyd, “A study on the early-stage decomposition in the Al–Mg–Si–Cu alloy AA6111 by electrical resistivity and three-dimensional atom probe,” *Philos. Mag.*, vol. 87, no. 25, pp. 3797–3816, Sep. 2007.

[33] S. Saimoto *et al.*, “Method to decode stress-strain diagrams to identify the structure-strength relationships in aged aluminum alloys,” *Mater. Sci. Eng. A*, vol. 709, pp. 9–16, Jan. 2018.

[34] S. Saimoto, M. A. Singh, M. R. Langille, A. Kula, and M. Niewczas, “Identification of the role of Al-Fe-Mn-Si large casting dispersoids in age-hardenable aluminum alloys using small angle X-ray scattering,” *Mater. Sci. Eng. A*, vol. 734, pp. 51–58, Sep. 2018.

[35] L. M. Cheng, W. J. Poole, J. D. Embury, and D. J. Lloyd, “The influence of precipitation on the work-hardening behavior of the aluminum alloys AA6111 and AA7030,” *Metall. Mater. Trans. A*, vol. 34, no. 11, pp. 2473–2481, 2003.

[36] W. J. Poole, X. Wang, D. J. Lloyd, and J. D. Embury, “The shearable–non-shearable transition in Al–Mg–Si–Cu precipitation hardening alloys: implications on the distribution of slip, work hardening and fracture,” *Philos. Mag.*, vol. 85, no. 26–27, pp. 3113–3135, Sep. 2005.

[37] A. S. Argon and P. Haasen, “A new mechanism of work hardening in the late stages of large strain plastic flow in F.C.C. and diamond cubic crystals,” *Acta Metall. Mater.*, vol. 41, no. 11, pp. 3289–3306, Nov. 1993.

[38] N. A. Fleck, M. F. Ashby, and J. W. Hutchinson, “The role of geometrically necessary dislocations in giving material strengthening,” *Scr. Mater.*, vol. 48, pp. 179–183, 2003.

[39] M. F. Ashby, “The deformation of plastically non-homogeneous materials,” *Philos. Mag.*, vol. 21, no. 170, pp. 399–424, Feb. 1970.

[40] L. M. Brown, “Transition from laminar to rotational motion in plasticity,” *Philos. Trans. R. Soc. Lond. Math. Phys. Eng. Sci.*, vol. 355, no. 1731, pp. 1979–1990, 1997.

[41] J. C. M. Li and Y. T. Chou, “The Role of Dislocations in the Flow Stress Grain Size Relationships,” *Metall. Trans. A*, vol. 1, pp. 1145–1159, 1970.

[42] T. Narutani and J. Takamura, “Grain-size strengthening in terms of dislocation density measured by resistivity,” *Acta Metall. Mater.*, vol. 39, no. 8, pp. 2037–2049, 1991.

[43] S. Saimoto and H. Jin, “Effects of Solubility Limit and the Presence of Ultra-Fine Al6Fe on the Kinetics of Grain Growth in Dilute Al-Fe Alloys,” *Mater. Sci. Forum*, vol. 550, pp. 339–344, 2007.

[44] D. V. Wilson, A. R. Mirshams, and W. T. Roberts, “AN EXPERIMENTAL STUDY OF THE EFFECT OF SHEET THICKNESS AND GRAIN SIZE ON LIMIT-STRAINS IN BIAXIAL STRETCHING,” *Int. J. Mech. Sci.*, vol. 25, no. 12, pp. 859–870, 1983.

[45] R. Hill, *The Mathematical Theory of Plasticity*. Oxford: Claredon Press, 1950.

[46] C.-S. Man, “On the r-value of textured sheet metals,” *Int. J. Plast.*, vol. 18, no. 12, pp. 1683–1706, 2002.

[47] K. O. Pedersen, O.-G. Lademo, T. Berstad, T. Furu, and O. S. Hopperstad, “Influence of texture and grain structure on strain localisation and formability for AlMgSi alloys,” *J. Mater. Process. Technol.*, vol. 200, no. 1–3, pp. 77–93, May 2008.

[48] K. Yoshida, T. Ishizaka, M. Kuroda, and S. Ikawa, “The effects of texture on formability of aluminum alloy sheets,” *Acta Mater.*, vol. 55, no. 13, pp. 4499–4506, Aug. 2007.

[49] M. Niewczas, “Latent hardening effects in low cycle fatigue of copper single crystals,” *Philos. Mag.*, vol. 93, no. 1–3, pp. 272–303, Jan. 2013.

[50] L. E. Collins, “Plane strain deformation and subsequent recovery of ideally oriented copper single crystals,” M. Sc., Queen’s University, Kingston, Canada, 1977.

[51] M. R. Langille, “Structure, strength, ductility in aluminium alloys: constitutive relations analysis for performance evaluation,” M.A.Sc, Queen’s University, Kingston, Canada, 2016.

[52] S. Saimoto, P. Van Houtte, K. Inal, and M. R. Langille, “New biaxial yield function for aluminum alloys based on plastic work and work-hardening analyses,” *Acta Mater.*, vol. 118, pp. 109–119, Oct. 2016.

[53] J. Friedel, “CXXX. On the linear work hardening mate of face-centred cubic single crystals,” *Lond. Edinb. Dublin Philos. Mag. J. Sci.*, vol. 46, no. 382, pp. 1169–1186, Nov. 1955.

[54] A. Seeger, “The temperature dependence of the critical shear stress and of work-hardening of metal crystals,” *Lond. Edinb. Dublin Philos. Mag. J. Sci.*, vol. 45, no. 366, pp. 771–773, Jul. 1954.

[55] A. Seeger, “CXXXII. The generation of lattice defects by moving dislocations, and its application to the temperature dependence of the flow-stress of F.C.C. crystals,” *Lond. Edinb. Dublin Philos. Mag. J. Sci.*, vol. 46, no. 382, pp. 1194–1217, Nov. 1955.

[56] A. Seeger, J. Diehl, S. Mader, and H. Rebstock, “Work-hardening and work-softening of face-centred cubic metal crystals,” *Philos. Mag.*, vol. 2, no. 15, pp. 323–350, Mar. 1957.

[57] A. Seeger and P. Haasen, “Density changes of crystals containing dislocations,” *Philos. Mag.*, vol. 3, no. 29, pp. 470–475, May 1958.

[58] S. Mader, A. Seeger, and H.-M. Thieringer, “Work Hardening and Dislocation Arrangement of fcc Single Crystals. II. Electron Microscope Transmission Studies of Ni[Single Bond]Co Single Crystals and Relation to Work-Hardening Theory,” *J. Appl. Phys.*, vol. 34, no. 11, p. 3376, 1963.

[59] F. R. N. Nabarro, Z. S. Basinski, and D. B. Holt, “The plasticity of pure single crystals,” *Adv. Phys.*, vol. 13, no. 50, pp. 193–323, Apr. 1964.

[60] F. R. N. Nabarro, “XX. The law of constant resolved shear stress in crystal plasticity,” *Lond. Edinb. Dublin Philos. Mag. J. Sci.*, vol. 42, no. 325, pp. 213–214, Feb. 1951.

[61] F. C. Frank, “LXXXIII. Crystal dislocations.—Elementary concepts and definitions,” *Lond. Edinb. Dublin Philos. Mag. J. Sci.*, vol. 42, no. 331, pp. 809–819, Aug. 1951.

[62] J. F. Nye, “Some geometrical relations in dislocated crystals,” *Acta Metall.*, vol. 1, no. 2, pp. 153–162, 1953.

[63] E. Hornbogen and E. A. Starke Jr, “Overview no. 102 Theory assisted design of high strength low alloy aluminum,” *Acta Metall. Mater.*, vol. 41, no. 1, pp. 1–16, 1993.

[64] E. O. Hall, “The Deformation and Ageing of Mild Steel: III Discussion of Results,” *Proc. Phys. Soc. Sect. B*, vol. 64, no. 9, pp. 747–753, Sep. 1951.

[65] N. J. Petch, “The Cleavage Strength of Polycrystals,” *J. Iron Steel Inst.*, vol. 173, pp. 25–28, 1953.

[66] U. F. Kocks and H. Mecking, “Physics and phenomenology of strain hardening: the FCC case,” *Prog. Mater. Sci.*, vol. 48, no. 3, pp. 171–273, 2003.

[67] M. J. Starink, L. F. Cao, and P. A. Rometsch, “A model for the thermodynamics of and strengthening due to co-clusters in Al–Mg–Si-based alloys,” *Acta Mater.*, vol. 60, no. 10, pp. 4194–4207, Jun. 2012.

[68] B. J. Diak, K. R. Upadhyaya, and S. Saimoto, “Characterization of thermodynamic response by materials testing,” *Prog. Mater. Sci.*, vol. 43, no. 4, pp. 223–363, 1998.

[69] F. R. N. Nabarro, “Cottrell-Stokes law and activation theory,” *Acta Metall. Mater.*, vol. 38, no. 2, pp. 161–164, 1990.

[70] R. C. Picu and R. Li, “On the relationship between the Cottrell–Stokes law and the Haasen plot,” *Mater. Sci. Eng. A*, vol. 527, no. 20, pp. 5303–5306, Jul. 2010.

[71] S. Saimoto, “Dynamic dislocation–defect analysis,” *Philos. Mag.*, vol. 86, no. 27, pp. 4213–4233, Sep. 2006.

[72] A. H. Cottrell and R. J. Stokes, “Effects of Temperature on the Plastic Properties of Aluminium Crystals,” *Proc. R. Soc. Math. Phys. Eng. Sci.*, vol. 233, no. 1192, pp. 17–34, Dec. 1955.

[73] Z. S. Basinski, “Thermally activated glide in face-centred cubic metals and its application to the theory of strain hardening,” *Philos. Mag.*, vol. 4, no. 40, pp. 393–432, Apr. 1959.

[74] S. Saimoto and M. S. Duesbery, “Strain rate sensitivity: the role of dislocation loop and point defect recovery,” *Acta Metall.*, vol. 32, no. 1, pp. 147–155, 1984.

[75] M. Bull and S. Saimoto, “Role of solute-vacancy interaction on the temperature dependence of strain rate sensitivity.,” in *Solute-Defect Interation: Theory and Experiment*, Pergamon Press, Oxford, 1986, pp. 375–381.

[76] B. J. Diak and S. Saimoto, “Role of Strain Rate Sensitivity on Diffuse Necking,” in *Dynamic Plasticity and Structural Behaviours*, 1995, pp. 5–8.

[77] R. C. Picu, G. Vincze, J. J. Gracio, and F. Barlat, “Effect of solute distribution on the strain rate sensitivity of solid solutions,” *Scr. Mater.*, vol. 54, no. 1, pp. 71–75, Jan. 2006.

[78] R. C. Picu, F. Ozturk, E. Esener, and R. Li, “Aluminum Alloys with Identical Plastic Flow and Different Strain Rate Sensitivity,” *Metall. Mater. Trans. A*, vol. 41, no. 13, pp. 3358–3364, Dec. 2010.

[79] R. C. Picu, G. T. Vincze, and J. J. Gracio, “Deformation and microstructure-independent Cottrell–Stokes ratio in commercial Al alloys,” *Int. J. Plast.*, vol. 27, no. 7, pp. 1045–1054, Jul. 2011.

[80] H. J. Harun and P. G. McCormick, “EFFECT OF PRECIPITATION HARDENING ON STRAIN RATE SENSITIVITY AND YIELD BEHAVIOUR IN AN Al-Mg-Si ALLOY,” *Acta Metall.*, vol. 27, pp. 155–159, 1978.

[81] C. P. Ling and P. G. McCormick, “Strain rate sensitivity and transient behaviour in an Al Mg Si alloy,” *Acta Metall. Mater.*, vol. 38, no. 12, pp. 2631–2635, 1990.

[82] C. P. Ling and P. G. McCormick, “The effect of temperature on strain rate sensitivity in an Al-Mg-Si alloy,” *Acta Metall. Mater.*, vol. 41, no. 11, pp. 3127–3131, 1993.

[83] W. A. Curtin, “New interpretation of the Haasen plot for solute-strengthened alloys,” *Scr. Mater.*, vol. 63, no. 9, pp. 917–920, Nov. 2010.

[84] P. Haasen, “Plastic deformation of nickel single crystals at low temperatures,” *Philos. Mag.*, vol. 3, no. 28, pp. 384–418, Apr. 1958.

[85] M. J. Starink and S. C. Wang, “A model for the yield strength of overaged Al–Zn–Mg–Cu alloys,” *Acta Mater.*, vol. 51, no. 17, pp. 5131–5150, 2003.

[86] L. C. Wong and S. Saimoto, “Superposition of thermal activation processes in quenched aluminum-1.7 at% copper,” *Scr. Metall. Mater.*, vol. 29, no. 3, pp. 341–346, 1993.

[87] J. E. Bird and J. L. Duncan, “Strain hardening at high strain in aluminum alloys and its effect on strain localization,” *Metall. Trans. A*, vol. 12, no. 2, pp. 235–241, Feb. 1981.

[88] M. Considère, *Mémoire sur l’emploi du fer et de l’acier dans les constructions*, vol. 1. Dunod, 1885.

[89] G. H. Tao, C. H. Liu, J. H. Chen, Y. X. Lai, P. P. Ma, and L. M. Liu, “The influence of Mg/Si ratio on the negative natural aging effect in Al–Mg–Si–Cu alloys,” *Mater. Sci. Eng. A*, vol. 642, pp. 241–248, Aug. 2015.

[90] F. A. Martinsen, F. J. H. Ehlers, M. Torsæter, and R. Holmestad, “Reversal of the negative natural aging effect in Al–Mg–Si alloys,” *Acta Mater.*, vol. 60, no. 17, pp. 6091–6101, Oct. 2012.

[91] L. Cao, P. A. Rometsch, and M. J. Couper, “Effect of pre-ageing and natural ageing on the paint bake response of alloy AA6181A,” *Mater. Sci. Eng. A*, vol. 571, pp. 77–82, Jun. 2013.

[92] L. He, H. Zhang, and J. Cui, “Effects of Pre-Ageing Treatment on Subsequent Artificial Ageing Characteristics of an Al-1.01Mg-0.68Si-1.78Cu Alloy,” *J. Mater. Sci. Technol.*, vol. 26, no. 2, pp. 141–145, 2010.

[93] C.-H. Shen and B.-L. Ou, “Pre-Ageing to Improve the Microstructure and Tensile Properties of Al-0.72Mg-0.42Si-0.1Cu Artificially Aged Alloy,” *Can. Metall. Q.*, vol. 47, no. 4, pp. 449–458, Dec. 2008.

[94] B.-L. Ou and C.-H. Shen, “Impact of pre-aging on the tensile and bending properties of AA 6061,” *Scand. J. Metall.*, vol. 34, no. 6, pp. 318–325, Dec. 2005.

[95] W. J. Poole, D. J. Lloyd, and J. D. Embury, “The effect of natural ageing on the evolution of yield strength during artificial ageing for Al-Mg-Si-Cu alloys,” *Mater. Sci. Eng. A*, vol. 234, pp. 306–309, 1997.

[96] S. Esmaeili and D. J. Lloyd, “Characterization of the evolution of the volume fraction of precipitates in aged AlMgSiCu alloys using DSC technique,” *Mater. Charact.*, vol. 55, no. 4–5, pp. 307–319, Nov. 2005.

[97] L. Zhen and S. B. Kang, “DSC analyses of the precipitation behavior of two Al–Mg–Si alloys naturally aged for different times,” *Mater. Lett.*, vol. 37, pp. 349–353, 1998.

[98] L. Zhen, S. B. Kang, and H. W. Kim, “Effect of natural aging and preaging on subsequent precipitation process of an AI-Mg-Si alloy with high excess silicon,” *Mater. Sci. Technol.*, vol. 13, no. 11, pp. 905–911, Nov. 1997.

[99] S. Esmaeili, D. J. Lloyd, and W. J. Poole, “Effect of natural aging on the resistivity evolution during artificial aging of the aluminum alloy AA6111,” *Mater. Lett.*, vol. 59, no. 5, pp. 575–577, Feb. 2005.

[100] F. De Geuser, W. Lefebvre, and D. Blavette, “3D atom probe study of solute atoms clustering during natural ageing and pre-ageing of an Al-Mg-Si alloy,” *Philos. Mag. Lett.*, vol. 86, no. 4, pp. 227–234, Apr. 2006.

[101] J. Banhart, M. D. H. Lay, C. S. T. Chang, and A. J. Hill, “Kinetics of natural aging in Al-Mg-Si alloys studied by positron annihilation lifetime spectroscopy,” *Phys. Rev. B*, vol. 83, no. 1, Jan. 2011.

[102] J. Banhart, C. S. T. Chang, Z. Liang, N. Wanderka, M. D. H. Lay, and A. J. Hill, “Natural Aging in Al-Mg-Si Alloys - A Process of Unexpected Complexity,” *Adv. Eng. Mater.*, vol. 12, no. 7, pp. 559–571, Jul. 2010.

[103] C. Wolverton, “Solute–vacancy binding in aluminum,” *Acta Mater.*, vol. 55, no. 17, pp. 5867–5872, Oct. 2007.

[104] M. Mantina, Y. Wang, L. Q. Chen, Z. K. Liu, and C. Wolverton, “First principles impurity diffusion coefficients,” *Acta Mater.*, vol. 57, no. 14, pp. 4102–4108, Aug. 2009.

[105] V. Fallah, B. Langelier, N. Ofori-Opoku, B. Raeisinia, N. Provatas, and S. Esmaeili, “Cluster evolution mechanisms during aging in Al–Mg–Si alloys,” *Acta Mater.*, vol. 103, pp. 290–300, Jan. 2016.

[106] S. Hirosawa, F. Nakamure, and T. Sato, “First-Principles Calculation of Interation Energies between solutes and/or Vacancies for Predicting Atomistic Behaviors of Microalloying Elements in Aluminum Alloys,” *Mater. Sci. Forum*, vol. 561–565, pp. 283–286, 2007.

[107] A. Serizawa, S. Hirosawa, and T. Sato, “Three-Dimensional Atom Probe Characterization of Nanoclusters Responsible for Multistep Aging Behavior of an Al-Mg-Si Alloy,” *Metall. Mater. Trans. A*, vol. 39, no. 2, pp. 243–251, Feb. 2008.

[108] D. Yin *et al.*, “Effect of natural ageing and pre-straining on the hardening behaviour and microstructural response during artificial ageing of an Al–Mg–Si–Cu alloy,” *Mater. Des.*, vol. 95, pp. 329–339, Apr. 2016.

[109] W. F. Miao and D. E. Laughlin, “A differential scanning calorimetry study of aluminum alloy 6111 with different pre-aging treatments,” *J. Mater. Sci. Lett.*, vol. 19, no. 3, pp. 201–203, 2000.

[110] W. F. Miao and D. E. Laughlin, “Effects of Cu content and preaging on precipitation characteristics in aluminum alloy 6022,” *Metall. Mater. Trans. A*, vol. 31, no. 2, pp. 361–371, 2000.

[111] M. Murayama, K. Hono, W. F. Miao, and D. E. Laughlin, “The effect of Cu additions on the precipitation kinetics in an Al-Mg-Si alloy with excess Si,” *Metall. Mater. Trans. A*, vol. 32, no. 2, pp. 239–246, 2001.

[112] M. Liu *et al.*, “DSC analyses of static and dynamic precipitation of an Al–Mg–Si–Cu aluminum alloy,” *Prog. Nat. Sci. Mater. Int.*, vol. 25, no. 2, pp. 153–158, Apr. 2015.

[113] Z. Zhang, H. Xu, S. Wu, and Y. Liu, “Effects of combined pre-straining and pre-aging on natural aging and bakehardening response of an Al-Mg-Si alloy,” *Acta Metall. Sin. Engl. Lett.*, vol. 26, no. 3, pp. 340–344, Jun. 2013.

[114] H. Zhong, “Effect of composition and processing on the microstructure and formability of aluminium automotive body sheet alloys,” PhD, Monash University, 2014.

[115] H. Zhong, P. A. Rometsch, and Y. Estrin, “The Influence of Si and Mg Content on the Microstructure, Tensile Ductility, and Stretch Formability of 6xxx Alloys,” *Metall. Mater. Trans. A*, vol. 44, no. 8, pp. 3970–3983, Aug. 2013.

[116] H. Zhong, P. Rometsch, and Y. Estrin, “Effect of alloy composition and heat treatment on mechanical performance of 6xxx aluminum alloys,” *Trans. Nonferrous Met. Soc. China*, vol. 24, no. 7, pp. 2174–2178, Jul. 2014.

[117] H. Zhong, P. A. Rometsch, L. Cao, and Y. Estrin, “The influence of Mg/Si ratio and Cu content on the stretch formability of 6xxx aluminium alloys,” *Mater. Sci. Eng. A*, vol. 651, pp. 688–697, Jan. 2016.

[118] S. M. Hirth, G. J. Marshall, S. A. Court, and D. J. Lloyd, “Effects of Si on the aging behaviour and formability of aluminium alloys based on AA6016,” *Mater. Sci. Eng. A*, vol. 319, pp. 452–456, 2001.

[119] A. K. Sachdev, “Development of an aluminum sheet alloy with improved formability,” *Metall. Trans. A*, vol. 21, no. 1, pp. 165–175, 1990.

[120] S. Esmaeili and D. J. Lloyd, “Effect of composition on clustering reactions in AlMgSi(Cu) alloys,” *Scr. Mater.*, vol. 50, no. 1, pp. 155–158, Jan. 2004.

[121] M. Werinos *et al.*, “Design strategy for controlled natural aging in Al–Mg–Si alloys,” *Acta Mater.*, vol. 118, pp. 296–305, Oct. 2016.

[122] M. Liu, J. Čížek, C. S. T. Chang, and J. Banhart, “Early stages of solute clustering in an Al–Mg–Si alloy,” *Acta Mater.*, vol. 91, pp. 355–364, Jun. 2015.

[123] V. Fallah *et al.*, “Atomic-scale pathway of early-stage precipitation in Al–Mg–Si alloys,” *Acta Mater.*, vol. 82, pp. 457–467, Jan. 2015.

3 Materials and experimental methodology

Nine (9) different alloy compositions were chosen, having systematically varying levels of Mg, Si, and Cu to determine their effects on the plastic properties of AA6xxx series sheet. These alloys coupled with two different heat treatment schedules, tested using microstructure and mechanical characterization methods, allow for the composition-structure-strength-ductility/formability relationships to be assessed in a hierarchal and systematic way.

3.1 Alloy compositions and heat treatments

The nine alloys selected to be studied in this work are shown below in Table 3-1, each being Si-rich whereby there is greater Si content compared to the total of Mg and Cu.

Table 3-1: *The alloy designation and corresponding solute elements. The values listed are all in at% and for the remained of the work, only the Mg, Si, and Cu contents will be discussed. The effects of more minor elements were not explicitly studied in this work.*

Sample Name	Mg (at%)	Si (at%)	Cu (at%)	Fe (at%)	Mn (at%)	Cr (at%)	Ti (at%)	Al (at%)
C0S0	0.404	0.895	0.008	0.070	0.029	0.005	0.011	
C2S0	0.381	0.896	0.089	0.072	0.029	0.005	0.013	
C8S0	0.379	0.879	0.333	0.079	0.031	0.006	0.012	
C8S0M	0.557	0.899	0.337	0.078	0.031	0.006	0.013	
C2S1	0.372	1.069	0.087	0.071	0.030	0.006	0.015	Bal.
C0S3	0.387	1.299	0.004	0.075	0.030	0.005	0.009	
C2S3	0.400	1.262	0.088	0.076	0.030	0.005	0.010	
C5S3	0.372	1.284	0.218	0.078	0.032	0.006	0.011	
C8S3	0.385	1.324	0.329	0.079	0.032	0.006	0.010	

It can be seen that four systematic studies for compositional effects are available for study; the effects of Cu at 0.9 and 1.3 at% Si, the effects of Si at 0.1 at% Cu, and the effects of Mg at 0.3 at% Cu with 0.9 at% Si. The heat treatment schedule for each of the alloys to produce the NA1m (naturally aged 1 month), sNA1w (secondary natural ageing 1 week), and sNA1m (secondary natural ageing 1 month) conditions are shown below in Figure 3-1.

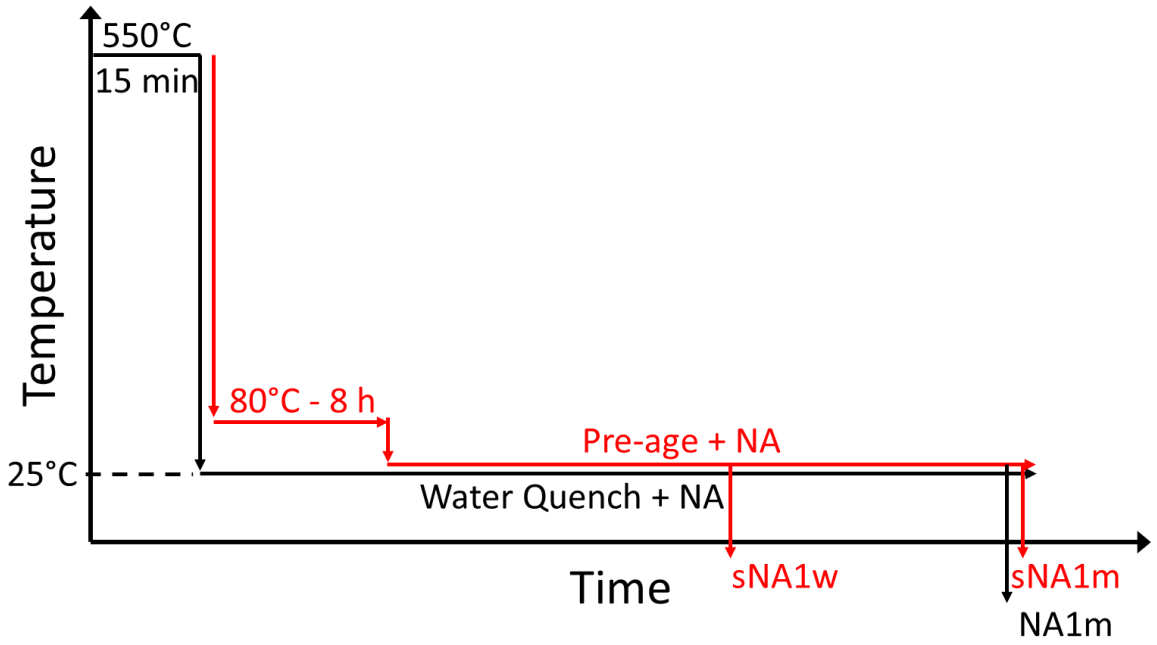

Figure 3-1: *The heat treatment schedule performed on each of the materials received from Constellium in the as-received condition. The sNA1w, sNA1m, and NA1m conditions will be used throughout this thesis primarily in the sections pertaining to tensile and strain rate sensitivity testing. Note that during differential scanning calorimetry and hardness testing, other times were used depending on the desired information to be determined, these other states will be noted.*

The samples were received in the form of cold-rolled sheet from the Constellium Technology Centre (C-TEC) in Voreppe, France in the form of 1000 mm x 400 mm x 1 mm sheet. Samples were cut according to the required dimensions/size specifications (depending on experiment type), and solutionized in an air furnace with a feedback loop to maintain a constant temperature. The samples were then either water quenched (WQ) in room temperature water, or quenched into water at 80°C, held at temperature using a hot plate, and transferred to a temperature controlled oil bath at 80°C for 8 hours within 1 minute. The samples were then removed, cleaned with ethanol and let naturally age for up to 1 month. The notation of *NA* will be reserved for samples that were WQ directly to room temperature and then allowed to naturally age at ambient temperatures. The notation of *sNA* will refer to *secondary natural ageing* whereby samples were first given a pre-ageing treatment (80 °C – 8 hours) and then allowed to secondarily naturally age at ambient temperatures.

3.2 Microstructure characterization

In order to properly characterize the effects of composition and heat treatment on the formation of clusters within the material indirect observation methods are used.

3.2.1 Hardness testing

The use of hardness testing will be to quickly identify the ageing curves and conditions for each of the alloys under the two different heat treatment schedules; WQ with NA, and PA with sNA, as well as the artificial ageing characteristics whereby samples in the sNA1w condition were then artificially aged (AA) at 185 °C for various lengths of time. The evolution of the ageing conditions will directly reflect the evolution of the cluster state over time spent at room temperature. From this information, it is possible to select the limits for more complicated studies that require more material and/or preparation time, such as tensile testing, strain rate sensitivity, atom probe tomography (APT), etc. Hardness samples were prepared using standard polishing methods; 600-grit paper, 9 µm then 3 µm diamond, and finally colloidal silica were used to produce a mirror

finish. Samples were finally immersed in a solution of bright etchant for 30 seconds, rinsed in water, and dipped in a 5% nitric acid (HNO_3) solution to remove any oxide layers that formed, rinsed in ethanol and finally dried. A Wilson Tukon 1202 (S/N 1202-02-0158) automated hardness indenter with a 100g mass and a 20 second dwell time was used to make the indentations. Ten indents, spaced 1 mm apart were made and analyzed using the Buehler OmniMet MHT, the values reported are the average of the 10 indents, standard deviations found to be on the order of ± 2 HV_{100} are not plotted for clarity.

3.2.2 Differential scanning calorimetry

The purpose of differential scanning calorimetry (DSC) is to examine the amount of energy required (endothermic) or released (exothermic) in order to increase the temperature of a sample compared to a reference. Since extensive work has already been performed coupling either High Resolution Transmission Electron Microscopy (HR-TEM) and/or APT to DSC in the AA6xxx series [1]–[6], it will be possible to couple changes in heat treatment and DSC signatures to the changes in the cluster evolution within the alloys tested in this work.

DSC samples were prepared from heat treated coupons (either PA or WQ) and allowed to sNA or NA until the final conditions. Samples were then cut using a disc cutter at 1500 rpm to a final size of 3.5 x 3.5 mm^2, and lightly ground by hand using 600-grit SiC paper. Samples were then rinsed in ethanol, allowed to dry and massed using a Mettler Toledo balance. The samples were placed into an aluminium crucible, capped, and placed into a Mettler Toledo DSC using an empty crucible as reference. The DSC scans performed at outlined below in Figure 3-2 and were tested using an external N_2 gas flow rate of 200 mL/min with a cell flow rate of 50 mL/min.

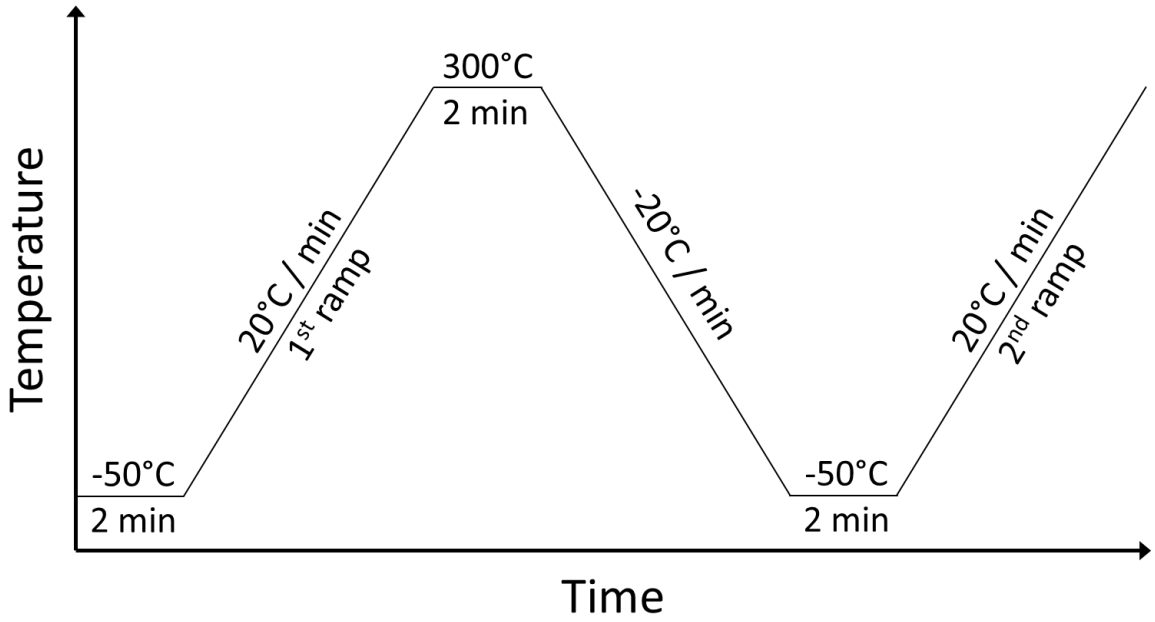

Figure 3-2: *The heating ramps and hold times used in the present work. Since this thesis focuses primarily on the clustering effects in the Al-Mg-Si-Cu alloy system, 300 °C was adequate for completing these reactions and observing their effects on the first precipitation peak.*

In traditional DSC testing, a 4^{th} or 6^{th} order polynomial fit is used to determine the baseline of the sample such that any reaction taking place in the sample will be above or below the baseline where in this work, these will represent exothermic or endothermic reactions, respectively. The purpose of cyclic heating used in this work is to eliminate the need to use a polynomial fit in order

to correct for the baseline but to use the second ramp as the baseline data set such that each sample, in each condition, will have its own unique baseline, based on the specific sample. The premise is that the initial ramp is the actual experiment whereby the exothermic and endothermic signals will be realized during the heating, and by holding at a high temperature above the main precipitation reaction, the solutes are able to be fully precipitated out such that no reaction should take place below this temperature during the second run, only the thermal effect due to the heat capacity shall remain. The second ramp thus provides an ideal baseline for the data set obtained during the first heating ramp. This process is shown below in Figure 3-3a with the resulting, mass normalized final data shown in Figure 3-3b.

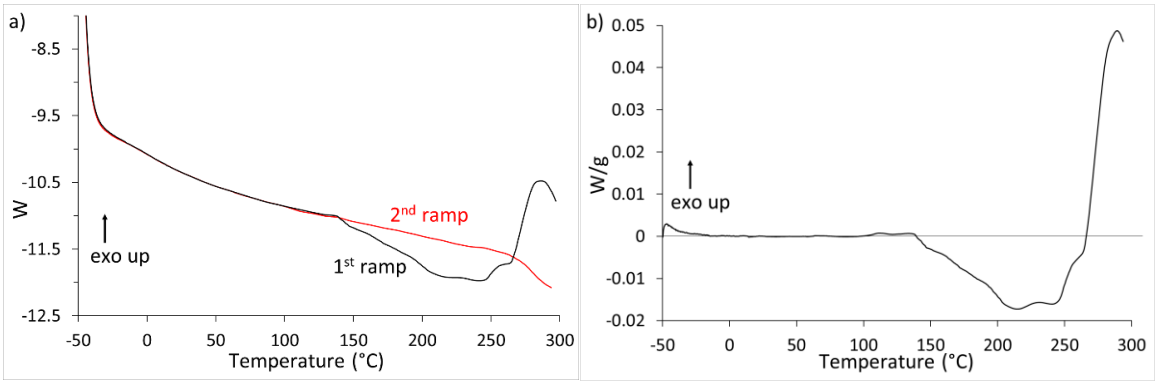

Figure 3-3: *The DSC thermographs obtained from* ***a)*** *the first (black) and second (red) DSC heating cycles outlined in Figure 3-2 and* ***b)*** *the mass-normalized difference between the first ramp and second ramp. The exothermic direction is up.*

It can be seen that there is an initial transition region extending from -50 °C to -20 °C as the system and heating rate settles to its prescribed 20 °C/min. In certain tests, it was seen as advantageous to perform a full heating ramp extending to 600 °C and in these cases, a second order polynomial was fit to the two regions perceived to contain only the heat capacity of the sample; directly before the observance of clustering events, (between 20 – 50 °C) and after the final precipitation peak but prior to the solvus (550 – 580 °C). The correction process for these samples are shown below in Figure 3-4 along with the removal of a “spike” in the data which appeared to cause a vertical offset in the final data.

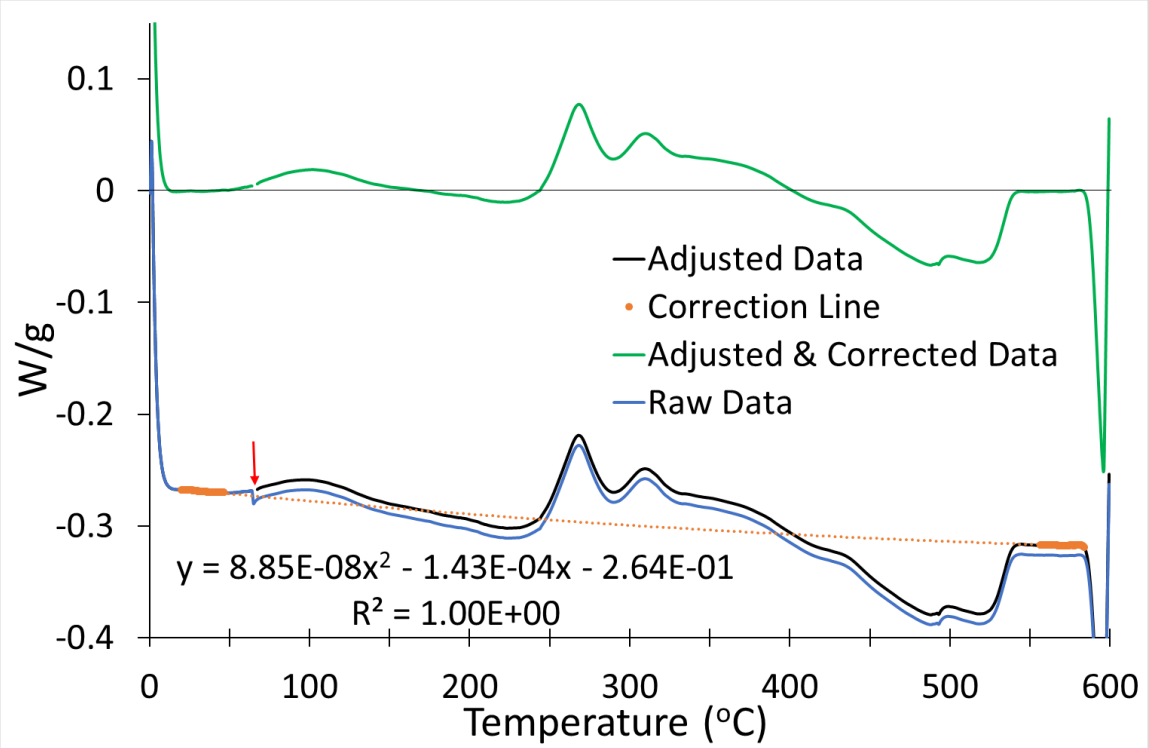

Figure 3-4: *The procedural correction for a full-DSC thermograph. The raw data is shown in blue, which was adjusted to create the black line due to the "spike" in the data at 60 °C (see red arrow) by shifting all of the data at higher temperatures up by the size of the spike. A parabolic fit was then found using the two regions in orange (located along the adjusted line) and this was then used as the baseline to generate the final data (in green). A very small discontinuity may be seen at 60 °C where the "spike" took place but the curve remains continuous nonetheless.*

Each of the test samples are normalized to their mass such that samples of different sizes may be compared (although test samples were all 30 ± 3 mg in total mass). Any exothermic peak observed (above the x-axis) indicates the presence of a clustering or precipitation reaction that has taken place during the heating ramp while endothermic peaks (below the x-axis) are those requiring additional energy in order to dissolve any clusters or precipitates that formed during the heat treatments. The evolution of the endothermic and exothermic peaks with heat treatment and NA time, as well as between sample compositions will give insight into the amount of clustering available to the system or the amount of clustering that has already occurred. This information will then be connected to the other microstructure characterization techniques performed and be used as evidence to support the observed mechanical properties of the tested alloys.

3.2.3 Atom probe tomography

Atom probe tomography (APT) samples were prepared by cutting 20 mm x 15 mm samples from the grip and gauge regions of the tensile specimen selected for APT testing. Samples were ground from the original thickness of 1 mm to 250 µm using 600-grit, 9 µm, and 3 µm diamond polish. Samples were then mounted of a thick piece of aluminium (for support) and cut using a slow-speed diamond blade to create matchsticks of 350 µm x 350 µm x 20 mm. Samples were then electropolished using a homemade electropolishing system to create atom probe tips having a nominal radius of curvature of 200 nm.

A second set of samples were prepared using Plasma Focused Ion Beam Microscopy (PFIB) using an accelerating voltage of 15 kV, and Xe+ ions to prevent sample damage or Ga+ implantation confounding the results. Samples were cut from the grip and gauge section of the tensile

specimen, prepared using standard grinding and polishing practices until colloidal silica to produce a mirror finish. Samples were then initially cut into triangular prisms, 200 µm in width, 20 µm in length and 20 µm in depth using the FEI control software. One side of the sample was cut, a nanomanipulator was then inserted into the system, and welded to the cut end using platinum deposition. The other side of the sample was cut, and segments of the bar were welded (via platinum deposition) to a sample holder and cut from the bar. This was repeated until 4 samples were mounted on individual specimen posts. Each sample was then milled using an annular pattern in stages, beginning with a 500 nm inner radius, down to a 100 nm inner radius. Once the tip-radii were reduced to under 100 nm, a final cleaning was performed using an accelerating voltage of 5 kV and a small aperture size to prepare the most pristine samples possible and reduce any surface damage or Xe+ implementation which would result in potentially incorrect APT data. The APT experiments were performed at the Max Planck Institüt fur Eisenforschlung in Düsseldorf, Germany using a LEAP 5000 atom probe with a detector efficiency of 80%. The experiments were performed with a sample temperature of 50 K, a detection rate of 0.8%, pulse fraction of 20%, a pulse rate of 250 kHz and a field estimate of 20 V/nm. Between 40 and 70 million atoms were collected during each of the experiments.

3.3 Mechanical characterization

To adequately characterize the influence of microstructure on the mechanical properties that control the formability in AA6xxx series alloys, several lab-scale tests were performed. Two sets of samples were created for the mechanical testing; small-size tensile specimen (see Figure 3-5) and sub-size tensile specimen (Figure 3-5) taken from the grip region of the small-size tensile samples to be used in the SRS testing at dry-ice temperatures.

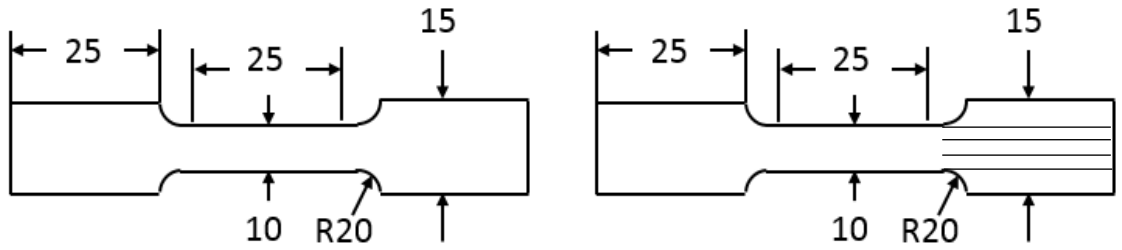

Figure 3-5: *The geometry of the tensile specimen prepared for tensile and strain rate sensitivity testing. The left image shown the standard specimen size which the right image shows the "sub-size" specimen which were extracted from the head region of the standard dog-bone samples.*

Tensile specimen were machined by Constellium in the rolling direction after cold rolling but prior to recrystallization or solution heat treatments. All samples were heat treated using the aforementioned equipment and let sit to NA until in the desired state. The cross-sectional area of the standard dog-bone samples was 10 x 1 mm^2 having a gauge length of 25 mm, the sub-size specimen has a cross section of 2 x 1 mm^2 with a gauge length of 15 mm.

3.3.1 Tensile testing

The tensile testing in this work was performed at Queen's University, Kingston, Canada using a hydraulic INSTRON tensile machine equipped with a 10kN and 100kN load cell for the ambient and low-temperature tests, respectively. Testing was performed at a constant true strain rate, $\dot{\epsilon_0}$, of 5 x 10^{-4} s^{-1} using a 25 ± 10 mm extensometer and a PID system to actively control the deformation rate. The load-displacement curve was collected electronically and then converted to engineering stress-engineering strain (s - e), then to true stress-true strain ($\sigma - \epsilon$) and finally to true stress, plastic strain ($\sigma - \epsilon_p$).

3.3.2 Strain rate sensitivity testing

The strain rate sensitivity (SRS) testing was performed at Queen's University, Kingston, Canada, using a hydraulic INSTRON tensile machine equipped with a 10 kN and 100 kN load cell. The samples were instrumented with a 25 ± 10 mm extensometer, and tested at a base true strain rate, $\dot{\epsilon}_0$, of 5 x 10^{-4} s^{-1}. SRS changes were by both increasing (up-change) or decreasing (down-change) the active strain rate by either a factor of 4 and 10, or ¼ and 1/10, for the up-change and down-change tests respectively. The use of the step-ramp method, previously described by Carlone and Saimoto [7] was employed whereby a compensation or adjustment to the active true strain is inserted during the rate-change in order to eliminate the transient on the sample due to the change in machine compliance from the change in the strain rate. An example of undercompensated and ideally compensated systems for down-changes with the corresponding stress response (over time) are shown below in Figure 3-6a and 3-6b, respectively.

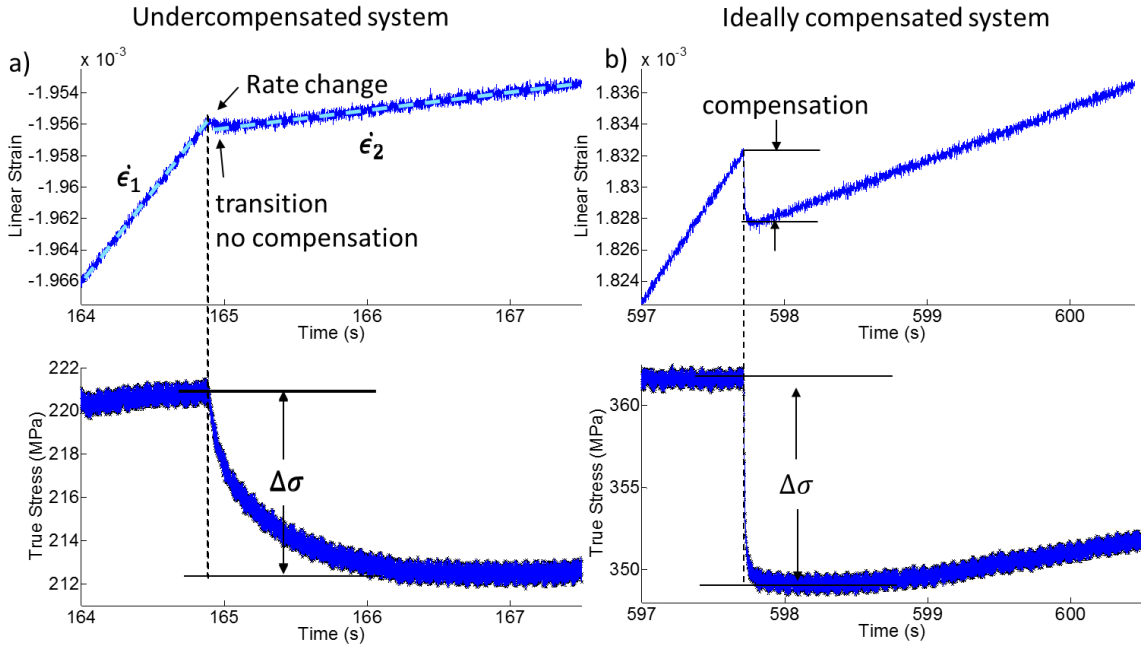

Figure 3-6: *The time dependence of the true strain control and true stress response with a strain rate change for an Al-0.35Mg-1.3Si-0.5Cu test sample with* ***a)*** *no compensation (traditional method), and* ***b)*** *ideal compensation. Note the stress relaxation over longer time to reach a minimum stress in the un-compensated test compared to the compensated one.*

As can be observed above, a "step" is inserted into the strain evolution over time in order for the strain rate response to only be "felt" by the sample and not the tensile machine. The difference between these two are due to the machine stiffness whereby a decrease in the strain rate changes the machine compliance of the system resulting in an incorrect stress reading that requires time to stabilize. If the sample is correctly compensated (ie: a sufficiently large "step" is inserted) the relaxation time of the sample is considerably reduced and a better measurement of the true stress-drop caused by the changed strain rate is observed. This same process may be used in the determination of the stress change due to an increase in the applied strain rate whereby the instantaneous change in the stress is determined (see Figure 3-7) rather than the commonly determined steady state stress change or the back-extrapolated change in stress [8]–[10].

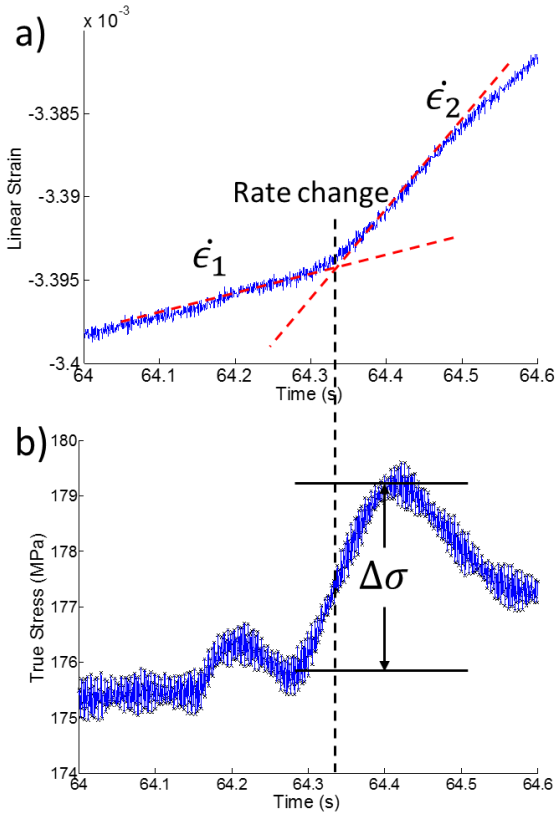

Figure 3-7: *The method of compensation and determining the stress change due to an increase in the applied strain rate. Note there is a small "bump" at 64.2 seconds, just prior to the actual rate change taking place. The actual rate change taking place is from the minimum prior to the rate change (64.3 seconds) to the maxima after the rate change (64.42 seconds) yet prior to the transient occurring after 64.5 seconds.*

3.3.3 Low-temperature testing

The low temperature testing in this work utilized two different testing machines with similar principles for force application and isolation for the tensile specimen. Both systems implemented the aforementioned step-ramp method for machine compensation to account for the machine stiffness and compliance since down-change testing was used at the lower temperatures.

Dry ice testing

The data collection and system calibration using the mechanical tensometer consisted of collecting data on chart recorder paper using an HP Chart Recorder and an ink pen, connected to the drive shift using a custom gear system, see Figure 3-8. Testing at dry ice temperatures required the use of dry ice (solidified CO_2) within a carrier medium (ethanol used for this work) in order to provide adequate cooling of both the sample and the machine components. The ethanol-dry ice solution was made in a vacuum dewar, dry ice slowly added to prevent boiling and overspill. The tested sample was measured (width and thickness, nominally, 2 mm x 1 mm) and mounted square into the top grip of the tensile machine. The top grip was screwed into the pull rod of the testing machine and the bottom grip was secured, allowing for a small amount of slack to be present to allow for the contraction of the material when cooled. The dewar full of ethanol-dry ice mixture was slowly raised around the system and the temperature regulation system (water pump) was turned on in order to prevent cooling of unnecessary components. The system was allowed to equilibrate for one hour, the temperature measured using a thermocouple and dry ice added to maintain a constant source of cooling.

Figure 3-8: *The tensometer used to perform the dry-ice ethanol sub-size strain rate sensitivity tests located at Queen's University, Kingston, Canada. The mechanical assembly is shown on the left with the control panel shown on the right side. Great care was taken to ensure the temperature remained constant and was adequately low prior to testing by waiting over one hour prior to testing.*

Liquid nitrogen testing

Liquid nitrogen testing was performed on a hydraulic INSTRON using a 100 kN load cell with an external testing frame used to transfer the load from the hydraulic ram to the sample contained within the liquid nitrogen tank, shown in Figure 3-9. The sample was measured, a J-type thermocouple attached to the grip segment of the sample to monitor the temperature, mounted into the grips, and the top grip was attached to the pull-rod of the system. The drive cylinder was attached to the top plate, and the bottom grip was secured to the bottom plate using a low-temperature hemispherical nut. The ram was driven down to reduce space and to slightly load the sample (around 7.5 kg) and then unloaded to create space to allow for the contraction of the sample during cooling. The 30 litre liquid nitrogen (LN_2) tank was partially filled, lifted around the sample and placed on the support rod where it was subsequently filled using a transfer dewar. Once filled, cotton insulation was placed on the surface of the container to prevent excessive LN_2 loss, and the temperature of the sample was monitored. As the LN_2 boiled off, the LN_2 was periodically filled to prevent icing of the components and after approximately one hour (or once the temperature was stabilized) the temperature was recorded and the test began. The same step-ramp method previously described was used to the SRS testing at LN_2 temperatures albeit with significantly larger compensation values to the added slack in the system caused by the external support structure.

Figure 3-9: *The testing apparatus connected to the hydraulic INSTRON used for testing at liquid nitrogen temperatures (78 K). The hydraulic assembly and the external support structure is shown on the right with the control electronics (PC and control board) shown on the left. All compensation levels were manually adjusted during the testing sequence and manually applied.*

3.4 References

[1] S. Esmaeili, D. Vaumousse, M. W. Zandbergen, W. J. Poole, A. Cerezo, and D. J. Lloyd, "A study on the early-stage decomposition in the Al–Mg–Si–Cu alloy AA6111 by electrical resistivity and three-dimensional atom probe," *Philos. Mag.*, vol. 87, no. 25, pp. 3797–3816, Sep. 2007.

[2] F. De Geuser, W. Lefebvre, and D. Blavette, "3D atom probe study of solute atoms clustering during natural ageing and pre-ageing of an Al-Mg-Si alloy," *Philos. Mag. Lett.*, vol. 86, no. 4, pp. 227–234, Apr. 2006.

[3] A. Serizawa, S. Hirosawa, and T. Sato, "Three-Dimensional Atom Probe Characterization of Nanoclusters Responsible for Multistep Aging Behavior of an Al-Mg-Si Alloy," *Metall. Mater. Trans. A*, vol. 39, no. 2, pp. 243–251, Feb. 2008.

[4] C. S. T. Chang and J. Banhart, "Low-Temperature Differential Scanning Calorimetry of an Al-Mg-Si Alloy," *Metall. Mater. Trans. A*, vol. 42, no. 7, pp. 1960–1964, Jul. 2011.

[5] M. W. Zandbergen, Q. Xu, A. Cerezo, and G. D. W. Smith, "Study of precipitation in Al–Mg–Si alloys by Atom Probe Tomography I. Microstructural changes as a function of ageing temperature," *Acta Mater.*, vol. 101, pp. 136–148, Dec. 2015.

[6] M. W. Zandbergen, A. Cerezo, and G. D. W. Smith, "Study of precipitation in Al–Mg–Si Alloys by atom probe tomography II. Influence of Cu additions," *Acta Mater.*, vol. 101, pp. 149–158, Dec. 2015.

[7] M. Carlone and S. Saimoto, “Precision strain rate sensitivity measurement using the step-ramp method,” *Exp. Mech.*, vol. 36, no. 4, pp. 360–366, 1996.

[8] R. C. Picu, F. Ozturk, E. Esener, and R. Li, “Aluminum Alloys with Identical Plastic Flow and Different Strain Rate Sensitivity,” *Metall. Mater. Trans. A*, vol. 41, no. 13, pp. 3358–3364, Dec. 2010.

[9] C. P. Ling and P. G. McCormick, “Strain rate sensitivity and transient behaviour in an Al Mg Si alloy,” *Acta Metall. Mater.*, vol. 38, no. 12, pp. 2631–2635, 1990.

[10] C. P. Ling and P. G. McCormick, “The effect of temperature on strain rate sensitivity in an Al-Mg-Si alloy,” *Acta Metall. Mater.*, vol. 41, no. 11, pp. 3127–3131, 1993.

4 Formation of clusters during natural and pre-ageing of Al-Mg-Si-Cu alloys

The initial step in being able to formulate an understanding of how the variation of composition will inevitably yield an influence on the subsequent mechanical properties of Al-Mg-Si-Cu alloys lies within the ability to determine the effect of solute additions on the corresponding microstructure formed during different heat treatments. This chapter will look at the evolving microstructure caused by the effects of Cu additions at two different levels of Si (0.9 and 1.3 at%), the effects of Si additions at 0.1 at% Cu, as well as Mg additions at 0.3 at% Cu on nine alloys. The solute effects will be coupled with the resulting influence on total potential for clustering and precipitation via differential scanning calorimetry (DSC) for samples in the naturally aged (NA), pre-aged (PA) and the resulting artificially aged (AA) states. The differences in NA kinetics for samples with and without PA treatments will be compared and connected to the results obtained from DSC. In general, this paper will serve as a design reference for those who desire to better understand the general impact of Si, Cu, and Mg additions on the NA, PA with secondary NA, and AA kinetics in Al-Mg-Si-Cu alloys.

Formation of clusters during natural and pre-ageing of Al-Mg-Si-Cu alloys

Abstract

The Al-Mg-Si-Cu alloy system is used in the automotive industry for body-in-white (BIW) components that undergo processing routes that end with paint baking; the method used to cure paint onto automotive doors, roofs, and hoods. This alloy type is age-hardenable meaning that if given sufficient time and temperature, a super saturated solid solution will reduce its energy through the formation of second phases having a local concentration differing from the bulk alloy concentration. This system is unique whereby the formation of clusters, regions containing high solute, can occur at room temperature, a process known as natural ageing (NA). However, if these alloys were allowed to NA for long periods of time, the hardening that took place during the subsequent paint baking resulted in a diminished hardness. This anomaly was termed the negative natural ageing effect and was deemed undesirable, resulting in aluminium manufacturers introducing a stabilization treatment known as pre-ageing (PA) prior to allowing the samples to NA. This PA process produced clusters thought to have a different chemistry than those formed during NA only. This chapter studies the effects of solute additions combined with NA, PA with secondary NA (sNA), and artificial ageing (AA), on the clustering behaviours in this alloy series. Hardness testing is used to observe the evolution of the clustering state via their influence on strengthening while differential scanning calorimetry will determine the state of clustering and their influence on the precipitation behaviour of the alloys via the positioning and intensity of exothermic and endothermic peaks. The kinetics of NA, sNA, and AA will be presented and discussed.

1.0 Introduction

The widespread use of age-hardenable aluminium alloys in the automotive and aerospace industries requires an intricate understanding of the clustering and precipitation of second phases resulting in added strength. The use of age-hardenable 6000-series aluminium alloy in sheets for body-in-white (BIW) components requires that the material combines a high formability while in the naturally aged (NA) or pre-aged (PA) conditions and a high capacity for precipitation hardening during subsequent artificial ageing (AA), referred to as the paint bake (PB) treatment (typically 20 minutes at 170-190°C). When sheet alloys are solutionized, water quenched (WQ) and allowed to naturally age while being shipped prior to automotive manufacturers forming the BIW components, the material suffers from a reduced ductility and from insufficient hardening during the PB treatment. This effect is known as the negative natural ageing effect [1], [2] due to the formation of clusters during NA. In order to prevent this detrimental effect, producers either introduced Cu into these alloy systems at a cost of corrosion resistance or gave the sheets a PA treatment after solutionizing in order to preserve the formability and hardenability potential of the material while it is shipped to automotive manufacturers [3]–[6]. Although these phenomena have been previously studied, a systematic evaluation of the effect of alloy composition via the specific effects of each alloy species is still missing to understand the differences between NA and PA, and the resulting thermal and mechanical stability of the clusters that form during the two treatments, and thus to understand the resulting mechanical properties and formability of these alloys.

2.0 Background

The clustering and precipitation sequence in the 6000-series aluminium alloys have been extensively studied [7]–[9] and can be summarized as follows

$$\text{SSSS} \rightarrow \text{solute clusters} \rightarrow \text{pre-}\beta'' \rightarrow \beta'' \rightarrow \beta' \rightarrow \beta, \text{Si}$$

Where SSSS is the supersaturated solid solution which have been shown to evolve into clusters during NA, PA, or early stage AA processes prior to the formation of precipitates. The clusters that form have been shown to have a large range of stoichiometry [9]–[11] and are less defined than those of precipitates. However, reasonable support has been found suggesting that two main types of clusters may form in this system: cluster types i and ii, said to form at temperatures below and above 70 °C, respectively [7], [12]–[14]. The differences between these cluster types have been described as having a (Mg + Cu)/Si ratio less than one (Si-rich) or greater than one (Mg- or Cu-rich), for cluster types i, and ii, respectively. Since the higher order precipitates in these alloys have stoichiometry of (Mg + Cu)/Si close to or greater than unity (Mg_5Si_6 for β'', $Mg_{1.8}Si$ for β', and Mg_2Si for β) [15], having a cluster with a matching or more closely related stoichiometry to the precipitates will reduce the energy barrier required for the clusters to evolve into precipitates [2], [16], [17]. However, it must be stated that unlike the precipitates, cluster types do not have a fixed stoichiometry and it is very difficult to define specific definitions of *cluster type i* and *cluster type ii* due to the wide range of specific cluster chemistries and the temperature of their formation. Thus clusters in this work will be referred to as Si-rich or Mg- or Cu-rich for clusters having a (Mg + Cu)/Si ratio less than or greater than unity, respectively. Subjecting the alloys to pre-ageing has actually been shown [18]–[20] to increase the PB response, which is correlated to the production of clusters with stoichiometry closer to the precipitates (Mg- or Cu-rich). Separately, Cu additions have been shown to promote to formation of Mg-rich and Cu-rich clusters formed at room temperature during NA and reduce the negative natural ageing effect in the 6000-series [3], [4] while changing the precipitation sequence to [21]

$$SSSS \rightarrow \text{solute clusters} \rightarrow \text{pre-}\beta'' \rightarrow \beta'' \rightarrow \beta', U1, U2, C, L, B', Q' \rightarrow \beta, Q, Si$$

It is also important to understand the clustering kinetics in these alloys either during direct NA or secondary NA (PA with subsequent NA) to guide designing an alloy whose hardening between sheet production and the forming process will be delayed. Banhart et al. [22], [23] have studied clustering during NA in the 6000-series system using positron annihilation lifetime spectroscopy (PALS). They describe the kinetics by five separate stages, separately analyzed by Werinos et al. [24], [25], the duration of each stage depending on the solute content, either specifically or as combination of several species. They are summarized as follows [22]:

- Stage 0: free-diffusion of vacancies in the alloy prior to the formation of solute/vacancy complexes.
- Stage 1: formation of small Si-rich aggregates.
- Stage 2: increase in vacancies trapped and immobilized in Si-rich clusters.
- Stage 3: diffusion of Mg and Cu into the Si-rich clusters formed during Stage 2.
- Stage 4: not confirmed but is speculated to be due to ordering of the solute species within the clusters and the release of vacancies from the clusters; annihilated at other sinks.

Although this model exists, this work will focus primarily on the later stages of NA and the sNA process and the differences observed. The observations will be related back into this context to explain the various observations. In parallel, atom probe tomography (APT) measurements of the atomic scale pathways of clustering [26], [27], [28], [29] and high resolution transmission electron microscopy (HR-TEM) [30] has lead to similar conclusions regarding the influences of specific solute species on the evolution of clustering during NA. Cluster states after PA and secondary natural ageing (sNA) have been studied using APT by De Geuser et al. [10], Aruga et al. [27], [31]–[33] and complemented by PALS by Chang et al. [16], [34] for several alloy compositions. It is of great importance to state that although the idea of two cluster types being present in the precipitation sequence exists, all references report the average stoichiometry of the clusters formed during the various ageing treatments strongly suggesting that the cluster chemistries exist along a continuum rather than in a discrete manner.

In this context, the present work aims at providing a comprehensive dataset of the influence of Si, Cu, and Mg content on the kinetics of natural ageing, on the effect of pre-ageing on secondary natural ageing, and on the kinetics and strengthening during artificial ageing and the paint bake treatment. One of the specific aspects of our study is that the studied alloys are “Si-rich”, namely they have a (Mg + Cu)/Si ratio smaller than unity whereas the majority of previous studies were performed on “Si-lean” alloys [35], [36]. The study will be carried out by combining hardness testing and differential scanning calorimetry, both of which providing an indirect characterization of the clustering and precipitation states.

3.0 Materials and methods

Nine alloys from the Al-Mg-Si-Cu (AA6xxx) series were chosen for testing having varying levels of Si, Mg, and Cu, their solute contents are shown in Table 4-1. All of the alloys are Si-rich, having a (Mg + Cu)/Si ratio smaller than one; their compositions are plotted in Figure 4-1 compared to two common industrial alloys, AA6016 and AA6022. The alloys contain four levels of Cu denoted C0 (no Cu), C2 (0.1 at%), C5 (0.2 at%) and C8 (0.3 at%), three levels of Si denoted S0 (0.9 at%), S1 (1.1 at%) and S3 (1.3 at%), and two levels of Mg (0.4 and 0.6 at%). Thus, this series of alloy compositions makes it possible to evaluate separately the influence of each alloying element, in the context of several contents of the other alloying species.

Sample Name	Si (at%)	Cu (at%)	Mg (at%)
C0S0	0.895	0.008	0.404
C2S0	0.896	0.089	0.381
C8S0	0.879	0.333	0.379
C8S0M	0.899	0.337	0.557
C2S1	1.069	0.087	0.372
C0S3	1.299	0.004	0.387
C2S3	1.262	0.088	0.400
C5S3	1.284	0.218	0.372
C8S3	1.324	0.329	0.385

Table 4-1: The nominal concentrations of each of the alloy contents for the nine alloys tested in this work. Note: The naming convention was originally made for the wt% of the alloys: C0S0 had 0.0 wt% Cu and 0.9 wt% Si, while C2S3 had 0.2 wt% Cu and 1.3 wt% Si.

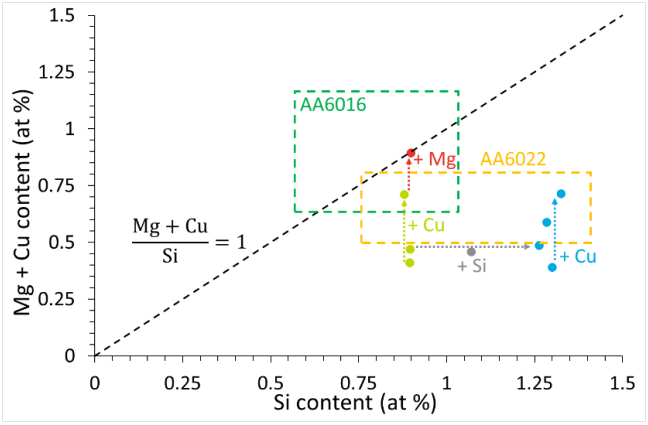

Figure 4-1: *A plot of the Cu and Mg contents compared to the Si content of the nine Al-Mg-Si-Cu alloys tested in this work. The black dashed line indicates a 1:1 (Mg + Cu) to Si ratio. The green and blue dotted arrows indicate the additions of Cu at constant Si, the red dotted arrow indicates the addition of Mg at constant Cu and Si, while the grey arrow indicates the addition of Si at constant Cu and Mg. The composition range of two common alloys; AA6016 and AA6022 are shown for comparison.*

As described above, two separate heat treatment pathways were selected; one with and one without pre-ageing, followed by natural ageing at room temperature (15 °C – 25 °C). All samples were received in the as-rolled condition, having a nominal thickness of 1 mm. The samples were then solution heat treated (SHT) in an air furnace for 15 minutes at 550 °C and either WQ at 15 °C and allowed to NA or WQ at 80 °C, transferred to an oil bath at 80 °C for 8 hours resulting in the PA condition, and then allowed to secondary naturally age. For evaluating the paint bake response during AA, samples in the PA condition were allowed to sNA for 1 week (sNA1w) and then AA for various times at 185 °C where 20 minutes at 185 °C was named PB. Differential scanning calorimetry (DSC) measurements were performed using a sample size of 3.5 x 3.5 x 1 mm^3 cut using a SiC cut-off wheel (nominal mass of 35 mg) on a Mettler Toldedo DSC using an empty Al crucible as reference. Samples were briefly ground by hand using 600-grit paper to remove any surface damage possibly inflicted by the cut-off wheel. The DSC scan cycle was as follows:

1. Cooling of the sample to -50 °C and holding for 2 minutes.
2. Heating to 300 °C at 20 °C/min, holding at 300 °C for 2 minutes.
3. Cooling to -50 °C at -20 °C/min, holding at -25 °C for 2 minutes.
4. Reheating to 300 °C at 20 °C/min.

The data and thermal signature of the sample was assumed to be completed during the first heating ramp (Step 2), and was corrected for using the second heating ramp (Step 4) as the baseline rather than using a 4^{th} or 6^{th} order fit for the baseline correction (see Chapter 3.2.2 for more details). This method implies that the alloy does not experience significant transformations during the second heating ramp. The DSC measurements were made only at particular times of ageing: WQ, WQ with 1 month NA (NA1m), and directly after PA (as-PA). These three different points in time allow for the determination of: i) the initial clustering potential, ii) the corresponding clusters formed during NA, and iii) the corresponding clusters formed during PA. The differences between the DSC thermograms will give insight into the differences between the two heat treatment procedures and the corresponding microstructure features that are formed.

For hardness testing, samples were prepared using standard metallographic preparation methods: samples were cut using a SiC cut-off wheel, then polished using 600-grit paper, 9 µm then 3 µm diamond, and finally colloidal silica were used to produce a mirror finish. Samples were then tested using a Wilson Tukon 1202 testing machine (S/N 1202-02-0158) with a 100 g mass and a 20 second dwell time. Measurements were taken as the average of 10 indents, spaced 1 mm apart, and measured using the Buehler OmniMet MHT program with a standard deviation commonly found to be ± 2 HV_{100}, that will not be plotted in the following for clarity. The natural ageing, secondary natural ageing, and artificial ageing kinetics of the alloys, were fit using an exponential [25], [37], [38] with t_0 being the incubation time directly after the PA process prior to the observation of any substantial sNA [37], [39]. The relative errors of k were found to be ± 7.5%, 5%, and 2.5% for k_{NA}, k_{sNA}, and k_{AA}, respectively. An example of the parameters that will be obtained from the three different heat treatment processes (NA, sNA, and AA) is shown for alloy C8S0 in Figures 4-2a and 4-2b.

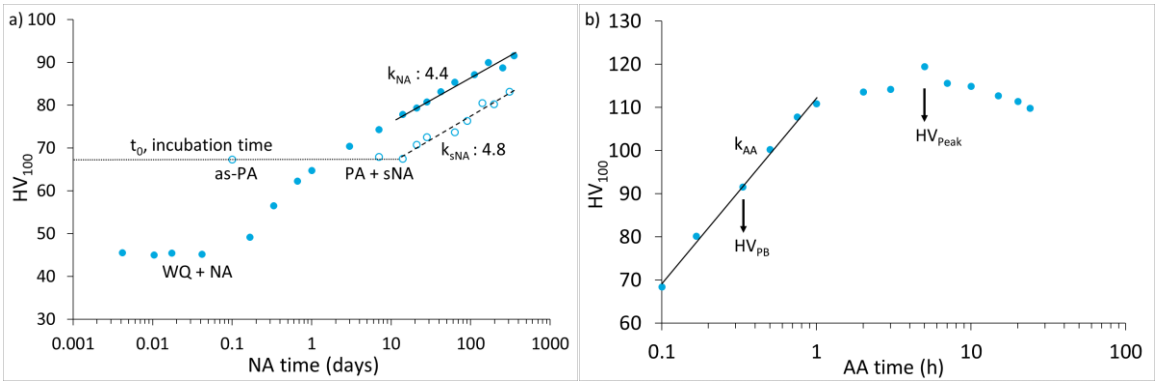

Figure 4-2: *A schematic of how* ***a)*** *the NA and sNA kinetics, and* ***b)*** *the AA kinetics are determined in the 6000-series alloys for the C8S0 alloy (Al-0.35Mg-0.9Si-0.3Cu). Note that the start time of calculation for the k_{NA} kinetics matches that of the k_{sNA} kinetics. This was done to allow for a direct comparison the kinetics of the two states.*

The critical parameters explored in this work are the kinetics of NA, sNA, and AA. Due to the long incubation times experienced in the PA samples (see horizontal line in Figure 4-2a), the hardness evolution during NA [22], [23], will begin at the same time interval as in the sNA such that they maybe compared directly (14 days for Figure 4-2a). Since the application of the present work is for automotive sheet forming, only the early stage AA kinetics, k_{AA} were determined, from the initial condition, sNA1w up until 1 h of AA at 185 °C.

4.0 Experimental Results and Analysis

As shown in the alloy composition table, this work involves the study of the effects of Cu at 0.9 at% Si and 1.3 at% Si, the effects of Si at 0.1 at% Cu, and the effects of both Mg and Si at 0.3 at% Cu. In order to limit the number of graphs shown in the main text body, only the effects of Cu at 0.9 at% Si and the effects of Si at 0.1 at% Cu are presented below. The effects of Cu at 1.3 at% Si, and effects of Mg and Si at 0.3 at% Cu are shown in Appendix 1, while the results of the kinetics and key hardness values from all alloys will be summarized and discussed later in the chapter.

4.1 Effects of Cu addition with 0.9 at% Si

The effect of Cu content at 0.9 at% Si on the hardness evolution during NA, sNA, and AA is shown below in Figures 4-3a-c.

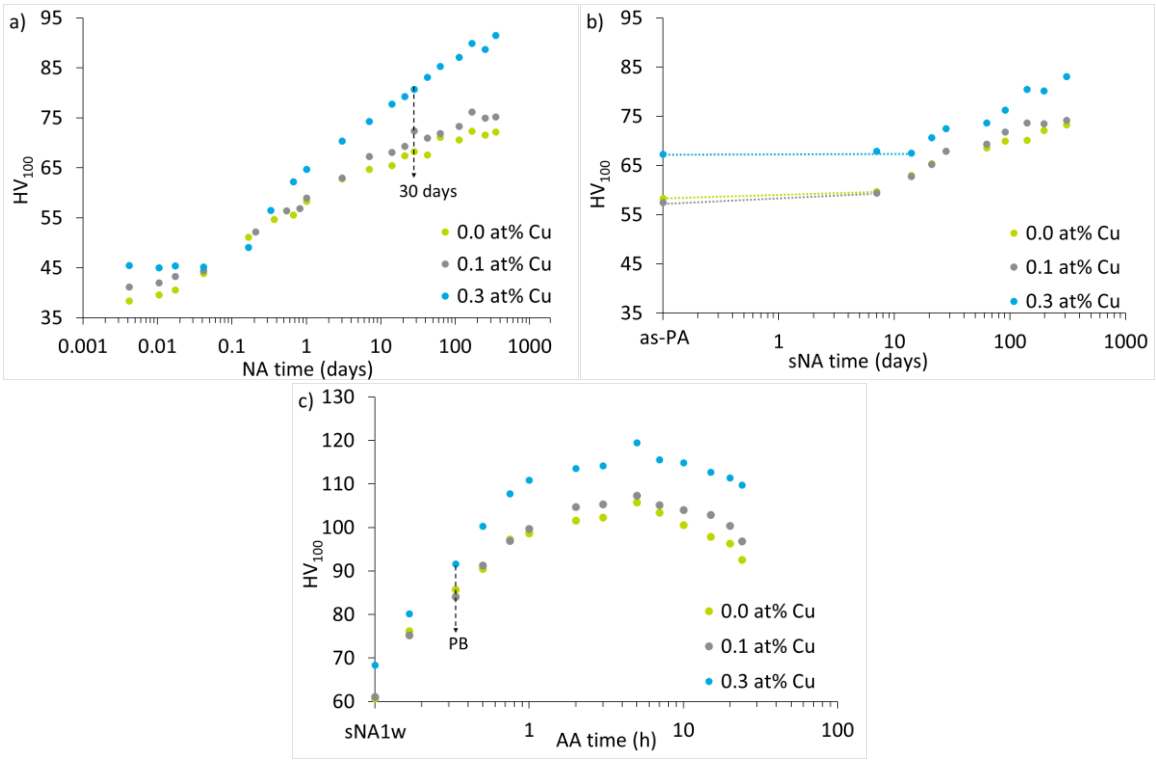

Figure 4-3: *The effects of Cu content at Si level of 0.9 at% on the age hardening curves for* ***a)*** *NA,* ***b)*** *sNA, and* ***c)*** *AA after sNA1w. The incubation times prior to sNA are shown in dotted lines in b).*

As is apparent from Figure 4-3a, the initial hardness after WQ increases with Cu content as does the duration before hardening (incubation time) whereby the three alloys have identical hardness after one hour of NA. The final hardness (assuming hardening has completed) after 360 days of NA increases with Cu content. The same is true with the hardness in the PA condition and the incubation time after the PA process whereby both of these properties increase with Cu content, hardening is not taking place for up to 14 days of sNA in the 0.3 at% Cu samples compared to 7 days in 0 and 0.1 at% Cu. After 360 days of sNA, the hardneness does increase with total Cu content. The 0 and 0.1 at% Cu alloys have almost identical hardness during both NA and sNA. The alloy with 0.3 at% Cu is significantly stronger, although its hardness difference with the other alloys is lower during sNA compared to NA suggesting that the types of clusters formed during these two processes are not the same nor are the kinetics. These trends of Cu additions continue to extend to the AA curves whereby the initial, PB, and peak hardness all increase with Cu content, most significantly between 0.1 and 0.3 at%. It should be noted that the peak age condition occurs at around 5h of AA time for all alloys, independently of Cu content.

The thermograms corresponding to the WQ, NA1m, and as-PA conditions are shown in Figures 4-4a-c.

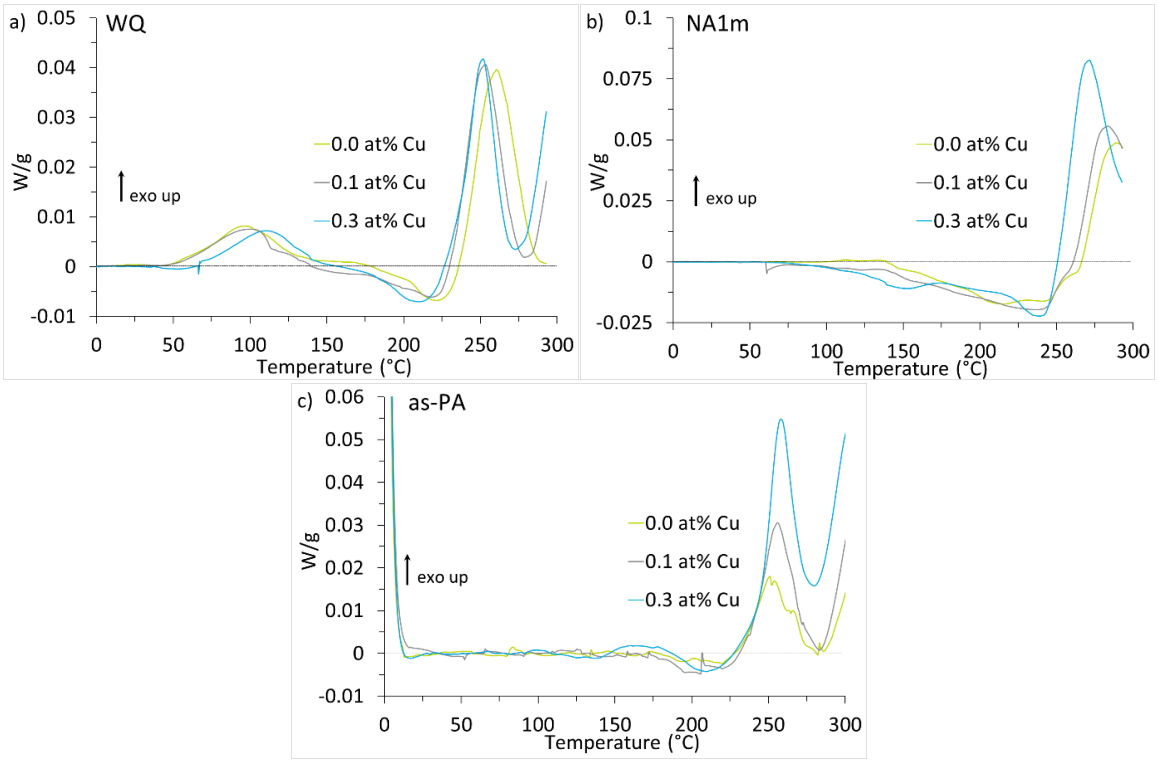

Figure 4-4: *The effects of Cu content at Si level of 0.9 at% on the DSC curves in the* ***a)*** *WQ,* ***b)*** *30 day NA, and* ***c)*** *as-PA conditions.*

Increasing the level of Cu with 0.9 at% Si induces only minor changes in the DSC thermogram in the WQ condition. An increase in the clustering peak temperature (around 100 °C) is observed with increasing Cu content, together with a slight decrease of the dissolution peak temperature for these same clusters (around 220 °C). The precipitation peak is shifted to a slightly lower temperature suggesting that the PB response should be marginally enhanced by the Cu addition. After 30 days of NA, differences in the dissolution temperature of the clusters formed during NA appear. Increasing Cu results in the appearance of a low-temperature dissolution peak (centered at 150 °C) which is absent in the sample with no Cu. The total dissolution peak area between 100 °C and 250 °C increases with Cu, consistent with an increase in the total amount of solute that is able to contribute to cluster formation, and correlating to the increased hardness after 30 days of NA in Figure 4-3a. In the NA state the precipitation peak is strongly shifted to lower temperature by the addition of Cu, especially 0.3 at%, which illustrates a reduction of the negative effect of natural ageing on the paint-bake response. The total area of the precipitation peak, although not quantitatively accessible by our experiments, increases with Cu content, which is consistent with the enhanced peak hardness observed in Figure 4-3c. Directly after PA (Figure 4-4c) the 0.3 at% Cu sample exhibits a very minor clustering at 160 °C while this is absent in the lower Cu alloys. Unlike in the NA1m condition, there is only a single cluster dissolution peak, occurring at 210 °C and being very weak in its thermal signature. This suggests that the PA clusters are more thermally stable than those formed during the NA process. The precipitation peak intensity does increase with Cu content but now there is no shift in the peak temperature. Most importantly, for all alloys this precipitation peak temperature, at 250 °C, is much lower than for the NA materials, and is

close to that of the WQ materials, which illustrates the efficiency of the PA treatment to eliminate the negative effect of NA on paint bake response.

4.2 Effects of Si additions with 0.1 at% Cu

The effects of Si content at 0.1 at% Cu on the hardness evolution during NA, sNA, and AA are shown below in Figures 4-5a-c.

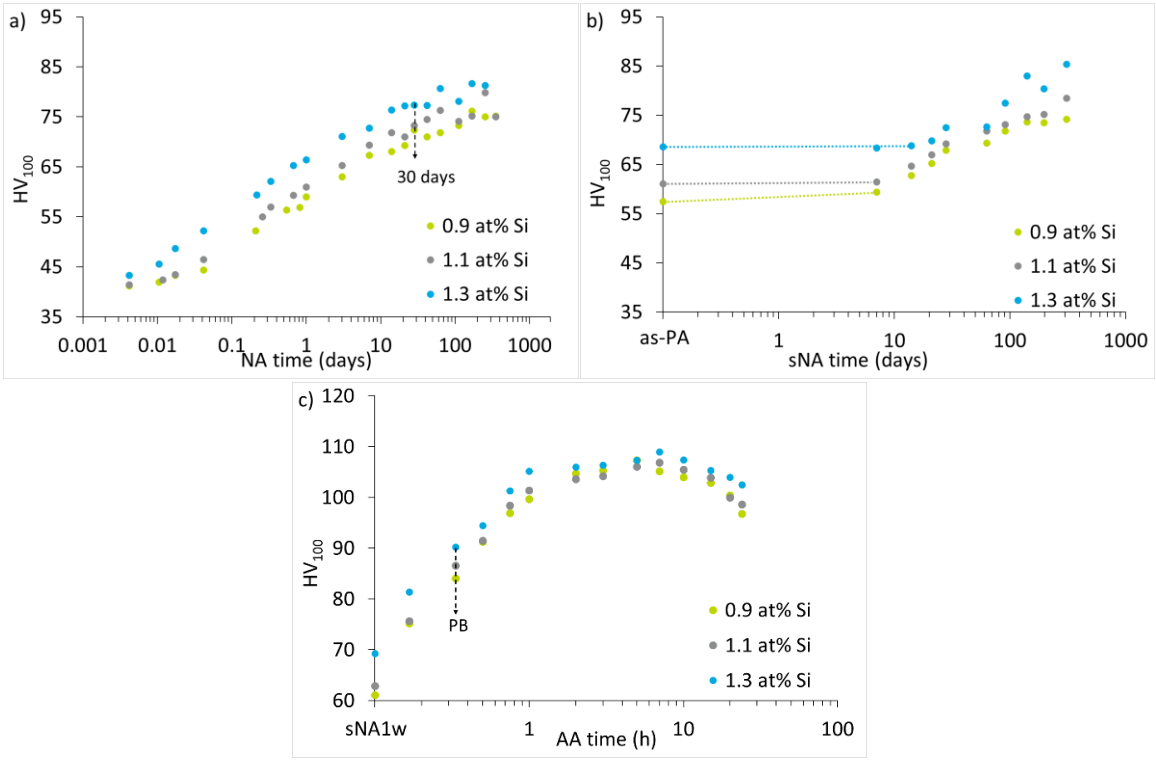

Figure 4-5: *The effects of Si content at Cu level of 0.1 at% on the age hardening curves for* ***a)*** *NA,* ***b)*** *PA with sNA, and* ***c)*** *AA after sNA1w. The incubation times prior to sNA are shown in dotted lines in b).*

Directly after WQ, the initial hardness does not significantly vary with the additions of Si but the incubation time is reduced. The strengthening effect of Si remains similar until the final hardness is obtained. As seen in Figure 4-5b, Si has a large effect on the hardness directly after PA but conversely the incubation time is increased, so that the 1.3 at% Si alloy does not exhibit much additional hardening during the sNA for times longer than 14 days of sNA. It should be noted that the hardness for all alloys after 360 days NA is comparable to the that after 360 days sNA. The hardening effect of Si addition applies also to the paint bake treatment, where the additional Si does yield an increase in the PB hardness. This additional hardening effect is significantly diminished during subsequent AA resulting in a peak hardness not significantly influenced by the addition of Si. The DSC thermograms of the main heat treatment conditions are shown below in Figures 4-6a-c.

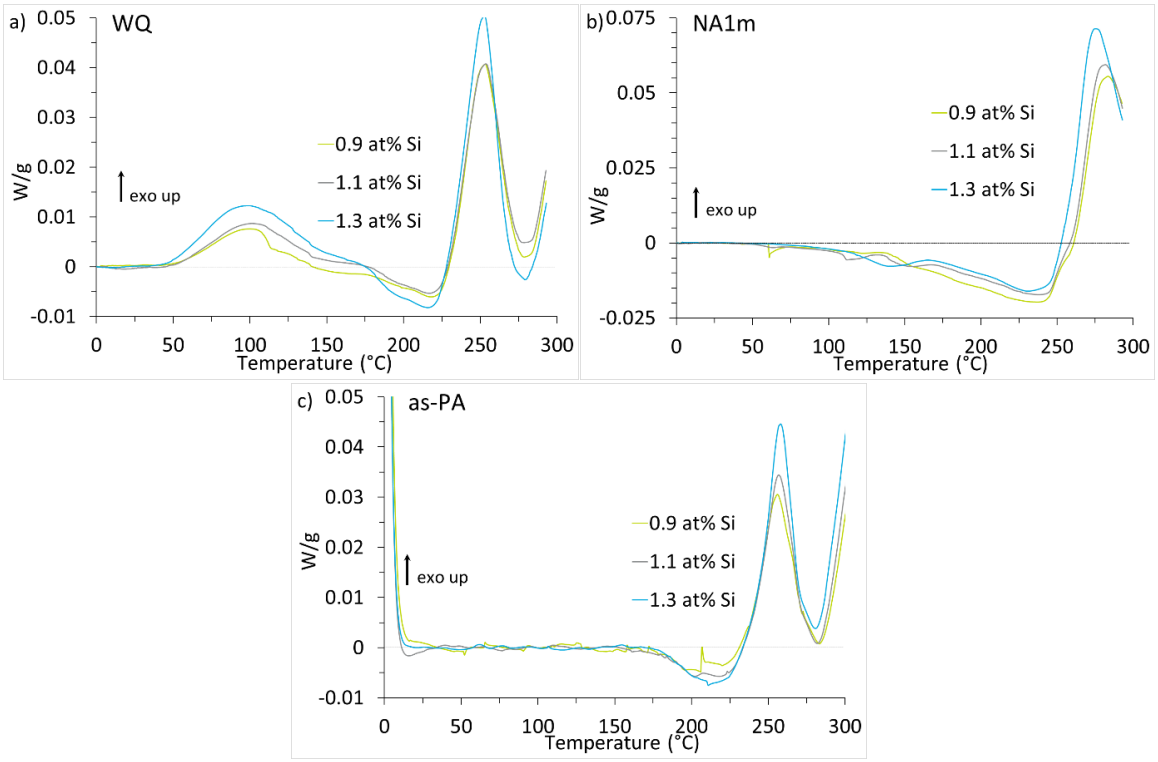

Figure 4-6: *The effects of Si content at Cu level of 0.1 at% on the DSC curves in the* ***a)*** *WQ,* ***b)*** *NA1m, and* ***c)*** *as-PA conditions.*

The DSC thermograms directly after WQ (Figure 4-6a) show that the intensity of the clustering peak around 100 °C increases with Si content correlating to the greater hardening capacity with increasing Si during NA shown in Figure 4-5a. The dissolution peak around 210 °C also increases in intensity as expected with the increase in clusters formed during the heating ramp. In the NA1m condition, all of the clustering signal has now disappeared and the NA clusters begin to dissolve at lower temperatures compared to those in the as-PA condition in Figure 4-6c. In the NA1m condition, the 1.1 and 1.3 at% Si alloys appear to have two distinct dissolution peaks, 140 °C and 220 °C (see Appendix 1.2 to show the evolution of this second peak with Cu content where the difference is much more pronounced) whereas the 0.9 at% Si alloy has a single, gradually decreasing dissolution peak. The precipitation peak temperature is lowered when the Si content reaches 1.3 at%, suggesting a reduction of the negative effect of NA on paint-bake response but this effect is much less significant than in the case of Cu additions. Finally, in the as-PA condition, there does not appear to be any retained clustering taking place while the cluster dissolution does not begin until 175 °C, a stark contrast to the NA1m condition showing that the clusters formed during the PA process are more thermally stable than those formed during NA. The dissolution peak intensity does appear to slightly increase with additional Si and translates into a greater precipitation peak intensity but now there is no shift in the peak temperature, similar to the effect of Cu. The precipitation peak temperatures are similar to that in the WQ condition, similarly to what has been shown above for the effect of Cu content. This increased dissolution peak intensity also correlates with the enhanced hardness as-PA exhibited by increasing the Si content in Figure 4-5b. As there is no large difference in the precipitation peak intensity with additional Si, it correlates to the equally minor increase in peak hardness of the alloys during AA.

4.3 Effects of composition on hardness

The key hardness parameters from the three different heat treatments performed on the nine different Al-Mg-Si-Cu alloys are summarized below in Table 4-2.

Table 4-2: *Key hardness parameters for the nine different alloys tested in the three different heat treatment procedures. HV_0 is the hardness directly after WQ, $HV_{as\text{-}PA}$, the hardness directly after the PA treatment, HV_{sNA1w}, the value after 1 week sNA (used as the initial point in the AA curve), HV_{PB}, the paint bake hardness (20 min AA at 185 °C), and HV_{Peak}, the peak AA hardness of the alloys. The average error for these measurements was ± 2 HV_{100}.*

Sample Name	HV_0	$HV_{as\text{-}PA}$	HV_{sNA1w}	HV_{PB}	HV_{Peak}
C0S0	38.4	58.3	60.8	85.7	102.3
C2S0	41.2	57.5	61.1	84.1	107.3
C8S0	45.5	67.3	68.4	91.6	119.6
C8S0M	48.1	79.6	79.5	102.6	132.6
C2S1	41.4	61.1	62.9	86.6	106.9
C0S3	43.9	67.8	69.6	89.4	108.6
C2S3	43.3	68.6	69.3	90.2	109.0
C5S3	51.4	75.0	74.0	89.9	113.9
C8S3	48.1	80.1	80.0	92.7	119.6

Based on the table above, it is clear that the initial hardness directly after quenching increases with the total solute content. In the as-PA condition, all solute elements appear to increase the hardness and this effect is similar to sNA1w. To understand the role of the different solutes on these key hardness parameters, they are plotted versus total solute content in Figure 4-7.

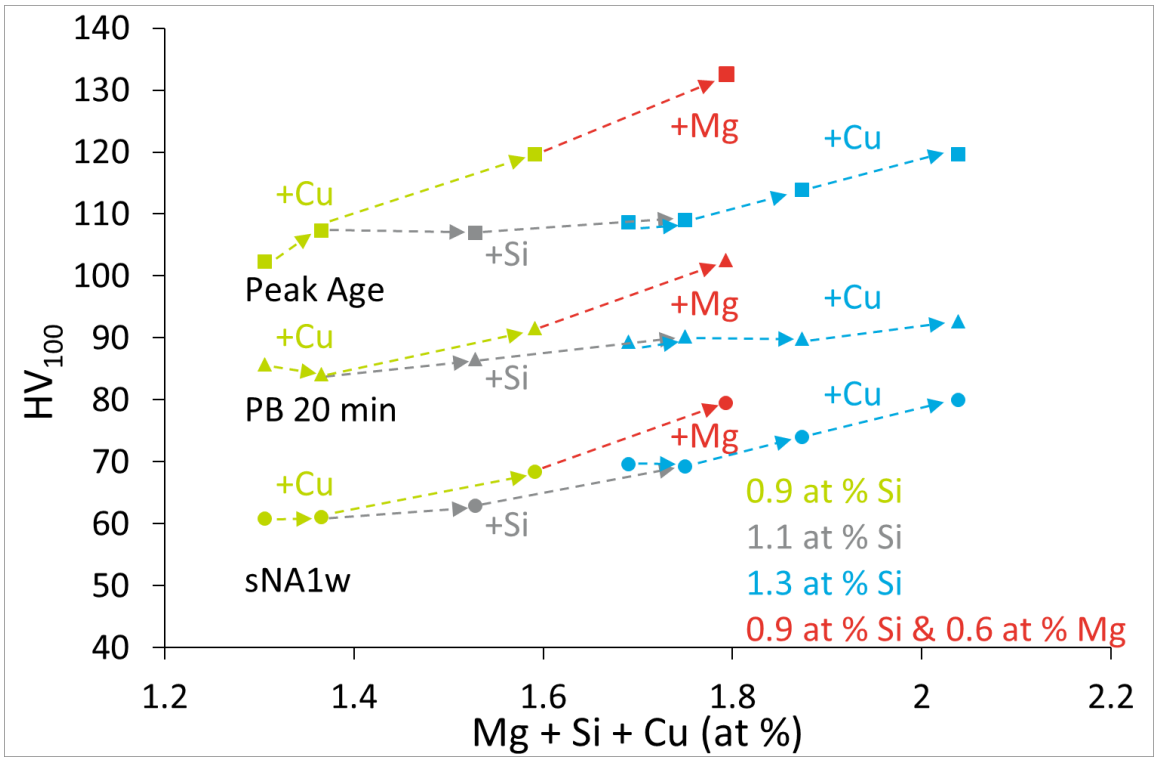

Figure 4-7: *The evolution of the HV_{sNA1w} (circles), HV_{PB} (triangles), and HV_{Peak} (squares) hardness properties with total solute content to illustrate the dependency of certain properties of the different solutes. For clarity, the effects of Cu additions at 0.9 and 1.3 at% Si, are connected in green and blue dashed arrows, respectively. The effects of Si additions at 0.2 at% Cu and 0.4 at% Mg are connected with the grey dashed arrows. The effects of Mg addition at 0.9 at% Si and 0.3 at% Cu are connected with red dashed arrows.*

In the sNA1w condition, the hardness increases uniformly with total solute content showing that the effect of Cu and/or Si additions (in at%) on the hardness increase is similar. This is in contrast to the Mg addition which appears to have a slightly stronger effect on the hardness. For the PB hardness, the effect of the different solutes is also similar to the sNA1w conditions, Mg having a

stronger effect compared to Si and Cu which retain their strengthening effects. Once samples are in the peak age condition, the stronger effects are now that of Cu and Mg while the effect of Si addition appears to be non-existent.

In order to illustrate the hardening response during artificial ageing, Figure 4-8 represents the hardness difference between the PB state and the peak age state with respect to the sNA1w state, for the nine alloys tested.

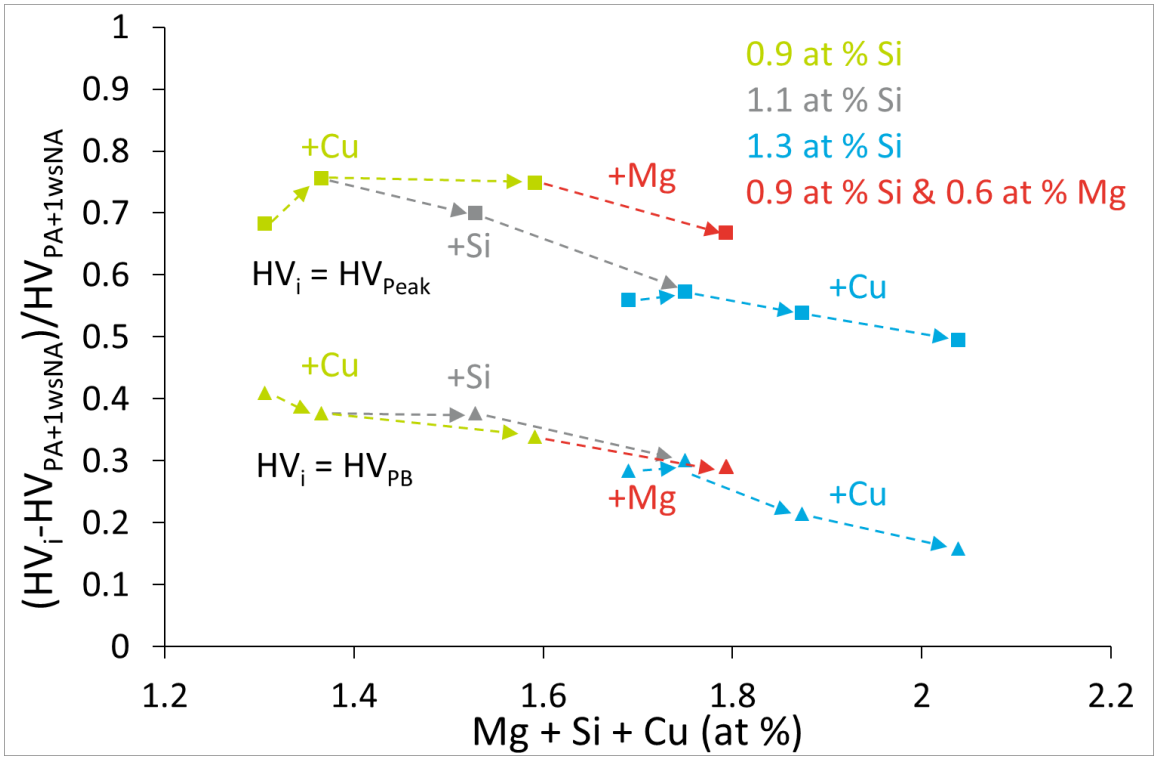

Figure 4-8: *The paint bake (triangles) and peak age (squares) response compared to the total solute content of the nine tested alloys. For clarity, the effects of Cu additions at 0.9 and 1.3 at% Si, are connected in green and blue dashed arrows, respectively. The effects of Si additions at 0.2 at% Cu and 0.4 at% Mg are connected with the grey dashed arrows. The effects of Mg addition at 0.9 at% Si and 0.3 at% Cu are connected with red dashed arrows.*

Figure 4-8 shows that the PB response of the alloys has a negative correlation with the total solute content, where Cu, Si and Mg all show very similar effects. The sensitivity of each solute species changes in the peak age response whereby at 0.9 at% Si, Cu has a positive effect but this is eliminated at 1.3 at% Si. Increased level of Si has an identical effect to added Mg such that the general picture is that increased solute reduces the peak age response. These effects are related to the combination of the increased initial hardness prior to AA (in the sNA1w condition) and the lack of effect of Si on increasing the peak hardness value.

4.4 Effects of composition on kinetics

In addition to the absolute values of hardness, it is important to study the kinetics of hardness evolution in order to gain insight into what solute additions control the hardening kinetics for the various heat treatments. The tabulation of the kinetics studied for each of the nine alloys tested are shown in Table 4-3.

Table 4-3: *The ageing kinetics for the two different NA routes, k_{NA} and k_{sNA}, and the AA kinetics, k_{AA} for the nine alloys tested. The NA time to reach maximum hardness, t_{NA}, and the incubation time prior to hardening in sNA, t_0, which was*

used as the start time for the both k_{NA} and k_{sNA} fits, are shown. Note that the incubation time prior to the onset of NA was not recorded due to the lack of data points at very low NA times.

Sample Name	k_{NA} ± 7.5%	t_{NA} (days)	k_{sNA} ± 5%	t_0 (days)	k_{AA} ± 2.5%
C0S0	2.4	168	3.3	7	15.9
C2S0	2.6	168	4.0	7	16.3
C8S0	4.4	350	4.8	14	18.6
C8S0M	3.4	63	3.2	7	17.7
C2S1	2.3	112	4.2	7	16.3
C0S3	1.8	168	3.2	7	12.3
C2S3	2.4	63	5.4	14	14.9
C5S3	3.0	42	3.8	7	13.6
C8S3	4.0	28	3.3	7	12.9

In order to understand how these properties evolve with alloy composition, the values are plotted against the total solute contents. The differences between the NA and sNA kinetics, k_{NA} and k_{PA}, are shown in Figure 4-9a and the k_{AA} kinetics are plotted versus the total solute content in Figure 4-9b.

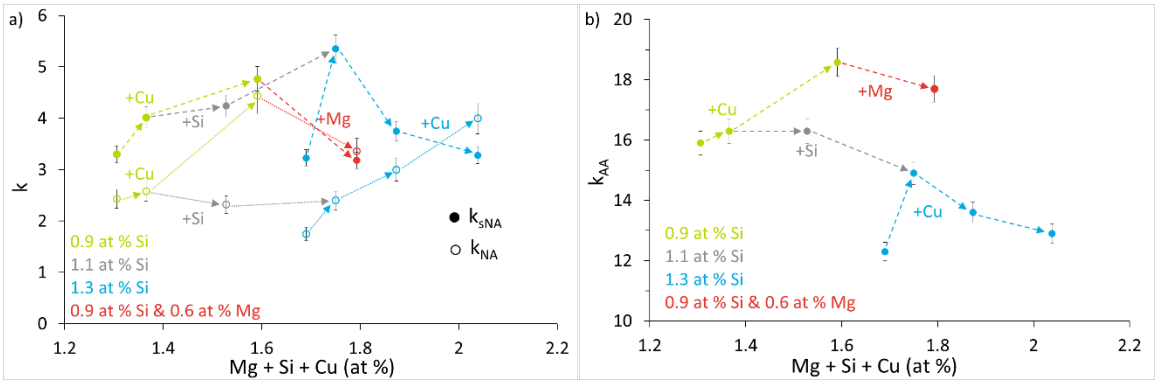

Figure 4-9: *The compositional correlation of **a)** the k_{NA} and k_{sNA} kinetics and **b)** the evolution of k_{AA} with total solute content. For clarity, the effects of Cu additions at 0.9 and 1.3 at% Si, are connected in green and blue dashed arrows, respectively. The effects of Si additions at 0.2 at% Cu and 0.4 at% Mg are connected with the grey dashed arrows. The effects of Mg addition at 0.9 at% Si and 0.3 at% Cu are connected with red dashed arrows.*

The NA kinetics depend on not only the solute content of the alloy but also the heat treatment as shown in Figure 4-9a. The k_{NA} parameter strongly increases with the addition of Cu at constant Si, is independent of Si content at constant Cu, and decreases with the addition of Mg at constant Si + Cu. In almost every case, the sNA kinetic parameter, k_{sNA}, is greater than its NA counterpart (although the global kinetics is delayed by the incubation time). For k_{sNA}, the effect of Cu at constant Si is weaker but there is the appearance of an initial "spike" in the k_{sNA} rate with Cu additions at 1.3 at% Si which decreases with added Cu; this is not present with the effects of Cu at 0.9 at% Si. However, Si addition increases the k_{sNA} parameter, unlike k_{NA}, while an addition of Mg also decreases the sNA kinetics, similarly to the NA kinetics. It is interesting that the AA kinetics appears to have a complex relation with Cu, Si, and Mg. At 0.9 at% Si, Cu increases k_{AA}, while at 1.3 at% Si, there is the same initial "spike" with the first Cu addition, followed by a subsequent decrease with further additions that was observed in the k_{sNA} behaviour. Si additions slightly decreases k_{AA}, which is also the case for an Mg addition.

4.5 Results Summary

- NA: the initial and final hardness increases most with Cu and Mg, Si has a smaller effect.

- PA: initial hardness increases with total solute content.
- AA: HV_{PB} depends most on Mg, while Cu and Si have similar effects; PB response decreases with the total solute content.
- AA: HV_{peak} depends only on Mg and Cu content, both having similar effects; peak response increases with Cu content at low Si, but decreases with total solute content.
- NA kinetics: k_{NA} increases with Cu and Mg but has strongest effect at low solute levels; Si does not strongly affect $k_{NA.}$
- sNA kinetics: increase with Cu and Si, decrease with Cu at 1.3 at% Si and with Mg additions.
- AA kinetics: decreases with Si and Mg content, appears to increase with Cu content at 0.9 at% Si levels.

5.0 Discussion

5.1 Natural Ageing

The effects of solute additions on the NA behaviour of the set of Al-Mg-Si-Cu alloys under study follows similar trends that were observed and explained by Banhart et al. [22] and expanded on by Werinos et al. [24], [25] pertaining to the five stages of NA. During NA, the first stage is an incubation time where hardness remains constant and is related to the free-vacancy content. The duration of this stage decreases with Si addition, due to the suggested rapid Si clustering taking place [25]. While the incubation time increases with Cu content, suggested to be related to the positive Cu-vacancy binding energy [34], [40] reducing their mobility and thus solute diffusion. It was found that added Cu increases the k_{NA} kinetics of NA [34], being most prominent at lower Cu and Mg levels (see stage 3 of hardening being related to Cu and Mg). This may be due to the increased number density of NA clusters formed with Cu additions. It is interesting to note that the addition of Si reduces the time it takes for the NA process to stabilize in these alloys. This is likely due to the enhanced NA kinetics as there is an increase in the number density of Si-rich clusters formed during the early stages (1 and 2) of NA permitting their rapid growth during Cu and Mg enrichment (stage 3) requiring smaller diffusion distances. At lower levels of Si, the number density of Si-rich clusters is likely reduced such that it takes significantly longer for the Cu solutes to be removed from the matrix ultimately extending the duration of k_{NA} kinetics prior to obtaining the final hardness. However, at the end the Cu and Mg enrichment of the clusters (stage 3 in the Banhart formulation), the final hardness in the NA condition increases with the total solute content, with Cu and Mg having the largest influences.

Within these alloys, it is very interesting to note that two cluster dissolution peaks are observed by DSC when Cu and Mg are added into the system (see Figure 4-4b and Appendix 1.2). The additions of Si cause a shift of the first dissolution peak to lower temperatures (see Figure 4-6b and Appendix 1.2) which strongly suggests that a distribution of cluster chemistries exist during the NA process, the lower temperature being primarily Mg- and Cu-related with their dissolution temperature being Si-related. Aruga et al. [27] found that Si-rich clusters formed during the NA process did not dissolve/evolve during subsequent AA giving rise to the negative NA effect. This result is consistent with the higher temperature dissolution peak intensity decreasing with Cu additions, whereby if less thermally stable clusters (being rich in Cu and Mg) are able to be dissolved at lower temperatures, the now free solutes may form the β'' precipitates as observed by the increased precipitation peak area and decreased peak temperature shown in Figure 4-4b.

5.2 Pre-Ageing

During the PA process, the clusters that form are certainly different than those formed during NA, being formed at temperatures greater than 70°C [32], [41] and appear to have a (Cu + Mg)/Si ratio

greater than unity suggested by the reduction in the precipitation peak temperature compared to the NA1m condition. The hardness in the as-PA condition is equally sensitive to Si, Cu, and Mg addition supported by the single dissolution peak in the as-PA thermographs (Figures 4-4c and 4-6c, and Appendix 1.2) increasing in intensity from any solute addition suggesting that all solutes take place in the initial clustering process. Cu additions in these alloys increases the incubation time prior to the onset of sNA. Since Cu has a greater vacancy binding energy than Si [34], [40], the increased incubation time may be explained by a delayed onset of diffusion of free solutes to the existing Mg- and Cu- rich clusters formed during PA [32].

At 0.9 at% Si, the thermograms in the as-PA condition (Figure 4-4c) show a very small clustering peak present in the samples with 0.3 at% Cu. This would suggest that there is some amount of retained Cu in the matrix able to contribute to the growth of the clusters that were formed during the PA process whereby at 0.3 at% Cu, Si becomes the limiting solute in cluster formation. This is consistent with the increased k_{sNA} observed with increasing Cu and it may be postulated that at higher levels of Cu, there is not an adequate amount of Si available in the system to deplete all of the Mg and Cu during the PA process. This would thus allow for further Cu-enrichment driving the increase in the sNA kinetics with Cu content at 0.9 at% Si with there being both additional free-Cu in the matrix and an increase in the number density of clusters formed during the PA process.

This situation is reversed when the effects of Cu additions are observed at 1.3 at% Si, whereby the first addition of Cu "spikes" the k_{sNA} rate while subsequent additions decrease the k_{sNA} kinetics. The reason for the initial spike is not understood but it may be speculated that the initial "spike" is caused by the more favourable cluster stoichiometry of Mg- and Cu-rich clusters formed during PA allowing for the aggregation of excess fast-diffusing Si during sNA. With the subsequent additions of Cu, there is a more complete removal of Si from the matrix during the PA process so that any additional Si that remains in the matrix will be reduced, requiring additional time to diffuse to the existing clusters and possibly making Si the limiting solute. It is possible that these two competing effects are optimized at 0.1 at% Cu, with the cluster chemistry being more Si-rich with no Cu, and there being insufficient retained Si in the matrix to permit cluster growth with 0.2 and 0.3 at% Cu.

The addition of Si (at 0.1 at% Cu) shows there is a small increase in the dissolution peak intensity suggesting that Si increases the amount of solutes taking place in clustering during the PA process. If the retention of Si in solution exists, during the agglomeration phase of the clusters during sNA, the Si enrichment of the PA clusters is able to occur more rapidly due to the smaller diffusion distances required. This explains the increase in the observed sNA kinetics. It was previously suggested that the independent formation of unique NA clusters may coincide with the sNA process after PA [42], [43]. This is less likely to be the case in this work as the DSC thermograms after the PA process do not display any further clustering signal at the lower temperatures (50 °C – 100 °C) and contains a single cluster dissolution peak.

With the additions of Mg there is a coupled effect of a more complete removal of total solute from the matrix (increased dissolution peak in Appendix 1.2) while also having the slowest diffusion of the three species yielding a decrease in the sNA kinetics with Mg additions, as observed.

5.3 Artificial Ageing

The trends observed during the AA process are quite well understood and follow the many studies performed on PB process as well as on peak ageing [18], [27], [35], [44]. Although the stoichiometry of clusters tend to greatly vary [10], [27], [34], [43], the stoichiometry of

precipitates tend to be more well defined [8], [19], [30], [45]–[47]. It is clear that the additions of Cu and Mg both increase the PB and peak hardness values. Since the basis of these alloys have a (Mg + Cu)/Si ratio significantly less than unity, any Cu or Mg addition will thus contribute to the formation of the precipitates by allowing for an additional volume fraction of precipitates to form. Si additions have a minor effect on the PB hardness, likely due to a retained effect of enhanced hardness after PA, but this effect is completely eliminated for the peak hardness, consistent with Si not being the limiting solute for precipitate formation.

In terms of kinetics, it is important to remember that the starting condition of these alloys prior to AA is the PA with one week of sNA during which none of the alloys show any significant hardening from the direct PA condition. The increase in kinetics with additional Cu at 0.9 at% Si is most likely attributed to the amount of retained Cu in solution that is able to diffuse and grow the PA clusters having a more favorable stoichiometry for precipitate formation, being Mg- and Cu-rich. At 1.3 at% Si, the additions of Cu have a similar trend to that on k_{sNA}, whereby the initial addition of Cu causes an initial increase in the AA kinetics with subsequent additions causing further decreases. The initial spike in kinetics may be explained by an initial transition to a more favorable stoichiometry of the clusters that are formed, maintaining a small and easily dissolvable cluster size while retaining Si in solution to allow for cluster growth and transition to precipitates. The subsequent additions may then result in a two-fold effect: a decrease in the free-Si available to precipitate transition and an increase in PA cluster size improving their thermal stability. The addition of Mg causes a reduction in k_{AA} likely due to an enhanced stability of the clusters formed during PA. Si additions retard the AA kinetics likely due to decrease in the (Mg + Cu)/Si ratio of the PA clusters that are formed increasing the energy barrier to permit precipitate formation [18], [27], [35], [44].

6.0 Conclusions

The roles of the different solutes during the NA, PA plus sNA, and AA processes were studied and from the current work, the following conclusions may be made:

- In the WQ condition, Si, Mg, and Cu additions increase the potential for clustering.
- After 30 days of NA there are two type of clusters that form. One type that dissolves at a lower temperature, the intensity depending on the on the Cu content while Si additions decrease their thermal stability. The second type dissolving at a higher temperature has a very small sensitivity due to solute additions.
- Directly after PA, there is only one cluster type that is produced and dissolves at similar temperatures to the second cluster type formed during NA, its intensity increasing with total solute content.
- The total solute content appears to increase the PA hardness but decreases the PB response.
- The peak hardness increases with Cu and Mg content while the peak hardness response decreases primarily based on the Si content of the alloy.
- The k_{NA} NA kinetics rely solely on the Cu and Mg content of the alloys while the k_{sNA} kinetics appear to have a more complex relationship, similar to k_{AA}.

7.0 Acknowledgements

The authors would like to thank D. Sejani for performing a portion of the DSC and hardness testing.

8.0 References

[1] F. A. Martinsen, F. J. H. Ehlers, M. Torsæter, and R. Holmestad, “Reversal of the negative natural aging effect in Al–Mg–Si alloys,” *Acta Mater.*, vol. 60, no. 17, pp. 6091–6101, Oct. 2012.

[2] G. H. Tao, C. H. Liu, J. H. Chen, Y. X. Lai, P. P. Ma, and L. M. Liu, “The influence of Mg/Si ratio on the negative natural aging effect in Al–Mg–Si–Cu alloys,” *Mater. Sci. Eng. A*, vol. 642, pp. 241–248, Aug. 2015.

[3] L. Ding, Z. Jia, Z. Zhang, R. E. Sanders, Q. Liu, and G. Yang, “The natural aging and precipitation hardening behaviour of Al-Mg-Si-Cu alloys with different Mg/Si ratios and Cu additions,” *Mater. Sci. Eng. A*, vol. 627, pp. 119–126, Mar. 2015.

[4] M. Murayama, K. Hono, W. F. Miao, and D. E. Laughlin, “The effect of Cu additions on the precipitation kinetics in an Al-Mg-Si alloy with excess Si,” *Metall. Mater. Trans. A*, vol. 32, no. 2, pp. 239–246, 2001.

[5] Y. Weng, Z. Jia, L. Ding, Y. Pan, Y. Liu, and Q. Liu, “Effect of Ag and Cu additions on natural aging and precipitation hardening behavior in Al-Mg-Si alloys,” *J. Alloys Compd.*, vol. 695, pp. 2444–2452, Feb. 2017.

[6] M. W. Zandbergen, A. Cerezo, and G. D. W. Smith, “Study of precipitation in Al–Mg–Si Alloys by atom probe tomography II. Influence of Cu additions,” *Acta Mater.*, vol. 101, pp. 149–158, Dec. 2015.

[7] X. Wang, S. Esmaeili, and D. J. Lloyd, “The sequence of precipitation in the Al-Mg-Si-Cu alloy AA6111,” *Metall. Mater. Trans. A*, vol. 37, no. 9, pp. 2691–2699, 2006.

[8] G. A. Edwards, K. Stiller, G. L. Dunlop, and M. J. Couper, “THE PRECIPITATION SEQUENCE IN Al±Mg±Si ALLOYS,” *Acta Metall.*, vol. 46, no. 11, pp. 3893–3904, 1998.

[9] M. W. Zandbergen, Q. Xu, A. Cerezo, and G. D. W. Smith, “Study of precipitation in Al–Mg–Si alloys by Atom Probe Tomography I. Microstructural changes as a function of ageing temperature,” *Acta Mater.*, vol. 101, pp. 136–148, Dec. 2015.

[10] F. De Geuser, W. Lefebvre, and D. Blavette, “3D atom probe study of solute atoms clustering during natural ageing and pre-ageing of an Al-Mg-Si alloy,” *Philos. Mag. Lett.*, vol. 86, no. 4, pp. 227–234, Apr. 2006.

[11] R. K. W. Marceau, A. de Vaucorbeil, G. Sha, S. P. Ringer, and W. J. Poole, “Analysis of strengthening in AA6111 during the early stages of aging: Atom probe tomography and yield stress modelling,” *Acta Mater.*, vol. 61, no. 19, pp. 7285–7303, Nov. 2013.

[12] S. Esmaeili, D. J. Lloyd, and W. J. Poole, “Modeling of precipitation hardening for the naturally aged Al-Mg-Si-Cu alloy AA6111,” *Acta Mater.*, vol. 51, no. 12, pp. 3467–3481, Jul. 2003.

[13] S. Esmaeili, D. Vaumousse, M. W. Zandbergen, W. J. Poole, A. Cerezo, and D. J. Lloyd, “A study on the early-stage decomposition in the Al–Mg–Si–Cu alloy AA6111 by electrical resistivity and three-dimensional atom probe,” *Philos. Mag.*, vol. 87, no. 25, pp. 3797–3816, Sep. 2007.

[14] S. Esmaeili and D. J. Lloyd, “Effect of composition on clustering reactions in AlMgSi(Cu) alloys,” *Scr. Mater.*, vol. 50, no. 1, pp. 155–158, Jan. 2004.

[15] C. D. MARIOARA, S. J. ANDERSEN, H. W. ZANDBERGEN, and R. HOLMESTAD, “The influence of alloy composition on precipitates of the Al-Mg-Si system,” *Metall. Mater. Trans. A*, p. 12.

[16] C. S. T. Chang, Z. Liang, E. Schmidt, and J. Banhart, “Influence of Mg/Si ratio on the clustering kinetics in Al–Mg–Si alloys,” *Int. J. Mater. Res.*, vol. 103, no. 8, pp. 955–961, 2012.

[17] S. Wenner, C. D. Marioara, S. J. Andersen, and R. Holmestad, “Effect of room temperature storage time on precipitation in Al–Mg–Si (–Cu) alloys with different Mg/Si ratios,” *Int. J. Mater. Res.*, vol. 103, no. 8, pp. 948–954, 2012.

[18] L. Cao, P. A. Rometsch, and M. J. Couper, “Effect of pre-ageing and natural ageing on the paint bake response of alloy AA6181A,” *Mater. Sci. Eng. A*, vol. 571, pp. 77–82, Jun. 2013.

[19] A. I. Morley, M. W. Zandbergen, A. Cerezo, and G. D. W. Smith, “The Effect of Pre-Ageing and Addition of Copper on the Precipitation Behaviour in Al-Mg-Si Alloys,” *Mater. Sci. Forum*, vol. 519–521, pp. 543–548, 2006.

[20] Y. Yan, Z. Q. Liang, and J. Banhart, “Influence of Pre-Straining and Pre-Ageing on the Age-Hardening Response of Al-Mg-Si Alloys,” *Mater. Sci. Forum*, vol. 794–796, pp. 903–908, Jun. 2014.

[21] C. D. Marioara *et al.*, “The effect of Cu on precipitation in Al–Mg–Si alloys,” *Philos. Mag.*, vol. 87, no. 23, pp. 3385–3413, Aug. 2007.

[22] J. Banhart, C. S. T. Chang, Z. Liang, N. Wanderka, M. D. H. Lay, and A. J. Hill, “Natural Aging in Al-Mg-Si Alloys - A Process of Unexpected Complexity,” *Adv. Eng. Mater.*, vol. 12, no. 7, pp. 559–571, Jul. 2010.

[23] J. Banhart, M. D. H. Lay, C. S. T. Chang, and A. J. Hill, “Kinetics of natural aging in Al-Mg-Si alloys studied by positron annihilation lifetime spectroscopy,” *Phys. Rev. B*, vol. 83, no. 1, Jan. 2011.

[24] M. Werinos *et al.*, “Design strategy for controlled natural aging in Al–Mg–Si alloys,” *Acta Mater.*, vol. 118, pp. 296–305, Oct. 2016.

[25] M. Werinos, H. Antrekowitsch, T. Ebner, R. Prillhofer, P. J. Uggowitzer, and S. Pogatscher, “Hardening of Al–Mg–Si alloys: Effect of trace elements and prolonged natural aging,” *Mater. Des.*, vol. 107, pp. 257–268, Oct. 2016.

[26] A. Serizawa, S. Hirosawa, and T. Sato, “Three-Dimensional Atom Probe Characterization of Nanoclusters Responsible for Multistep Aging Behavior of an Al-Mg-Si Alloy,” *Metall. Mater. Trans. A*, vol. 39, no. 2, pp. 243–251, Feb. 2008.

[27] Y. Aruga, M. Kozuka, Y. Takaki, and T. Sato, “Formation and reversion of clusters during natural aging and subsequent artificial aging in an Al–Mg–Si alloy,” *Mater. Sci. Eng. A*, vol. 631, pp. 86–96, Apr. 2015.

[28] V. Fallah *et al.*, “Atomic-scale pathway of early-stage precipitation in Al–Mg–Si alloys,” *Acta Mater.*, vol. 82, pp. 457–467, Jan. 2015.

[29] V. Fallah, B. Langelier, N. Ofori-Opoku, B. Raeisinia, N. Provatas, and S. Esmaeili, “Cluster evolution mechanisms during aging in Al–Mg–Si alloys,” *Acta Mater.*, vol. 103, pp. 290–300, Jan. 2016.

[30] K. Teichmann *et al.*, “HRTEM study of the effect of deformation on the early precipitation behaviour in an AA6060 Al–Mg–Si alloy,” *Philos. Mag.*, vol. 91, no. 28, pp. 3744–3754, Oct. 2011.

[31] Y. Aruga, M. Kozuka, Y. Takaki, and T. Sato, “Evaluation of Solute Clusters Associated with Bake-Hardening Response in Isothermal Aged Al-Mg-Si Alloys Using a Three-Dimensional Atom Probe,” *Metall. Mater. Trans. A*, vol. 45, no. 13, pp. 5906–5913, Dec. 2014.

[32] Y. Aruga, M. Kozuka, Y. Takaki, and T. Sato, “Effects of natural aging after pre-aging on clustering and bake-hardening behavior in an Al–Mg–Si alloy,” *Scr. Mater.*, vol. 116, pp. 82–86, Apr. 2016.

[33] Y. Aruga, M. Kozuka, and T. Sato, “Formulation of initial artificial age-hardening response in an Al-Mg-Si alloy based on the cluster classification using a high-detection-efficiency atom probe,” *J. Alloys Compd.*, vol. 739, pp. 1115–1123, Mar. 2018.

[34] M. Liu and J. Banhart, “Effect of Cu and Ge on solute clustering in Al–Mg–Si alloys,” *Mater. Sci. Eng. A*, vol. 658, pp. 238–245, Mar. 2016.

[35] L. He, H. Zhang, and J. Cui, “Effects of Pre-Ageing Treatment on Subsequent Artificial Ageing Characteristics of an Al-1.01Mg-0.68Si-1.78Cu Alloy,” *J. Mater. Sci. Technol.*, vol. 26, no. 2, pp. 141–145, 2010.

[36] H. Zhong, P. A. Rometsch, and Y. Estrin, “The Influence of Si and Mg Content on the Microstructure, Tensile Ductility, and Stretch Formability of 6xxx Alloys,” *Metall. Mater. Trans. A*, vol. 44, no. 8, pp. 3970–3983, Aug. 2013.

[37] H. S. Zurob and H. Seyedrezai, “A model for the growth of solute clusters based on vacancy trapping,” *Scr. Mater.*, vol. 61, no. 2, pp. 141–144, Jul. 2009.

[38] M. D. H. Lay, H. S. Zurob, C. R. Hutchinson, T. J. Bastow, and A. J. Hill, “Vacancy Behavior and Solute Cluster Growth During Natural Aging of an Al-Mg-Si Alloy,” *Metall. Mater. Trans. A*, vol. 43, no. 12, pp. 4507–4513, Dec. 2012.

[39] H. Seyedrezai, D. Grebennikov, P. Mascher, and H. S. Zurob, “Study of the early stages of clustering in Al–Mg–Si alloys using the electrical resistivity measurements,” *Mater. Sci. Eng. A*, vol. 525, no. 1–2, pp. 186–191, Nov. 2009.

[40] C. Wolverton, “Solute–vacancy binding in aluminum,” *Acta Mater.*, vol. 55, no. 17, pp. 5867–5872, Oct. 2007.

[41] L. Zhen, S. B. Kang, and H. W. Kim, “Effect of natural aging and preaging on subsequent precipitation process of an AI-Mg-Si alloy with high excess silicon,” *Mater. Sci. Technol.*, vol. 13, no. 11, pp. 905–911, Nov. 1997.

[42] J. Kim, E. Kobayashi, and T. Sato, “Effects of Cu addition on behavior of nanoclusters during multi-step aging in Al-Mg-Si alloys,” *Mater. Trans.*, vol. 52, no. 5, pp. 906–913, 2011.

[43] J. H. Kim and T. Sato, “Effects of Cu Addition on Nanocluster Formation and Two-Step Aging Behaviors of Al–Mg–Si Alloys,” *J. Nanosci. Nanotechnol.*, vol. 11, no. 2, pp. 1319–1322, Feb. 2011.

[44] D. Yin *et al.*, “Effect of natural ageing and pre-straining on the hardening behaviour and microstructural response during artificial ageing of an Al–Mg–Si–Cu alloy,” *Mater. Des.*, vol. 95, pp. 329–339, Apr. 2016.

[45] S. Esmaeili, X. Wang, D. J. Lloyd, and W. J. Poole, “On the precipitation-hardening behavior of the Al-Mg-Si-Cu alloy AA6111,” *Metall. Mater. Trans. A*, vol. 34, no. 3, pp. 751–763, 2003.

[46] W. F. Miao and D. E. Laughlin, “Precipitation hardening in aluminum alloy 6022,” *Scr. Mater.*, vol. 40, no. 7, pp. 873–878, 1999.

[47] A. K. Gupta, D. J. Lloyd, and S. A. Court, “Precipitation hardening in Al–Mg–Si alloys with and without excess Si,” *Mater. Sci. Eng. A*, vol. 316, no. 1, pp. 11–17, 2001.

5 Effect of Si on the strain rate sensitivity of naturally aged Al-Mg-Si-Cu alloys

One of the most important factors regarding the formability behaviour of aluminium alloys is their ability to both undergo strain hardening and their sensitivity to the rate of deformation, known as the strain rate sensitivity. In general, strain rate sensitivity tests are performed by the abrupt perturbation of a constant strain rate by that of an increased strain rate. During deformation and upon the onset of localized deformation, necking, the region interior of the neck undergoes a rapid increase in the applied strain rate. Thus, most laboratories have performed strain rate jump tests to probe the strain rate sensitivity of various alloys. This chapter will explore and detail key parameters to consider when performing strain rate sensitivity tests as well as demonstrate the importance of performing not only increases to the applied strain rate, but also decreases which will be shown to be experimentally more complicated. The apparent differences and resulting asymmetry in the strain rate sensitivity between the increasing and decreasing strain rate jump tests will be discussed and the effects of Si on each of these parameters will be highlighted to provide an example of the applicability of these methods. These will be extended to the apparent activation volumes and the possible causes of the observed asymmetry during testing at room temperature.

Effect of Si content on the strain rate sensitivity of naturally aged Al-Mg-Si-Cu alloys

Abstract

Increasing demand for a reduction in fuel emissions in passenger vehicles has generated the need for lighter weight materials to be used in automobile manufacture for body-in-white applications. Aluminum alloys in the 6000-series, containing Mg and Si are ideal candidates for these applications but lack the formability found in commonly used steels providing a need to more fully understand the factors influencing the formability of these alloys at high strains. Conventionally, a high strain rate sensitivity (SRS) is tied to increased formability due to the increase in the local strain rate found in the diffuse neck interior. However, most experimental work neglects that the regions exterior to the neck will undergo a local decrease in the strain rate which causes a corresponding material softening. Observations of an asymmetry between up-change and down-change SRS of these alloys in the natural aged condition show that different mechanisms are controlling the SRS depending on the direction of rate change. Differential scanning calorimetry, continuous tensile, and precision strain rate sensitivity testing results are presented, elucidating the differences between the up-change and down-change SRS tests, shown to be due to the activation of different thermal obstacles during the two directions of rate changes. The role of Si additions on these mechanical properties are explored and their suspected role on the asymmetric SRS are discussed.

1.0 Introduction

The use of aluminium alloy sheet metal in the automotive industry for body-in-white applications has established the requirement for a better understanding of the deformation behaviour and high-strain mechanical properties of these alloys. The production of automobile doors, roofs, and hoods, all introduce plastic strain to the sheet metal with industrial designers constantly pushing the limits of the material properties to produce the most desirable vehicles while manufacturers are attempting to reduce the mass of passenger vehicles to meet environmental standards [1], [2]. The result is that automotive manufacturers desire aluminium alloy sheets with increased formability to allow more complex designs to be created using thinner sheet metal without failure. In forming practices, once a sheet has developed a localized neck, it is considered to be in a failed state and the material may not be used.

The transition from diffuse to localized necking is not fully understood but conventionally, the Considère criterion [3] is employed to determine the onset of diffuse necking. It relates the current strain hardening, $\frac{d\sigma}{d\epsilon}$, to the current flow stress, σ, whereby once $\frac{d\sigma}{d\epsilon} = \sigma$ is met, a geometric instability develops resulting in flow localization [4]–[6]. This flow localization results in an increased strain rate within the neck interior where studies have shown that materials with a large strain rate sensitivity (SRS) at high strains near the Considère criterion will delay the onset of localized necking [4], [6]–[10]. This effect is attributed to the local increase in the strain rate upon diffuse necking, which changes the local flow stress and strain hardening states. Conversely, little attention has been given to the region outside of the neck whereby the local strain rate will inevitably decrease [7] in order to maintain the overall imposed deformation rate. Therefore, the strain rate sensitivity of the flow stress becomes a most valuable parameter for understanding the necking behaviour, but its determination requires significant care. Strain rate sensitivity has historically being measured by tensile testing multiple specimens at various strain rates [11], [12], stress relaxation, or by strain rate change or jump tests of single specimens [13]–[17]. When performing strain rate change tests, the machine and specimen stiffness result in an elastic response to the newly imposed strain rate, and the associated stress change, which can lead to additional experimental errors. This effect is magnified if a decrease in the strain rate is applied or if the change in the strain rate is significantly large [18], [19]. Consequently, reliable instantaneous strain rate sensitivity values to determine thermodynamic parameters are elusive for most laboratories with most measurements being reported from tests that increase the strain rate (system stiffens).

When reliable strain rate sensitivity measurements are made by either increasing or decreasing strain rates, an asymmetry of the SRS for dilute alloys has been observed at high strains (high flow stresses) [13], [20], [21] whereby the rate sensitivity of a decrease is found to be greater than the corresponding increase. Such an asymmetry will undoubtedly cause a difference between the relative increase and decrease in stress-state within the neck interior and exterior, respectively, whereby the magnitude of the stress decrease in the neck exterior is greater than the relative increase in stress of the neck interior, which may be hypothesized to reduce the localization of plastic flow. Since in the common formability literature the strain rate sensitivity of aluminum and aluminum alloys has been perceived to be negligible compared to materials like steels, there has been little effort to consider how alloying and microstructural design might contribute to this asymmetry to enhance neck prevention in sheets. Design of 6000-series aluminium alloys for automotive sheets has been a very active research area over the last 10 years, with much focus on optimizing the paint bake hardening response, i.e. the strength increase that happens due to precipitation during the paint bake heat treatment, consisting of 20 min at 185 °C. It is now well

chartered that in 6000-series alloys, the paint bake hardening response strongly depends on alloy composition and on the presence of clusters, whose characteristics depend on the heat treatment (time of natural ageing, pre-ageing treatment) [22]–[25]. Conversely, the influence of alloy composition and the presence of clusters on the strain hardening behaviour and on the SRS has been the object of very little research, despite the necessity to optimize globally the formability of the alloys and their end mechanical properties.

The aim of the present paper is to precisely measure the strain rate sensitivity of the flow stress for different 6000-series Al alloys containing variable amounts of Si, and determine if there is asymmetry in the rate sensitivity. The paper starts with a brief review of the theory of thermally active flow in order to present the important measureable parameters before describing the experimental details.

2.0 Background

Strain rate sensitivity experiments are used to determine the reversible component of deformation during plastic flow, that is, the portion of activation energy dislocations carry as they overcome obstacles within the material [14], [26]–[28]. In the initial variable temperature experiments by Cottrell and Stokes [29], the components of thermal energy within the material were adjusted by temperature changes and the resulting changes in stress were measured. Since then, experimentally easier tests have been employed whereby the current strain rate is adjusted by a factor and the resulting change in the applied stress is measured. The basis of SRS is derived from the rate equation for plasticity such that

$$\dot{\epsilon} = \dot{\epsilon_0} \exp\left(-\frac{\Delta G(\sigma)}{kT}\right) \tag{1}$$

where $\dot{\epsilon}$ is the applied plastic strain rate, $\dot{\epsilon}_0$ the base strain rate, $\Delta G(\sigma)$ is the stress-dependent activation energy barrier, k is the Boltzmann constant and T the absolute temperature. During strain rate change tests, the strain rate is experimentally manipulated, thus Eq. 1 is differentiated with respect to $\dot{\epsilon}$ such that

$$\left.\frac{\partial \ln \dot{\epsilon}}{\partial \sigma}\right|_{\Sigma,T} = \left.\frac{\partial \ln \dot{\epsilon_0}}{\partial \sigma}\right|_{\Sigma,T} - \frac{1}{kT}\left.\frac{\partial \Delta G(\sigma)}{\partial \sigma}\right|_{\Sigma,T} \tag{2}$$

At constant structure, Σ, and temperature, while $\frac{\partial \ln \dot{\epsilon}_0}{\partial \sigma}$, is assumed to be zero, thus from equation (2) it is possible to define the inverse apparent activation volume 1/V':

$$\frac{1}{V'} = \frac{1}{kT}\left.\frac{\partial \sigma}{\partial \ln \dot{\epsilon}}\right|_{T,\Sigma} \tag{3}$$

so that $\frac{1}{V'} = -\frac{\partial \sigma}{\partial \Delta G(\sigma)}$. The apparent activation volume is directly related to the spacing between the rate controlling obstacles, l, the activation distance, d, and the Burgers vector, b, as $V' = bdl$. An increase in the strain rate is analogous to a decrease of the test temperature performed by Cottrell and Stokes, thus probing the obstacles that control the plastic flow at lower temperature, whereas a decrease in the strain rate probes the rate-controlling obstacles equivalent to testing at a relatively higher temperatures [30], [31]. The evolution of V' during deformation, and thus with increasing flow stress due to strain hardening, is the method to determine the thermodynamic strain rate sensitivity, S, which may be calculated as

$$S = \frac{1}{T}\frac{\partial \sigma}{\sigma\, \partial \ln \dot{\epsilon}} = \frac{1}{T}\frac{\partial \ln \sigma}{\partial \ln \dot{\epsilon}} \tag{4}$$

Plotting $\frac{1}{T}\frac{\Delta\sigma}{\Delta \ln \dot{\epsilon}} = Mk/V'$ versus the true stress, σ, yields the Haasen plot [32], where M is a Taylor factor of 3 used in this work. For simplicity in this work, Haasen plots and analyses will be constructed using the change in the flow stress, $\frac{1}{T}\frac{\Delta\sigma}{\Delta \ln \dot{\epsilon}}$ versus the reduced flow stress, $\sigma - \sigma_{0.2\%}$, to account for the grown-in obstacles from the heat treatments. In the case of fully-recrystallized, pure aluminium, the Haasen plot intersects the plot origin and evolves linearly until failure as the rate controlling obstacles are forest dislocations where $1/V' \propto \sqrt{\rho} \propto (\sigma - \sigma_{0.2\%})$ [14], [29], [32]. However, in age-hardenable alloys, the intercept and initial slope of the Haasen plot are expected to be different from pure aluminium due to the presence of obstacles other than forest dislocations such as solute atoms, clusters, and precipitates. In such materials, as strain hardening progresses and the dislocation density rapidly increases, a change in density of rate-controlling obstacles and thus in activation volume occurs. If one assumes a linear summation of the relative contributions of different obstacles to strengthening [33], [34], [35], then the linearity of the Haasen plot is preserved:

$$\sigma = \sigma_0 + \sigma_1 + \sigma_2 \tag{5}$$

whereby σ_0 is the intrinsic strength of the material, σ_1 is the contribution due to the presence of clusters or precipitates (assumed to be constant with $\sigma_0 + \sigma_1 = \sigma_{0.2\%}$) and σ_2 is the contribution due to dislocations generated by subsequent deformation. This can then be extended and substituted into Eq. 4 for σ and then used to determine the total thermodynamic strain rate sensitivity as $S = S_1 + S_2$.

3.0 Experimental Details

Three aluminum alloys were tested having a nominal composition of Al-0.35Mg-0.2Cu (wt%) with 0.9, 1.1 or 1.3 wt% Si. The samples were received in the as-rolled condition, solution heat treated in an air furnace at 550 °C for 15 minutes, water-quenched (15 °C) and allowed to naturally age for one month. Specimens from each alloy were tested using a Mettler Toledo differential scanning calorimeter (DSC) at a heating rate of 20 °C /min up to 300 °C in both the water quenched (WQ) and 1 month NA conditions (NA1m). Tensile tests were performed using a servo-hydraulic Instron 8502 with a 10 kN load cell, equipped with a 25 ± 10 mm extensometer was used to capture the deformation of the samples of dog-bone tensile specimen that were machined from 1 mm thick sheet of Al-Mg-Si-Cu alloys having a gauge length of 30 mm and a width of 10 mm. The samples were pulled at 294 K and a true strain rate of 5 x 10^{-4} s^{-1} until failure to determine the true stress versus true plastic strain tensile curves and corresponding strain hardening evolution. Strain rate sensitivity tests were performed using the same base strain rate and strain rate change factors of 4, or ¼ and 1/10, for the up-change and down-change rate changes, respectively. A proprietary software controlling a feedback-loop to the initial and active extensometer displacement was used to control the true strain rate and strain rate change allowing for precise measurement of the strain rate sensitivity [18].

4.0 Results and Analysis

4.1 Microstructure and constant strain rate properties

Figures 5-1a and 5-1b show DSC thermograms for the three alloys respectively in the water quenched and naturally aged states, which give indications on the state of clustering in the conditions prior to tensile testing. In the water quenched condition, the thermogram shows a first exothermic peak centered around 100 °C, followed by an endothermic peak around 220 °C and a sharp exothermic peak around 250 °C. Based on the literature [36], [37], the first peak can be identified as the formation of clusters during the DSC heating ramp, the second to the partial

dissolution of these clusters, and the third to the formation of hardening precipitates such as β''. From the results of Figure 5-1a, an addition of Si results in an increased formation of clusters and an enhanced formation of β''. It can be expected that the increased formation of clusters happening during continuous heating also occurs during room temperature natural ageing, so that in a naturally aged condition the higher-Si content alloys contain a larger amount of clusters than lower-Si content alloys.

In the NA1m condition (Figure 5-1b), the first exothermic peak has disappeared, which can be related to the initial presence of clusters formed during natural ageing. These clusters are observed to dissolve progressively over a wide temperature range, starting at 50 °C and extending to the temperature where precipitation starts. This dissolution peak could be the convolution of the dissolution of two types of clusters (such as Si-rich and Mg-rich) as has been proposed in the literature [38]–[42]. Although the addition of Si results in a larger quantity of clusters, their dissolution peak in Figure 5-1b is globally of lower magnitude, meaning that Si increases their thermal stability. However, in a description by two types of clusters of this dissolution behaviour, the data suggests that the magnitude of the low-temperature dissolution peak (120-140 °C) is increased by the addition of Si whereas the contrary applies to the high-temperature peak (~240 °C) suggesting that Si additions increase the proportion of the lower thermal stability cluster species formed during NA. Additionally, the precipitation starting temperature is strongly shifted to higher temperatures as compared to the as-quenched condition, illustrating the well-documented negative effect of natural ageing on paint-bake hardening response [43]–[45]. This negative effect is of lower magnitude in the high Si alloy which shows in the naturally aged condition a lower precipitation temperature as compared to the other alloys.

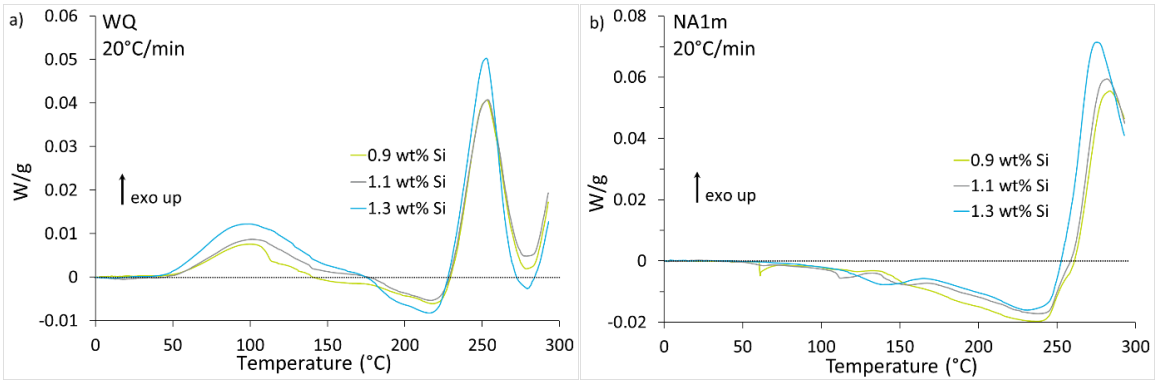

Figure 5-1: *DSC scans for the three alloys studied directly after solutionizing at 550 °C for 15 minutes, WQ and after* ***a)*** *zero NA, and* ***b)*** *NA1m. The exothermic (exo up) direction for clustering or precipitation is positive.*

Figure 5-2a shows the results of the constant strain rate tensile tests on the three alloys in the natural aged condition. Figure 5-2a presents the true stress-true plastic strain curves and Figure 5-2b the corresponding strain hardening behaviour in a Kocks-Mecking representation of the stain hardening rate versus the stress increment after yielding. The addition of Si increases the yield strength, tensile strength, and instantaneous strain hardening rate throughout the tensile test. As a consequence, despite a higher yield strength, the addition of Si results in an increased uniform elongation via an increase in the strain hardening capacity. The strength increase with Si addition is consistent with the higher amount of clustering observed during DSC experiments. All stress-strain responses displayed stable flow during straining.

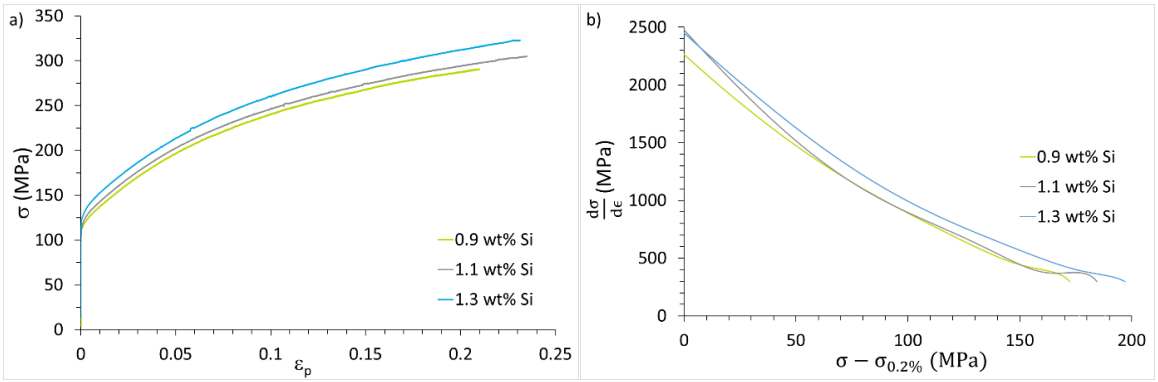

Figure 5-2: *The effects of Si additions after water quenching followed by NA for 1 month. Samples were tested at 294 K at a constant true strain rate of 5 x 10^{-4} s^{-1}.* ***a)*** *True stress versus true plastic strain and* ***b)*** *Kocks-Mecking plot showing the evolution of strain hardening.*

4.2 Strain rate sensitivity

In order to correctly perform the strain rate change tests, the step-ramp method originally implemented by Carlone and Saimoto [18] for servo-hydraulic systems was used whereby a "step" is inserted during the rate change in order to account for the difference in machine and specimen stiffness at the two different strain rates. The "step" described by Carlone and Saimoto is also referred to as compensation. It changes based on the strength of the sample (extent of strain hardening), the stiffness of the testing machine, and depends on both the direction of the strain rate change (up or down) as well as the change factor (4, 10, ¼, 1/10, etc). For the machine used in this work, compensation steps of 0.5 to 10 µm were used in down-changes depending on the sample, extent of strain hardening and rate-change magnitude. In Figures 5-3a and 5-3b, the strain and stress evolution over time is shown for a strain rate down change test without (Figure 5-3a) and with (Figure 5-3b) the step-ramp method.

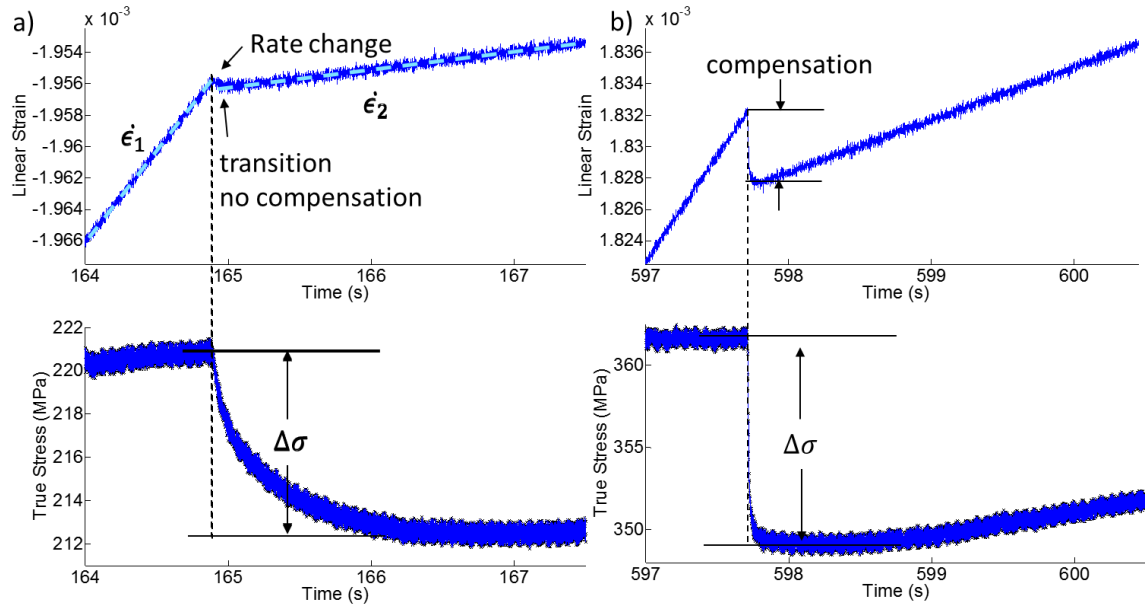

Figure 5-3: *The time dependence of the true strain control and true stress response with a strain rate change for an Al-0.35Mg-1.3Si-0.5Cu test sample with* ***a)*** *no compensation (traditional method), and* ***b)*** *ideal compensation. Note the stress relaxation over longer time to reach a minimum stress in the un-compensated test compared to the compensated one.*

When observing the evolution of both strain and stress over time, it is clear that elastically compensating the system to match the plastic strain rate change largely reduces the time taken

to reach the minimum stress. Without compensation (Figure 5-3a), the sample relaxes due to the elastic unloading of the machine and sample and a stress minimum is observed after several seconds compared to sub-second for the compensated tests. The result is that the total stress change is lower, and the apparent activation volume will be artificially higher than characteristic of the rate controlling obstacle (reducing its level on the Haasen plot and leading to a reduced apparent SRS). Without compensation, ad hoc back-extrapolation methods have been used in the literature to determine the "instantaneous" stress drop from after these relaxations [17], [46], [47].

The step-ramp method can be used when performing increasing strain rate changes but its necessity is much less due to the inherent increase in machine stiffness with strain rate increase in tension. Figure 5-4a and 5-4b shows the evolution of strain and true stress with time along an up-change of strain rate with a very small step ramp (steps of 0.05 – 1 µm were used for up-changes depending on the sample and extent of strain hardening). Two different stress changes can be identified corresponding to the instantaneous stress change measured at the peak stress, and the transient stress change corresponding to a stress plateau at much later times. Although both stresses have been used in the literature [15], [21], [31], we will use the instantaneous stress change throughout the paper as it is more relevant to the understanding of non-constant strain rate processes such as necking. The two strain rate regions are denoted in Figure 5-4a and the measured stress increase is indicated in Figure 5-4b.

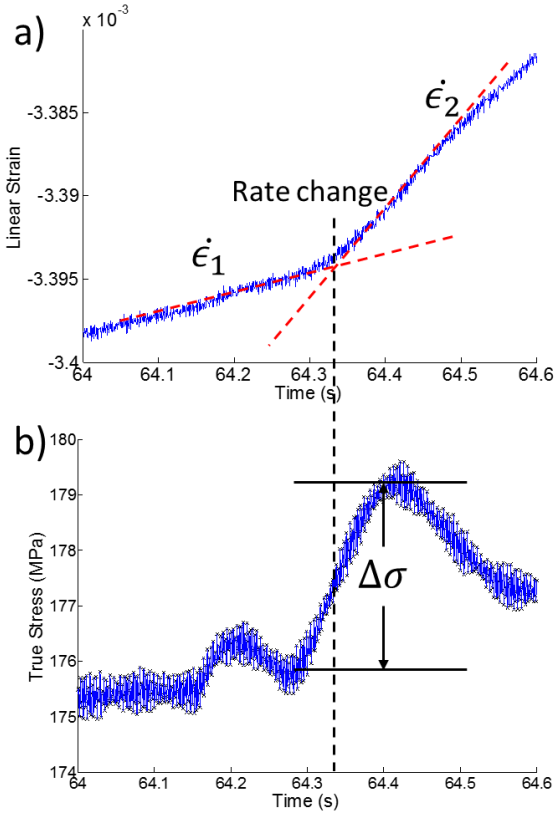

Figure 5-4: *Method used to determine the up-change response of strain-jump tests. The vertical line delineates the transition between the* ***a)*** *initial and the increased strain rate over time. The difference of the* ***b)*** *stress over time is between the region still within the first strain rate and the region where the increased strain rate is now active. The initial fluctuation in the stress before the rate change at 64.2 s is due to the start of a strain control segment just before the new rate and step are applied.*

4.3 Strain rate sensitivity results

Tensile tests with intermittent strain rate changes by a factor of 4, ¼, and 1/10 were carried out on the three alloys in the NA1m condition. The Haasen plots constructed from the measured stress changes are shown in Figures 5-5a-c. The key parameters for each of the curves on the Haasen plot were determined as follows. The different regions and directions of strain rate changes were

fit piece-wise. The S_4 curve (up-change 4x) was fit using a single straight line for the entire test, despite the flattening out that is observed in these tests at the highest stresses. The $S_{1/10}$ and $S_{1/4}$ (respectively 1/10 and ¼ down changes) slopes were taken at the point of deviation from the initial S_4 slope, starting at ~40 MPa of strain hardening until linear regression failed. Both the $S_{1/10}$ values and evolution slope are slightly but significantly larger than the $S_{1/4}$ values. In the following, the combined ¼ and 1/10 tests were used to determine an average intercept (used in further calculations). This was required due to the fact there is no difference in the inverse activation volumes directly after yield and in the early stages of strain hardening prior to the observation of the asymmetry in the strain rate sensitivity tests. In theory, as will be subsequently discussed, the onset of the asymmetry should be independent of the strain rate change amplitude and the Haasen plot slopes are the critical component. In order to visualize the effect of Si addition on the strain rate sensitivity, the data of the three alloys are plotted together in Figure 5-6.

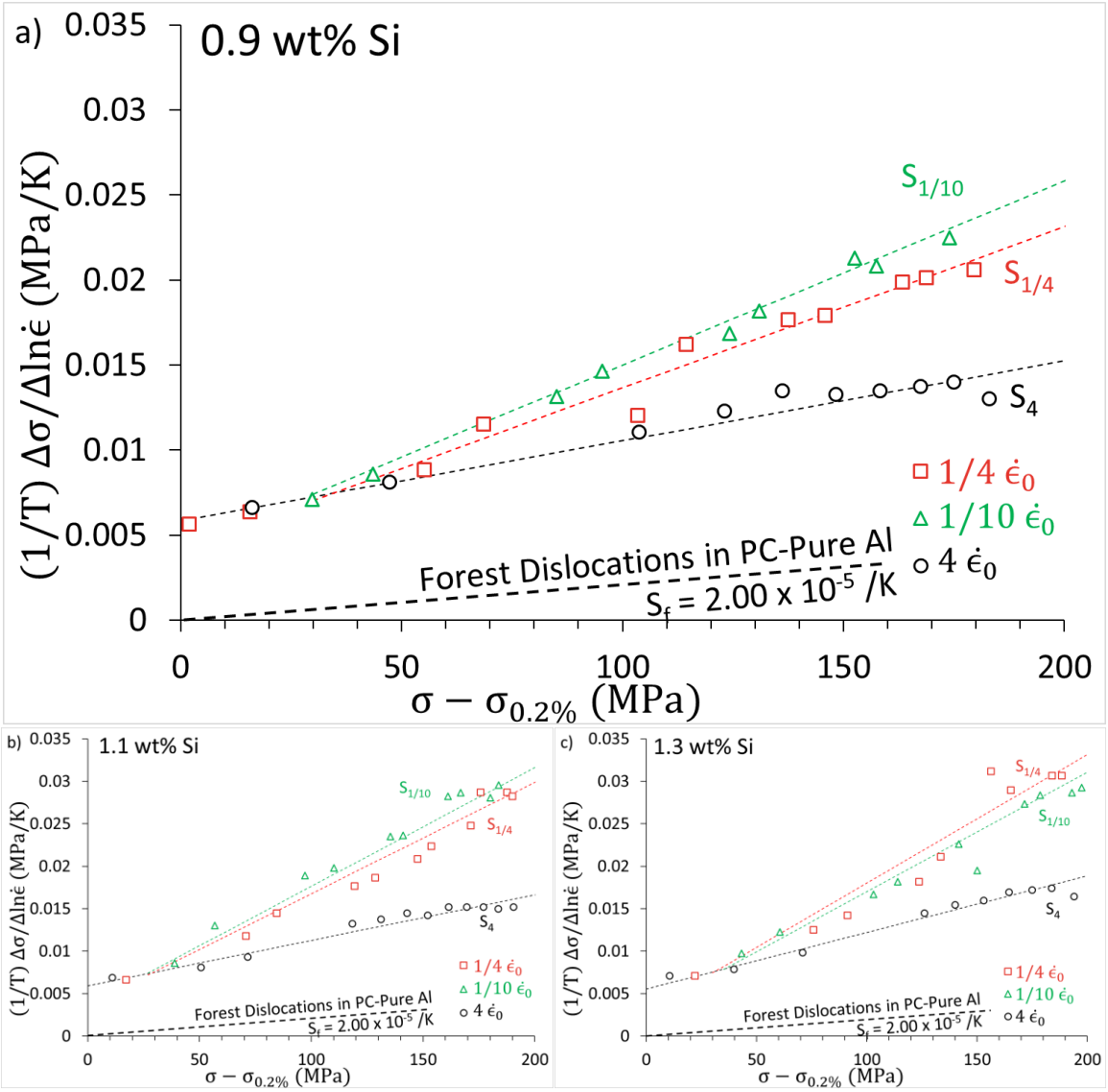

Figure 5-5: *The Haasen plots constructed using the compensation methods for the* ***a)*** *0.9 wt% Si,* ***b)*** *1.1 wt% Si, and* ***c)*** *1.3 wt% Si. The samples were tested at a base strain rate of 5 x 10^{-4} s^{-1} and a test temperature of 294 K. Note the large differences between the down-change and up-change tests at higher work-hardened states. The use of ¼ (open red squares) and 1/10 (open green triangles) strain rate changes were applied for the down-change tests, while a change factor of 4x (open black circles) was used for the up-change tests. Also shown is the behaviour for high purity polycrystalline aluminum at the same temperature.*

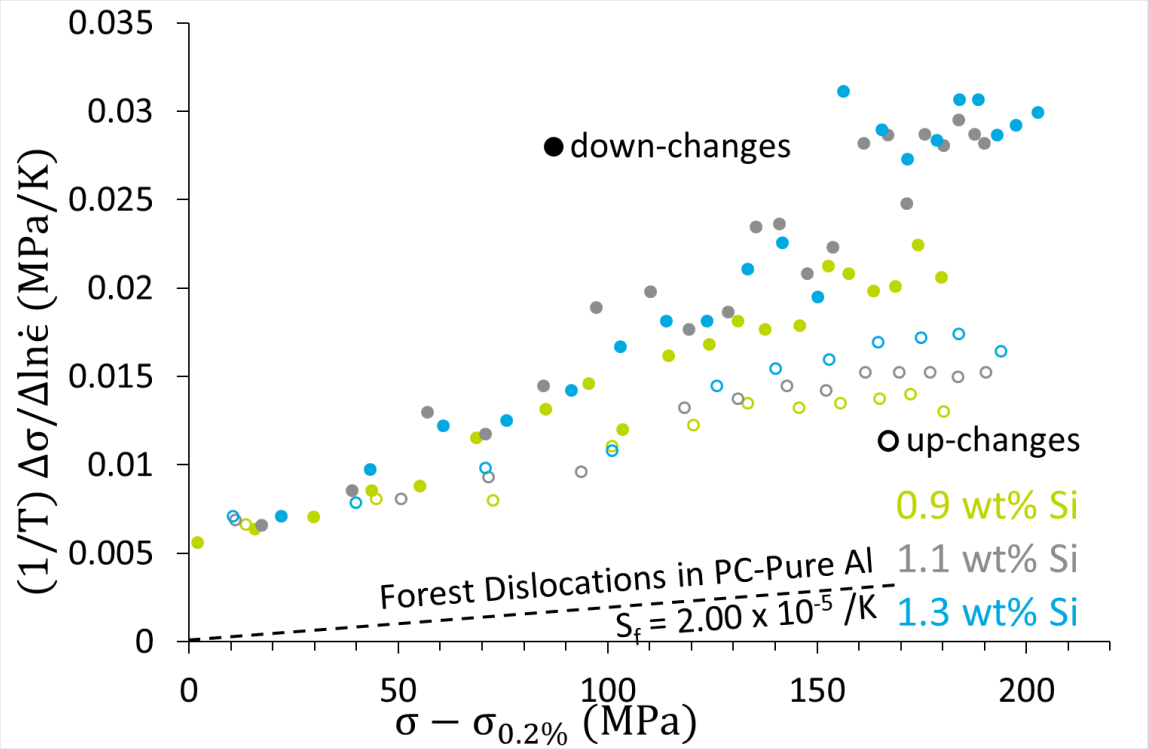

Figure 5-6: *The Haasen plot illustrating the effects of Si on the evolution of the inverse activation volume during strain hardening. The ¼ and 1/10 down-changes (closed symbols) are not identified separately in this plot. It is clear that the inverse activation volume from yield to about 40 MPa is similar for all alloys independent on the direction of the rate-change.*

Several trends can be observed in the Haasen plot and specifically the evolution of $\frac{1}{T}\frac{\Delta\sigma}{\Delta \ln \dot{\epsilon}} = Mk/V'$ with stress, where V' is the apparent activation volume. Initially, Mk/V' for all alloys whether by up or down ranges changes is similar at yield and follows a Cottrell-Stokes behaviour for the first 40 MPa of hardening similar to the pure Al dislocation-dislocation line (dashed line), which can be correlated to the first 0.04 strain in the Kocks-Mecking plot of Figure 5-2b. The positive intercept on the Haasen plot indicates an obstacle contribution to the flow stress that is more rate sensitive than dislocations. This behaviour continues with the up-change measurements to higher stresses, but increases more rapidly with the down-rate changes: the ¼ stress changes have a lower Haasen slope compared to the 1/10 stress changes for low 0.9 and 1.1 wt% Si alloys. The addition of Si increases Mk/V' at high strains for both the up-change and down-change tests compared to the 0.9 wt% Si base alloy. Since the initial values of Mk/V' are similar for all three alloys, this variation at large strains results in a slope change of the Haasen plot, i.e. in a larger thermodynamic strain rate sensitivity, S, for increasing Si content. The S values

determined from testing the three alloys with different strain rate changes are summarized in Figure 5-7, based on the fits in Figures 5-5a-c.

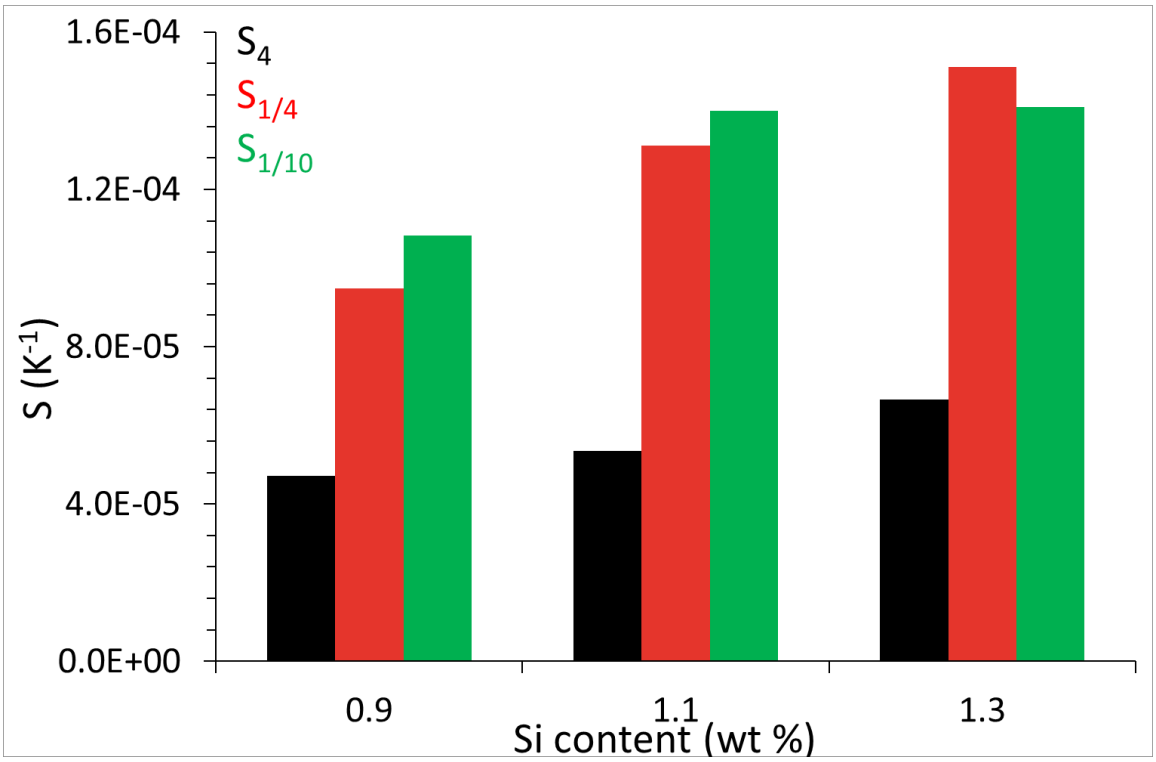

Figure 5-7: *A summary of S_4 (black), $S_{1/4}$ (red), and $S_{1/10}$ (green), taken from the Haasen plots in Fig. 5-6, using the analysis methods described for Fig. 5-5 a-c.*

The additions of Si increases S_4 and $S_{1/4}$, and the difference between S_4 and $S_{1/4}$. Silicon additions also appear to decrease the difference between $S_{1/10}$ and $S_{1/4}$ although this effect lies close to experimental scatter. An interesting correlation is that higher Si results in increased uniform elongation while simultaneously increasing both the up- and down-change SRS suggesting that alloys with higher Si contents may be more favourable for forming operations. The differences in the up- and down-change SRS will separately affect the interior and exterior parts of the diffuse neck, respectively, that develops during plastic deformation as the local strain rate is no longer equal to the imposed rate.

5.0 Discussion

In order to investigate the role of clusters formed during the NA process on the up-change and down-change tests, one can plot the evolution of the apparent activation volume normalized by b^3 with strain hardening. Figures 5-8a-c shows the data points and model fitting to the thermodynamic strain rate sensitivity, S, obtained from the Haasen slope.

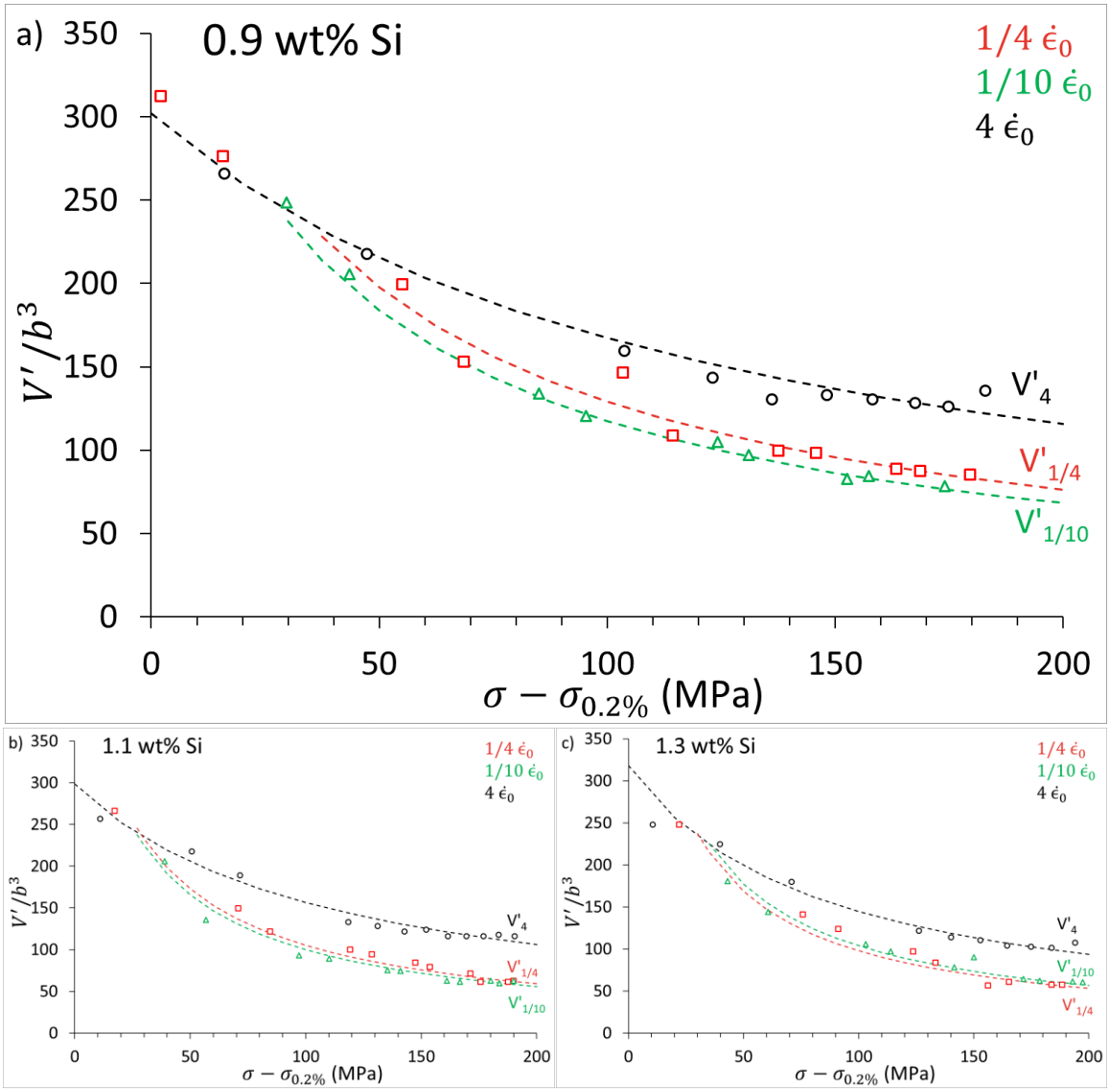

Figure 5-8: *The evolution of the normalized apparent activation volume versus reduced stress for the up-changes (open black circles), ¼ (open red squares) and 1/10 (open green triangles), each with the corresponding modeled curves based on the respective SRS shown in the coloured dashed line for the* ***a)*** *0.9 wt% Si,* ***b)*** *1.1 wt% Si, and* ***c)*** *1.3 wt% Si alloys.*

For all alloys tested, the apparent activation volume after initial yielding is similar at around 300 b^3. With straining the apparent activation volume progressively decreases due to the increasing dislocation density that follows V'_4 or the S_4 lines in Figures 5-5a-c. The decreasing activation volume measured by down-change tests ($V'_{1/4}$ and $V'_{1/10}$) starts to decrease more than the up-change measurements after some incubation stress suggesting that a different or second mechanism/obstacle is present. One explanation for this bifurcation could be dissolution of the solute clusters into smaller more complex objects, as described by Chen et al. [48] for Al-Cu, that ultimately decreases the apparent activation volume via a decrease in both the activation distance, d, and spacing of the obstacles, l, such that V' = bdl decreases. Alternatively, if dislocation interactions affected by the solute cluster field create dislocation debris (small loops) with straining, these weaker obstacles can recover during the down changes, though this effect is unexpected at such low strains [49], [50].

Based on the calculated S values shown for the three alloys in Figure 5-7, it is possible to estimate the activation distance, representative of the size of the rate-controlling obstacles, based on the relationship:

$$(\sigma - \sigma_{0.2\%})V' = Mk/S \quad (6)$$

Assuming that the Taylor equation applies, $(\sigma - \sigma_{0.2\%}) = M\alpha\mu b/l$, where α represents the obstacle strength associated with forest dislocations (0.3 used in this work), μ, the temperature dependent shear modulus of aluminium (24 739 MPa at 294 K) and l represents the obstacle spacing along the dislocation line, then

$$(\sigma - \sigma_{0.2\%})V' = \left(\frac{M\alpha\mu b}{l}\right)(bdl) = M\alpha\mu b^2 d = Mk/S \quad (7)$$

The activation distance d, can be calculated from the Haasen plot, and normalized by the Burgers vector, as represented in Figure 5-9 for the three alloys from the up and down strain rate changes as well as the difference.

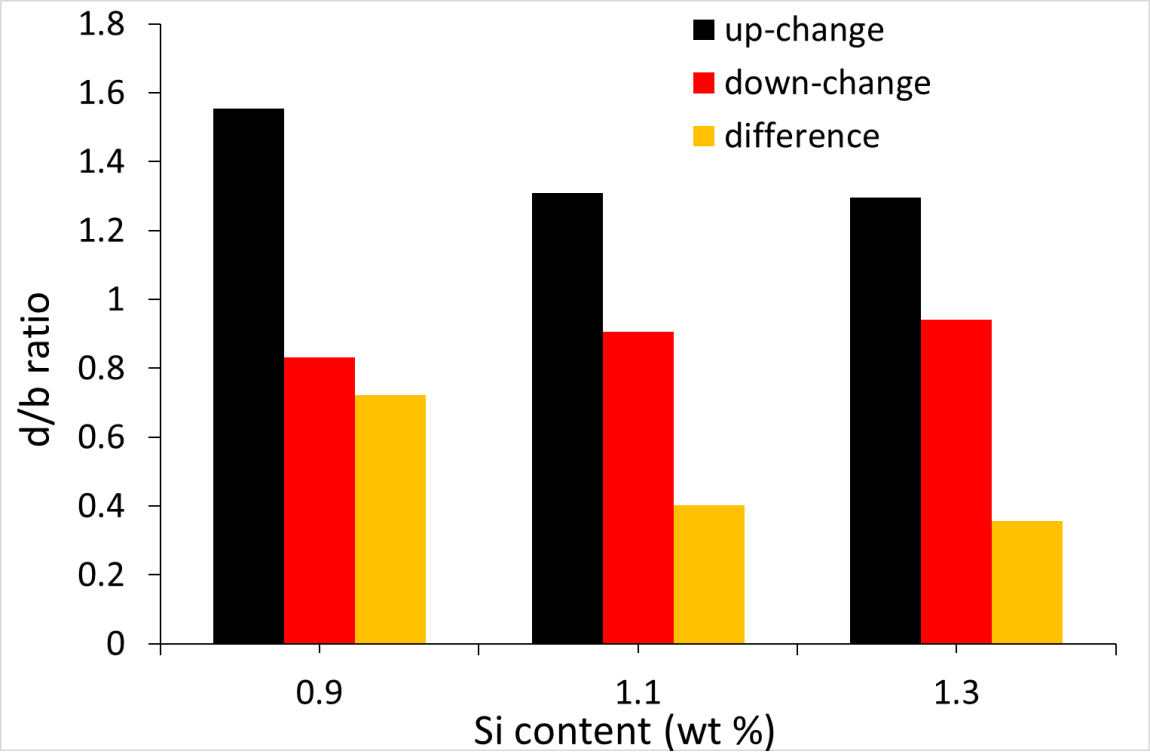

Figure 5-9: *The evolution of the d/b ratio for the up-change (black) and down-change (red) tests, with the difference (yellow) for each alloy tested in this work. The down-change values were taken from both the ¼ and 1/10 tests in combination determined, the slopes of V' vs. $(\sigma - \sigma_{0.2\%})^{-1}$ plots were taken from after the separation between the up- and down-change difference to eliminate effects of cluster contribution.*

It is evident that Si additions increase the down-change apparent obstacle size while having the contrary effect on the up-change values. The decrease in the up-change obstacle size follows the same trends found by Niewczas et al. [21] whereby additions of Mg was found to decrease d/b for up-change tests in Al-Mg alloys. The Niewczas et al. measurements were performed at 78 K compared to 294 K here, the latter temperature with more significant solute mobility and dislocation recovery, hence the significantly larger d/b ratio in the present work.

The increase in the down-change obstacle size with Si content contrasts with what Niewczas et al. [21] found at 78 K with Mg, whereby Mg additions also decreased the d/b ratio. The likely cause

of this is the ability for dislocation-dislocation and dislocation-solute/cluster interaction products to be recovered during the down-change strain rate change [51] whereby there is an effect on the spacing of l, rather than d. Niewczas and Park [51] showed that in pure Al, dislocation-dislocation interaction products do not anneal out at temperatures below 100 K; in contrast, such recoverable components must be considered here. Saimoto [28] and Saimoto and Duesbery [49] have argued that the presence of these dislocation interaction products contribute to the SRS in the down-change at ambient temperatures due to their likelihood to anneal out during the rate-change; in the strain rate change test, this effect would appear as an added relaxation during a perfectly compensated strain rate change. This would be coupled with the extensive work performed by Niewczas [50], [51] for observing the dislocation interaction products at low temperatures and the corresponding annealing temperatures, and how they influence the flow stress. It could be argued that certain dislocation-dislocation or dislocation-solute interaction products are able to influence the apparent obstacles size, being a second type of obstacle present and detectable during the strain rate change tests. A larger d/b indicates the presence of thermally activatable obstacles that are stronger in nature and thus, the relative increase in d/b with increased Si content may suggest that the production of these complex products depend on the Si content of the alloy whereby increased Si promotes the formation of dislocation-dislocation interaction products. The evolution of the d/b ratio for the up-change and down-change tests have clearly shown a distinct asymmetry that is directly related to the SRS difference. If it is proposed that the difference in the SRS between the down-change and up-change tests are due to the evolution or recovery of another type of obstacle, the difference in stress-change will be termed the asymmetric stress contributions (ASC), $\Delta\sigma_{ASC}$, related to the asymmetric SRS by

$$S_{ASC} = S_{dc} - S_{uc} \tag{8}$$

where S_{ASC} is the SRS of the asymmetric stress contributions (see Figure 5-10), and S_{dc} and S_{uc} are the down-change and up-change SRS values at high flow stresses (those after the deviation between up-change and down-change tests), respectively. From the calculation of S_{ASC}, the relative change in the flow stress due to the strain rate change test may be calculated by using Eq. 4 but substituting in the new S_{ASC}

$$\Delta\sigma_{ASC} = S_{ASC}\sigma_2 T\Delta \ln \dot{\epsilon}_{ucdc} \tag{9}$$

where $\Delta \ln \dot{\epsilon}_{ucdc}$ is the difference in strain rate between the up-change and down-change strain rates. It is interesting that the evolution of the ASC may be calculated and plotted versus strain hardening for the total ASC as shown in Figure 5-10.

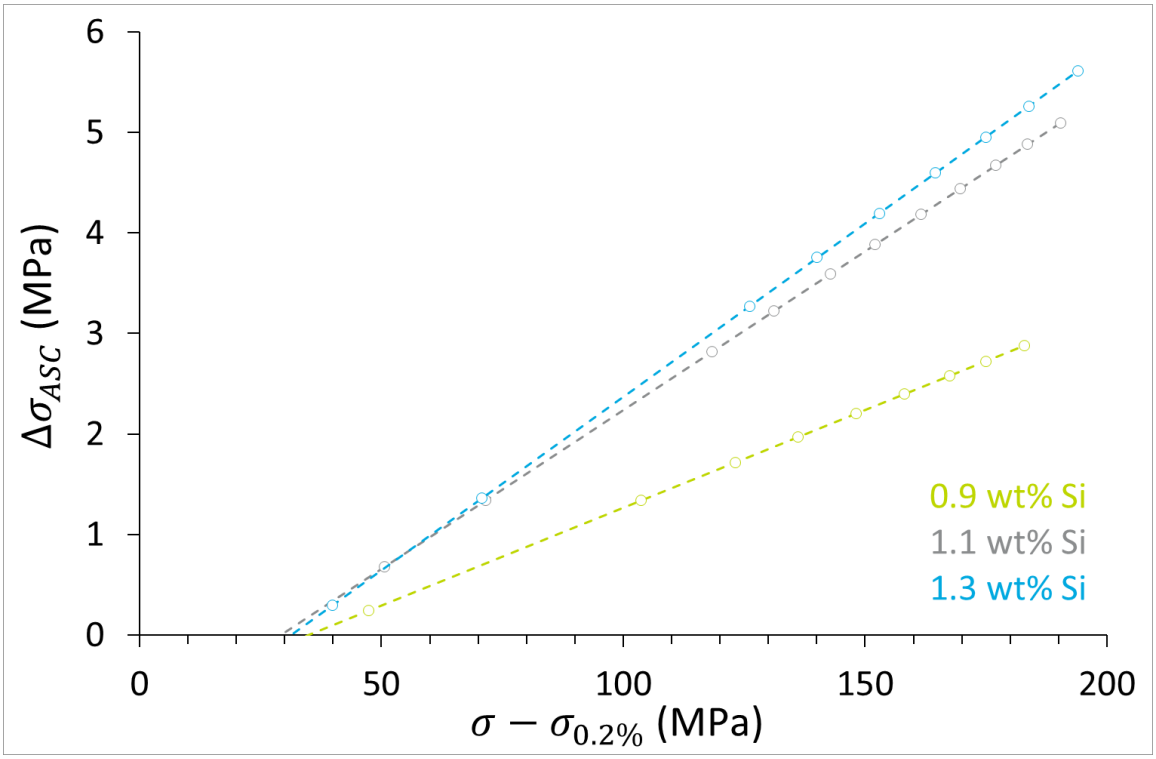

Figure 5-10: *The evolution of the asymmetric stress contribution for the varying levels of Si. The production rate of the asymmetric stress contribution appears to increase with Si content while the onset of the deviation appears to be independent of Si content. Note that the $S_{1/4}$ values were used along with the S_4 to produce this plots.*

Figure 5-10 clearly shows an evolution in the rate of ASC accumulation with increased Si content while the onset of the ASC does not appear to be affected. If the premise of recoverable dislocation products and recovery is postulated to be responsible for the evolution of the ASC, it may be said that the addition of Si either increases the amount of recoverable debris being produced or Si increases the ability of the produced debris to be recovered. Both of these postulations would result in a net increase in the slope of Figure 5-10. It is not understood at this point whether having a large ASC in the SRS is favourable or not, but its effect will certainly be manifested in the onset of diffuse necking and its transition to a localized neck formed during plastic deformation.

6.0 Conclusions

- The use of compensation during down-change strain rate jump tests enables the most experimentally precise measurement of stress changes due to strain rate changes by taking into account the change in machine stiffness.
- The strain rate sensitivity in 6000-series aluminium alloys was observed at 294 K to depend both on the magnitude of the strain rate change and on its sign. A difference between up- and down-changes was observed after an incubation strain hardening of 40 MPa (equivalent to about 0.04 plastic strain). At larger strains the down-change thermodynamic strain rate sensitivity becomes substantially larger than that of up-change tests and the magnitude of the stress changes become dependent on the magnitude of the rate change.
- The apparent activation distance derived from the up-change tests decreases with Si content indicating that the rate-controlling obstacles are more thermally activatable; the opposite correlation was found for Si additions and down-change tests.

- In the considerations of formability and the transition between diffuse and local necking, due to the large discrepancy between increasing or decreasing rate changes, it may be important to consider how the SRS affects the local stress state within the neck interior and exterior.

7.0 References

[1] J. Hirsch, “Automotive trends in aluminium-The European perspective,” in *Materials Forum*, 2004, vol. 28, pp. 15–23.

[2] J. Hirsch, “Recent development in aluminium for automotive applications,” *Trans. Nonferrous Met. Soc. China*, vol. 24, no. 7, pp. 1995–2002, Jul. 2014.

[3] M. Considère, *Mémoire sur l’emploi du fer et de l’acier dans les constructions*, vol. 1. Dunod, 1885.

[4] A. K. Ghosh, “The Influence of Strain Hardening and Strain-Rate Sensitivity on Sheet Metal Forming,” *J. Eng. Mater. Technol.*, vol. 99, no. 3, p. 264, 1977.

[5] K. W. Neale and E. Chater, “Limit strain predictions for strain-rate sensitive anisotropic sheets,” *Int. J. Mech. Sci.*, vol. 22, no. 9, pp. 563–574, Jan. 1980.

[6] A. K. Ghosh, “Tensile instability and necking in materials with strain hardening and strain-rate hardening,” *Acta Metall.*, vol. 25, no. 12, pp. 1413–1424, Dec. 1977.

[7] B. J. Diak and S. Saimoto, “Role of Strain Rate Sensitivity on Diffuse Necking,” in *Dynamic Plasticity and Structural Behaviours*, 1995, pp. 5–8.

[8] J. W. Hutchinson and K. W. Neale, “SHEET NECKING-III. STRAIN-RATE EFFECTS,” p. 17.

[9] J. W. Hutchinson and K. W. Neale, “Influence of strain-rate sensitivity on necking under uniaxial tension,” *Acta Metall.*, vol. 25, no. 8, pp. 839–846, Aug. 1977.

[10] E. W. Hart, “Theory of the tensile test,” *Acta Metall.*, vol. 15, no. 2, pp. 351–355, Feb. 1967.

[11] Y. M. Wang and E. Ma, “Strain hardening, strain rate sensitivity, and ductility of nanostructured metals,” *Mater. Sci. Eng. A*, vol. 375–377, pp. 46–52, Jul. 2004.

[12] N. Chibane, H. Ait-Amokhtar, and C. Fressengeas, “On the strain rate dependence of the critical strain for plastic instabilities in Al-Mg alloys,” *Scr. Mater.*, vol. 130, pp. 252–255, Mar. 2017.

[13] S. Esmaeili, L. M. Cheng, A. Deschamps, D. J. Lloyd, and W. J. Poole, “The deformation behaviour of AA6111 as a function of temperature and precipitation state,” *Mater. Sci. Eng. A*, vol. 319–321, pp. 461–465, Dec. 2001.

[14] B. J. Diak, K. R. Upadhyaya, and S. Saimoto, “Characterization of thermodynamic response by materials testing,” *Prog. Mater. Sci.*, vol. 43, no. 4, pp. 223–363, 1998.

[15] W. A. Curtin, “New interpretation of the Haasen plot for solute-strengthened alloys,” *Scr. Mater.*, vol. 63, no. 9, pp. 917–920, Nov. 2010.

[16] P. S. BATE, “The effects of combined strain-path and strain-rate changes in aluminum,” *Metall. Trans. A*, p. 11.

[17] R. C. Picu, F. Ozturk, E. Esener, and R. Li, “Aluminum Alloys with Identical Plastic Flow and Different Strain Rate Sensitivity,” *Metall. Mater. Trans. A*, vol. 41, no. 13, pp. 3358–3364, Dec. 2010.

[18] M. Carlone and S. Saimoto, “Precision strain rate sensitivity measurement using the step-ramp method,” *Exp. Mech.*, vol. 36, no. 4, pp. 360–366, 1996.

[19] S. Gupta, A. J. Beaudoin, and J. Chevy, “Strain rate jump induced negative strain rate sensitivity (NSRS) in aluminum alloy 2024: Experiments and constitutive modeling,” *Mater. Sci. Eng. A*, vol. 683, pp. 143–152, Jan. 2017.

[20] B. J. Diak, *Microplastic bases for constitutive characterization of aluminum alloys and their correlation to sheet formability*. 1997.

[21] M. Niewczas, M. Jobba, and R. K. Mishra, “Thermally activated flow of dislocations in Al–Mg binary alloys,” *Acta Mater.*, vol. 83, pp. 372–382, Jan. 2015.

[22] L. Ding, Z. Jia, Z. Zhang, R. E. Sanders, Q. Liu, and G. Yang, “The natural aging and precipitation hardening behaviour of Al-Mg-Si-Cu alloys with different Mg/Si ratios and Cu additions,” *Mater. Sci. Eng. A*, vol. 627, pp. 119–126, Mar. 2015.

[23] M. Murayama, K. Hono, W. F. Miao, and D. E. Laughlin, “The effect of Cu additions on the precipitation kinetics in an Al-Mg-Si alloy with excess Si,” *Metall. Mater. Trans. A*, vol. 32, no. 2, pp. 239–246, 2001.

[24] Y. Weng, Z. Jia, L. Ding, Y. Pan, Y. Liu, and Q. Liu, “Effect of Ag and Cu additions on natural aging and precipitation hardening behavior in Al-Mg-Si alloys,” *J. Alloys Compd.*, vol. 695, pp. 2444–2452, Feb. 2017.

[25] M. W. Zandbergen, A. Cerezo, and G. D. W. Smith, “Study of precipitation in Al–Mg–Si Alloys by atom probe tomography II. Influence of Cu additions,” *Acta Mater.*, vol. 101, pp. 149–158, Dec. 2015.

[26] F. R. N. Nabarro, “Cottrell-Stokes law and activation theory,” *Acta Metall. Mater.*, vol. 38, no. 2, pp. 161–164, 1990.

[27] R. C. Picu and R. Li, “On the relationship between the Cottrell–Stokes law and the Haasen plot,” *Mater. Sci. Eng. A*, vol. 527, no. 20, pp. 5303–5306, Jul. 2010.

[28] S. Saimoto, “Dynamic dislocation–defect analysis,” *Philos. Mag.*, vol. 86, no. 27, pp. 4213–4233, Sep. 2006.

[29] A. H. Cottrell and R. J. Stokes, “Effects of Temperature on the Plastic Properties of Aluminium Crystals,” *Proc. R. Soc. Math. Phys. Eng. Sci.*, vol. 233, no. 1192, pp. 17–34, Dec. 1955.

[30] S. Saimoto, J. Cooley, H. Larsen, and C. Scholler, “Kinetic analysis of dynamic point defect pinning in aluminium initiated by strain rate changes,” *Philos. Mag.*, vol. 89, no. 10, pp. 853–868, Apr. 2009.

[31] J. R. Klepaczko and C. Y. Chiem, “On rate sensitivity of f.c.c. metals, instantaneous rate sensitivity and rate sensitivity of strain hardening,” *J. Mech. Phys. Solids*, vol. 34, no. 1, pp. 29–54, Jan. 1986.

[32] P. Haasen, “Plastic deformation of nickel single crystals at low temperatures,” *Philos. Mag.*, vol. 3, no. 28, pp. 384–418, Apr. 1958.

[33] M. J. Starink and S. C. Wang, “A model for the yield strength of overaged Al–Zn–Mg–Cu alloys,” *Acta Mater.*, vol. 51, no. 17, pp. 5131–5150, 2003.

[34] E. Hornbogen and E. A. Starke Jr, “Overview no. 102 Theory assisted design of high strength low alloy aluminum,” *Acta Metall. Mater.*, vol. 41, no. 1, pp. 1–16, 1993.

[35] L. C. Wong and S. Saimoto, “Superposition of thermal activation processes in quenched aluminum-1.7 at% copper,” *Scr. Metall. Mater.*, vol. 29, no. 3, pp. 341–346, 1993.

[36] X. Wang, S. Esmaeili, and D. J. Lloyd, “The sequence of precipitation in the Al-Mg-Si-Cu alloy AA6111,” *Metall. Mater. Trans. A*, vol. 37, no. 9, pp. 2691–2699, 2006.

[37] S. Esmaeili and D. J. Lloyd, “Characterization of the evolution of the volume fraction of precipitates in aged AlMgSiCu alloys using DSC technique,” *Mater. Charact.*, vol. 55, no. 4–5, pp. 307–319, Nov. 2005.

[38] V. Fallah, B. Langelier, N. Ofori-Opoku, B. Raeisinia, N. Provatas, and S. Esmaeili, “Cluster evolution mechanisms during aging in Al–Mg–Si alloys,” *Acta Mater.*, vol. 103, pp. 290–300, Jan. 2016.

[39] V. Fallah *et al.*, “Atomic-scale pathway of early-stage precipitation in Al–Mg–Si alloys,” *Acta Mater.*, vol. 82, pp. 457–467, Jan. 2015.

[40] Y. Aruga, M. Kozuka, Y. Takaki, and T. Sato, “Effects of natural aging after pre-aging on clustering and bake-hardening behavior in an Al–Mg–Si alloy,” *Scr. Mater.*, vol. 116, pp. 82–86, Apr. 2016.

[41] J. Kim, E. Kobayashi, and T. Sato, “Effects of Cu addition on behavior of nanoclusters during multi-step aging in Al-Mg-Si alloys,” *Mater. Trans.*, vol. 52, no. 5, pp. 906–913, 2011.

[42] S. Kim, J. Kim, H. Tezuka, E. Kobayashi, and T. Sato, “Formation behavior of nanoclusters in Al–Mg–Si alloys with different Mg and Si concentration,” *Mater. Trans.*, vol. 54, no. 3, pp. 297–303, 2013.

[43] G. H. Tao, C. H. Liu, J. H. Chen, Y. X. Lai, P. P. Ma, and L. M. Liu, “The influence of Mg/Si ratio on the negative natural aging effect in Al–Mg–Si–Cu alloys,” *Mater. Sci. Eng. A*, vol. 642, pp. 241–248, Aug. 2015.

[44] L. Cao, P. A. Rometsch, and M. J. Couper, “Effect of pre-ageing and natural ageing on the paint bake response of alloy AA6181A,” *Mater. Sci. Eng. A*, vol. 571, pp. 77–82, Jun. 2013.

[45] D. Yin *et al.*, “Effect of natural ageing and pre-straining on the hardening behaviour and microstructural response during artificial ageing of an Al–Mg–Si–Cu alloy,” *Mater. Des.*, vol. 95, pp. 329–339, Apr. 2016.

[46] C. P. Ling and P. G. McCormick, “The effect of temperature on strain rate sensitivity in an Al-Mg-Si alloy,” *Acta Metall. Mater.*, vol. 41, no. 11, pp. 3127–3131, 1993.

[47] C. P. Ling and P. G. McCormick, “Strain rate sensitivity and transient behaviour in an Al Mg Si alloy,” *Acta Metall. Mater.*, vol. 38, no. 12, pp. 2631–2635, 1990.

[48] Y. Chen, M. Weyland, and C. R. Hutchinson, “The effect of interrupted aging on the yield strength and uniform elongation of precipitation-hardened Al alloys,” *Acta Mater.*, vol. 61, no. 15, pp. 5877–5894, Sep. 2013.

[49] S. Saimoto and M. S. Duesbery, “Strain rate sensitivity: the role of dislocation loop and point defect recovery,” *Acta Metall.*, vol. 32, no. 1, pp. 147–155, 1984.

[50] M. Niewczas, “Transmission electron microscopy observations of debris structure in deformed copper single crystals,” *Philos. Mag. A*, vol. 82, no. 2, pp. 393–414, Jan. 2002.

[51] M. Niewczas and D.-Y. Park, “Flow stress and electrical resistivity in plastically deformed Al subjected to intermittent annealing,” *Mater. Sci. Eng. A*, vol. 706, pp. 256–268, 2017.

6 Influence of composition on the material properties in Al-Mg-Si-Cu alloys

After establishing the influence of alloy composition on the microstructure formed in the different heat treatments in the Al-Mg-Si-Cu system, it is now possible to evaluate the resulting effects of microstructure on the macroscopic mechanical properties. This chapter will take a unique approach on combining the tensile and strain rate sensitivity testing results and how the roles of Si, Mg, and Cu change depending on the specific heat treatment performed. The effects of the various alloying elements will all be presented in terms of total solute atomic percentage to give a direct relative sensitivity to each mechanical property with respect to each element. Mechanical properties such as the 0.2% yield strength, tensile strength, strain hardening capacity, uniform elongation, post-uniform elongation, strain hardening rate, and strain rate sensitivity are presented. At the end, an alloy design table is shown to give a very high level understanding of how to tune the relative mechanical properties via a combinatorial addition of specific solute types depending on the desired or current heat treatment practice.

Influence of composition on the material properties in Al-Mg-Si-Cu alloys

Abstract

The specific application of 6000-series alloys in automotive applications depend on the automotive manufacturers requirements. Having an understanding on the specific influences of solute additions on the yield strength, tensile strength, strain hardening rate and capacity, uniform elongation, and strain rate sensitivities, allow for alloys to be designed and tuned for specific applications. For example, structural automotive components must be strong and ductile, while their surface quality is not important due to them being hidden. Whereas body-in-white components much be formable, have good surface finish and provide sufficient corrosion resistance as they are exposed to the elements. The effect of solute additions is not direct on the effect to mechanical properties but rather on the formation of the microstructure, in this situation, the formation of clusters under two separate heat treatments. The expression of these microstructure features on the mechanical properties are discussed and compared. Surprisingly, certain solute additions were found to play largely different roles on the same mechanical property strictly depending on the heat treatment performed. This chapter is summarized by providing a table showing the relative change of a mechanical property based on the addition of Mg, Si, or Cu.

1.0 Introduction

The ability of aluminium alloys to have a wide range of mechanical properties while also having a low density has allowed them to be implemented for diverse applications in order to provide light-weighting where steels are conventionally being used. Specifically, the age-hardenable 6000-series aluminium alloys being comprised primarily of aluminium (Al), magnesium (Mg), silicon (Si), and copper (Cu), have shown to have good strength, elongation, corrosion resistance, surface quality while maintaining adequate formability [1]–[3]. For example, this combination of properties complies with applications requiring crash resistance and thus a high tensile strength, large strain hardening and large uniform elongation for enhanced energy absorption, or for outer body panels that should have high strength, high formability and adequate surface quality. The levels of alloying elements that are added into the alloys vary, within ranges being denoted as specific alloy series, such as AA6063, AA6016, and AA6022. Within these domains, extensive work has been carried out to study the effects of composition on the clustering [4]–[10], the dependence of clustering on processing [11]–[19] and the subsequent artificial ageing (AA) behaviour [5], [12], [20]–[22]. It has been shown by Zhong et al. [23]–[25] and Prillhofer et al. [1], that the portfolio of mechanical properties varies broadly within the acceptable ranges of each alloy series. By determining the influence of alloying elements on each of the mechanical properties, such as strain hardening, uniform elongation, yield strength, and strain rate sensitivity, it becomes possible to design specific alloys for unique applications.

The present work lies on the context of alloy optimization for outer body panel applications. For this application, the alloys undergo a process route implying a quench from a solutionizing treatment, some low temperature ageing (natural ageing and/or pre-ageing), followed by a forming operation and a paint-bake heat treatment. While a considerable research effort has been carried out to understand how to counterbalance the adverse effect of natural ageing on the paint bake response by optimizing the alloy composition and pre-ageing treatment, the influence of these parameters on the plastic properties involved in determining the formability has received little attention. Relating formability to simple alloy properties involves both strain hardening rate capacity and strain rate sensitivity. Increasing the strain hardening rate $\frac{d\sigma}{d\epsilon}$ improves the uniform elongation ϵ_L by delaying the Considère criterion ($\frac{d\sigma}{d\epsilon} = \sigma = \sigma_L$) while an increased strain rate sensitivity delays the transition from diffuse to local necking [26]–[30]. Both up-change and down-change strain rate sensitivities (i.e. determined respectively by increasing and decreasing the strain rate) are of interest as they contribute to necking formation and propagation [28]. Finally, the yield strength, $\sigma_{0.2\%}$, is also of interest in order to aid in determining the initial state of clustering within the alloys for each of the respective heat treatments and each composition. The aim of this paper is to provide a design guide describing the specific effect of alloying elements (Mg, Si, Cu) within the 6000-series alloys on the mechanical properties that influence the formability under two common heat treatments; direct natural ageing, and pre-ageing with subsequent natural ageing.

2.0 Background

The interaction between the initial microstructure formed due to composition and processing (solutes, clusters, precipitates, dislocations, grain boundaries), and those generated during plastic flow (dislocations, vacancies, voids) confounds any clear and direct relation between the solute content and resulting mechanical properties. Furthermore, the nature of each obstacle does not necessarily have an effect on all of the mechanical properties but rather a select few. For instance, it can be postulated that the 0.2% yield strength will be controlled primarily by the cluster size,

distribution and/or chemistry as these are the dominant obstacles present in the material [31]–[33]. During the deformation and production of dislocations, the evolution of these obstacles is not clear but through use of constitutive relations, it is possible to detect correlations between solute additions and their key parameters which are related to deformation phenomena and then may be compared for different processing routes. In this work, a two region power-law fit will be used to model the stress-strain curve, having the form of

$$\sigma = \sigma_0 + K_i \epsilon^{n_i}$$

Where K_i and n_i, are the pre-exponential and strain hardening exponents for the first or second regions, respectively. The two curves share a common proportional limit, σ_0, (similar to the yield strength but accounts for any yield point effects) such that the two curves begin at the same stress and cross-over at a specific strain, ϵ_3 and the fit ends at the uniform elongation, ϵ_L. A sample fit is shown in Figure 6-1.

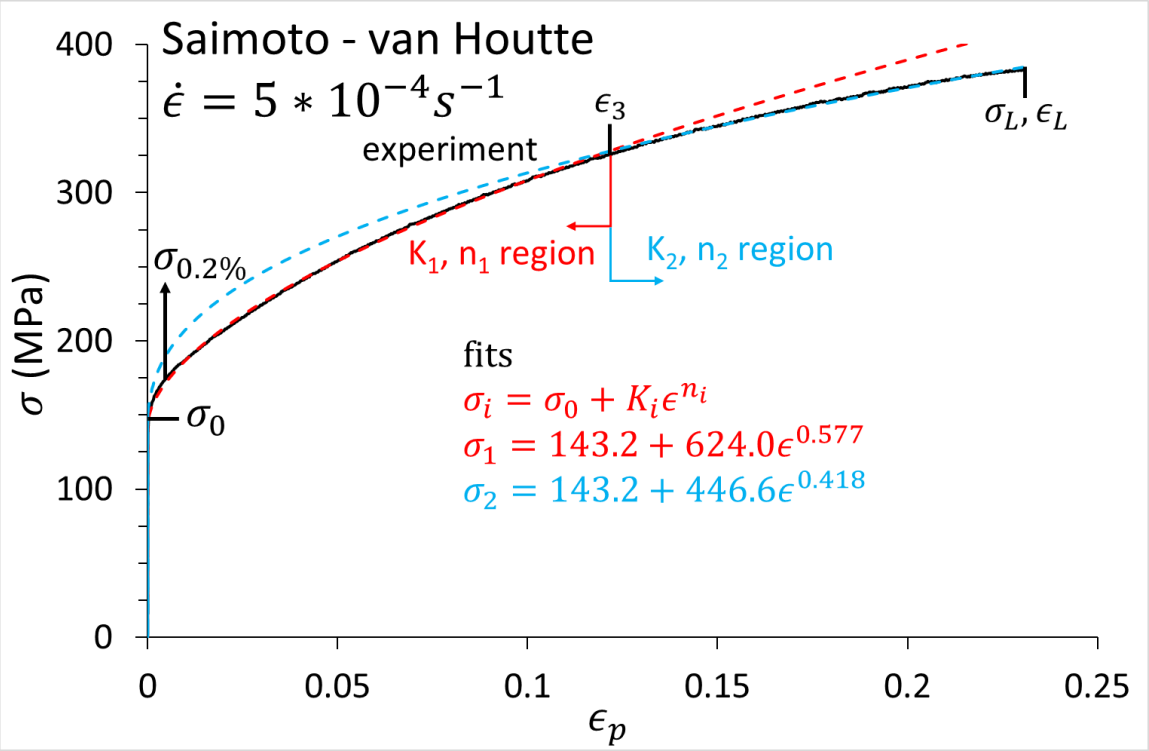

Figure 6-1: *The method used to determine the fit parameters shown on the C8S0M sample pulled at a true strain rate of 5 x 10^{-4} s^{-1} until failure in the NA1m condition. Note a fit was taken from a 6th order polynomial fit made from the yield strength until the uniform elongation in order to eliminate any transient effects potentially caused by yield point effects.*

Although the fit may seem arbitrary, Saimoto and van Houtte [34] have developed the Saimoto-van Houtte (SvH) consitutitive equation in order to determine specific parameters within the power law. The power-law relation can equally be written as

$$\sigma = \sigma_0 + \left[M^{3+\beta_i}\left(\frac{P}{4A}\right)(2+\beta_i)(\alpha\mu b)^2 \frac{1}{C_i b}\right]^{\frac{1}{2+\beta_i}} \epsilon^{\frac{1}{2+\beta_i}}$$

Whereby the variables, σ_0, β_i, and C_i, are the fitting variables, representing the proportional limit, strain hardening, and inter-obstacle spacing, respectively for the i part of the curve; the first half and second half of the fit. The term, α, the obstacle strength factor, μ, the shear modulus, b, the Burgers vector, M, the Taylor factor (a value of 3 used in this work), and P/A, representing the

production to annihilation ratio of dislocations generated during deformation, characterized for each material at yield. From this equation, it can be seen that

$$K_i = \left[M^{3+\beta_i}\left(\frac{P}{4A}\right)(2+\beta_i)(\alpha\mu b)^2\frac{1}{C_i b}\right]^{\frac{1}{2+\beta_i}} \; and \; n_i = \frac{1}{2+\beta_i}$$

The fit parameters; C_i, β_i, and σ_0, are determined, first by fitting a 6th order polynomial to the data and determining the work hardening slope at 0.2% to determine the P/A ratio, by assuming that the mean-slip distance, $\lambda = \phi\frac{b}{2}\mu^2\frac{1}{M^3}\left(\frac{(\sigma-\sigma_0)d\sigma}{d\epsilon}\right)^{-1}$, (see Nabarro et al. [35]) is equal to the inter-obstacle spacing, $l = M\alpha\mu b/(\sigma-\sigma_0)$, at yield, whereby

$$\frac{P}{A} = \frac{2\phi}{\alpha^2}; \frac{1}{\phi} = \frac{M^2}{2\alpha}\mu\left(\frac{d\epsilon}{d\sigma}\right)_{0.2\%}$$

As such, the total fit contains 5 total fit parameters; a common σ_0, C_1 and β_1, and C_2 and β_2 for the two respective fit regimes. Within this fit, σ_0 is the proportional limit and is able to account for any yield point phenomena such as yield point elongation [36] which is largely absent in this work and thus is considered analogous to the 0.2% yield strength. The pre-power law factor, K_i is the strengthening coefficient, and n_i is the strain hardening exponent, where i represents region 1 or 2 of the stress-strain curve. This constitutive relation has been applied to many different aluminium alloy systems [37]–[39] and steels [36]; expanded to explain the effects of vacancy production [40], nano-void formation and growth [41], [42], yield locus predictions [43] and used in crystal plasticity finite element models [44]. The focus in this work will be how the high-strain, strain hardening, n_2, and pre-power law factor, K_2, change with solute content and heat treatment condition. These fit parameters will be coupled with other critical material properties such as the uniform elongation along with the engineering strain rate sensitivity parameters to give a more complete picture of solute additions on the mechanical performance in Al-Mg-Si(-Cu) alloys. The strain rate sensitivity measurements reported were determined using the previously described step-ramp method by Carlone and Saimoto [45] and Chapter 5, for both up-changes and down-changes. Since the focus of this work is for the application of formability, the up-change and down-change engineering strain rate sensitivities will be determined from the final 4 data points for down-changes, and final 3 data points for up-changes, directly from the rate change using

$$m_i = \frac{\Delta \log \sigma}{\Delta \log \dot{\epsilon}}$$

The evolution of these values are shown below in Figure 6-2.

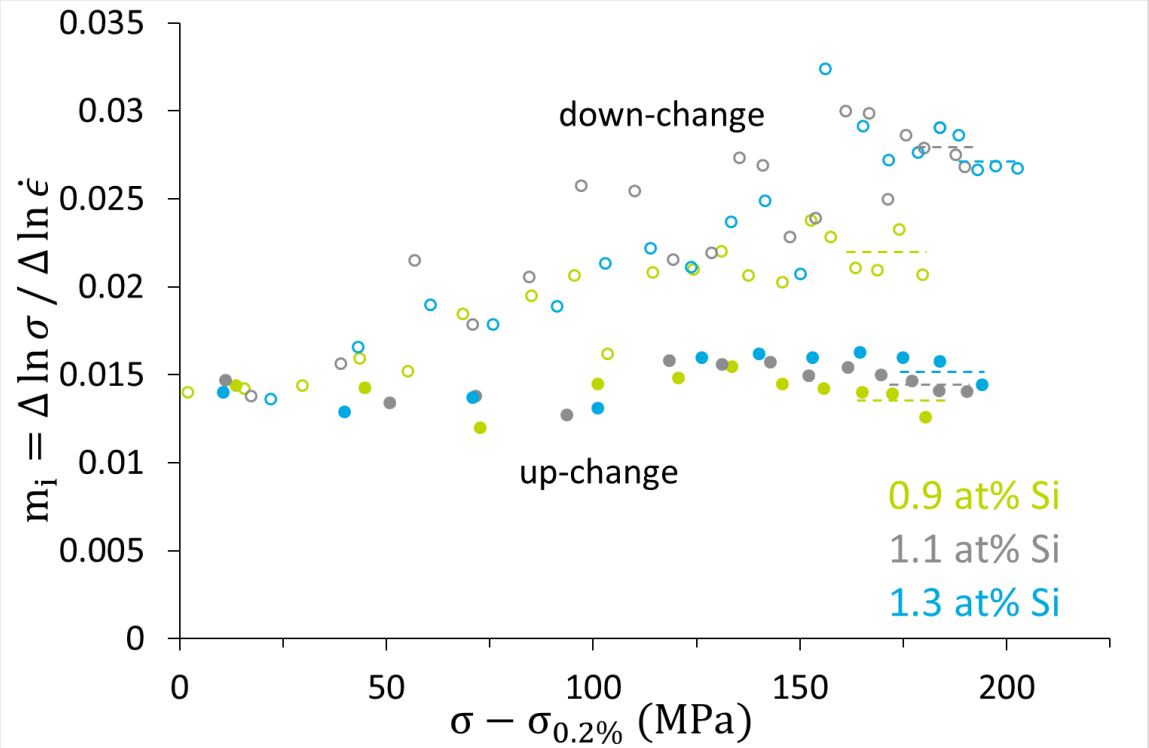

Figure 6-2: *The effects of Si at 0.1 at% Cu on the engineering strain rate sensitivity parameters for both up-change and down-change tests. The dashed lines illustrate the average engineering SRS for the final 3 or 4 points for* m_{uc} *and* m_{dc}*, respectively.*

As it is speculated that there is an influence of both strain hardening and SRS on the formation of necking, the post-uniform elongation in the engineering stress versus engineering strain context was determined. The engineering uniform elongation, e_L, is the engineering strain at the ultimate tensile strength, the fracture elongation, e_f, is the final engineering strain prior to material failure and the post-uniform elongation is the difference, $e_f - e_L$.

3.0 Materials and Methods

Nine aluminum alloys were tested having varying levels of solutes, having compositions similar to the AA6016 and AA6022 series, shown in Table 6-1. The alloys contain four levels of Cu denoted C0 (no Cu), C2 (0.1 at%), C5 (0.2 at%) and C8 (0.3 at%), three levels of Si denoted S0 (0.9 at%), S1 (1.1 at%) and S3 (1.3 at%), and two levels of Mg (0.4 and 0.6 at%). Thus, this series of alloy compositions makes it possible to evaluate separately the influence of each alloying element, in the context of several contents of the other alloying species.

Standard dog-bone tensile specimens were machined from 1 mm thick sheets in the as-rolled condition having a width of 10 mm and a gauge length of 30 mm. The samples were solution heat treated in an air furnace at 550 °C for 15 minutes, then either water-quenched (15 °C) and allowed to naturally age (NA) for one month (NA1m) or quenched in water at 80 °C, pre-aged (PA) at 80 °C for 8 hours in an oil bath, then let to naturally age for one week (sNA1w) or one month (sNA1m). For this work, a servo-hydraulic Instron machine 8502 with a 10 kN load cell, equipped with a 25 ± 10 mm extensometer was used to capture the deformation of the samples that were pulled at a true strain rate of 5 x 10^{-4} s^{-1} until failure to determine the true stress versus true plastic strain tensile curves and corresponding strain hardening evolution until failure. Strain rate sensitivity tests were performed using the same base strain rate and strain rate jump factors of 4 , ¼ and 1/10, for the up-change and down-change rate jumps, respectively, using the step-ramp method

including compensation [45] and described in Chapter 5. A proprietary software controlling a feedback-loop to the initial and active extensometer displacement was used to control the true strain rate.

Table 6-1: *The compositions of the nine alloys tested (in at%). The superscripts indicate the effects of:* ***1a)*** *Cu at 0.9 at% Si,* ***1b)*** *Cu at 1.3 at% Si,* ***2)*** *Si at 0.09 at% Cu, and* ***3)*** *Mg at 0.9 at% Si and 0.3 at% Cu.*

Sample Name	Mg (at%)	Si (at%)	Cu (at%)	Al (at%)
C0S0	0.404	0.895	0.008[1a]	Bal.
C2S0	0.381	0.896	0.089[1a,2]	
C8S0	0.379	0.879	0.333[1a,3]	
C8S0M	0.557	0.899	0.337[3]	
C2S1	0.372	1.069	0.087[2]	
C0S3	0.387	1.299	0.004[1b]	
C2S3	0.400	1.262	0.088[1b]	
C5S3	0.372	1.284	0.218[1b]	
C8S3	0.385	1.324	0.329[1b,3]	

The effects of Cu were studied at 0.9 at% Si with samples; C0S0, C2S0, and C8S0, and 1.3 at% Si with samples; C0S3, C2S3, C5S3, and C8S3. The effects of Si at 0.1 at% Cu with samples; C2S0, C2S1, and C2S3. The effects of Mg additions and Si additions at 0.3 at% Cu were studied with samples: C8S0 and C8S0M, and C8S0 and C8S3, respectively.

4.0 Results and analysis

As a first analysis of the tensile true stress – true strain data, a series of classical parameters has been measured on all alloys and processing conditions, such as the yield strength $\sigma_{0.2\%}$, the true stress at uniform elongation, σ_L, the strain hardening capacity, $\sigma_L - \sigma_{0.2\%}$, and the uniform elongation, ε_L. These data are shown in Table 6-2.

Table 6-2: *A tabulation of each of the mechanical properties for each of the alloys under each heat treatment condition. These properties are those coming directly from the* $\sigma - \epsilon$ *curve.*

Condition	Sample Name	$\sigma_{0.2\%}$ (MPa)	σ_L (MPa)	$\sigma_L - \sigma_{0.2\%}$ (MPa)	ε_L	$e_f - e_L$

NA1m	C0S0	112.7	281.8	169.1	0.219	0.090
	C2S0	119.0	291.6	172.7	0.212	0.060
	C8S0	143.6	364.7	221.1	0.241	0.056
	C8S0M	163.6	378.2	214.6	0.215	0.043
	C2S1	123.4	307.6	184.2	0.239	0.065
	C0S3	124.7	302.5	177.8	0.233	0.087
	C2S3	131.2	324.4	193.2	0.235	0.080
	C5S3	147.4	365.9	218.5	0.241	0.090
	C8S3	152.5	376.1	223.6	0.242	0.077
sNA1m	C0S0	103.5	262.5	159.0	0.204	0.057
	C2S0	105.2	278.5	173.3	0.217	0.059
	C8S0	112.4	319.4	206.9	0.235	0.016
	C8S0M	132.3	355.8	223.5	0.240	0.039
	C2S1	106.3	288.4	182.2	0.230	0.067
	C0S3	118.7	302.9	184.2	0.229	0.111
	C2S3	116.1	312.9	196.7	0.240	0.059
	C5S3	128.0	351.4	223.3	0.252	0.066
	C8S3	138.8	371.0	232.1	0.253	0.059
sNA1w	C0S0	93.0	255.2	162.2	0.216	0.053
	C2S0	89.6	261.0	171.4	0.223	0.047
	C8S0	108.6	313.0	204.4	0.230	0.034
	C8S0M	127.2	345.4	218.3	0.230	0.040
	C2S1	95.5	277.5	181.9	0.232	0.041
	C0S3	110.4	296.0	185.6	0.236	0.090
	C2S3	110.2	311.6	201.4	0.250	0.069
	C5S3	122.4	339.9	217.5	0.244	0.053
	C8S3	134.5	362.8	228.2	0.233	0.025

In order to determine what solute addition most significantly influences each of the mechanical properties, the properties from Table 6-2 are plotted versus total (Mg + Si + Cu) content (see Figures 6-5a-f and Figures 6-6a-f), in atomic concentration, which is more relevant for comparing the effect of solutes of very different atomic numbers. An example of how $\sigma_{0.2\%}$ changes with total solute content is given for the NA1m (Figures 6-3) and sNA1m (Figures 6-4) conditions, shown below.

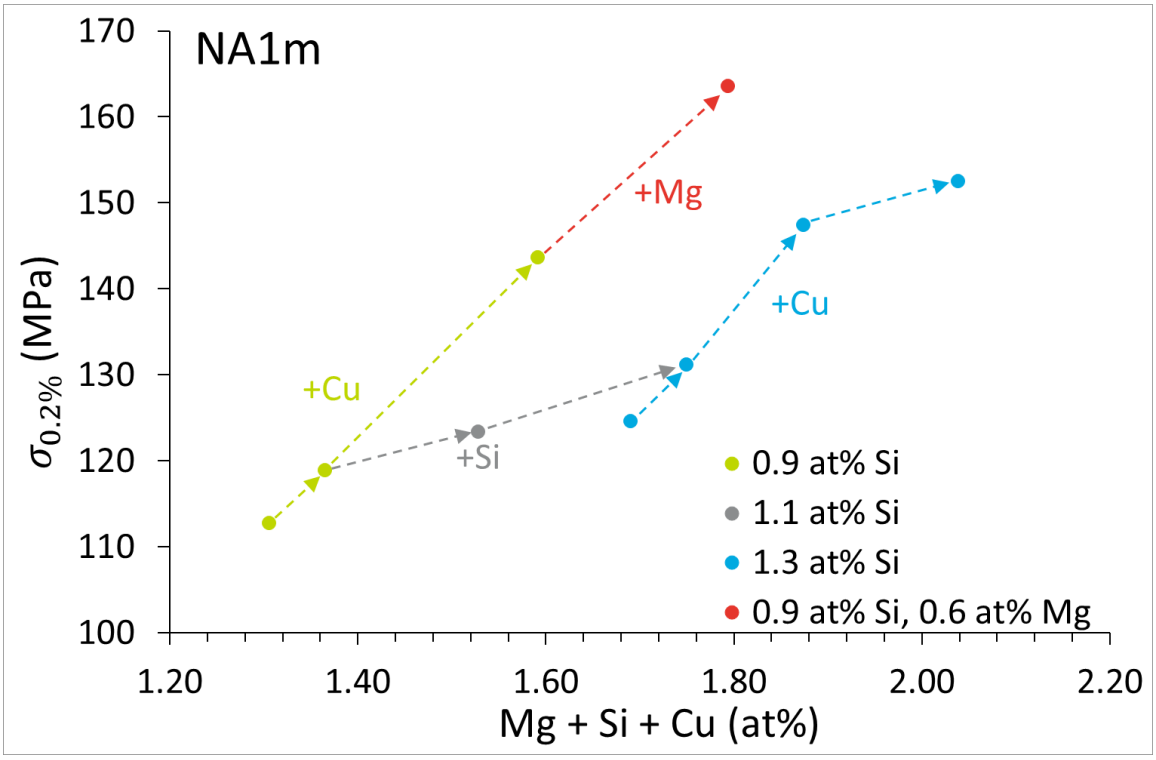

Figure 6-3: *The evolution of the 0.2% yield strength with total solute content in the NA1m condition. For clarity, the effects of Cu additions at 0.9 and 1.3 at% Si, are connected in green and blue dashed arrows, respectively. The effects of Si additions at 0.2 at% Cu and 0.4 at% Mg are connected with the grey dashed arrows. The effects of Mg addition at 0.9 at% Si and 0.3 at% Cu are connected with red dashed arrows.*

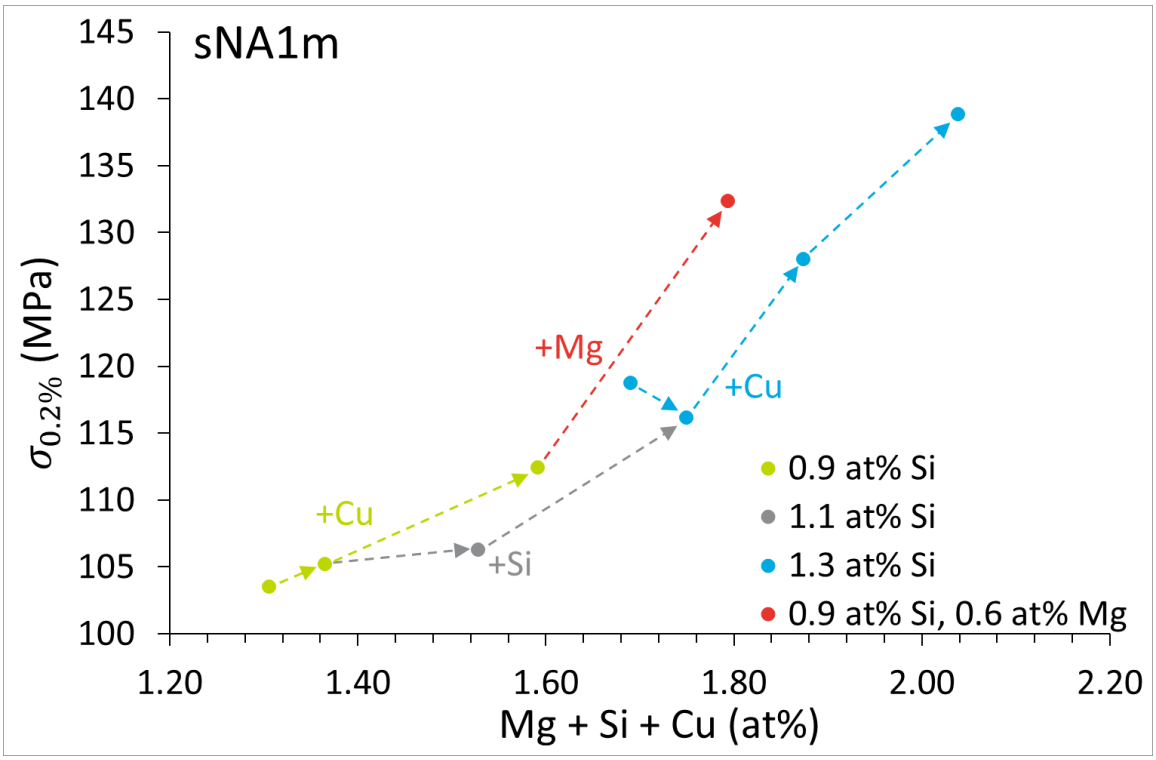

Figure 6-4: *The evolution of the 0.2% yield strength with total solute content in the sNA1m condition. For clarity, the effects of Cu additions at 0.9 and 1.3 at% Si, are connected in green and blue dashed arrows, respectively. The effects of Si additions at 0.2 at% Cu and 0.4 at% Mg are connected with the grey dashed arrows. The effects of Mg addition at 0.9 at% Si and 0.3 at% Cu are connected with red dashed arrows.*

The evolution of $\sigma_{0.2\%}$ with solute content in the NA1m condition (Figure 6-3) is quite different from the sNA1m condition (Figure 6-4). In the NA1m condition, both Cu and Mg have similar levels of strengthening while Si had a considerably lower strengthening effect. It is very interesting to note that despite having similar levels of strength, the sNA1m samples and the NA1m samples demonstrate largely different behaviours with respect to cluster strengthening due to solute additions where all solutes have similar strengthening effects in the sNA1m condition. These trends of specific solute effects in the two conditions parallel those for hardness in Chapter 4.

Now the effect of solute content on the stress-strain behaviour will be evaluated, based on the fitting values of the the Saimoto – van Houtte relation that are tabulated in Table 6-3, along with the engineering strain rate sensitivities from up-changes (uc) and down-changes (dc).

Table 6-3: *The fit parameters generated from the SvH constitutive relation for each sample at a true strain rate of* $\dot{\epsilon} = 5x10^{-4}\ s^{-1}$*. Due to sample complications, no data was available for the up-change strain rate sensitivity of the C8S3 alloy in the NA1m condition.*

Condition	Sample Name	σ_0 (MPa)	ϵ_3	n_1	n_2	K_1	K_2	m_{uc}	m_{dc}
NA1m	C0S0	87.5	0.123	0.51	0.33	466.0	319.5	0.014	0.022
	C2S0	99.8	0.106	0.57	0.38	528.2	345.5	0.014	0.022
	C8S0	118.6	0.132	0.55	0.40	591.0	431.6	0.013	0.022
	C8S0M	143.2	0.122	0.58	0.42	624.0	446.6	0.012	0.023
	C2S1	98.9	0.113	0.53	0.36	496.2	349.3	0.014	0.028
	C0S3	101.3	0.122	0.54	0.35	493.1	333.1	0.015	0.028
	C2S3	106.3	0.122	0.53	0.36	519.0	367.6	0.015	0.027
	C5S3	117.9	0.138	0.51	0.37	556.5	417.3	0.016	0.025
	C8S3	126.9	0.137	0.55	0.38	594.1	423.8	N/A	0.027
sNA1m	C0S0	84.3	0.098	0.56	0.36	503.6	315.7	0.012	0.018
	C2S0	83.6	0.109	0.55	0.37	513.9	339.3	0.011	0.017
	C8S0	87.2	0.112	0.58	0.40	612.2	418.8	0.008	0.015
	C8S0M	108.8	0.131	0.56	0.40	604.9	438.3	0.010	0.022
	C2S1	84.0	0.108	0.55	0.37	528.7	353.1	0.012	0.026
	C0S3	89.6	0.136	0.50	0.34	482.0	349.8	0.014	0.029
	C2S3	93.4	0.113	0.55	0.39	548.9	380.3	0.014	0.027
	C5S3	99.4	0.133	0.53	0.37	581.0	419.5	0.011	0.026
	C8S3	114.7	0.126	0.57	0.40	621.9	445.2	0.014	0.026
sNA1w	C0S0	72.4	0.097	0.55	0.37	491.0	321.7	0.010	0.015
	C2S0	67.5	0.097	0.57	0.39	525.9	345.6	0.007	0.014
	C8S0	92.2	0.097	0.64	0.44	680.6	423.9	0.006	0.013
	C8S0M	105.7	0.118	0.57	0.43	614.0	450.6	0.008	0.020
	C2S1	75.5	0.100	0.58	0.39	556.3	359.4	0.008	0.022
	C0S3	83.5	0.120	0.52	0.34	503.4	346.2	0.014	0.027
	C2S3	88.1	0.112	0.56	0.39	559.8	383.6	0.013	0.027
	C5S3	96.7	0.129	0.54	0.39	574.7	421.2	0.016	0.019
	C8S3	112.1	0.113	0.58	0.44	642.0	472.5	0.013	0.026

By looking at how the total solute content in at% influences each of the fit parameters and the engineering strain rate sensitivity, the nature of solute-dislocation and cluster-dislocation interactions may be postulated. Figures 6-5a-f and 6-6a-f show the correlations of the different parameters of the constitutive laws and strain rate sensitivity for the NA1m and sNA1m conditions, respectively. Note that only the strain hardening parameters (K_2 and n_2) corresponding to the large strain behaviour are shown in these graphs, since they are more relevant to the evaluation of formability than the low strain values. The sNA1w data is shown in Appendix 1.3 for the sake of space but will be discussed within the main body of the paper.

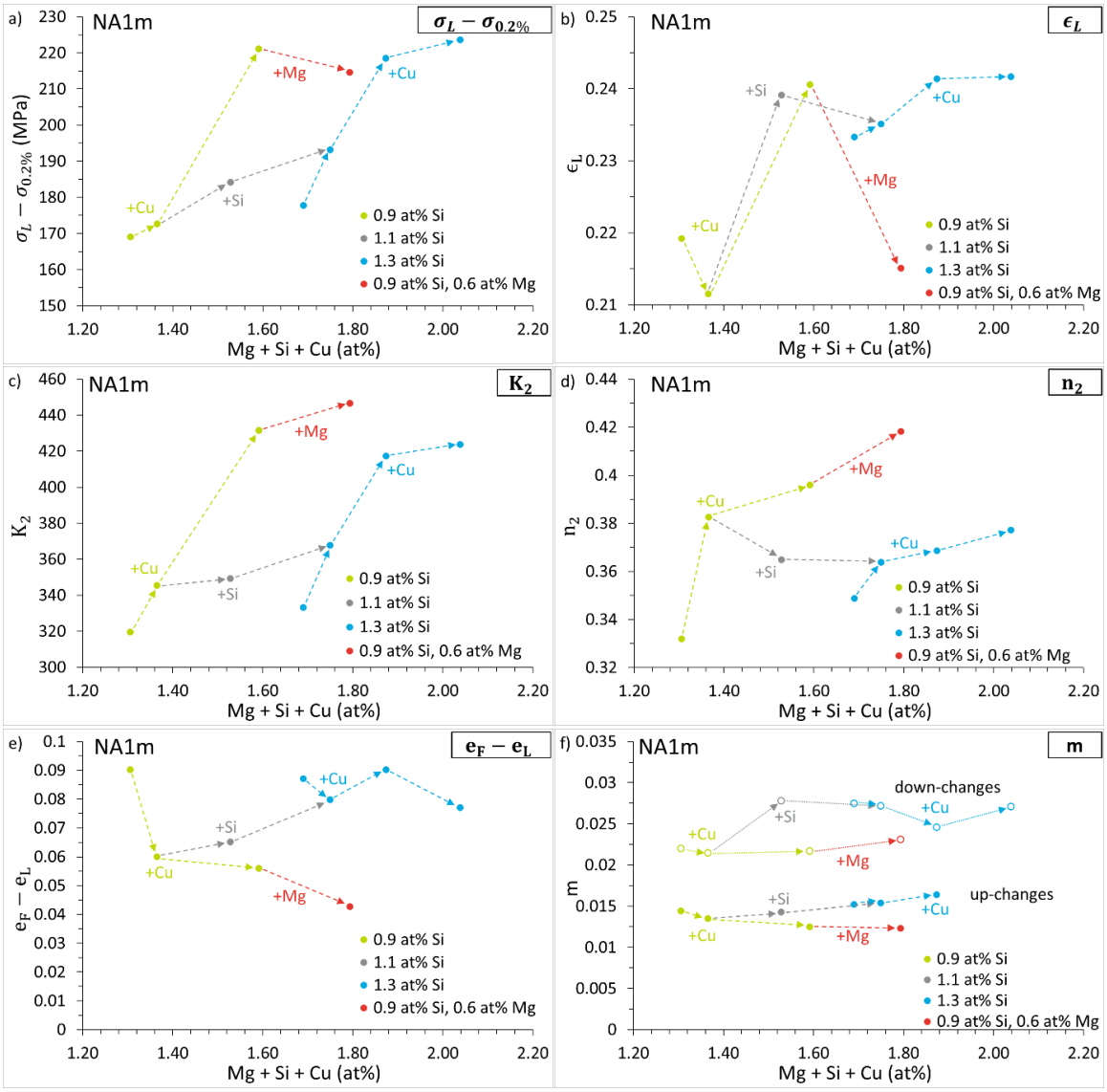

Figure 6-5: *The effects of total solute content on the* ***a)*** *strain hardening capacity,* ***b)*** *the uniform elongation,* ***c)*** *pre-exponential, K_2, for the second part of the constitutive relation,* ***d)*** *the strain hardening exponent, n_2,* ***e)*** *the post-uniform elongation, and* ***f)*** *the up-change (closed circles) and down-change (open circles) engineering SRS for the alloys tested in the NA1m condition. For clarity, the effects of Cu additions at 0.9 and 1.3 at% Si, are connected in green and blue dashed arrows, respectively. The effects of Si additions at 0.2 at% Cu and 0.4 at% Mg are connected with the grey dashed arrows. The effects of Mg addition at 0.9 at% Si and 0.3 at% Cu are connected with red dashed arrows.*

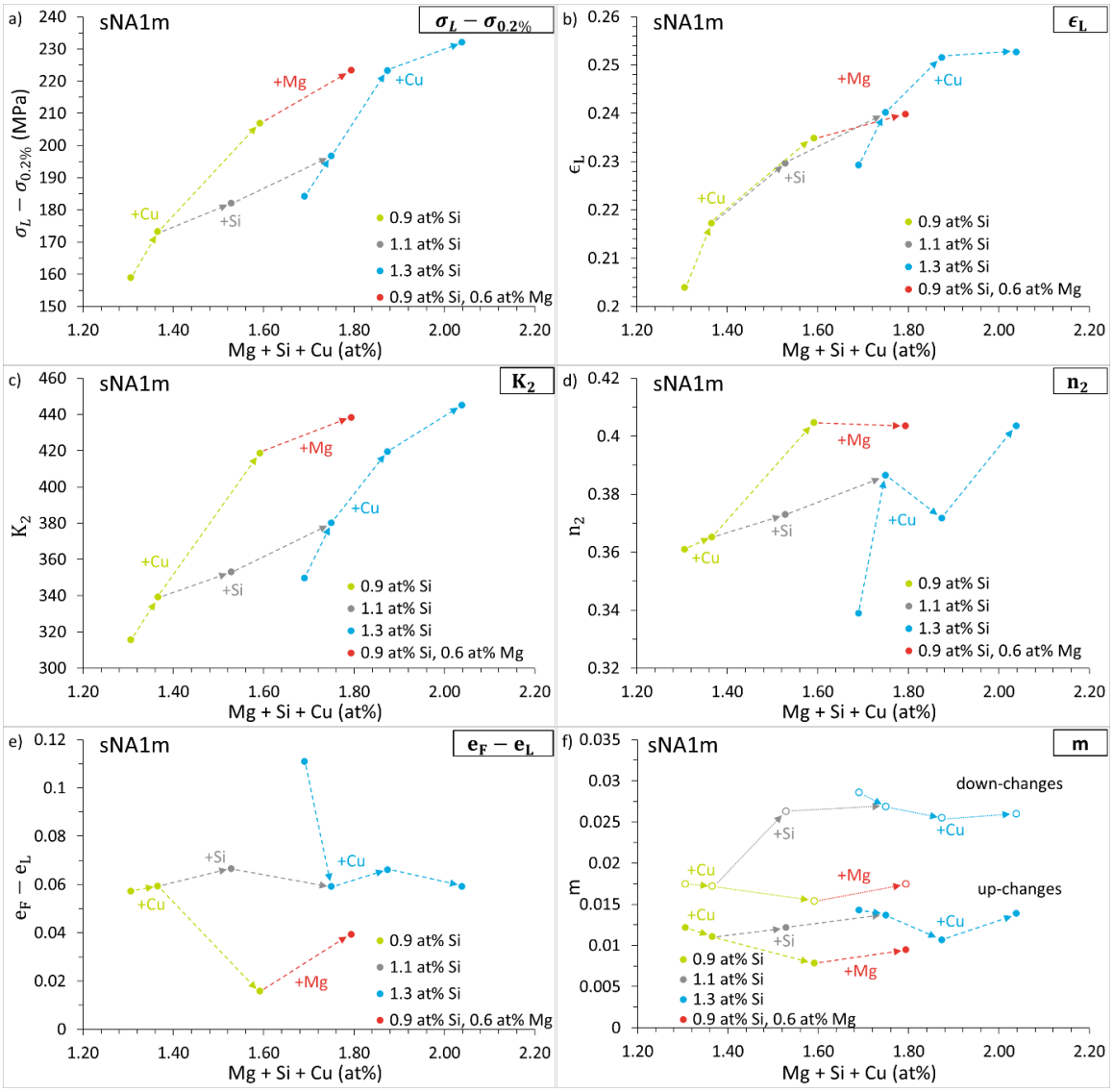

Figure 6-6: *The effects of total solute content on the* ***a)*** *strain hardening capacity,* ***b)*** *the uniform elongation,* ***c)*** *pre-exponential, K_2, for the second part of the constitutive relation,* ***d)*** *the strain hardening exponent, n_2,* ***e)*** *the post-uniform elongation, and* ***f)*** *the up-change (closed circles) and down-change (open circles) engineering SRS for the alloys tested in the sNA1m condition. For clarity, the effects of Cu additions at 0.9 and 1.3 at% Si, are connected in green and blue dashed arrows, respectively. The effects of Si additions at 0.2 at% Cu and 0.4 at% Mg are connected with the grey dashed arrows. The effects of Mg addition at 0.9 at% Si and 0.3 at% Cu are connected with red dashed arrows.*

The relative effects of solute additions for the three different heat treatments are summarized in Table 6-4.

Table 6-4: *A summary of the influence of each alloying element on the corresponding mechanical properties. '+' indicates an increase on the property with increased solute, '++' indicates a stronger increase for the same increase in solute content, and '-' indicates a decrease of the property with increased solute. *The effect of Cu appears to depend on the level of Si present in the alloy.*

Property	NA1m			sNA1m			sNA1w		
	Cu	Mg	Si	Cu	Mg	Si	Cu	Mg	Si
$\sigma_{0.2\%}$	++		+	+			+		
σ_L	++	+		++	+		+		
$\sigma_L - \sigma_{0.2\%}$	++	-	+	++		+	++		+
ϵ_L	+	-	=	+			+/-*	=	+
m_{dc}	=		+	-	+	++	-	+	++
m_{uc}	=			-	+		-	+	
K_2	++	+		++	+		++	+	
n_2	+		-	++	=	+	++	-	=
$e_f - e_L$	-/=*	-	+	+	-	=	-/--*	+	

4.1 NA1m

In the NA1m condition, there appear to be significant differences on the relative sensitivities of each solute element on each of the mechanical properties. All the parameters describing the large-strain constitutive law ($\sigma_{0.2\%}$, K_2 and n_2), are positively influenced by additions of Cu and Mg, having similar sensitivities. The addition of Si, however, presents a much smaller influence on the same parameters, slightly positive for $\sigma_{0.2\%}$ and K_2, and slightly negative for n_2. It is particularly interesting to observe that the effect of the same solutes on strain rate sensitivity (SRS) is very different from that on the constitutive law. The addition of Cu and/or Mg has no effect on the engineering SRS at large strains (whether for up- or down-changes) whereas the addition of Si increases the down-change SRS while not affecting the up-change SRS.

4.2 sNA1m

The effect of solute additions on the constitutive parameters is quite different in the sNA1m condition as compared to the NA1m case. Considering the effect of solute additions on the constitutive law at large strains ($\sigma_{0.2\%}$, K_2, and n_2), is similar to the NA1m case, a strongly positive effect of Cu addition, but now a comparable moderate positive effect of Si and Mg. Concerning the engineering SRS at large strains, the sNA1m condition presents no effect of Cu addition (or even a slightly negative effect), a slightly positive effect of Mg addition, and a positive effect of Si addition, especially on the down-change SRS.

4.3 sNA1w

The sNA1w condition, whose data are presented in Appendix 1.3, shows similar solute effects as compared to the sNA1m condition. Although some minor effects can vary, generally speaking the strong effect of Cu addition and smaller positive effect of Si and Mg on the constitutive laws are found, and on the large strain engineering SRS one finds also a positive effect of Si and Mg and a slightly negative effect of Cu.

5.0 Discussion

5.1 Effects on mechanical properties

The relative sensitivity of each material property to the effects of each solute clearly depends on the type of heat treatment performed and the nature of the clusters formed during the respective heat treatments as illustrated in Table 6-4.

As previously shown in Chapter 4, Cu and Mg additions introduce a second family of clusters whose presence results in a secondary dissolution peak at lower temperatures in the NA1m condition, compared to the PA conditions whereby all clusters appear to dissolve in a single peak, at a significantly higher temperature compared to the NA1m conditions second peak. Interestingly, this initial dissolution peak shifts to lower temperatures with Si additions suggesting that these clusters are less thermally stable as shown in Chapter 4 (see Appendix 1.2 for the effects of Si addition at 0.3 at% Cu where this effect is more pronounced). This correlates to the yield strength evolution of the NA1m condition having a greater sensitivity to Cu and Mg additions compared to Si. The appearance of this earlier dissolution peak being highly sensitive to added Cu and Mg suggests that a separate, Cu/Mg-rich cluster is forming with a large effect on the yield strength [18]. Conversely, both the DSC and the strength data after pre-ageing strongly suggests that a single type of cluster forms during the PA process, which has an equal dependency on all solutes contributing to its formation [5], [8], [11], [13] supported by the evidence of the yield strength evolving uniformly with any of these solute additions.

It is surprising that the Mg additions in the NA1m condition decreases the total strain hardening capacity, contrary to the results found by Chen et al. [46] and Jobba et al. [47] in Al-Mg alloys. This is the only case whereby additional solute do not increase the strain hardening capacity and is coupled with a decrease in the uniform elongation as would be expected for a sample with a reduced strain hardening capacity. In both PA conditions, the strain hardening capacity was found to increase with solute additions with Cu and Mg having a stronger effect than Si as observed by Chen et al. [46] due to the increased initial strain hardening rate exhibited by Cu and Mg as compared to Si. This coupled with the decrease in recovery rate found in binary alloys yielding a net increase in the total strain hardening capacity.

The effects of total solute content on the up-change engineering SRS at large strain is consistent with the work performed by Zhong et al. [23], [25] whereby Si additions were shown to increase the m_{uc} values under all heat treatment conditions. The current work does not display as much of a dynamic strain ageing effect as observed by Zhong et al. [23] possibly due to the longer NA times used in this work and the more complete removal of solute from the matrix, resulting also in the present work displaying no negative strain rate sensitivity values. In the sNA1m and sNA1w conditions, the addition of Cu was found to decrease or not change the m_{uc} values at 0.9 and 1.3 at% Si, respectively. It may be argued that the decrease in m_{uc} at 0.9 at% Si is due to a retention of solute in the matrix with added Cu (see hardening plots in Chapter 4) yielding a negative contribution of solutes to the strain rate sensitivity. In contrast, at 1.3 at% Si, there may be a more complete removal of Cu from the matrix and the clusters that are formed are more thermally (and thus speculated to be more mechanically) stable due to the higher dissolution temperature than those formed during NA only (see Chapter 4).

Unfortunately, there is not extensive down-change engineering SRS data available in the literature to compare to the current work, thus depending on the interpretation used, there are a few possible explanations to the observed trends in m_{dc} with solute additions. It is well established

that in Cu and Al systems, the interaction of dislocations with other dislocations, stacking fault tetrahedra and other microstructural objects are able to produce sub-microscopic dislocation-obstacle interaction products, called debris [48]. During a strain rate decrease test, the reduction of dislocation velocity and increase of waiting times at obstacles can allow the recovery of these generated debris [49], so that it would result in an enhancement of the decrease in the stress drop associated with the strain rate down-change. In a similar way as for a stress relaxation test, and keeping in mind that different types of debris anneal out at different temperatures [50], the corresponding stress change would be enhanced as compared to that measured during a strain rate up-change. In the framework of this interpretation of down-change SRS by the recovery of dislocation debris, the observed effects of (Si, Mg) and Cu could correspond to opposite effects on either the production rate of debris (which would be enhanced by the addition of Mg & Si and not by the addition of Cu) and/or on their annihilation during the strain rate decrease. However, other effects need to be considered as well. The addition of Si has been shown to increase the NA kinetics [8], [9] (see Chapter 4), resulting in an enhanced removal of solute from the matrix which negatively contribute to the SRS via dynamic strain ageing thus yielding an increase in the net SRS. Cu on the other hand, contribute more to the later-stage clustering behaviour and their additions may result in a greater total free solute in the matrix, having a negative effect on the SRS. Finally, the mechanical stability of the clusters during plastic deformation needs to be considered as well. If clusters are mechanically dissolved during plastic flow, their contribution to the flow stress and to the SRS can change dynamically. As an example, in an Al-Cu binary alloy, Chen et al. [46] have shown that GP zones were able to be mechanically dissolved. This phenomenon could be especially present in the case of the 1.3 at% Si alloys where the dissolution of clusters in the NA1m alloys during a heating ramp from the DSC thermographs occurs at lower temperatures (see Chapter 4) indicating they are less thermally stable and thus possibly less mechanically stable, coupled with the increase in cluster dissolution intensity.

It is still not fully understood what obstacles are being activated during the up-change tests and the down-change tests but it is important to state that the asymmetry of strain rate sensitivity in the two direction certainly exist with m_{dc} always being greater than m_{uc} at room temperature.

5.2 Effects on constitutive parameters

Fitting the stress-strain curves with constitutive relations provide the ability to connect solute contents to the microstructure evolution in different heat treatments whereby the fit parameters represent various physical phenomena that exist throughout the plastic deformation process. In the context of the present work, the focus is on the large-strain behaviour since it is more relevant to the study of formability.

The increase in K_2 reflects a decrease in dislocation annihilation/recovery during deformation whereby Cu and Mg additions have a stronger effect on decreasing annihilation compared to Si as shown by Chen et al. [46] in binary alloys. In the current work, Cu and Mg decrease recovery in the NA1m condition. This is made possible by additional obstacles formed during the NA process hindering the unzipping of dislocations which are pinned by the clusters [51]. The contributions of Cu and Mg are more pronounced than Si, suggesting that although the three solute species decrease the recovery rate, Cu and Mg play a larger role than Si. The difference with the aforementioned [46] work is likely due to the more complex alloys in the present work compared to their studying binary systems. The decrease in the dislocation recovery rate may either be due to the shearing and mechanical dissolution of clusters [46], [52], [53] increasing the total effective solute content in the alloy, or by the retardation of dislocation recovery during deformation [47], [54] due to an existing increased solute content in the alloy. Finally, the strain hardening exponent

increases with both Cu and Mg additions in the NA1m condition. The increase may be explained by an enhanced slip homogenization due to the added Mg and Cu due to the mechanical dissolution of the clusters. Si additions, decrease the strain hardening exponent, possibly due to the increase in cluster density and the reduction of free solute in the matrix. The situation changes for Mg and Si in the sNA1m and sNA1w conditions whereby Mg decreases the strain hardening in sNA1w and does not change the sNA1m strain hardening rate whereas Si does not change sNA1w but increases the sNA1m strain hardening behaviour. The decreased effects are assumed to be similar to those in the NA1m conditions with Mg increasing the number density of clusters formed in the sNA1w conditions decreasing the slip homogenization [55], [56], while Si additions are able to assist in slip homogenization via a greater fraction of Si remaining in solution due to the PA treatment (see Chapter 4).

6.0 Conclusions

- Cu, Mg, and Si all increase the yield strength of the alloys, independent of heat treatment, however, the effect of Cu and Mg is most pronounced in the NA1m condition compared to that of Si. In the sNA1m and sNA1w conditions, the total solute content is most important for the yield strength.
- Cu additions decrease m_{dc} at high flow stresses whereas both Mg and Si additions increase the m_{dc} for all of the conditions while simultaneously increasing m_{uc}.
- Individual solute contents appear to affect the various mechanical properties in differing proportions more so in the NA1m but not in the sNA1m suggesting that the cluster types that are formed in the two heat treatments are significantly different in nature.
- If the NA1m heat treatment is to be used; the addition of Cu and Si is preferred to maximize both the up change and down change strain rate sensitivity while increasing the high strain work hardening
- If the sNA1m heat treatment is to be used; Si and Mg additions show no detrimental effects to any of the material properties such that both of these additions are recommended.

7.0 References

[1] R. Prillhofer, G. Rank, J. Berneder, H. Antrekowitsch, P. Uggowitzer, and S. Pogatscher, “Property Criteria for Automotive Al-Mg-Si Sheet Alloys,” *Materials*, vol. 7, no. 7, pp. 5047–5068, Jul. 2014.

[2] J. Hirsch, “Automotive trends in aluminium-The European perspective,” in *Materials Forum*, 2004, vol. 28, pp. 15–23.

[3] J. Hirsch, “Recent development in aluminium for automotive applications,” *Trans. Nonferrous Met. Soc. China*, vol. 24, no. 7, pp. 1995–2002, Jul. 2014.

[4] A. Poznak, R. K. W. Marceau, and P. G. Sanders, “Composition dependent thermal stability and evolution of solute clusters in Al-Mg-Si analyzed using atom probe tomography,” *Mater. Sci. Eng. A*, vol. 721, pp. 47–60, Apr. 2018.

[5] Y. Aruga, M. Kozuka, and T. Sato, “Formulation of initial artificial age-hardening response in an Al-Mg-Si alloy based on the cluster classification using a high-detection-efficiency atom probe,” *J. Alloys Compd.*, vol. 739, pp. 1115–1123, Mar. 2018.

[6] S. Esmaeili and D. J. Lloyd, “Effect of composition on clustering reactions in AlMgSi(Cu) alloys,” *Scr. Mater.*, vol. 50, no. 1, pp. 155–158, Jan. 2004.

[7] M. Torsæter *et al.*, “The influence of composition and natural aging on clustering during preaging in Al–Mg–Si alloys,” *J. Appl. Phys.*, vol. 108, no. 7, p. 073527, 2010.

[8] M. Werinos *et al.*, “Design strategy for controlled natural aging in Al–Mg–Si alloys,” *Acta Mater.*, vol. 118, pp. 296–305, Oct. 2016.

[9] M. Werinos, H. Antrekowitsch, T. Ebner, R. Prillhofer, P. J. Uggowitzer, and S. Pogatscher, “Hardening of Al–Mg–Si alloys: Effect of trace elements and prolonged natural aging,” *Mater. Des.*, vol. 107, pp. 257–268, Oct. 2016.

[10] Z. Jia, L. Ding, L. Cao, R. Sanders, S. Li, and Q. Liu, “The Influence of Composition on the Clustering and Precipitation Behavior of Al-Mg-Si-Cu Alloys,” *Metall. Mater. Trans. A*, vol. 48, no. 1, pp. 459–473, Jan. 2017.

[11] Y. Aruga, M. Kozuka, Y. Takaki, and T. Sato, “Effects of natural aging after pre-aging on clustering and bake-hardening behavior in an Al–Mg–Si alloy,” *Scr. Mater.*, vol. 116, pp. 82–86, Apr. 2016.

[12] Y. Aruga, M. Kozuka, Y. Takaki, and T. Sato, “Formation and reversion of clusters during natural aging and subsequent artificial aging in an Al–Mg–Si alloy,” *Mater. Sci. Eng. A*, vol. 631, pp. 86–96, Apr. 2015.

[13] V. Fallah, B. Langelier, N. Ofori-Opoku, B. Raeisinia, N. Provatas, and S. Esmaeili, “Cluster evolution mechanisms during aging in Al–Mg–Si alloys,” *Acta Mater.*, vol. 103, pp. 290–300, Jan. 2016.

[14] V. Fallah *et al.*, “Atomic-scale pathway of early-stage precipitation in Al–Mg–Si alloys,” *Acta Mater.*, vol. 82, pp. 457–467, Jan. 2015.

[15] M. D. H. Lay, H. S. Zurob, C. R. Hutchinson, T. J. Bastow, and A. J. Hill, “Vacancy Behavior and Solute Cluster Growth During Natural Aging of an Al-Mg-Si Alloy,” *Metall. Mater. Trans. A*, vol. 43, no. 12, pp. 4507–4513, Dec. 2012.

[16] J. Banhart, C. S. T. Chang, Z. Liang, N. Wanderka, M. D. H. Lay, and A. J. Hill, “Natural Aging in Al-Mg-Si Alloys - A Process of Unexpected Complexity,” *Adv. Eng. Mater.*, vol. 12, no. 7, pp. 559–571, Jul. 2010.

[17] H. Seyedrezai, D. Grebennikov, P. Mascher, and H. S. Zurob, “Study of the early stages of clustering in Al–Mg–Si alloys using the electrical resistivity measurements,” *Mater. Sci. Eng. A*, vol. 525, no. 1–2, pp. 186–191, Nov. 2009.

[18] F. De Geuser, W. Lefebvre, and D. Blavette, “3D atom probe study of solute atoms clustering during natural ageing and pre-ageing of an Al-Mg-Si alloy,” *Philos. Mag. Lett.*, vol. 86, no. 4, pp. 227–234, Apr. 2006.

[19] L. Cao, P. A. Rometsch, and M. J. Couper, “Clustering behaviour in an Al–Mg–Si–Cu alloy during natural ageing and subsequent under-ageing,” *Mater. Sci. Eng. A*, vol. 559, pp. 257–261, Jan. 2013.

[20] L. He, H. Zhang, and J. Cui, “Effects of Pre-Ageing Treatment on Subsequent Artificial Ageing Characteristics of an Al-1.01Mg-0.68Si-1.78Cu Alloy,” *J. Mater. Sci. Technol.*, vol. 26, no. 2, pp. 141–145, 2010.

[21] S. Esmaeili, D. J. Lloyd, and W. J. Poole, “Effect of natural aging on the resistivity evolution during artificial aging of the aluminum alloy AA6111,” *Mater. Lett.*, vol. 59, no. 5, pp. 575–577, Feb. 2005.

[22] W. J. Poole, D. J. Lloyd, and J. D. Embury, “The effect of natural ageing on the evolution of yield strength during artificial ageing for Al-Mg-Si-Cu alloys,” *Mater. Sci. Eng. A*, vol. 234, pp. 306–309, 1997.

[23] H. Zhong, P. A. Rometsch, L. Cao, and Y. Estrin, “The influence of Mg/Si ratio and Cu content on the stretch formability of 6xxx aluminium alloys,” *Mater. Sci. Eng. A*, vol. 651, pp. 688–697, Jan. 2016.

[24] H. Zhong, P. Rometsch, and Y. Estrin, “Effect of alloy composition and heat treatment on mechanical performance of 6xxx aluminum alloys,” *Trans. Nonferrous Met. Soc. China*, vol. 24, no. 7, pp. 2174–2178, Jul. 2014.

[25] H. Zhong, P. A. Rometsch, and Y. Estrin, “The Influence of Si and Mg Content on the Microstructure, Tensile Ductility, and Stretch Formability of 6xxx Alloys,” *Metall. Mater. Trans. A*, vol. 44, no. 8, pp. 3970–3983, Aug. 2013.

[26] A. K. Ghosh, “The Influence of Strain Hardening and Strain-Rate Sensitivity on Sheet Metal Forming,” *J. Eng. Mater. Technol.*, vol. 99, no. 3, p. 264, 1977.

[27] A. K. Ghosh, “Tensile instability and necking in materials with strain hardening and strain-rate hardening,” *Acta Metall.*, vol. 25, no. 12, pp. 1413–1424, Dec. 1977.

[28] B. J. Diak and S. Saimoto, “Role of Strain Rate Sensitivity on Diffuse Necking,” in *Dynamic Plasticity and Structural Behaviours*, 1995, pp. 5–8.

[29] J. W. Hutchinson and K. W. Neale, “SHEET NECKING-III. STRAIN-RATE EFFECTS,” p. 17.

[30] J. W. Hutchinson and K. W. Neale, “Influence of strain-rate sensitivity on necking under uniaxial tension,” *Acta Metall.*, vol. 25, no. 8, pp. 839–846, Aug. 1977.

[31] M. J. Starink and S. C. Wang, “A model for the yield strength of overaged Al–Zn–Mg–Cu alloys,” *Acta Mater.*, vol. 51, no. 17, pp. 5131–5150, 2003.

[32] E. Hornbogen and E. A. Starke Jr, “Overview no. 102 Theory assisted design of high strength low alloy aluminum,” *Acta Metall. Mater.*, vol. 41, no. 1, pp. 1–16, 1993.

[33] L. C. Wong and S. Saimoto, “Superposition of thermal activation processes in quenched aluminum-1.7 at% copper,” *Scr. Metall. Mater.*, vol. 29, no. 3, pp. 341–346, 1993.

[34] S. Saimoto and P. Van Houtte, “Constitutive relation based on Taylor slip analysis to replicate work-hardening evolution,” *Acta Mater.*, vol. 59, no. 2, pp. 602–612, Jan. 2011.

[35] F. R. N. Nabarro, Z. S. Basinski, and D. B. Holt, “The plasticity of pure single crystals,” *Adv. Phys.*, vol. 13, no. 50, pp. 193–323, Apr. 1964.

[36] S. Saimoto, I. B. Timokhina, and E. V. Pereloma, “Constitutive Relations Analyses of Plastic Flow in Dual-Phase Steels to Elucidate Structure–Strength–Ductility Correlations,” *JOM*, vol. 69, no. 7, pp. 1228–1235, Jul. 2017.

[37] S. Saimoto *et al.*, “Method to decode stress-strain diagrams to identify the structure-strength relationships in aged aluminum alloys,” *Mater. Sci. Eng. A*, vol. 709, pp. 9–16, Jan. 2018.

[38] M. R. Langille, “Structure, strength, ductility in aluminium alloys: constitutive relations analysis for performance evaluation,” M.A.Sc, Queen’s University, Kingston, Canada, 2016.

[39] S. Saimoto and D. J. Lloyd, “A new analysis of yielding and work hardening in AA1100 and AA5754 at low temperatures,” *Acta Mater.*, vol. 60, no. 18, pp. 6352–6361, Oct. 2012.

[40] S. Saimoto and B. J. Diak, “Point defect generation, nano-void formation and growth. I. Validation,” *Philos. Mag.*, vol. 92, no. 15, pp. 1890–1914, May 2012.

[41] S. Saimoto, B. J. Diak, and D. J. Lloyd, “Point defect generation, nano-void formation and growth. II. Criterion for ductile failure,” *Philos. Mag.*, vol. 92, no. 15, pp. 1915–1936, May 2012.

[42] M. A. Singh, S. Saimoto, M. R. Langille, J. Lévesque, K. Inal, and A. R. Woll, “Small-angle X-ray scattering investigation of deformation-induced nanovoids in AA6063 aluminium alloy,” *Philos. Mag.*, pp. 1–18, Jun. 2017.

[43] S. Saimoto, P. Van Houtte, K. Inal, and M. R. Langille, “New biaxial yield function for aluminum alloys based on plastic work and work-hardening analyses,” *Acta Mater.*, vol. 118, pp. 109–119, Oct. 2016.

[44] A. P. Brahme, K. Inal, R. K. Mishra, and S. Saimoto, “A new strain hardening model for rate-dependent crystal plasticity,” *Comput. Mater. Sci.*, vol. 50, no. 10, pp. 2898–2908, Aug. 2011.

[45] M. Carlone and S. Saimoto, “Precision strain rate sensitivity measurement using the step-ramp method,” *Exp. Mech.*, vol. 36, no. 4, pp. 360–366, 1996.

[46] Y. Chen, M. Weyland, and C. R. Hutchinson, “The effect of interrupted aging on the yield strength and uniform elongation of precipitation-hardened Al alloys,” *Acta Mater.*, vol. 61, no. 15, pp. 5877–5894, Sep. 2013.

[47] M. Jobba, R. K. Mishra, and M. Niewczas, “Flow stress and work-hardening behaviour of Al–Mg binary alloys,” *Int. J. Plast.*, vol. 65, pp. 43–60, Feb. 2015.

[48] M. Niewczas, “Transmission electron microscopy observations of debris structure in deformed copper single crystals,” *Philos. Mag. A*, vol. 82, no. 2, pp. 393–414, Jan. 2002.

[49] S. Saimoto and M. S. Duesbery, “Strain rate sensitivity: the role of dislocation loop and point defect recovery,” *Acta Metall.*, vol. 32, no. 1, pp. 147–155, 1984.

[50] M. Niewczas and D.-Y. Park, “Flow stress and electrical resistivity in plastically deformed Al subjected to intermittent annealing,” *Mater. Sci. Eng. A*, vol. 706, pp. 256–268, 2017.

[51] N. Yu. Zolotorevsky, A. N. Solonin, A. Yu. Churyumov, and V. S. Zolotorevsky, “Study of work hardening of quenched and naturally aged Al–Mg and Al–Cu alloys,” *Mater. Sci. Eng. A*, vol. 502, no. 1–2, pp. 111–117, Feb. 2009.

[52] M. J. Starink and S. C. Wang, “The thermodynamics of and strengthening due to co-clusters: General theory and application to the case of Al–Cu–Mg alloys,” *Acta Mater.*, vol. 57, no. 8, pp. 2376–2389, May 2009.

[53] M. J. Starink, L. F. Cao, and P. A. Rometsch, “A model for the thermodynamics of and strengthening due to co-clusters in Al–Mg–Si-based alloys,” *Acta Mater.*, vol. 60, no. 10, pp. 4194–4207, Jun. 2012.

[54] W. J. Poole, X. Wang, D. J. Lloyd, and J. D. Embury, “The shearable–non-shearable transition in Al–Mg–Si–Cu precipitation hardening alloys: implications on the distribution of slip, work hardening and fracture,” *Philos. Mag.*, vol. 85, no. 26–27, pp. 3113–3135, Sep. 2005.

[55] L. M. Brown, “Transition from laminar to rotational motion in plasticity,” *Philos. Trans. R. Soc. Lond. Math. Phys. Eng. Sci.*, vol. 355, no. 1731, pp. 1979–1990, 1997.

[56] E. Christiansen, C. D. Marioara, K. Marthinsen, O. S. Hopperstad, and R. Holmestad, “Lattice rotations in precipitate free zones in an Al-Mg-Si alloy,” *Mater. Charact.*, vol. 144, pp. 522–531, Oct. 2018.

7 Characterization of Thermally Activated Dislocation Glide in Naturally Aged Al-Mg-Si-Cu Alloys: What it tells us about clusters

To compliment the initial observations of the effects of alloy composition on the resulting clustering behaviour in the Al-Mg-Si-Cu system, the evolution of the strain rate sensitivity with temperature and its connection to the apparent activation volumes and distances are presented in this chapter. From the changes in specific properties such as the yield strength, initial apparent activation volume and distance, underlying information regarding the rate controlling obstacles and microstructure may be elucidated. This may serve as a basis for providing additional information regarding cluster size, density, and potentially relative strength, compared to experimentally difficult but more direct means such as small angle x-ray or neutron scattering, atom probe tomography, differential scanning calorimetry, and hardness testing. Additionally, the work will be directly compared to the observations made in pure polycrystalline aluminium and the complexities that arise when working with industrial alloys at high (ambient) temperatures.

Characterization of Thermally Activated Dislocation Glide in Naturally Aged Al-Mg-Si-Cu Alloys: What it tells us about clusters

Abstract

The use of strain rate sensitivity testing at 78, 198, and 294 K was performed on nine Al-Mg-Si-Cu alloys. The effects of alloy composition combined with three clustered states (heat treatments) allowed for the examination of the obstacle profile and the effects of retained solute in solution. The effects of yield strength and both initial and final thermodynamic strain rate sensitivities were related to both the unique solute addition and clustered state. Using samples tested in the as-quenched condition, the Taylor relation was used in conjunction with the initial strain rate sensitivity in order to isolate the initial activation distance from the apparent activation volume allowing for the deconvolution of cluster density, representing the obstacle spacing, and the cluster size, related to the activation distance. Each of the values were compared to those of forest dislocations in polycrystalline pure aluminium, serving as a benchmark. In general, the clusters were found to behave more closely to a solid solution than precipitates with the clusters being shearable in nature and thus evolving during deformation.

1.0 Introduction

The increased use of age-hardenable aluminium alloys in the automotive market, specifically, that of rolled sheets, has brought the need for an enhanced understanding of the deformation mechanics and strengthening mechanisms due to the presence of microstructure obstacles (solute atoms, clusters, and precipitates) formed during their processing via heat treatments. Automotive sheets used for exterior body panels are deformed in the naturally aged, NA, or pre-aged, PA, states where the primary obstacles that control the deformation behaviour are clusters, prior to being submitted to what is known as the paint bake (PB) cycle (185 °C for 20 minutes) where a portion of these clusters are replaced by precipitates. The formation of clusters during both the NA and PA processes have been well studied using a variety of techniques [1]–[3]for the effects of both composition [4]–[8]and treatment temperatures and durations [9]–[12]combined with their effects on the PB response [13], [14].

The chemistry-sensitive structural changes occurring during natural ageing (NA), pre-ageing (PA), and secondary natural ageing (sNA) that follows pre-ageing, affect the mechanical properties as measured by tensile testing, such as yield stress, strain hardening rate, strain rate sensitivity of the flow stress, and elongation, differently. Thermodynamic and structural models have been developed to predict strengthening, i.e. hardness, yield stress [15], but similar level of insight into strain hardening, strain rate sensitivity and total elongation from structure and chemistry is still missing. Zhong [16]–[19] has measured tensile behaviour (strain hardening, strain rate sensitivity, elongation, etc) of NA and PA with sNA of AA6xxx at room temperature and by observing the onset of phenomena like jerky flow, interpreted as the balance between solute atoms moving between the solid solution and the clusters. While the importance of room temperature properties for industrial forming and ultimately the behaviour of the component in service is obvious, changing the testing temperature provides the opportunity to drastically change the energy provided for thermal activation and thus to improve the understanding of the respective role of the different obstacle types to dislocation movement during plasticity. The aim of the present work is to assess the temperature dependent (78 to 300 K) strengthening for different compositions of 6000-series Al alloys, in different ageing conditions where the cluster microstructure has been previously evaluated (see Chapters 4 to 6).

2.0 Background and Theory

It is well established that thermal fluctuations can provide energy to help gliding dislocations over-come short range obstacles such as forest dislocations, solute atoms, and clusters during plastic deformation [20]. The plastic shear strain rate, $\dot{\gamma}$, and absolute temperature, T, dependence on the reversible part of the shear flow stress, τ, for plasticity by dislocation glide can be expressed as

$$\dot{\gamma} = \dot{\gamma}_0 \exp\left(-\frac{\Delta\mathcal{F} - \tau V'}{kT}\right) \quad (1)$$

where $\dot{\gamma}_o$ is a structure dependent term, $\Delta\mathcal{F}$ is the Helmholtz enthalpy describing the dislocation-obstacle intersection, V' is the apparent activation volume describing the work done by the dislocation on the glide plane to overcome the obstacle, τ is the shear stress, and k is the Boltzmann constant. The thermal energy assists the dislocation in over-coming the barrier $\Delta\mathcal{F}$ at some applied stress, so that a more familiar Gibbs free energy description of the obstacle is

$$\Delta G = \Delta\mathcal{F} - \tau\mathrm{V}' \quad (2)$$

[20] discuss the differences of these energies in detail. The right hand side of equation (1) can be differentiated with respect to shear stress into

$$\left.\frac{\partial ln\,\dot{\gamma}}{\partial \tau}\right|_{T,\Sigma} = \left.\frac{\partial ln\,\dot{\gamma}_o}{\partial \tau}\right|_{T,\Sigma} - \left.\frac{\partial \Delta \mathcal{F}}{kT\partial \tau}\right|_{T,\Sigma} + \left.\frac{\mathrm{V}'}{kT}\right|_{T,\Sigma} \tag{3}$$

The first and second term become zero when the structure, Σ, is constant during a stress change. This idealization immediately leads to the important relationship

$$\left.\frac{\partial ln\dot{\gamma}}{\partial \tau}\right|_{T,\Sigma} = \left.\frac{\mathrm{V}'}{kT}\right|_{T,\Sigma} \tag{4}$$

which relates on the left side an experimental measurement to a structural parameter on the right side, V', indicating the nature of the rate-controlling process. Re-expressing (4) in terms of macroscopic stress and strain rate of a polycrystal corrected by the Taylor factor, M, as

$$\frac{k}{\mathrm{V}'} = \left.\frac{1}{\mathrm{MT}}\frac{\Delta\sigma}{\Delta ln\dot{\varepsilon}}\right|_{T,\Sigma} \tag{5}$$

yields a relationship to determine V' if the change in stress with change in strain rate is made at constant structure – that is instantaneous. A robust experimental technique to make such measurements using strain rate change tests has been fully documented [21]. The apparent activation volume, V', can be related to geometrical features of the dislocations' interaction with the lattice obstacles as

$$\mathrm{V}' = \mathrm{b}a' = \mathrm{b}d'l \tag{6}$$

where b is the Burgers vector of the dislocation, a' is the apparent activation area, d' is the apparent activation distance of the obstacle, and l is the inter-obstacle spacing. The true activation volume (area x distance) is difficult to determine absolutely due to the unknown effect of stress on the barrier energy, and instead relative apparent values are reported, corresponding to the experimental measurements.

In single obstacle systems like pure metal crystals, the yield stress, σ_o, is controlled by the initial dislocation density; plastic deformation results in an evolution of dislocation density that induces a decrease of V' with increasing strain via a decrease in the inter-obstacle spacing. In alloys, the identification and accounting of different obstacles' contributions, i.e. forest dislocation, solute atoms, solute clusters, etc. to impeding dislocations and therefore strengthening assumes a model for n types of obstacles

$$\sigma_o{}^p = \sigma_1{}^p + \sigma_2{}^p + \ldots \sigma_n{}^p \tag{7}$$

where p is an exponent that in the simplest linear case is 1. One effective way to test the additivity relationship is using the Haasen plot. Assuming linear additivity, equation (7) becomes

$$\left(\frac{1}{V'}\right)^p = \left(\frac{1}{V_1'}\right)^p + \left(\frac{1}{V_2'}\right)^p + \ldots \left(\frac{1}{V_n'}\right)^p \tag{8}$$

For illustrative and analytical reasons this behaviour is best represented in a form that plots equation (5) versus the increase of stress after yield, $\sigma - \sigma_0$. Figure 7-1 shows a schematic so-called Haasen plot with idealized behaviours expected for different materials microstructures. With the pure metal being the prototype behaviour with only the first term on the right side of equation (8), alloying to increase the solid solution will increase the thermal response relative to dislocations only by adding the second term to the right side of equation (8), while clustering and

later precipitation of new phases will remove the obstacles from the thermally activable spectrum, i.e. more athermal relative to the dislocations. With strain the dislocation forest density increases and with no changes in the density of the other obstacles, yields a constant slope, S. Thus, an effective experimental approach to characterize alloys with more than one obstacle is to measure the strain rate sensitivity of the flow stress during plasticity, where the initial values at yield describe the starting structure having a strain rate sensitivity, S_1, with the constant strain rate sensitivity, S, being determined at higher strain-hardened states. In the current analysis the grain size, crystallographic texture and initial forest dislocation density is assumed to be very similar for all of the alloys studied.

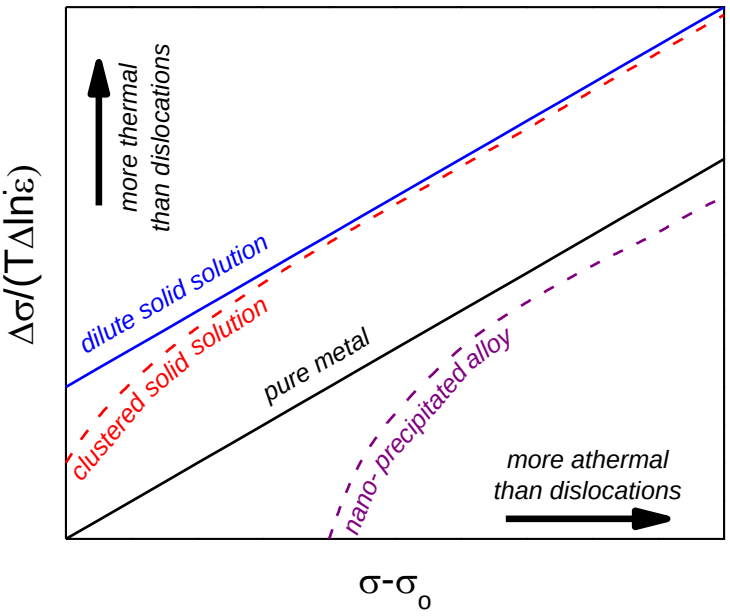

Figure 7-1: *Schematic of idealized Haasen plot at constant temperature showing the effect of relative obstacle thermal profile for a pure metal to a precipitated alloy state on the evolution of the strain rate sensitivity versus the flow stress. The slope of the curve represents the thermodynamic strain rate sensitivity, S, and is assumed constant here for all alloys at larger dislocation densities.*

Furthermore, it is experimentally possible to estimate the rate-controlling obstacle's glide resistance profile by reducing the testing temperature and measuring the changes in the yield stress and V'. Figure 7-2 illustrates that as temperature decreases the applied stress required to push the dislocation segment through an obstacle increases, since the complementary remaining energy comes from thermal activation and thus depends of kT; at absolute 0 K, the stress represents the mechanical threshold, $\hat{\tau}$, of the obstacle [20].

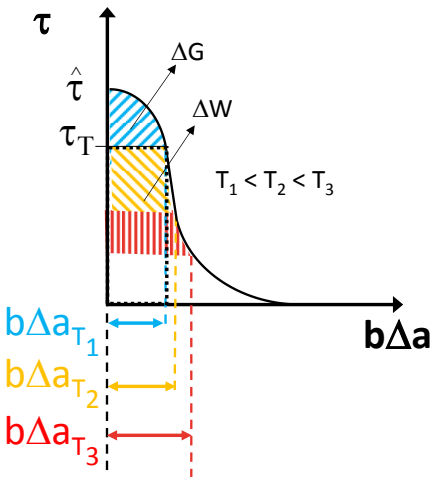

Figure 7-2: *Hypothetical sheared glide resistance profile plotting shear stress versus activation volume, and illustrating the effect of temperature T on the applied stress needed to overcome the obstacle to glide. At T_1 a stress of τ_T is required before the mobile dislocation is thermally activated. Without thermal activation the maximum glide resistance is $\hat{\tau}$.*

It is possible to calculate the initial obstacle activation size directly at yield by assuming all obstacles are point obstacles such that the activation work, Δw', to cut the obstacle is

$$d' = \frac{W'}{\alpha\mu(T)b^2} \tag{11}$$

where α is an obstacle strength parameter, $\mu(T)$ is the temperature dependent shear modulus, b is the Burgers vector and W' is equivalent to the inverse of the slope of the Haasen plot for the controlling obstacle times the Boltzmann constant, k/S [20]. Note that d' is not the size of the obstacle, but the dimension of the sheared obstacle.

If the point obstacle assumption is untrue, issues arise in separating d' and l from a'. It is possible that a low density of small obstacles (small d', large l) may yield the same a' as material comprised of a high density of larger obstacles (large d', small l). In theory, the two terms can be separated by comparing the evolution of V' with strain hardening directly after yielding via the evolving strain-rate sensitivity, S_1, compared to the initial activation volume at yield, V_o'.

Starting with a microstructure in the saturated solid solution state, the formation of clusters increases the yield strength with ageing. In the case of small clusters, it is not fully understood whether the strengthening is due to the cluster number density, i.e. average separation, or the specific cluster size. By comparing the clustered state to the saturated solid solution, the yield strength scaling can be tested with $d'l_0$, those determined solely from the Haasen plot intercept, or via the apparent activation distance determined from the initial Haasen slope, S_1. It is then possible to determine the scaling of σ_o with $d_1 l_0$. Although the two values for the activation distance, d' and d_1 should be identical, the advantage of d_1 is in that it is an average evolution, rather than a single point derived from V', such that it may be a better representation of the rate-controlling obstacles. If these mechanical tests are able to determine the relative change in apparent cluster size formed during the various heat treatments via a correlation of the apparent activation distance, it may be able to reduce the costly and experimentally difficult methods of cluster characterization by small angle x-ray scattering (SAXS), small angle neutron scattering (SANS), or atom probe tomography (APT). These other methods undoubtedly are necessary for detailed analyses of clusters but for a general understanding and engineering approach to clustering, the ability to perform strain rate sensitivity measurements would allow for a much more statistical and cost-effective means for microstructure characterization by industry.

The objective of the present work is to experimentally compare the thermally activated behaviour of dislocation motion in a series of clustering Al-Mg-Si-Cu alloys using the rate theory and the

Haasen plot analysis, and determine the effect of alloying on the cluster formation and strengthening. The chapter first examines the temperature dependence of the yield stress, and then the Haasen plot behaviours of the aged conditions, and contrasts them with the as-quenched saturated solid solution.

3.0 Methods and Materials

Tensile testing was performed on nine (9) Al-Mg-Si-Cu alloys (see Table 7-1) at 78, 198, and 294 K by immersing in environments of liquid nitrogen, alcohol and dry-ice mixture or ambient room temperature. All of the alloys are Si-rich, having a (Mg + Cu)/Si ratio smaller than one; their compositions are plotted in Figure 7-3 compared to two common industrial alloys, AA6016 and AA6022. The alloys contain four levels of Cu denoted C0 (no Cu), C2 (0.09 at%), C5 (0.2 at%) and C8 (0.3 at%), three levels of Si denoted S0 (0.9 at%), S1 (1.1 at%) and S3 (1.3 at%), and two levels of Mg (0.4 and 0.6 at%).

Sample Name	Si (at%)	Cu (at%)	Mg (at%)
C0S0	0.895	0.008	0.404
C2S0	0.896	0.089	0.381
C8S0	0.879	0.333	0.379
C8S0M	0.899	0.337	0.557
C2S1	1.069	0.087	0.372
C0S3	1.299	0.004	0.387
C2S3	1.262	0.088	0.400
C5S3	1.284	0.218	0.372
C8S3	1.324	0.329	0.385

Table 7-1: The nominal concentrations of each of the alloy contents for the nine alloys tested in this work.

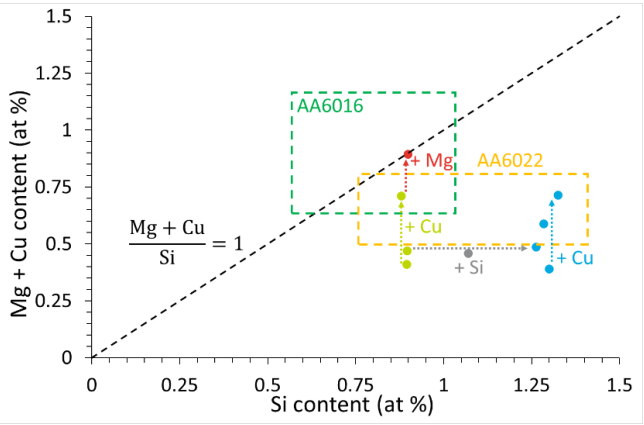

Figure 7-3: A plot of the Cu and Mg contents compared to the Si content of the nine Al-Mg-Si-Cu alloys tested in this work. The black dashed line indicates a 1:1 (Mg + Cu) to Si ratio. The green and blue dotted arrows indicate the additions of Cu at constant Si, the red dotted arrow indicates the addition of Mg at constant Cu and Si, while the grey arrow indicates the addition of Si at constant Cu and Mg. Two common alloys; AA6016 and AA6022 are shown for comparison.

Tensile specimens were machined from the as-received rolled alloy sheets into standard dog-bone specimen having a gauge length of 25 mm, and a nominal cross-section of 10 mm^2. The tensile specimens were batch solutionized at 550 °C for 15 minutes in an air furnace and then either: water quenched (WQ) and let to naturally age (NA) for one month to obtain the NA1m condition; or quenched into 80°C water, transferred to an oil bath and pre-aged (PA) at 80 °C for 8 hours, cooled and let to NA for either 1 week or 1 month to obtain the sNA1w and sNA1m conditions, respectively. Specimens were tested at a true strain-rate of 5 x 10^{-4} s^{-1} either continuously or with interrupted precise strain-rate change tests using a strain-rate change factor of ¼ or 1/10. Sub-size tensile specimen having a gauge length of 20 mm and a cross section of 2 mm^2 were spark cut from the larger tensile specimens and used for testing at 198 K using a specially designed cryostat [22]. Finally, 78 K tests were also made on each alloy in the as-quenched (AQ) condition, samples with minimal natural ageing (< 15 minutes) in order to characterize the saturated solid solution. The 0.2% offset yield stress, $\sigma_{0.2\%}$, is used as the yield stress in all analysis rather than σ_0 as previously outlined.

4.0 Results and Discussion

4.1 Yield strength dependence on temperature

The effect of temperature on the yield strength for different alloys in different aged conditions is reported in this section. Thermal activation is evident when the yield stress decreases with testing temperature. Since the elastic constants are also temperature dependent, this component of the strengthening is removed from the yield strength measurement by normalizing by the temperature dependent elastic shear modulus, μ, using the data from 99.93 at.% Al single crystals measured by Sutton [23] and fitting a polynomial to the temperature dependence (see Appendix 2). Figures 7-4a-d illustrate the temperature effect in the NA1m and sNA1m conditions for each of the groups of compositional effects.

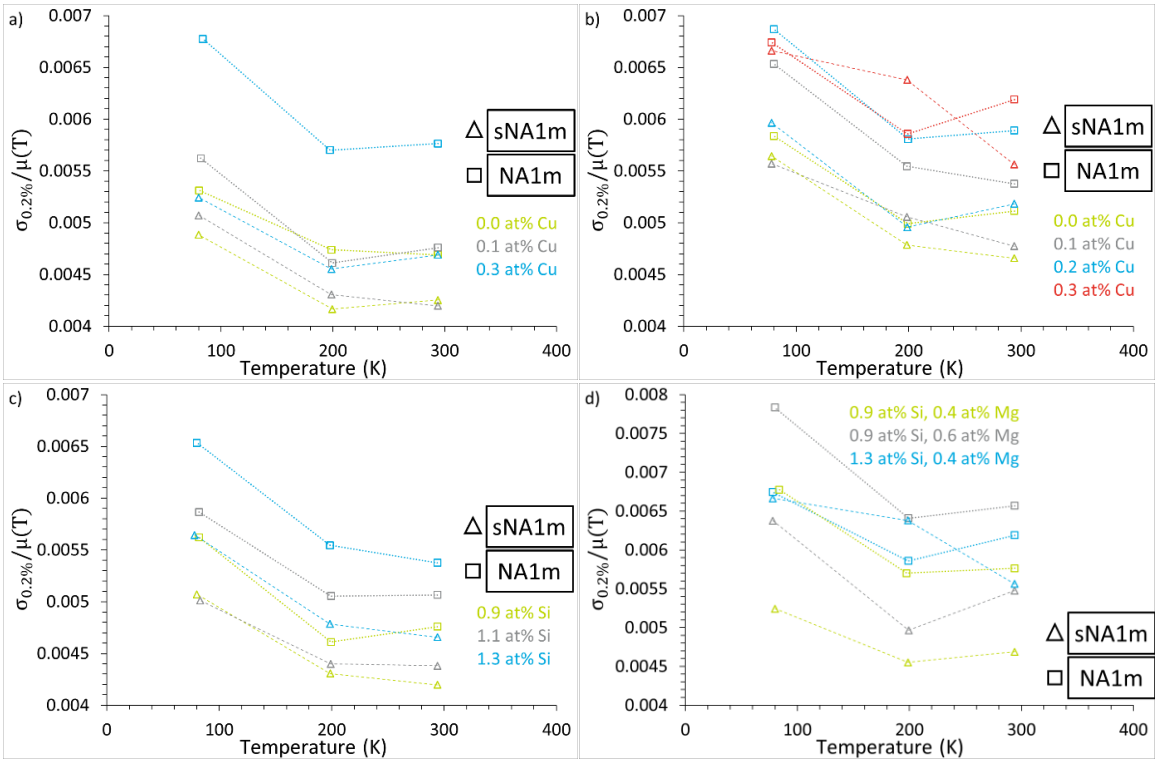

Figure 7-4: *Yield strength normalized by temperature dependent shear modulus versus test temperature in sNA1m and NA1m conditions highlighting the effects of* ***a)*** *Cu additions at 0.9 at% Si and 0.4 at% Mg,* ***b)*** *Cu additions at 1.3 at% Si and 0.4 at% Mg,* ***c)*** *Si additions at 0.1 at% Cu and 0.4 at% Mg, and* ***d)*** *Mg additions at 0.9 at% Si and 0.3 at% Cu and Si additions at 0.3 at% Cu and 0.4 at% Mg.*

The additions of solute atoms to the base chemistry always increases $\sigma_{0.2\%}/\mu(T)$ of the alloys with the strength sensitivity to solute additions being stronger in the NA1m condition compared to the sNA1m condition. Separately, at 1.3 at% Si, the additions of Cu appear to have a lower strengthening effect at lower temperatures compared to the room temperature strength in the NA1m condition, while this effect does not appear in the sNA1m condition. This behavior strongly suggests that the cluster types and obstacle profiles that are produced in the two conditions may be different. Figure 7-4 also shows that some of the normalized yield measurements at 294 K are higher than the values at 198 K. The observed increase of $\sigma_{0.2\%}/\mu(T)$ at higher temperatures compared to 198 K is likely associated with greater free solute mobility provoking dynamic strain ageing effects. Focusing on the 78 K data, the inter-obstacle spacing, l_o, characterizing the

clustering of the same objects can be estimated assuming an array of point obstacles compared to the AQ condition by the increase in the yield strength

$$l_o = \frac{M\alpha\mu b}{\sigma_{0.2\%Aged} - \sigma_{0.2\%AQ}} \quad (12)$$

Figure 7-5 shows that the inter-obstacle spacing calculated from 78 K test for the three heat treatment conditions evolves with total solute content. NA1m has the highest yield strength that corresponds to the smallest inter-obstacle spacing of the three heat treatment conditions, followed by sNA1m, and sNA1w. At 1.3 at% Si, the differences in the different heat treatment conditions decreases to the point where all samples register identical apparent inter-obstacle spacing at 0.3 at% Cu. The addition of Cu and Mg have the strongest effects on decreasing the inter-obstacle spacing parameter.

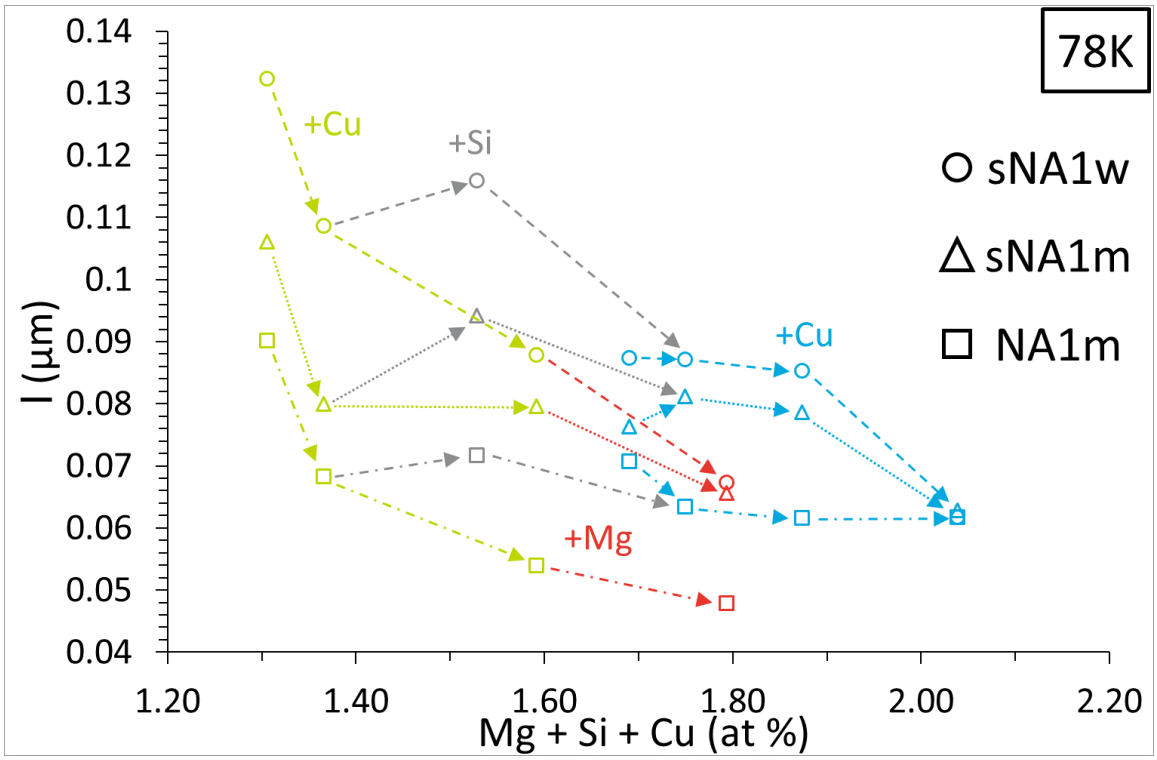

Figure 7-5: *Calculated Inter-obstacle spacing at yield determined from samples tested at 78 K in the sNA1w (open circles) sNA1m (open triangles) and NA1m (open squares) conditions. For clarity, the effects of Cu additions at 0.9 and 1.3 at% Si, are connected in green and blue dashed arrows, respectively. The effects of Si additions at 0.2 at% Cu and 0.4 at% Mg are connected with the grey dashed arrows. The effects of Mg addition at 0.9 at% Si and 0.3 at% Cu are connected with red dashed arrows.*

4.2 Haasen plot representation

Haasen plots, $\frac{1}{T}\frac{\Delta\sigma}{\Delta \ln \dot{\epsilon}}\Big|_{\Sigma,T}$ versus $\sigma - \sigma_{0.2\%}$, are shown in Figures 7-6 to 7-8 for the base alloy C0S0 with addition of Cu only (C2S0, C8S0) for sNA1w, sNA1m, and NA1m. All remaining Haasen plots are compiled in Appendix 1.4.1. Generally, the deformation of these alloys has a thermodynamic response characterized by positive intercepts and positive slopes indicating obstacles to dislocation motion more thermal than dislocations and with positive strain rate sensitivity, respectively. Note that ¼ and 1/10 rate change results are not separately identified in the plots, but a spread between the two measurements develops with deformation where the $\Delta\sigma$ with 1/10 rate change becomes larger than the ¼ rate change $\Delta\sigma$ particularly at higher temperatures. Only

the ¼ rate change data was used for the initial slope fits to determine S_1 and the intercept values as indicated numerically in each plot, because the ¼ rate changes introduced the smallest perturbation in the measurement of the obstacle profile. Three behaviours were observed in the evolution of the instantaneous slope, S, of the curve: high-to-low-to-high; constant-to-high; and low-to-high. All parameters extracted from the Haasen plots for the aged alloys is tabulated in Appendix 1.4.2.

The 78 K AQ data (SSS) is plotted as reference for all tests. In two low Si alloys, C0S0 and C8S0, the SSS curve is similar to the clustered alloy curves except for an offset in the vertical axis due to the increased yield strength. This upward shift in the curve is on first approximation a linear contribution that is directly attributed to the clustered objects being more thermally activable than dislocation-dislocation interactions (see the Figure 7-1 schematic).

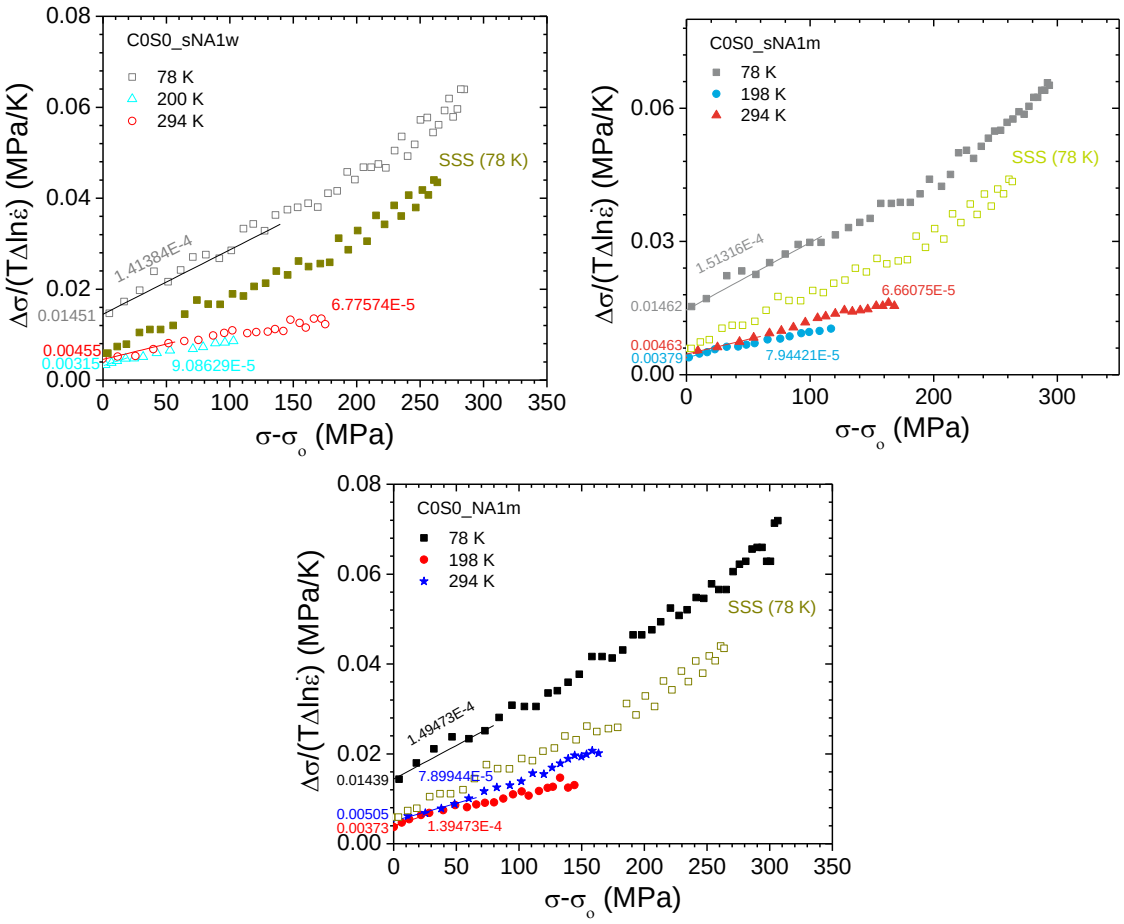

Figure 7-6: *C0S0 Haasen plots for the three ageing conditions and testing temperatures.*

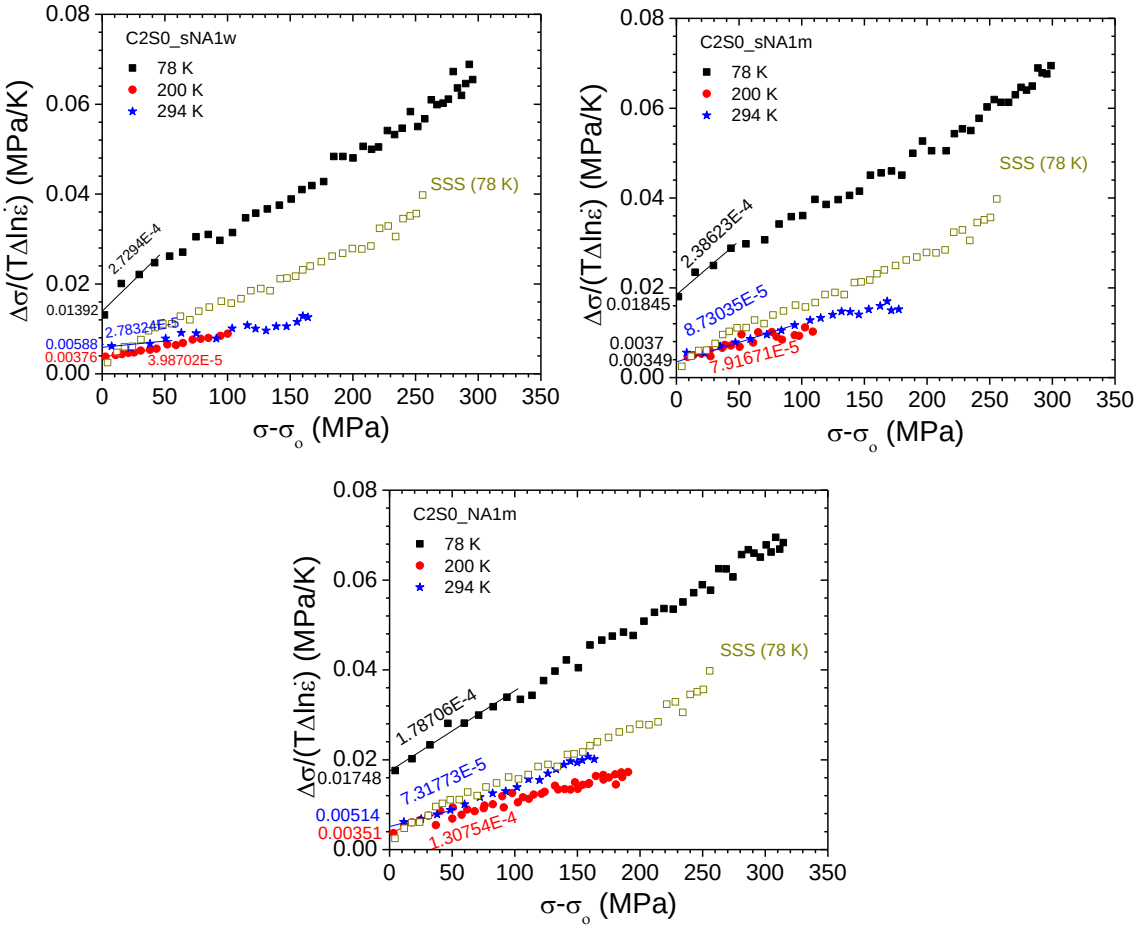

Figure 7-7: *C2S0 Haasen plots for the three ageing conditions and testing temperatures.*

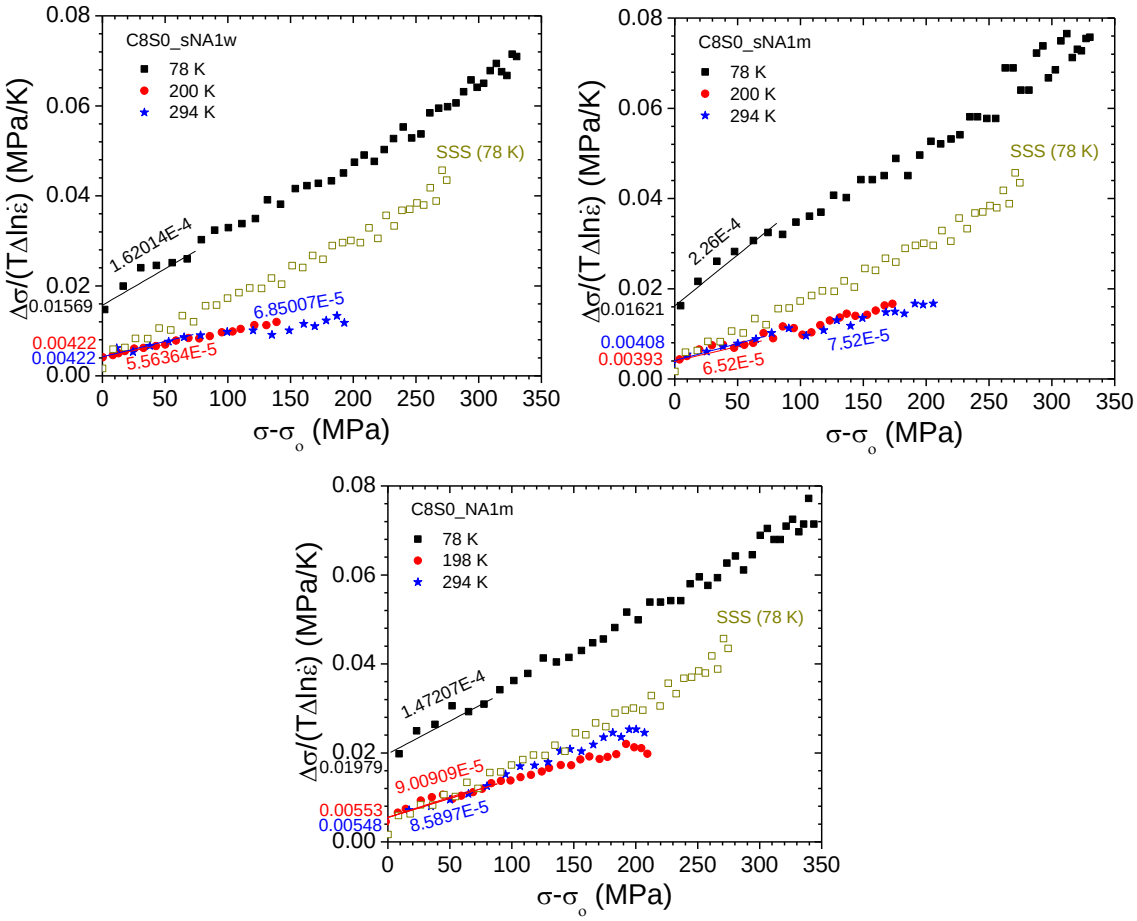

Figure 7-8: *C8S0 Haasen plots for the three ageing conditions and testing temperatures.*

The activation area at yield can be estimated by using the Haasen slope S_1 from initial hardening with the yield stress (not the intercept) to determine an activation area, $d_1 l$. Figure 7-9 plots the composite yield stress versus apparent activation area for the objects other than dislocations at the three test temperatures illustrating the role of chemistry and ageing treatment a) NA1m, b) sNA1m, and c) sNA1w on the strengthening. These composite plots resemble the schematic in Figure 7-2 albeit with the scatter due the different alloys and changes in the obstacle energy profiles with temperature and stress.

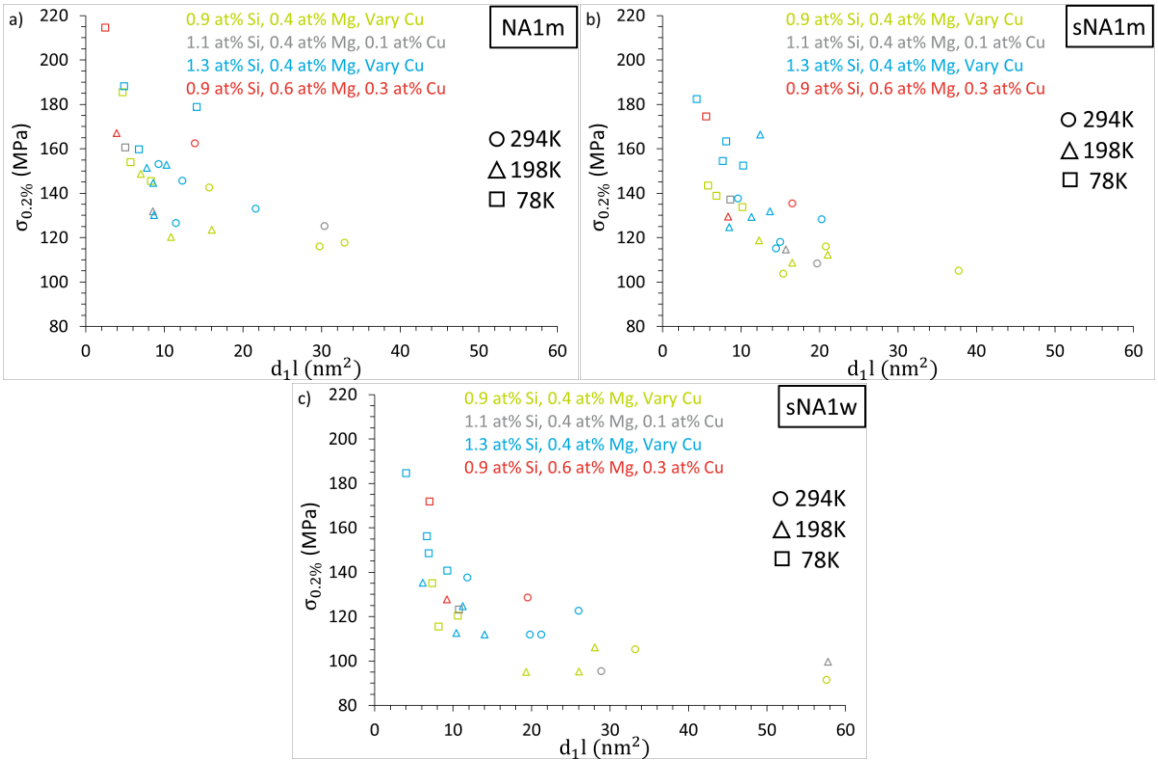

Figure 7-9: *Composite plots showing the evolution of the yield strength with derived apparent activation area determined from the initial Haasen plot slope at 78 K (open squares), 198 K (open triangles), and 294 K (open circles) for the **a)** NA1m, **b)** sNA1m, **c)** sNA1w conditions.*

4.3 T4 clusters compared to saturated solid solution state at 78 K

The most important characteristic from the above results is that many (though not all) of the NA clustered solid solutions have a thermally activated response very similar to the supersaturated solid solutions measured at 78 K after dissolving the clusters, but lower yield strength. This observation suggests that the transition from AQ to cluster hardening is a simple linear relationship with flow stress. Specific chemistries (i.e. C2S1) show a more athermal (higher initial Haasen plot slope) than the solid solution at 78 K, while other alloys like C8S0M in the sNA1w more closely resemble the SSS, except with stronger obstacles. This section investigates whether the clustered NA state resembles a solid solution or a precipitate obstacle to the dislocations' thermal activation process.

Figure 7-10 plots the normalized apparent activation volume at yield, V'/b^3, from the Haasen plot intercept for a) NA1m and b) sNA1m compared to the AQ. It is evident that the strain rate sensitivity response at yield is more sensitive to the chemistries in the AQ condition than NA, though the exact correlation with Mg, Si, and Cu in the solid solution is unclear with this analysis.

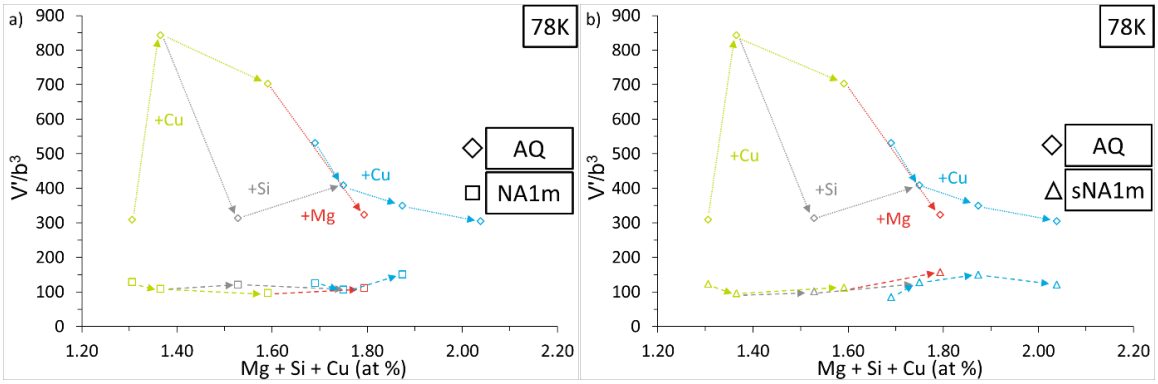

Figure 7-10: *The evolution of the apparent activation volume normalized by Burgers vector for aluminium at yield using the intercepts of the Haasen plot at 78 K for the **a)** NA1m (open squares) compared to the SSS (AQ, open diamonds) and **b)** sNA1m (open triangles) compared to the AQ conditions. For clarity, the effects of Cu additions at 0.9 and 1.3 at% Si, are connected in green and blue dashed arrows, respectively. The effects of Si additions at 0.2 at% Cu and 0.4 at% Mg are connected with the grey dashed arrows. The effects of Mg addition at 0.9 at% Si and 0.3 at% Cu are connected with red dashed arrows.*

The Haasen plot intercept, which is proportional to inverse activation volume of rate controlling obstacles at yield, is further deconstructed into the apparent obstacle size, d', using the yield strength to estimate the inter-obstacle spacing, l, and this is plotted in Figure 7-11 for all three ageing conditions at 78 K. Generally, both alloying and ageing results in an apparent increase in the obstacle size, with Cu and Mg yielding the largest increases, and Si either being neutral to effectively reducing the apparent obstacle size.

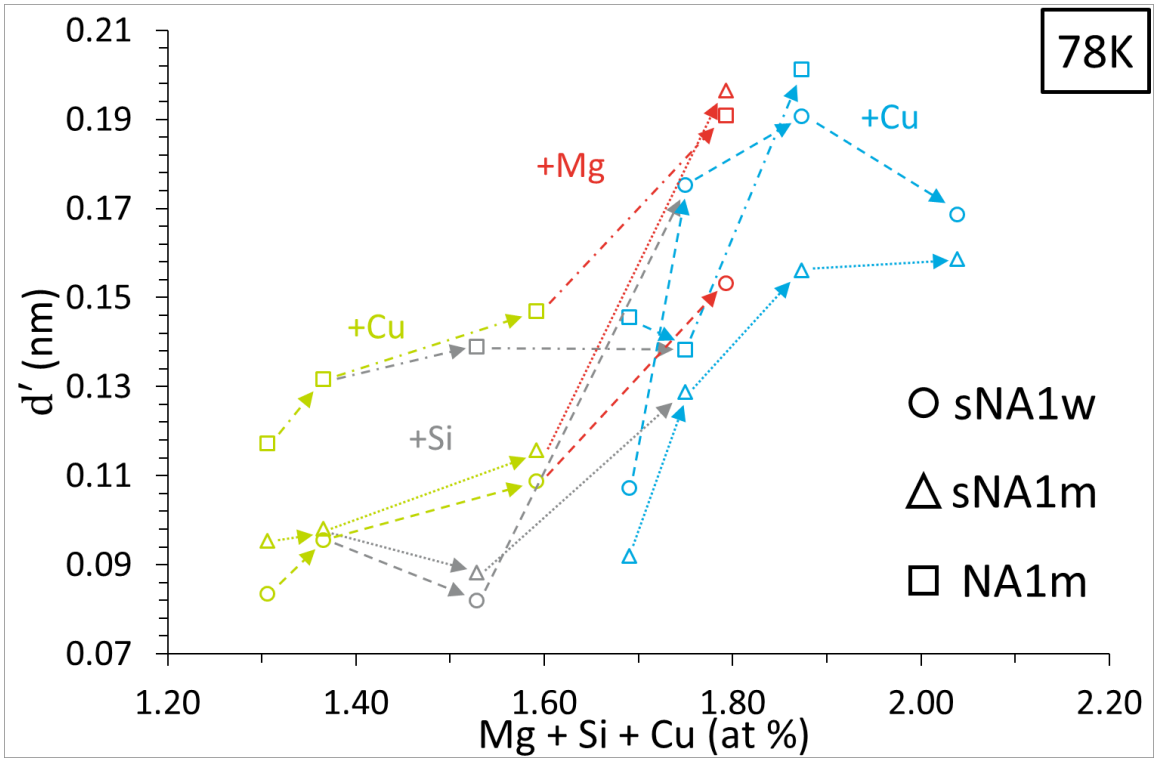

Figure 7-11: *Effect of composition for the sNA1w (open circles), sNA1m (open triangles) and NA1m (open squares) conditions on the activation distance determined from the intercept of the Haasen plot measured at 78 K. For clarity, the effects of Cu additions at 0.9 and 1.3 at% Si, are connected in green and blue dashed arrows, respectively. The effects of Si additions at 0.2 at% Cu and 0.4 at% Mg are connected with the grey dashed arrows. The effects of Mg addition at 0.9 at% Si and 0.3 at% Cu are connected with red dashed arrows.*

The Haasen plot intercept at yield correlates to the square root of the obstacle density. Figure 7-12 plots the Haasen intercept versus square root of the total alloy concentration at 78 K measured for all nine aluminum alloys in the SSS state. A linear fit of C0S3, C2S3, C5S3 and C8S3 data is shown.

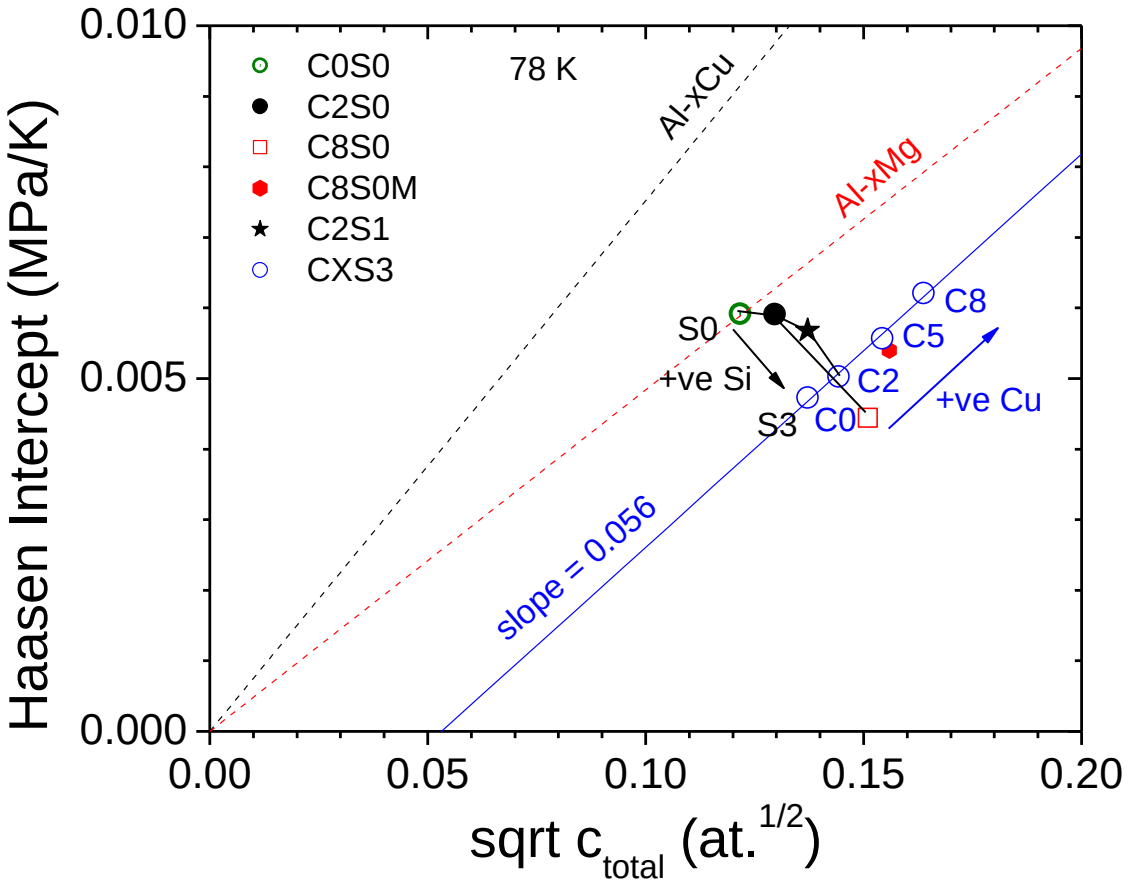

Figure 7-12: *Haasen plot intercept versus square root of the total alloy concentration at 78 K measured for all nine aluminum alloys in the SSS state. A linear fit of C0S3, C2S3, C5S3 and C8S3 data is shown. Also shown are trend lines (dashed) representing data measured previously for Al-xMg and Al-xCu binary alloys.*

For dilute binary solid solutions, the increase in Haasen intercept was shown previously by Diak and Saimoto [24] to scale with $c^{1/2}$ with different slopes for different alloying elements; trend-lines for Al-xCu and Al-xMg are shown in Figure 7-13 for comparison.

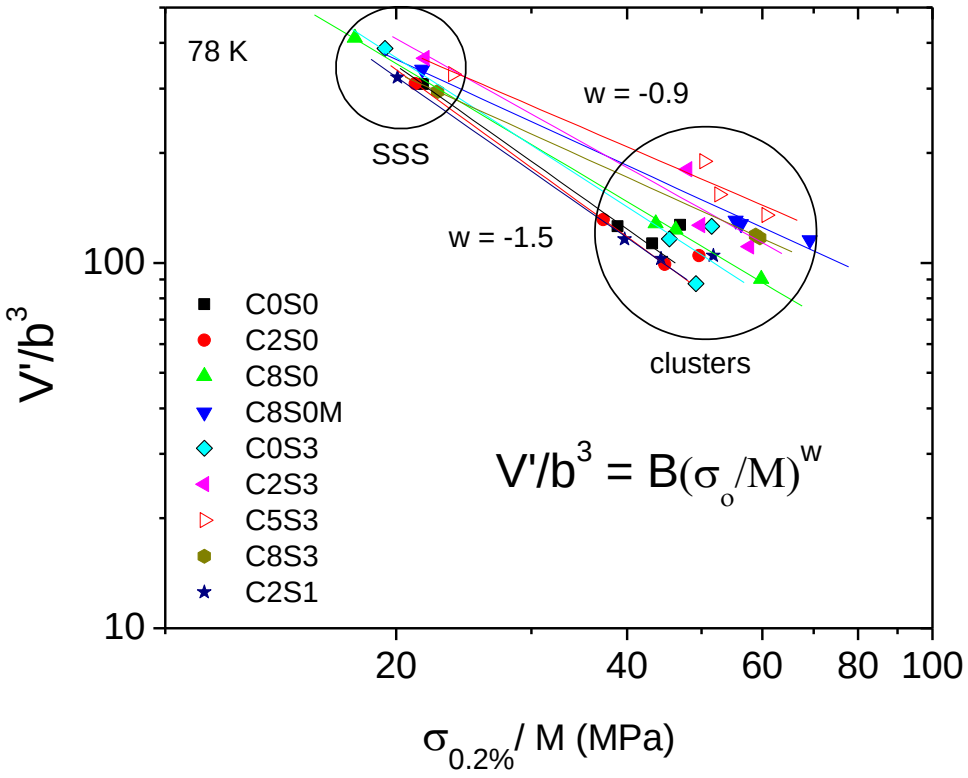

Figure 7-13: *Apparent activation volume normalized with the Burgers vector cubed versus the measured shear yield stress, $\sigma_{0.2\%}$/M, of all alloys in the SSS and aged states measured at 78 K. The straight line fits are made from the SSS alloy to its aged states with a power law exponent, w, ranging from -0.9 to -1.5. This range is between the Labusch (-2/3) and Friedel (-2) limits for a solid solution. The circled regions are drawn arbitrarily to separate the AQ (SSS) and the aged conditions.*

The current AA6xxx alloy systems are pseudo-ternary, where the collective solute effect for the Cu-Mg-Si is to offset the points as shown. The Si additions lower the intercept from the binary Al-xCu, while Cu and Mg in the AA6xxx alloys increases the intercept values. The data is consistent with alloying concentration, and the fact the data do not collapse on a single line for all alloys indicates a complex relationship between solute chemistry, clustering and dislocation-obstacle interactions.

A test of the solid solution strengthening mechanism is whether an alloy exhibits stress equivalence of the activation volume with respect to the shear yield stress when the testing temperature is changed:

$$\frac{V'}{b^3} = B\left(\frac{\sigma_o}{M}\right)^w \tag{13}$$

where B and w are experimental constants. Stress equivalence has previously only been reported for solid solutions with interpretations of possible clustering. The present alloys studied contain clusters in the NA state and Figure 7-13 clearly shows stress equivalence for individual alloys after different heat treatments, which indicates that these clusters are an evolving solid solution; the mobile dislocations do not see these objects as defined precipitates. The range of w from -1.5 to -0.9 is consistent with what Diak and Saimoto [24]measured in dilute aluminium binary solid solutions, but conflicts with observations by Niewczas et al. [25]for Al-xMg solid solutions in which w = -2/3.

What is clear is that addition of Cu to the highest Si containing alloy CXS3 increases the slope, which signifies a higher activation volume, or larger density of clusters. The lowest Si containing alloys tend to have the steepest negative slope, which is a sign of reduced clustering. The constant yet different slopes represents distinct pathways for the evolution of these solid solutions into clusters.

4.4 Dislocation-dislocation interactions in the alloys at larger strains

After about 50 MPa of strain hardening beyond the yield stress, the Haasen plots in Figures 7-6 to 7-8 (and Appendix 1.4.2) are characterized by a straight-line behaviour consistent with the Cottrell-Stokes relationship [26]. Unlike pure aluminium and its dilute alloys, this value of S differs from the dislocation-dislocation contribution, S_d, tending to be larger at temperatures above 150 K as summarized in Figure 7-14. At 78 K, the AQ data is lowest relative to the dislocation-dislocation line, but has the least variation in values for the different alloys. Ageing treatments tie up free matrix solute in the clustered objects, and so the Haasen slope tends to approach the pure metal value at 78 K. At 198 K, all the measured values exceed the pure metal value, but there is less variation in S due to the higher temperature normalization. At 294 K, the deformation mechanism is much more complex than below 198 K due to diffusion controlled solute-vacancy mobility and dynamic recovery of dislocations and point defects.

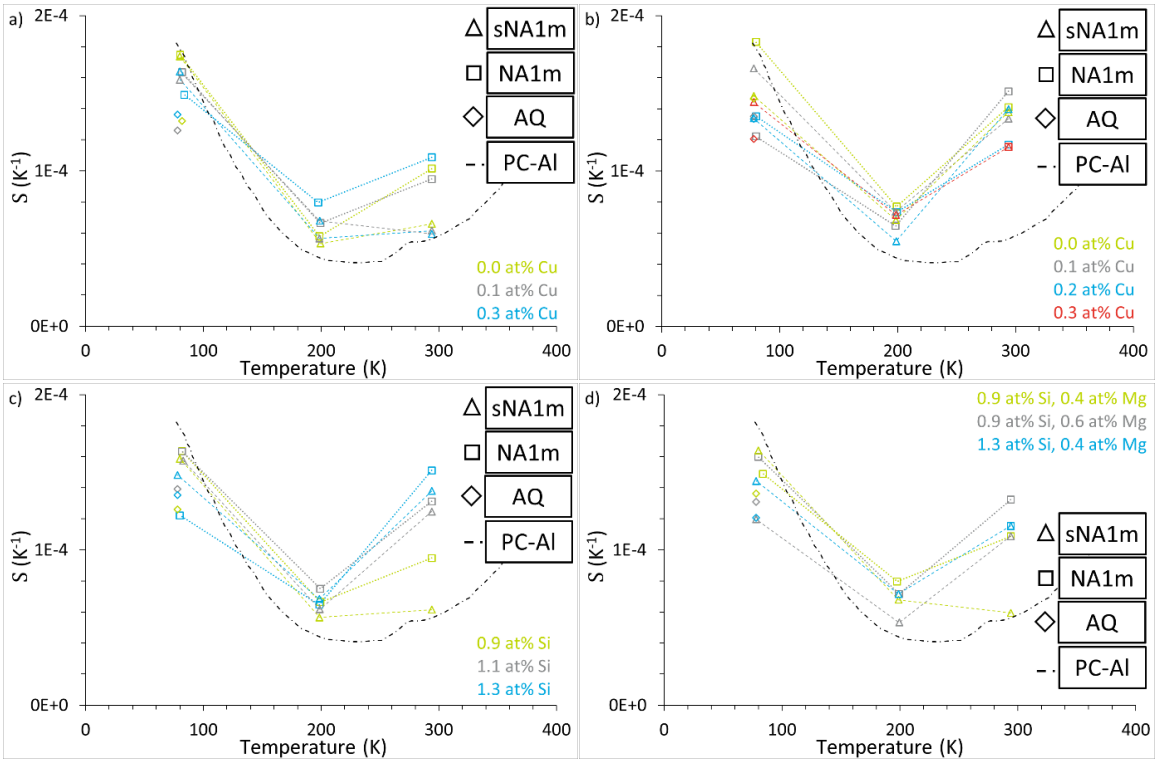

Figure 7-14: *The evolution of the large strain, dislocation-dislocation thermodynamic strain rate sensitivity, S, with absolute temperature for the sNA1M (open triangle), NA1m (open square) and SSS (AQ, open diamond) conditions as compared to pure polycrystalline aluminium (PC-Al, dash-dotted line) showing the effects of* ***a)*** *Cu additions at 0.9 at% Si and 0.4 at% Mg,* ***b)*** *Cu additions at 1.3 at% Si and 0.4 at% Mg,* ***c)*** *Si additions at 0.1 at% Cu and 0.4 at% Mg, and* ***d)*** *Mg additions at 0.9 at% Si and 0.3 at% Cu and Si additions at 0.3 at% Cu and 0.4 at% Mg.*

The correlation of S at large strains to composition at 78 K is summarized in Figure 7-15. Generally, alloying the SSS (AQ) leads to little change in S with chemistry, due to the similarities in strain hardening. In contrast, after one month ageing, there is a correlation with alloying to reduce S

towards the solid solution behaviour. There is expected to be a difference in the strain hardened dislocation sub-structure with this alloying and thus a different S.

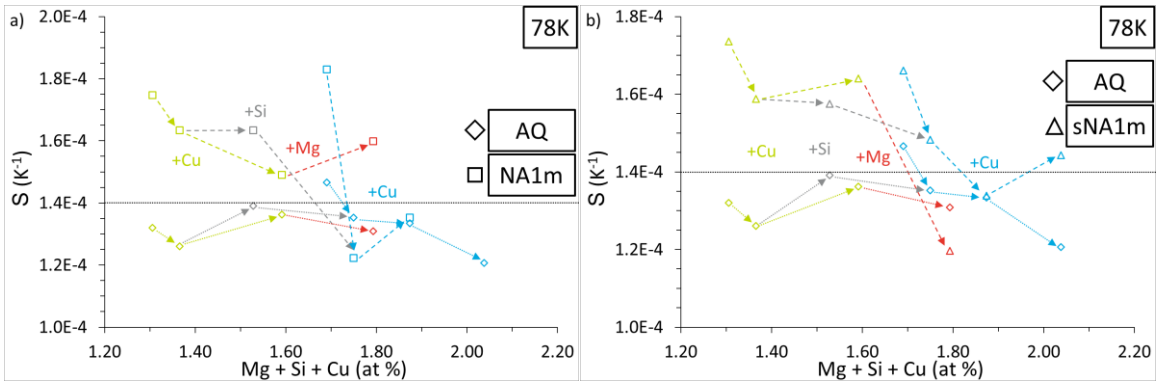

Figure 7-15: *Effects of alloy chemistry on the large-strain strain-rate sensitivity at 78K compared to the SSS (AQ, shown as open diamonds) for the* ***a)*** *NA1m and* ***b)*** *sNA1m conditions. For clarity, the effects of Cu additions at 0.9 and 1.3 at% Si, are connected in green and blue dashed arrows, respectively. The effects of Si additions at 0.2 at% Cu and 0.4 at% Mg are connected with the grey dashed arrows. The effects of Mg addition at 0.9 at% Si and 0.3 at% Cu are connected with red dashed arrows. Dotted arrows used for the reference, SSS (AQ) tests. The horizontal line at S equals 1.4x10^{-4} K^{-1} is for pure polycrystalline aluminum.*

5.0 Conclusions

A thorough study was made on the thermally activated deformation behaviour of nine experimental Al-Mg-Si-Cu alloys. The main purpose of this work is to understand the nature of the clusters formed during direct NA (NA1m) and secondary NA occurring after PA processes (sNA1w and sNA1m) to determine if any significant differences exist and the effects of alloy composition on these obstacles. The precise strain rate sensitivity was measured for nine alloys after T4 ageing by specialized tensile testing at 78, 198 and 294 K. The key results are:

- The yield stress of these alloys decreases with temperature up to 198 K and becomes athermal at 294 K due to increased solute atom mobility.
- Secondary natural ageing from one week to one month increases the yield strengths of all alloys with the highest strengthening measured in the Mg containing alloys.
- The measured Haasen plot ordinate values and slopes are all positive, indicating that all nine alloys in the T4 condition have a positive strain rate sensitivity.
- An analagous force-distance profile for different microstructural states was estimated from the yield stresses and Haasen plot activation area measured at different temperatures. The profiles correlate with expected changes in the clustered state with ageing.
- The strain rate sensitivity of the as-quenched alloys were measured at 78 K.
    - The square root of the alloying compositions correlate to the apparent inverse activation volume.
    - Cu and Mg additions decrease the activation volume
    - Si additions increase the activation volume.
- At 78 K stress equivalence was observed between the measured apparent activation volume and the approximate shear stress as $\frac{V'}{b^3} = B\left(\frac{\sigma_o}{M}\right)^w$, where w = -1.5 to -0.9. The clustered T4 state therefore resembles more a solid solution to the mobile dislocations than a precipitated state.
- At larger strains the evolution of the dislocation density exceeds the clustered object density and the constant slope follows the expected Cottrell-Stokes relationship albeit

with slopes different than pure aluminum due to the dynamic nature of the different dislocation structures that evolve with deformation.

6.0 References

[1] C. S. T. Chang, Z. Liang, E. Schmidt, and J. Banhart, “Influence of Mg/Si ratio on the clustering kinetics in Al–Mg–Si alloys,” *Int. J. Mater. Res.*, vol. 103, no. 8, pp. 955–961, 2012.

[2] F. De Geuser, W. Lefebvre, and D. Blavette, “3D atom probe study of solute atoms clustering during natural ageing and pre-ageing of an Al-Mg-Si alloy,” *Philos. Mag. Lett.*, vol. 86, no. 4, pp. 227–234, Apr. 2006.

[3] M. Liu, J. Čížek, C. S. T. Chang, and J. Banhart, “Early stages of solute clustering in an Al–Mg–Si alloy,” *Acta Mater.*, vol. 91, pp. 355–364, Jun. 2015.

[4] S. Esmaeili and D. J. Lloyd, “Effect of composition on clustering reactions in AlMgSi(Cu) alloys,” *Scr. Mater.*, vol. 50, no. 1, pp. 155–158, Jan. 2004.

[5] Z. Jia, L. Ding, L. Cao, R. Sanders, S. Li, and Q. Liu, “The Influence of Composition on the Clustering and Precipitation Behavior of Al-Mg-Si-Cu Alloys,” *Metall. Mater. Trans. A*, vol. 48, no. 1, pp. 459–473, Jan. 2017.

[6] A. Poznak, R. K. W. Marceau, and P. G. Sanders, “Composition dependent thermal stability and evolution of solute clusters in Al-Mg-Si analyzed using atom probe tomography,” *Mater. Sci. Eng. A*, vol. 721, pp. 47–60, Apr. 2018.

[7] Y. Weng, Z. Jia, L. Ding, Y. Pan, Y. Liu, and Q. Liu, “Effect of Ag and Cu additions on natural aging and precipitation hardening behavior in Al-Mg-Si alloys,” *J. Alloys Compd.*, vol. 695, pp. 2444–2452, Feb. 2017.

[8] M. W. Zandbergen, A. Cerezo, and G. D. W. Smith, “Study of precipitation in Al–Mg–Si Alloys by atom probe tomography II. Influence of Cu additions,” *Acta Mater.*, vol. 101, pp. 149–158, Dec. 2015.

[9] Y. Aruga, M. Kozuka, Y. Takaki, and T. Sato, “Effects of natural aging after pre-aging on clustering and bake-hardening behavior in an Al–Mg–Si alloy,” *Scr. Mater.*, vol. 116, pp. 82–86, Apr. 2016.

[10] Y. Aruga, M. Kozuka, Y. Takaki, and T. Sato, “Formation and reversion of clusters during natural aging and subsequent artificial aging in an Al–Mg–Si alloy,” *Mater. Sci. Eng. A*, vol. 631, pp. 86–96, Apr. 2015.

[11] V. Fallah, B. Langelier, N. Ofori-Opoku, B. Raeisinia, N. Provatas, and S. Esmaeili, “Cluster evolution mechanisms during aging in Al–Mg–Si alloys,” *Acta Mater.*, vol. 103, pp. 290–300, Jan. 2016.

[12] V. Fallah *et al.*, “Atomic-scale pathway of early-stage precipitation in Al–Mg–Si alloys,” *Acta Mater.*, vol. 82, pp. 457–467, Jan. 2015.

[13] F. A. Martinsen, F. J. H. Ehlers, M. Torsæter, and R. Holmestad, “Reversal of the negative natural aging effect in Al–Mg–Si alloys,” *Acta Mater.*, vol. 60, no. 17, pp. 6091–6101, Oct. 2012.

[14] G. H. Tao, C. H. Liu, J. H. Chen, Y. X. Lai, P. P. Ma, and L. M. Liu, “The influence of Mg/Si ratio on the negative natural aging effect in Al–Mg–Si–Cu alloys,” *Mater. Sci. Eng. A*, vol. 642, pp. 241–248, Aug. 2015.

[15] M. J. Starink, “A model for co-clusters and their strengthening in Al–Cu–Mg based alloys: a comparison with experimental data,” *Int. J. Mater. Res.*, vol. 103, no. 8, pp. 942–947, 2012.

[16] H. Zhong, “Effect of composition and processing on the microstructure and formability of aluminium automotive body sheet alloys,” PhD, Monash University, 2014.

[17] H. Zhong, P. A. Rometsch, and Y. Estrin, “The Influence of Si and Mg Content on the Microstructure, Tensile Ductility, and Stretch Formability of 6xxx Alloys,” *Metall. Mater. Trans. A*, vol. 44, no. 8, pp. 3970–3983, Aug. 2013.

[18] H. Zhong, P. Rometsch, and Y. Estrin, “Effect of alloy composition and heat treatment on mechanical performance of 6xxx aluminum alloys,” *Trans. Nonferrous Met. Soc. China*, vol. 24, no. 7, pp. 2174–2178, Jul. 2014.

[19] L. He, H. Zhang, and J. Cui, “Effects of Pre-Ageing Treatment on Subsequent Artificial Ageing Characteristics of an Al-1.01Mg-0.68Si-1.78Cu Alloy,” *J. Mater. Sci. Technol.*, vol. 26, no. 2, pp. 141–145, 2010.

[20] U. F. Kocks, A. S. Argon, and M. F. Ashby, *Thermodynamics and Kinetics of Slip*. Permagon Press, 1975.

[21] M. Carlone and S. Saimoto, “Precision strain rate sensitivity measurement using the step-ramp method,” *Exp. Mech.*, vol. 36, no. 4, pp. 360–366, 1996.

[22] Z. S. Basinski, M. Sahoo, and S. Saimoto, “Resistivity change with deformation of high purity Cu crystals and its subsequent recovery,” *Acta Metall.*, vol. 25, no. 6, pp. 657–665, Jun. 1977.

[23] P. M. Sutton, “The variation of the elastic constants of crystalline aluminum with temperature between 63 K and 773 K,” *Phys. Rev.*, vol. 91, no. 4, p. 816, 1953.

[24] B. J. Diak and S. Saimoto, “The determination of solute clusters in dilute aluminum alloys using strain rate sensitivity,” *Mater. Sci. Eng. A*, vol. 234–236, pp. 1019–1022, 1997.

[25] M. Niewczas, M. Jobba, and R. K. Mishra, “Thermally activated flow of dislocations in Al–Mg binary alloys,” *Acta Mater.*, vol. 83, pp. 372–382, Jan. 2015.

[26] R. C. Picu, G. T. Vincze, and J. J. Gracio, “Deformation and microstructure-independent Cottrell–Stokes ratio in commercial Al alloys,” *Int. J. Plast.*, vol. 27, no. 7, pp. 1045–1054, Jul. 2011.

8 An analysis of necking formation in Al-Mg-Si-Cu alloys: the effect of strain rate sensitivity

The main goal of the thesis is to provide a comprehensive understanding connecting alloy composition and processing to the corresponding microstructure formed, its influence on the resulting mechanical properties and finally, their connection to the formability of the Al-Mg-Si-Cu alloys. This paper will incorporate the observed effects of asymmetry in the strain rate sensitivity and be combined with a basic strain rate sensitivity-modified power law equation in order to initially perform a parameterized study via the adjustment of the two unique strain rate sensitivity parameters and their influence on the width of the neck formed when samples are deformed to a local strain of 30%. This distribution of strain and strain rate will serve as a basis for potentially understanding the differences between neck formation, localization, propagation, and stabilization, each of which will be given their own definition based on the observed effects. From the parameterized study, experimentally determined numbers will be input into the model in order to determine in the formation and distribution of strain found within the neck rely most heavily on the increasing, decreasing, or a combined strain rate sensitivity parameter.

An analysis of necking formation in age-hardenable aluminium alloys: the effects of strain hardening and strain-rate sensitivity

Abstract

Reducing fuel emissions in passenger vehicles has provided the need to lighter materials to be used in automotive manufacturing, specifically for body-in-white applications. The forming requirements for both exterior and interior panels is to prevent the onset of localized necking or, to extend the diffuse necking condition, which is controlled by the Considère criterion. The increased strain hardening and strain rate sensitivity (SRS) behaviours have been previously shown to correlate to enhanced ductility, however, these trends are only ever considered for the region within the diffuse neck. Recent work in SRS has shown an asymmetry in the SRS behaviour of these alloys between increasing and decreasing strain-rate jump tests which would affect the interior and exterior of the diffuse neck, respectively. The use of finite element modeling coupled with parametric studies using pairs of up-change and down-change SRS properties of 6000-series aluminium alloys will be used to model the neck evolution during tension using a constitutive relation. The distance between the nominal strain rate and the centre of the diffuse neck will be linked to both the strain hardening and SRS parameters based on the applied model. Additionally, both the strain and strain rate distributions of these parametric studies will be investigated to ascertain the specific influence of the up-change and down-change SRS and the effect of strain hardening. Finally, the constitutive properties from a real specimen in this work will be analyzed at varying levels of deformation to observe the temporal dependency on strain for both the strain and strain rate distributions along the length of the sample.

1.0 Introduction

The increased use of AA6xxx series sheet in the automotive industry has necessitated a more thorough understanding of the relationship between critical mechanical properties: strain hardening and strain-rate sensitivity (SRS), to the resulting formability. Although there are many factors that influence the mechanical properties of AA6xxx series alloys: composition, processing, and resulting microstructure, the relationship between these macroscopic properties and corresponding engineering parameters may be connected to the overall formability of the alloys. Formability is crucial in the production of body-in-white (BIW) automotive components where they are stamped in a "soft" temper and then run through a paint-bake cycle to simultaneously polymerize the paint, and harden the material. The formability of the material has a direct impact on the shapes and designs available to automotive manufacturers which directly affects the saleability, and the possibility of light-weighting through down-gauging or switching from steel to aluminium. A sheet is considered to be scrap once a local neck has formed; thus maintaining the aluminium sheet in either the uniform deformation or diffuse necked state is critical to extending its formability. Increasing the strain hardening and SRS of the alloys have been shown to increase the uniform and diffuse necked regimes of deformation, respectively. This work will use finite element modeling to assess the effect of the engineering mechanical properties of strain hardening and SRS of AA6xxx series sheets on the parameters relevant to formability: the uniform elongation, diffuse neck width and post-uniform elongation behaviour.

2.0 Background and Model Design

The onset of diffuse necking, the limit imposed by manufacturers during forming, is classically described using the Considère criterion whereby the onset of diffuse necking, ϵ_D, begins once

$$\frac{d\sigma}{d\epsilon} \leq \sigma \tag{1}$$

where $d\sigma/d\epsilon$ is the current strain hardening and σ is the current true stress. The transition to local necking, ϵ_L, may be schematically defined for a tensile test when $d\sigma/d\epsilon = \sigma/2$. If a modified Hollomon-type constitutive relation is used to calculate the stress in the form of $\sigma = \sigma_0 + K\epsilon^n\dot{\epsilon}^m$ [1]–[5] and then differentiation with respect to strain to obtain the Considère criterion given by [2], [4]

$$\frac{d\sigma}{d\epsilon} = \frac{K\epsilon^n\dot{\epsilon}^m}{\epsilon}\left(n + m\frac{\partial \ln \dot{\epsilon}}{\partial \ln \epsilon}\right) = \sigma = \sigma_0 + K\epsilon^n\dot{\epsilon}^m \tag{2}$$

Where n is the strain hardening exponent, m the engineering strain rate sensitivity, σ_0 is the proportional limit, ϵ is the current strain, $\dot{\epsilon}$ is the current strain-rate, and K, a pre-exponential constant. There is a clear dependency of $d\sigma/d\epsilon$ on both the strain hardening and strain rate sensitivity parameters whereby increasing m or n will increase $d\sigma/d\epsilon$ delaying the onset of the diffuse neck, all other parameters being held equal. One of the critical hypothesis is that the current strain rate is necessarily uniform prior to necking, yielding uniform deformation (not considering cases such as shear banding) such that the second parameter in brackets, $\frac{\partial \ln \dot{\epsilon}}{\partial \ln \epsilon}$ is zero. However, upon the formation of a diffuse neck, this strain rate sensitive term becomes non-zero and there are inevitably two separate regions, the region interior and exterior of the neck having an active deformation rate greater or less than the imposed rate, respectively. This results in the second term being either positive (in the neck interior) or negative (in the neck exterior) causing a local hardening and softening effect, respectively, assuming the strain rate sensitivity parameter is positive. Schematically, a situation such as that in Figure 8-1 is observed.

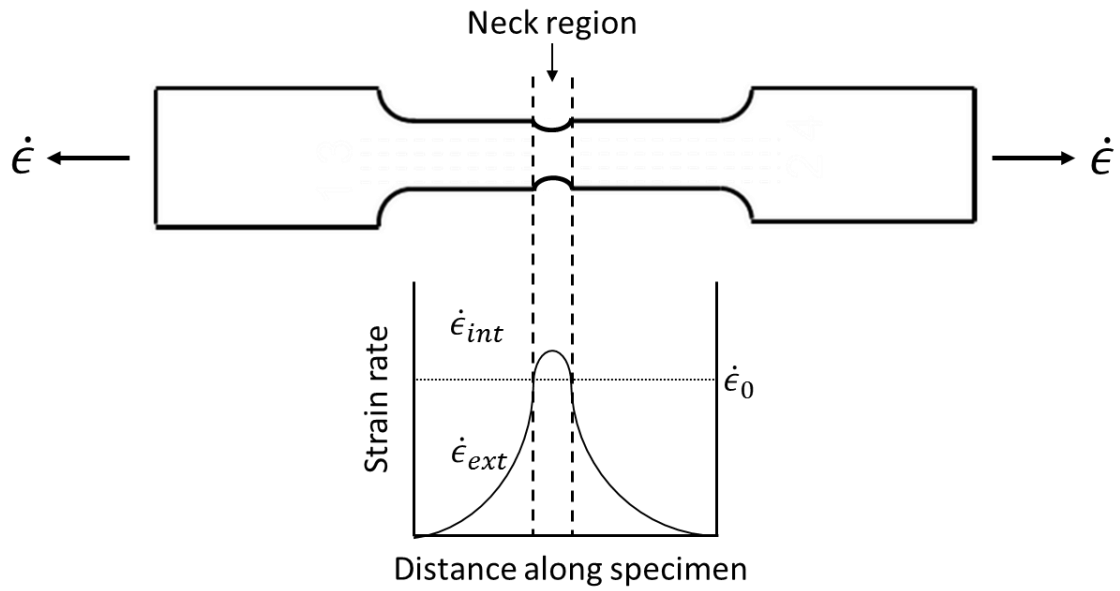

Figure 8-1: *A schematic showing the definition of the necked region of the sample. Due to requirement of strain and strain rate continuity, the strain rate within the neck interior is increased and the region exterior experiences a decrease, there must retain a region that continues to deform at the imposed experimental strain rate.*

Classical models and simulations work perfectly fine for this situation whereby the constitutive parameters are able to take into account the changes in the local strains and strain rates to adjust the local Considère condition. However, as previously shown in Chapter 5, there is an apparent asymmetry in the strain rate sensitivity being strictly dependent on the directionality of the rate-change and whether it is increasing or decreasing. This necessitates that two sets of constitutive parameters be used

$$\sigma_{uc} = \sigma_0 + K_{uc}\dot{\epsilon}^{m_{uc}}\epsilon^n \quad (3a)$$

$$\sigma_{dc} = \sigma_0 + K_{dc}\dot{\epsilon}^{m_{dc}}\epsilon^n \quad (3b)$$

Where the subscript *uc* represents *up-changes*, regions having a strain rate greater than that imposed, and *dc* representing *down-changes*, regions having a strain rate lower than that imposed. The net result of these two constitutive relations being required in their specific regimes is that the evolution of the Considère criterion is unique depending on the magnitude of the strain rate in the local regime. In the materials tested in this thesis, age-hardenable 6000-series aluminium, it was determined that the values for m_{dc} were greater than m_{uc} suggesting that the softening that is observed in materials having an equal and opposite decrease in the local strain rate is greater than the local increase in the hardening due to the increased strain rate, that is

$$|\Delta\sigma_{dc}| > |\Delta\sigma_{uc}| \quad (4)$$

This would trigger the possibility for the diffuse neck to either stabilize or propagate, in the spatial dimension along the length of the specimen, in the direction of the applied deformation. One of the matters to consider in this relationship is that σ_{uc} must equal σ_{dc} when the local strain rate is equal to the base strain rate, $\dot{\epsilon}_0$, which necessitates the proper derivation of this equation, allowing for the large-strain extrapolation of the stress-strain curve to strain unobtainable by traditional tensile testing methods. In the present work, the Saimoto – van Houtte (SvH) [1] constitutive relation (shown in Eq. 5, used see Chapter 6 for more details) will be used to capture

the true stress response with the evolution of true plastic strain using two fit loci separating the low- and high-strain regions.

$$\sigma = \sigma_0 + \left[M^{3+\beta_i}\left(\frac{P}{4A}\right)(2+\beta_i)(\alpha\mu b)^2\frac{1}{C_i b}\right]^{\frac{1}{2+\beta_i}}\epsilon^{\frac{1}{2+\beta_i}} \quad (5)$$

Where M is the Taylor factor, P/A is the ratio of the production of dislocation line-length to be compared to the annihilation of dislocations (see Chapter 6 for its derivation), α, the obstacle strength factor, μ, the shear modulus, b, the Burgers vector, with σ_0, β_i, and C_i, the fitting variables. A sample fit is shown in Figure 8-2.

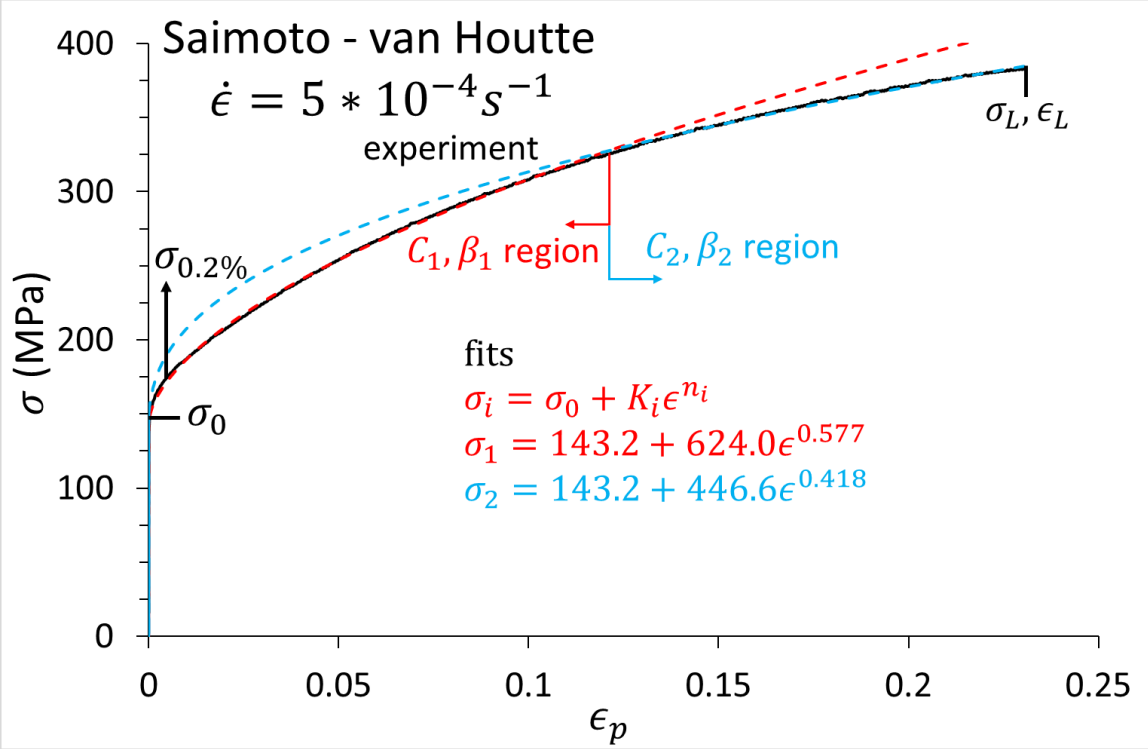

Figure 8-2: *The method used to determine the fit parameters shown on the C8S0M sample in the NA1m condition, pulled at a true strain rate of 5 x 10^{-4} s^{-1} until failure. Note the fit was taken from a 6th order polynomial fit made from the yield strength until the uniform elongation in order to eliminate any transient effects potentially caused by yield point effects. The two regions of the fit are clearly visible while they share a common σ_0. The power-law equivalent of the equations are shown but include the strain-rate sensitive pre-exponentials.*

The fitting routine has been previously explained [1], [6] and the current work uses the same fit parameters previously determined in Chapter 6. Since the fit uses two loci, it is possible to isolate the low-strain and high-strain regions of flow curve and in the case of formability, the high-strain regions are of significant interest. The SvH relation is able to be transformed into two power-law equations as

$$\sigma = \sigma_0 + K_{mi}\epsilon^{ni} \quad (6a)$$

$$K_{mi} = \left[M^{3+\beta_i}\left(\frac{P}{4A}\right)(2+\beta_i)(\alpha\mu b)^2\frac{1}{C_i b}\right]^{\frac{1}{2+\beta_i}} \quad (6b)$$

$$n_i = \frac{1}{2+\beta_i} \quad (6c)$$

n_i are the work-hardening exponents for the two strain regions, and K_{mi} are the corresponding strain-rate dependent pre-exponentials. The pre-exponential may be converted using either the

experimental strain rate and the up-change or down-change engineering strain-rate sensitivities, m_{uc} and m_{dc}, respectively, to create the strain rate independent pre-exponential given by

$$K_{uc} = K_m/\dot{\epsilon}^{m_{uc}};\ K_{dc} = K_m/\dot{\epsilon}^{m_{dc}} \quad (7)$$

Where K_{uc} and K_{dc} and the up-change and down-change pre-exponentials. It is clear that if the engineering SRS values are not the same, K_{uc} and K_{dc} must also be different which allows the determination of Eq. 3a and 3b. It is now possible to use the two different sets of Hollomon-type equations by implementing them into finite element modelling (FEM) but since the present work is concerned in the high-strain behaviour and the influence of these parameters on necking, only the large-strain, K_2/n_2 region (see Figure 8-2) will be used.

3.0 Methods and Materials

In order to aid in the understanding of the effects of strain rate sensitivity and strain hardening on the necking formation of aluminium alloys, finite element modelling was employed to simulate tensile testing to compute the strain and strain rate distributions around the formation of the neck. These simulations require input parameters that are representative of the material properties for which experiments are required. As previously described in Chapter 6, tensile and strain rate sensitivity tests were performed using standard dog-bone specimen having a gauge length of 25 mm with a 10 x 1 mm^2 cross section. Testing methods employed consisted of standard tensile testing at room temperature (294 K) at a true strain rate, $\dot{\epsilon}_0 = 5 \text{ x } 10^{-4}\ s^{-1}$, until failure on a servo-hydraulic Instron 8502, equipped with a 10 kN load cell and a 25 ± 10 mm Instron extensometer to capture the deformation. Strain rate change tests were performed on the same Instron using the step-ramp method described here [7] and in Chapter 5 with rate changes of 4x or 10x, or ¼ of the strain-rate for the up-change and down-change data, respectively. These tests were used to generate the constitutive parameters for all of the alloys used in this thesis but for the purpose of this section, serve as guidelines to determine realistic values to use in finite element simulations and establish the values for the parametric study.

Finite element modeling was performed using the commercial software Abaqus/CAE 6.14.3. In order to simulate the effects of strain rate sensitivity on the formation and propagation of the neck, a simplified sample geometry was designed having a length of 12.5 mm, a thickness of 1 mm, and a width of 5 mm and 4.9 mm at each end. This provided a sufficient instability to allow the computationally stable formation and propagation of a neck, this geometry is shown in Figure 8-3 left and the corresponding mesh used in the analysis in Figure 8-3 right.

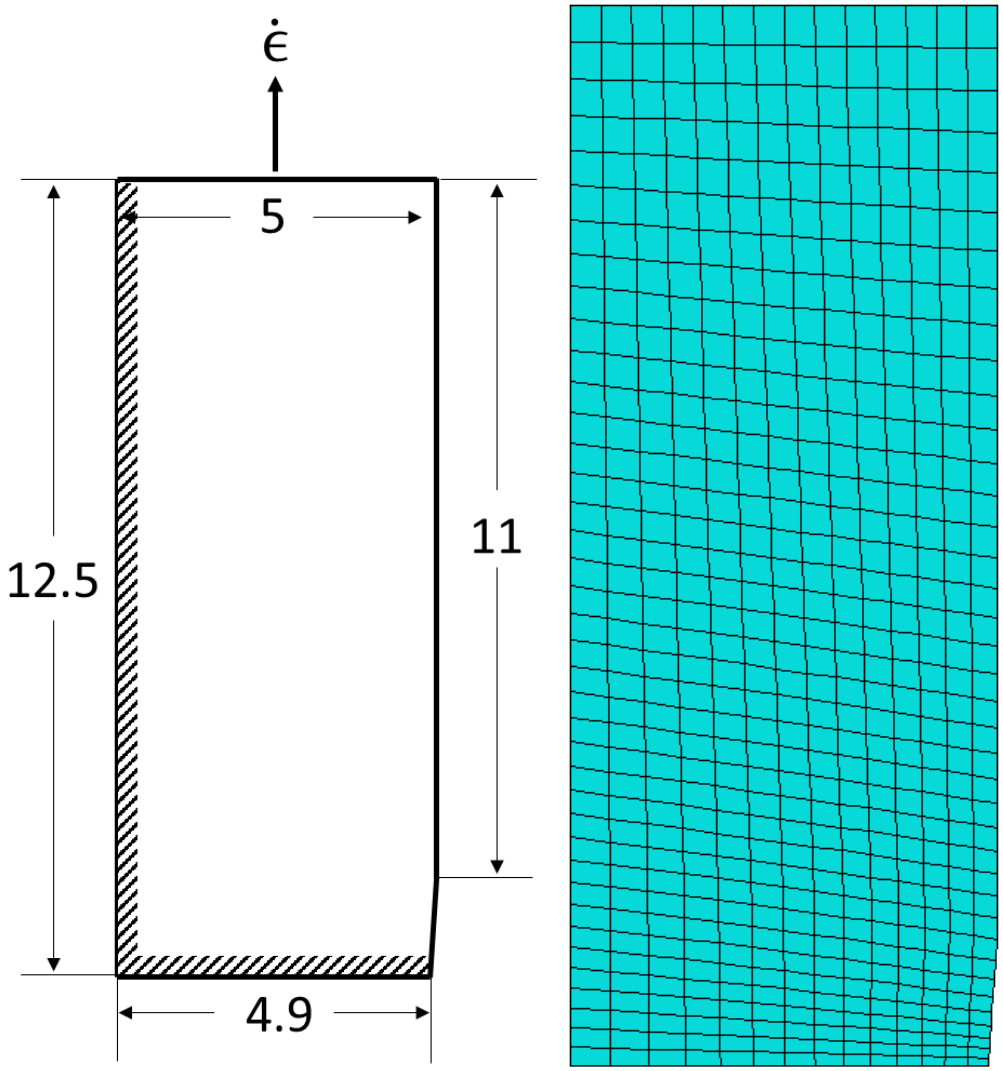

Figure 8-3: Left) *The geometry of the FEM model used in the simulations to aid in the understanding of the effects of strain rate sensitivity on the necking formation and evolution during deformation. All dimensions are in millimeters and the thickness of the sample is one millimeter.* ***Right)*** *The mesh of the FEM model rendered in ABAQUS. The global element size was 0.5 mm with local dimensions of 0.25 mm used near the artificial neck region.*

The test sample was placed under symmetric conditions along the tensile axis and along the reduced section dimension (see the hatched sides in Figure 8-3 left). An imposed deformation rate of 0.00625 mm s^{-1} was imposed in order to match the experimentally imposed strain rate, $\dot{\epsilon}$, of 5 x 10^{-4} s^{-1} used as the base strain rate for the strain rate sensitivity experiments and the continuous strain rate tests. A parametric study was performed using fictitious but reasonable constitutive parameters in order to isolate the unique effects of the strain hardening and both m_{uc} and m_{dc} strain rate sensitivity parameters on the formation and evolution of a neck. Several tests will be performed until a single element at the neck centre reaches the equivalent plastic strain levels of 0.20 to 0.50 in increments of 0.05 to observe how the strain and strain rate profiles evolve during deformation. In general, the FEM models will be deformed using the aforementioned conditions until the uniform region of the simulations reaches the experimentally determined onset of diffuse necking (determined from the Considère criterion, ϵ_D) as well as the local necking limit, ϵ_L, obtained once $d\sigma/d\epsilon = \sigma/2$, and at which point the model will be stopped and the strain and strain rate profiles will be plotted, these distributions are shown in Figure 8-4 for the C8S0 sample in the NA1m condition at ϵ_D.

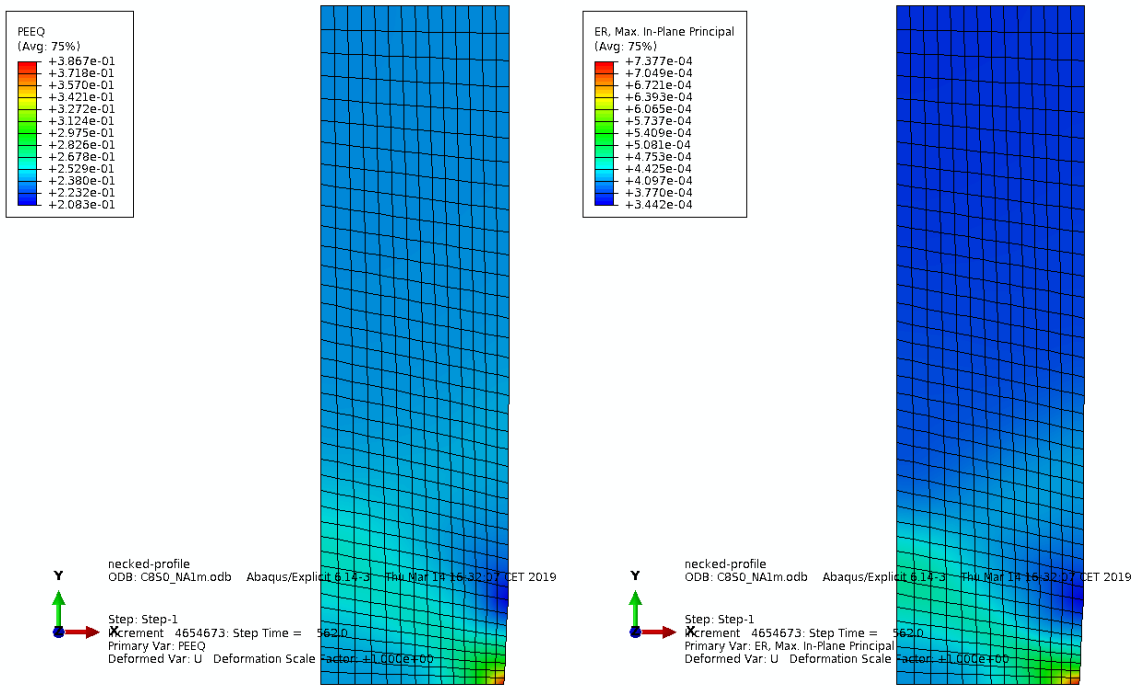

Figure 8-4: *The **Left)** strain and **Right)** strain rate distributions of a sample after being deformed to ϵ_D = 0.241 (in the uniform region). It is clear that the highest strain and strain rate is located at the neck centre and decreases until a minimum at the limit of the artificial neck, however, this minimum is well below the imposed strain rate of 5 x 10^{-4} s^{-1} and is due to the insertion of the artificial neck.*

It is of interest to observe the distribution of strain and strain rate between the most extreme part of the neck interior (the most deformed element, shown in red above) at either variable distances or variables strains from the maximum. Both strain and strain rate versus distance plots will be output going from 0 (the neck centre, bottom right red element in Figure 8-4) until a distance 1.5 mm (moving vertical along the right hand side of the model) away from the neck centre. In this work, the following properties will be determined and used in further analysis in order to better understand the effects of strain hardening and up-change and down-change strain rate sensitivity on the formation of both diffuse and local necking:

- $\dot{\epsilon}(d = 0)$ is the strain rate at the centre of the neck once the prescribed uniform elongation has been achieved at a large distance from the neck
- $\epsilon(d = 0)$ is the strain at the centre of the neck once the uniform elongation has been achieved at a large distance from the neck, ϵ_0, will be used in text
- $d(\dot{\epsilon} = \dot{\epsilon}_0)$ is the distance from the centre of the neck to the first occurrence of the imposed strain rate once the prescribed uniform elongation is achieved, $d_{\dot{\epsilon}_0}$, will be used in text
- $d(\epsilon = \epsilon_{L,D})$ is the distance from the centre of the neck to the first occurrence of the limit strain, either ϵ_D or ϵ_L, once the prescribed uniform elongation is achieved, d_{ϵ_D} or d_{ϵ_L}, will be used in text
- $\dot{\epsilon}\left(\epsilon = \epsilon_{L,D}\right)$ is the strain rate at $d(\epsilon = \epsilon_{L,D})$
- $d(\epsilon - 0.05)$ and $d(\epsilon - 0.10)$ is the distance from the centre of the neck to $\epsilon(d = 0) - 0.05$ and $\epsilon(d = 0) - 0.10$, respectively, $d_{0.05}$ or $d_{0.10}$ will be used in text

These values are shown below in Figure 8-5a and 8-5b for a sample deformed to a limit strain of 0.265 at a distance far from the neck.

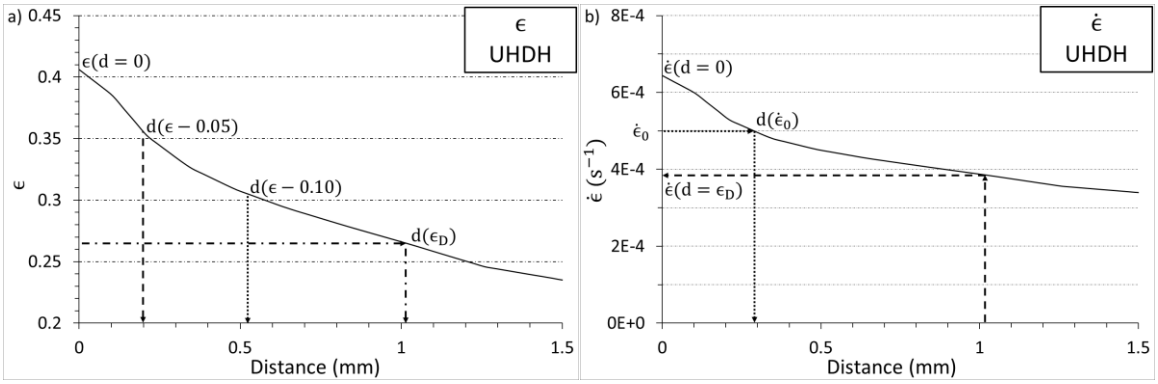

Figure 8-5: *The evolution of the* ***a)*** *strain with distance from the necked region of the finite element simulation illustrating the 0.05 (vertical dashed), 0.10 (vertical dotted), and the onset of diffuse necking, ϵ_D, (dotted and dashed), strain levels and* ***b)*** *the strain rate showing both the initial strain rate $\dot{\epsilon}_0 = 5x10^{-4}\ s^{-1}$ and the corresponding distance and strain rate based on the uniform elongation strain distance, d(ϵ_D) indicated with the corresponding output distance.*

It should be noted that, due to the sample symmetry, the actual size of the neck is twice the distance determined using the distance to base strain rate method . The distance of 0.3 mm found in Figure 8-5b above for $d_{\dot{\epsilon}_0}$ yields a total neck width of 0.6 mm which is appropriate compared to the size of a necked sample determined experimentally for one of the samples tested at room temperature.

4.0 Model implementation: parametric study on the effects of m_{uc} and m_{dc}

In order to establish the unique effects of the strain rate sensitivity parameters on the necking behaviour of the alloys, a set of hypothetical stress strain curves were created, having properties similar to those determined in this work (see Chapter 6 for the full list of constitutive values determined in this work). One curve had a relatively lower strain hardening exponent, 0.375, and the other a relatively larger, 0.400. The base constitutive relation for this curve was

$$\sigma = \sigma_0 + K\epsilon^n; \sigma_0 = 100, K = 400, n = 0.375 \text{ or } 0.400$$

From this basic power law, the strain rate sensitive pre-exponential was then converted to the strain rate independent pre-exponential factors using combinations of m_{uc} and m_{dc} of 0 and 0.05, for both levels of strain hardening. The full constitutive relations used in the FEM are shown below in Table 8-1 with the corresponding series name. For instance, ULDH stands for low SRS for up-changes and high SRS for down changes, and the subscript "n" stands for a higher strain hardening rate.

Table 8-1: *List of constitutive parameters used in the parametric study.*

Series Name	σ_0	K_{uc}	m_{uc}	K_{dc}	m_{dc}	n	ϵ_D
ULDL	100	400	0	400	0	0.375	0.265
ULDH	100	400	0	585	0.05	0.375	0.265
UHDL	100	585	0.05	400	0	0.375	0.265
UHDH	100	585	0.05	585	0.05	0.375	0.265
ULDLn	100	400	0	400	0	0.4	0.281
ULDHn	100	400	0	585	0.05	0.4	0.281
UHDLn	100	585	0.05	400	0	0.4	0.281
UHDHn	100	585	0.05	585	0.05	0.4	0.281

The model is governed by calculating the local strain rate compared to the imposed equivalent strain rate, $\dot{\epsilon}_0 = 5x10^{-4}s^{-1}$ whereby if the local strain rate is greater than $\dot{\epsilon}_0$, the parameters σ_0,

n_2, K_{uc} and m_{uc}, will be used whereas if the local strain rate is less than $\dot{\epsilon}_0$, σ_0, n_2, K_{dc}, and m_{dc} will be used. The value for the local stress state is computed and compared to the local strain hardening rate, $d\sigma/d\epsilon$ to determine how the load state and strain will be distributed in the next time step of deformation in order to maintain strain and strain rate compliance.

The main goal of this parametric study is to understand how the neck width is influenced by increasing the strain rate sensitivity either on the neck interior (manipulating m_{uc}), the neck exterior (manipulating m_{dc}) both uniquely and in combination. One of the critical hypotheses is that having an asymmetry in the m_{uc} and m_{dc} values may allow for the neck to either be destabilized or permit the propagation. The evolution of the strain and strain rate distribution for the effects of strain rate exponents, are shown in Figures 8-6a and 8-6b, respectively, for the parametric studies of samples with a strain hardening exponent of 0.375. Figures 8-7a and 8-7b show the corresponding strain and strain rate versus distance plots for the samples with a strain hardening exponent of 0.400.

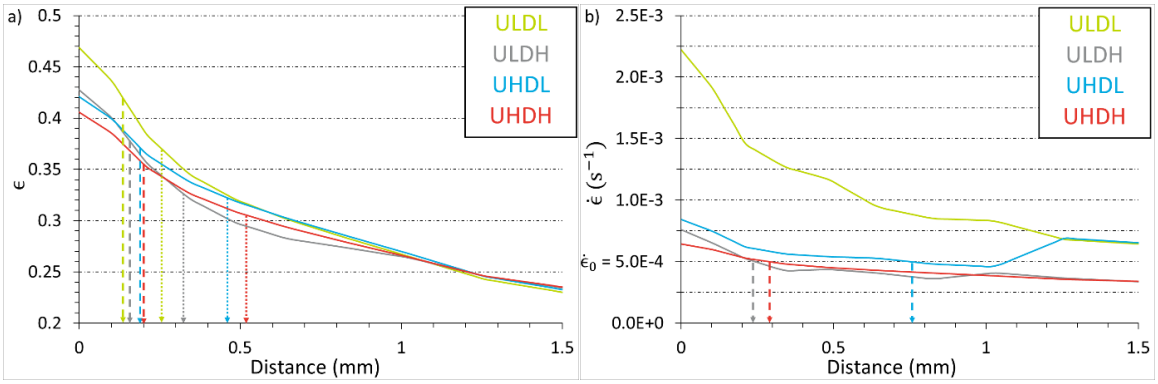

Figure 8-6: *The evolution of the* ***a)*** *strain and* ***b)*** *strain rate with distance from the artificial neck in the FEM for the ULDL (green), ULDH (grey), UHDL (blue) and UHDH (red) parametric samples. The vertical dashed lines in a) are the $d_{0.05}$ lines and the dotted lines being the $d_{0.10}$ lines. These lines aid to illustrate the general evolution of the distribution of strain along the formed neck. The vertical dashed lines in b) are the distances required to obtain the base strain rate, $d_{\dot{\epsilon}_0}$.*

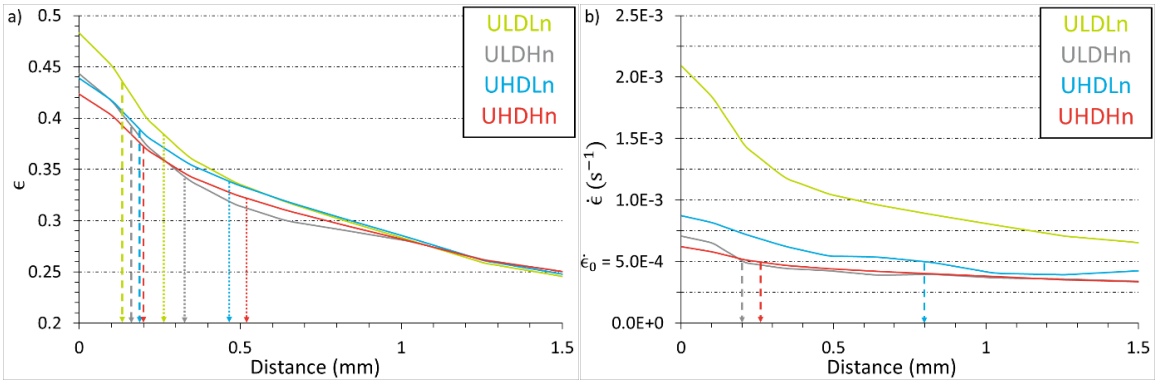

Figure 8-7: *The evolution of the* ***a)*** *strain and* ***b)*** *strain rate with distance from the artificial neck in the FEM for the ULDLn (green), ULDHn (grey), UHDLn (blue) and UHDHn (red) parametric samples. The vertical dashed lines in a) are the $d_{0.05}$ lines and the dotted lines being the $d_{0.10}$ lines. These lines aid to illustrate the general evolution of the distribution of strain along the formed neck. The vertical dashed lines in b) are the distances required to obtain the base strain rate, $d_{\dot{\epsilon}_0}$.*

The first consideration will be regarding the distribution of strain with distance for the effects of m_{uc} and m_{dc} at each level of strain hardening exponent, Figures 8-6a and 8-7a deformed to the uniform elongation limit. The trends observed in both cases are identical, the strain at the centre of the neck, ϵ_0 is the largest for the samples with $m_{uc} = m_{dc} = 0$. Next, increasing either m_{uc} (blue)

or m_{dc} (grey) uniquely exhibits nearly identical responses, both decreasing ϵ_0. This effect is further enhanced when both m_{uc} and m_{dc} are increased although the relative increase is less pronounced than the initial increase of either m_{uc} or m_{dc}. The same general trends were found when observing the effects of the strain rate sensitivity parameters on the evolution of strain rate with distance in Figures 8-6b and 8-7b. Increases in either m_{uc} or m_{dc} both provided a similar effect of decreasing the strain rate at the centre of the neck, with m_{dc} having a greater effect than m_{uc}. Increasing both of these parameters in unison provided a further decrease in the strain rate at the centre of the neck although the effect is significantly reduced in the same manner as their effect on the strain at the neck centre. The effects of the strain hardening exponent on both the strain and strain rate evolution with distance are shown below in Figures 8-8a and 8-8b, respectively for the ULDL and ULDLn, and UHDH and UHDHn, samples.

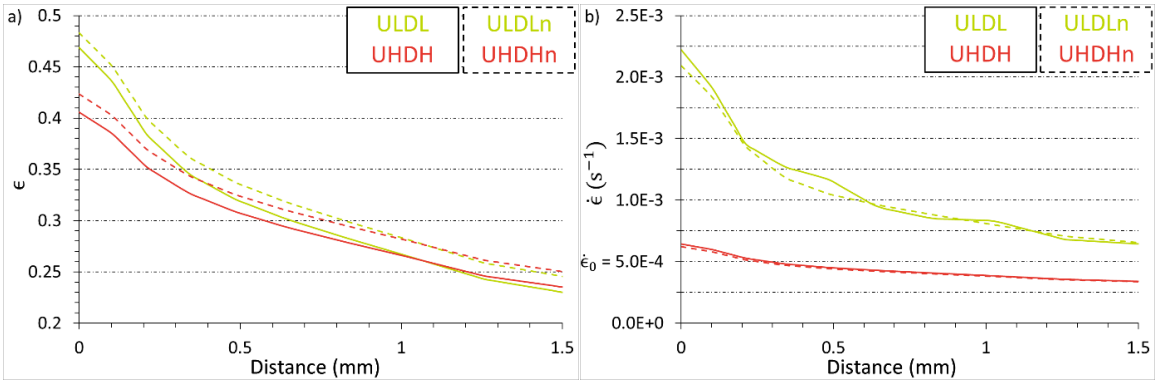

Figure 8-8: *A direct comparison between the effects of the strain hardening exponent n = 0.375 (solid lines) and n = 0.400 (dotted lines) for the evolution of* ***a)*** *strain and* ***b)*** *strain rate versus distance for the ULDL (green) and UHDH (red) studies.*

The increased n-value increases the strain along the entirety of the necked profile due to ϵ_D increasing. However, regarding the strain rate profile, the increased strain hardening exponent causes a larger decrease in the strain rate at the neck interface, being the most prominent with low m-values and this effect is effectively removed at greater distances from the neck. The key values described above are summarized and plotted for the effects of m_{uc}, m_{dc}, and n, for the either parametric study samples in Figures 8-9 to 8-11.

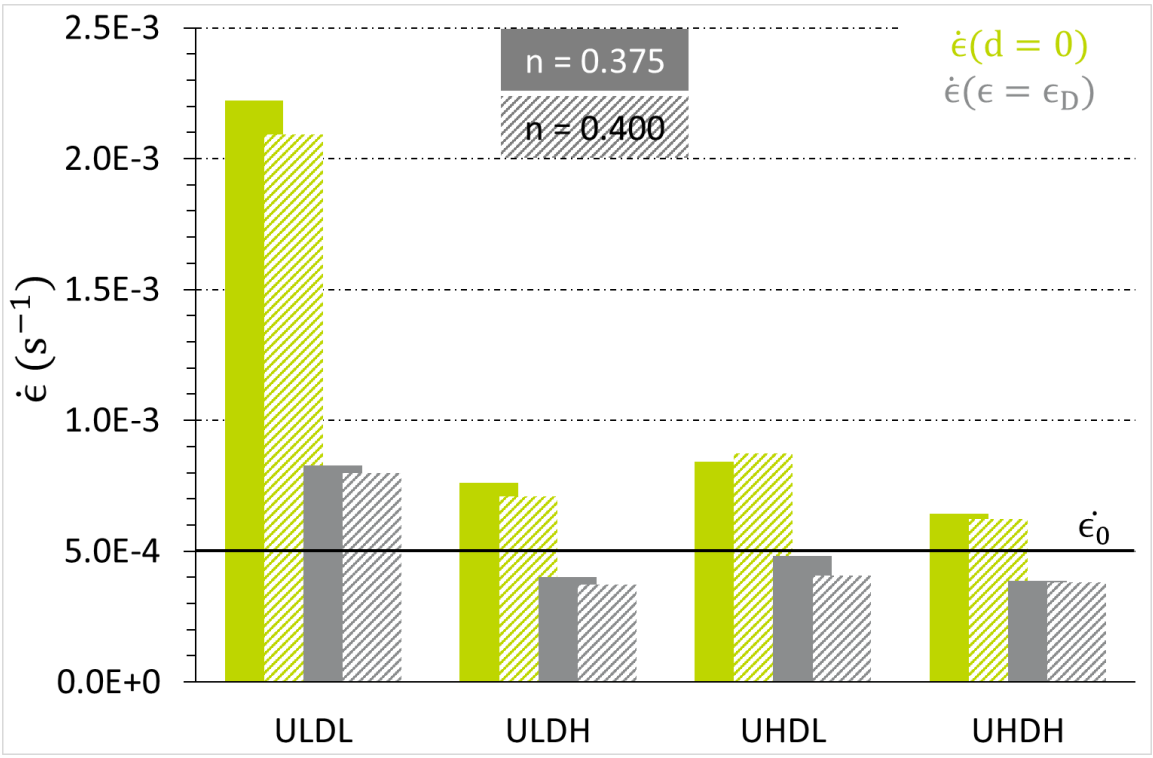

Figure 8-9: *The evolution of the strain rate determined at the centre of the artificial neck (green) and at the levels of the uniform elongation, ϵ_D, (grey) for the n = 0.375 (solid) and n = 0.400 (hatched) model parameters.*

Figure 8-9 clearly illustrates that the strain rate at the centre of the neck decreases significantly by increasing either m_{uc} or m_{dc}, with m_{dc} having an apparently larger effect than m_{uc}. By increasing both strain rate sensitivity parameters, even further decreases are obtained. In all cases except the high m_{uc}, low m_{dc}, increasing the strain hardening exponent causes a further decrease to the strain rate at the neck centre. At the level of the uniform elongation, the effects of strain rate sensitivity on the strain rate are significantly reduced but the same trends remain as those at the neck centre. It is interesting that despite the increase in ϵ_D caused by the increase in the strain hardening exponent, there is a decrease in the strain rate at the uniform elongation strain suggesting that the neck is less localized.

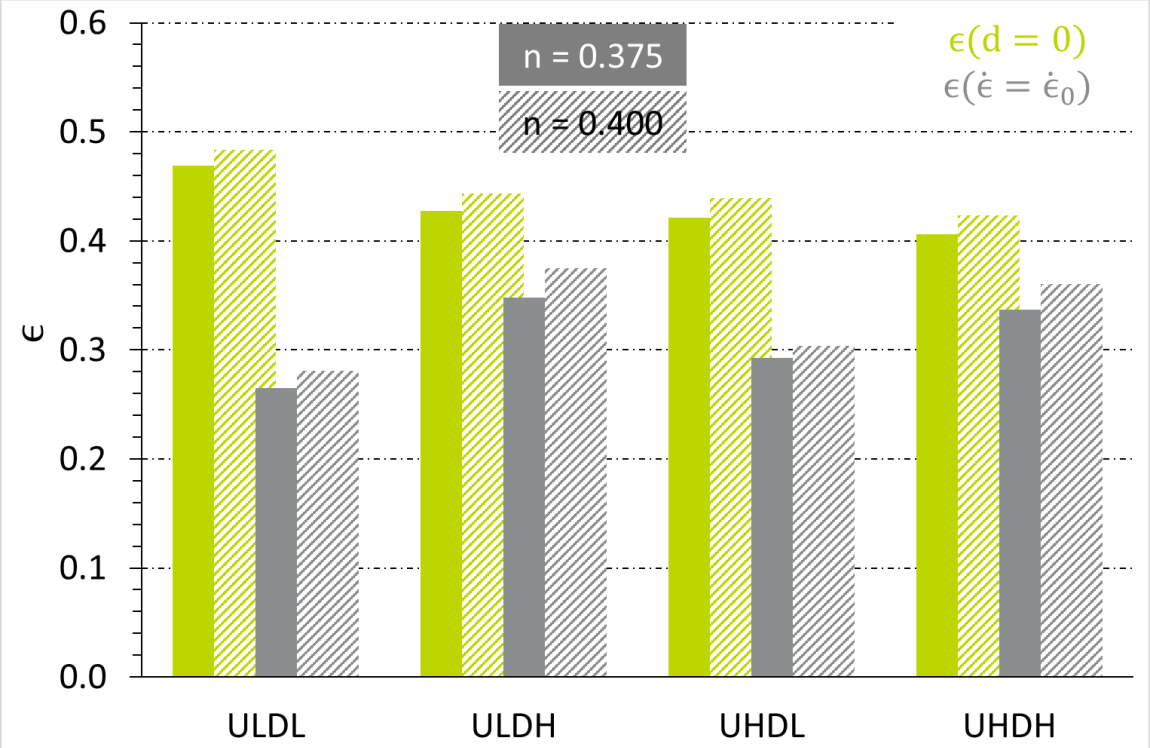

Figure 8-10: *The evolution of the strain determined at the centre of the artificial neck (green) and at the levels of the where the strain rate reaches the base strain rate, $\dot{\epsilon} = \dot{\epsilon}_0$, (grey) for the n = 0.375 (solid) and n = 0.400 (hatched) model parameters.*

The same general trends are observed regarding ϵ_0 where increasing either m_{uc} or m_{dc} or both decreases the strain. However, in this case, the decrease of strain is more significant when m_{uc} is increased as compared to m_{dc}. The increase in the strain hardening exponent now increases ϵ_0 (opposite to that of the strain rate) but this effect is due to the increase in the uniform elongation that has been used as the limit to stop the FEM simulation. The strain at the base strain rate increases with an increase in the strain rate sensitivity parameter suggesting that the distribution of strain along the length of the sample becomes more uniform as this coincides with a decrease in the strain at the sample centre. It is interesting to note that this effect is amplified when only m_{dc} is increased compared to the case of increasing m_{uc} such that the difference between the strain at neck centre and strain at the base strain rate is smaller for the case of an increased m_{dc}. This decrease is further diminished when both m_{uc} and m_{dc} are increased simultaneously. The effects of increasing the strain hardening exponent is identical for all parameters where it increases the strain at the base strain rate.

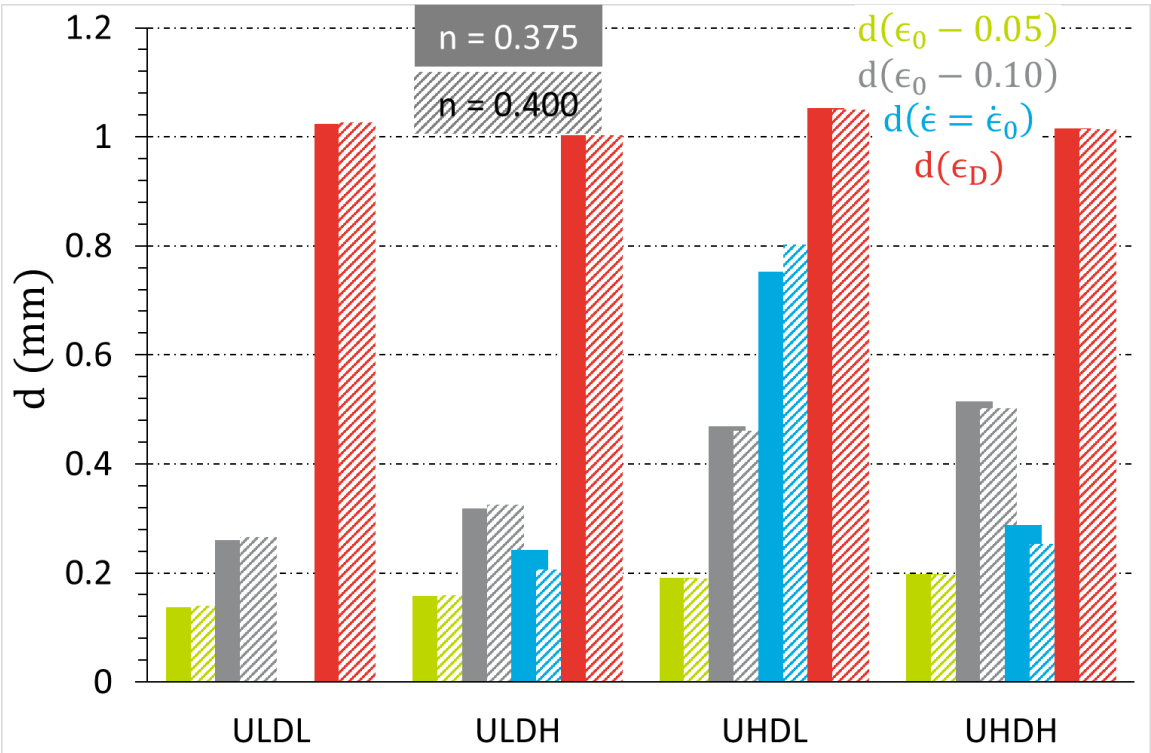

Figure 8-11: *The evolution of the distance from the centre of the neck to a decrease in 0.05 (green) and 0.10 (grey) of strain, to the point where the strain rate reaches the base strain rate, $\dot{\epsilon} = \dot{\epsilon}_0$, (blue), and the distance to the uniform elongation strain, ϵ_D, (red) for the n = 0.375 (solid) and n = 0.400 (hatched) model parameters.*

The parameters shown in Figure 8-11 will aid in illuminating the distribution of both strain and strain rate sensitivity in and around the sample neck. The $d_{0.05}$ and $d_{0.10}$ values from the neck centre are most closely related to the strain distribution right at the neck centre and increasing m_{dc}, m_{uc}, or both increase the distances for these two strain levels. The largest increases are due to increasing either both m_{uc} and m_{dc}, or m_{uc} only as the m_{uc} parameter operates on the region having a strain rate greater than the base strain rate occurring most commonly closer to the neck centre. This is evidenced by comparing both $d_{0.05}$ and $d_{0.10}$ to $d_{\dot{\epsilon}_0}$, in blue, whereby this delineates between the two regions being operated on by the m_{uc}, distances less than $d_{\dot{\epsilon}_0}$, and m_{dc}, distances greater than $d_{\dot{\epsilon}_0}$. The $d_{\dot{\epsilon}_0}$ lies between $d_{0.05}$ and $d_{0.10}$ in ULDH and the UHDH parametric samples. Due to the significant hardening taking place in the interior region of the neck, the increased m_{uc} yields the largest $d_{\dot{\epsilon}_0}$. It should be noted that the ULDL sample data is not shown due to its very high strain rate at the neck centre resulting in a very large distance (>2 mm) to obtain the nominal strain rate. Finally, there is very little difference in d_{ϵ_D} as this region is far (>1 mm) from the neck centre such that all parametric samples are within the m_{dc} region. There is almost no effect on the strain hardening exponent on the any of the distances to the key parameters. Attention is now turned towards the rate of change in space for both the variation of strain and strain rate from the centre of the sample to different distances, shown in Figure 8-12 and 8-13, respectively.

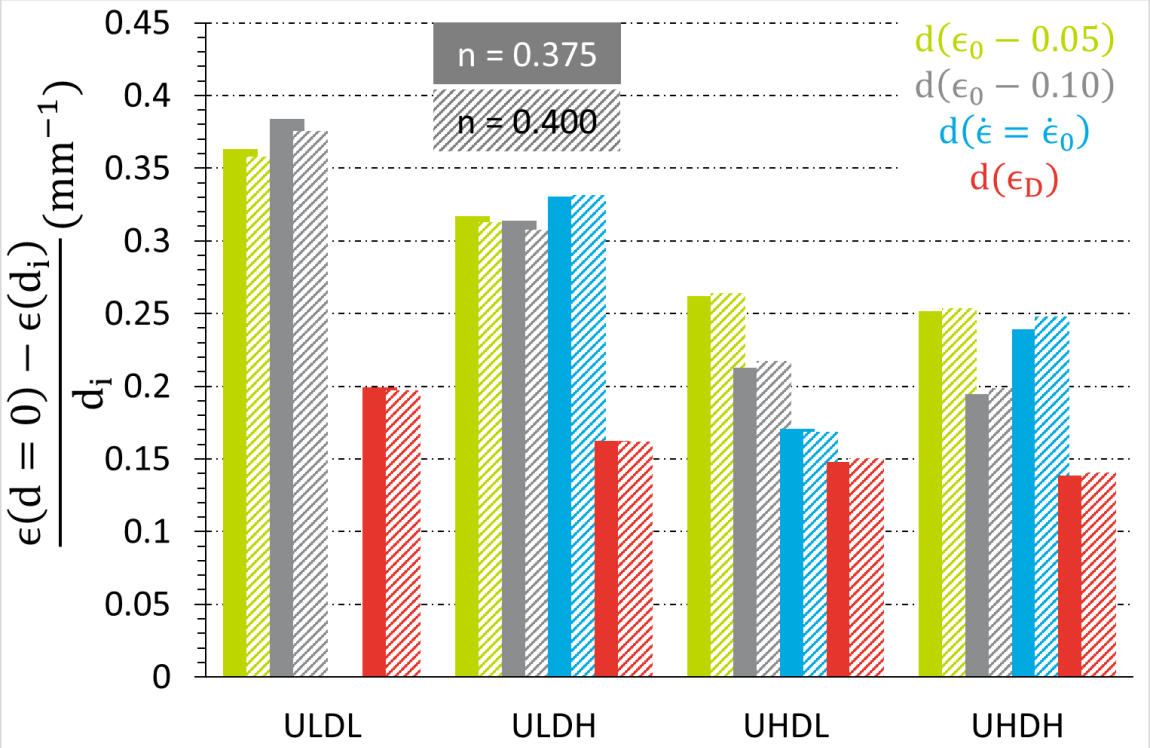

Figure 8-12: *The rate of change of strain from the neck centre to the $\epsilon_0 - 0.05$ (green), $\epsilon_0 - 0.10$ (grey), base strain rate (blue), and uniform elongation (red) for the n = 0.375 (solid) and n = 0.400 (hatched) model parameters.*

Aside from the unique values of strain and strain rate at various distances from the neck centre, understanding the distribution and localization of strain and strain rate along the length of the neck will give insight into the extent of necking and if it is possible for its stabilization or propagation whereby both the strain and strain rate distributions should ideally be zero for uniform elongation. For all cases with a non-zero m_{uc} or m_{dc}, the slope to $d_{0.05}$ strain drop is always greater than that of $d_{0.10}$ level indicating that the severity of the neck is decreasing with distance. As commonly understood, increasing the m_{uc} plays a large role on reducing the localization of necking as is supported in this parametric study with the UHDL sample having a reduced strain localization compared to the ULDH test which is not only significantly greater than UHDL but has 0.05 and 0.10 values being nearly identical suggesting that these two levels are both well within the neck. This is in comparison to the UHDL sample which has a significantly smaller strain distribution at $d_{0.05}$ which further decreases at $d_{0.10}$. When both m_{uc} and m_{dc} are increased, both strain distributions of $d_{0.05}$ and $d_{0.10}$ decrease and are the lowest of all parametric study samples. These same trends are withheld for the strain distributions at the uniform strain, d_{ϵ_D} (red in Figure 8-12). The most interesting is regarding the strain distribution to the base strain rate where there is a complex interplay between both the strain rate at the centre of the neck and the strain rate distribution moving away from the neck, this will be covered later. The observed results were expected, when m_{uc} only is changed, it reduces the strain distribution more as compared to the m_{dc} only. However, the most surprising of all is that when both m_{dc} and m_{uc} are increased in unison, the strain distribution is significantly greater than the m_{uc} only study. This brings into question whether or not $d_{\dot{\epsilon}_0}$ is a good method for defining the width of the neck, being discussed later. Finally, the increase of the strain hardening exponent tends to result in a minor decrease the strain distribution of all of the parametric studies.

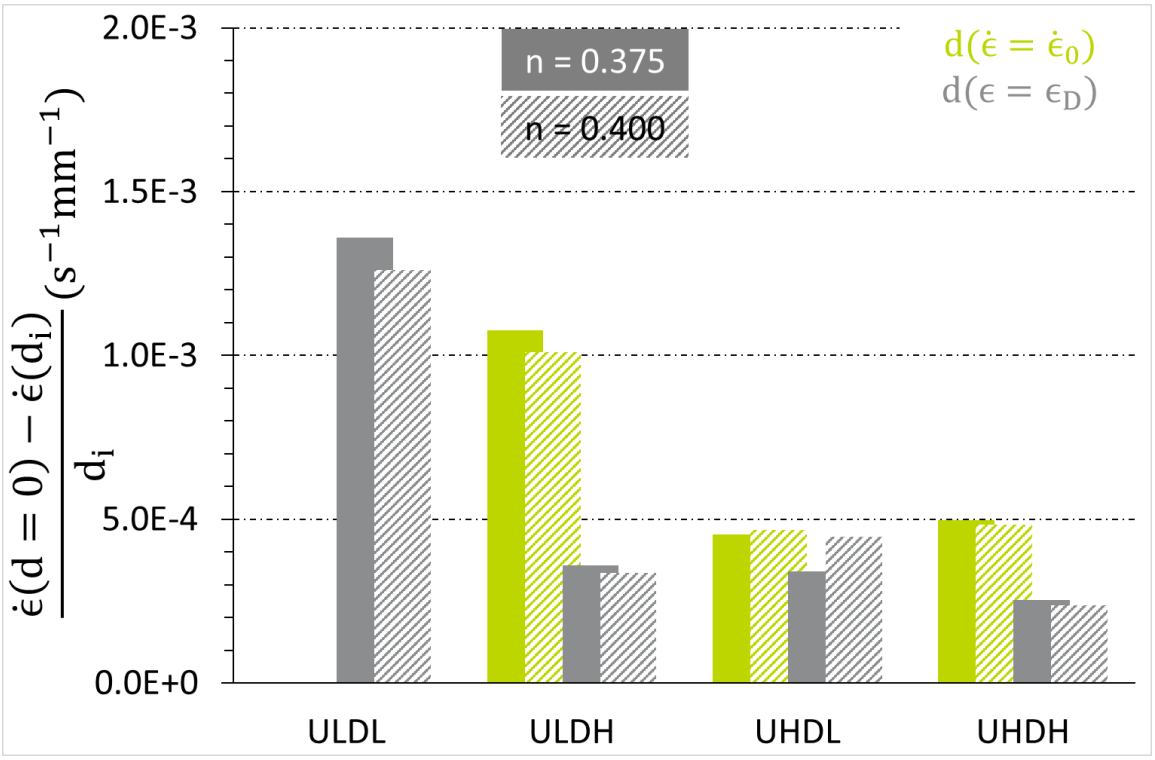

Figure 8-13: *The rate of change of strain rate from the neck centre to base strain rate (green) and uniform elongation (grey) for the n = 0.375 (solid) and n = 0.400 (hatched) model parameters. Note the ULDL sample strain rate change is not plotted for the base strain rate due to its unrealistically large distance.*

As a final measure to observe the possibility of necking, the strain rate distribution using $d_{\dot{\epsilon}_0}$ (green in Figure 8-13) and the d_{ϵ_D} (grey in Figure 8-13) is shown. It is clear that the effect of m_{dc} is significantly smaller than m_{uc} as these two strain rate sensitivity parameters play roles on distances less than or greater $d_{\dot{\epsilon}_0}$, respectively. However, in this case, having both m_{uc} and m_{dc} increasing in unison actually does not reduce the strain rate distribution as much as increasing m_{uc} only. Regarding the distance to the uniform elongation strain, all of which are very similar, the same trends remain. As expected, the strain rate distribution is the greatest in the ULDL, then ULDH, UHDL next, and finally UHDH. The change between UHDH now being lower than UHDL, unlike the rate using the distance to the base strain rate, is likely due to there being a region whereby m_{dc} is able to play a role as it is outside of the base strain rate distance. By increasing the strain hardening exponent, the strain rate distribution tends to decrease for all distances expect in the UHDL test whereby increases are observed.

5.0 Application of the model to experimental data

In order to establish the validity and sensitivity of the model to the real experimental constitutive parameters, the FEM model was performed on one of the studied AA6xxx alloy, Al-0.35Mg-0.9Si-0.8Cu (in at%) in the NA1m condition (see Chapter 3 for a full description of the heat treatment schedule). The constitutive parameters of this test are shown below in Table 8-2.

Table 8-2: *The SvH fit parameters determined for the C8S0 NA1m alloy in for the high strain region of the alloys. This is the only region of interest for use in finite element modeling since necking should never occur at low-strains. Thus to save computational time, only the second part of the fit will be considered.*

Sample	Condition	σ_0 (MPa)	K_{2m}	K_{2uc}	K_{2dc}	m_{uc}	m_{dc}	n_2	ϵ_D	ϵ_L

C8S0	NA1m	118.6	431.6	474.6	509.0	0.013	0.022	0.396	0.214	0.270

It was decided to run the FEM simulation on the strain development of the centre of the neck between 0.20 to 0.50 in increments of 0.05 using the constitutive parameters for the C8S0 sample in the NA1m condition to understand how the aforementioned FEM outputs (distances, strains, and strain rate values at critical points) develop during deformation and is shown below in Figures 8-12a and 8-12b. This should better elucidate a method for describing both the location and the evolution of the neck using the model output parameters.

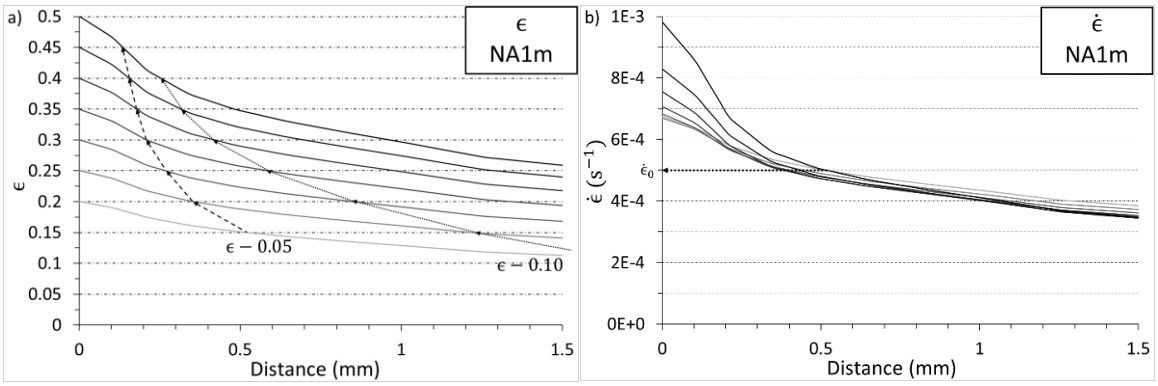

Figure 8-14: *The evolution of the* ***a)*** *strain with distance from the necked region of the finite element simulation illustrating the 0.05 (dashed) and 0.10 (dotted) strain decrease levels, and* ***b)*** *the strain rate. The initial strain rate* $\dot{\epsilon}_0 = 5x10^{-4}\ s^{-1}$ *is indicated with the corresponding output distance.*

In this simple example, it is easily shown that the distance to $d_{0.05}$ and $d_{0.10}$ of deformation decreases with increased deformation suggesting the localization of the neck. Additionally, $d_{\dot{\epsilon}_0}$ starts to decrease with deformation until a critical strain is achieved and then starts to increase. The corresponding evolution of $d_{0.05}$, $d_{0.10}$, and $d_{\dot{\epsilon}_0}$ are shown below in Figures 8-15.

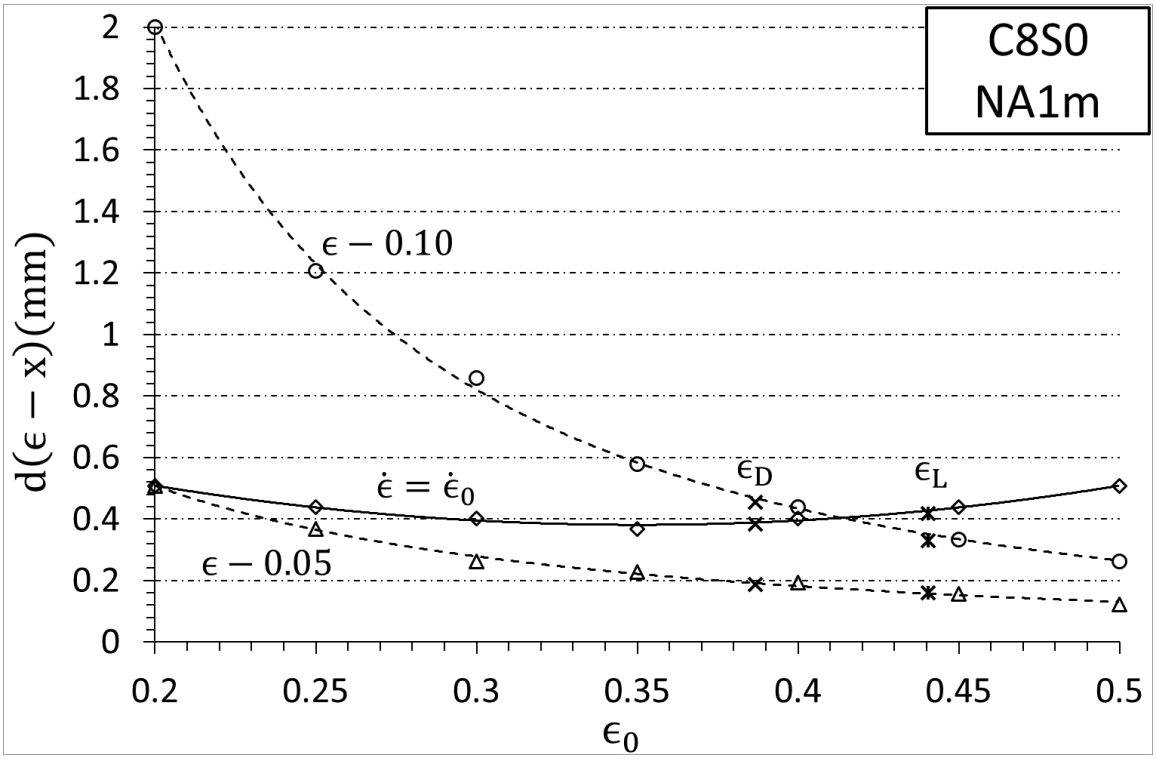

Figure 8-15: *The evolution of the distance between the centre of the neck interior and the ϵ – 0.05 and ϵ – 0.10 strain levels, and $d_{\dot{\epsilon}_0}$, for each of the maximum strain levels in the FEM simulation of the C8S0 sample in the NA1m condition. Note the ϵ_D (x) and ϵ_L (*) strains are shown and plotted using the ϵ_0 for their respective studies.*

When the physical distance values are plotted to evolve with maximum strain level, it is clear that two phenomena occur, the distribution of strain becomes much more localized (see the difference between $d_{0.05}$ and $d_{0.10}$) suggesting that the neck becomes more localized with increasing deformation and this is coupled with an initial decrease in $d_{\dot{\epsilon}_0}$. One of the most interesting results is that the spatial strain distribution for the $d_{0.10}$ decreases at a rate much faster with deformation compared to that of $d_{0.05}$ although they both have the same form of exponential decay suggesting that strain accumulation is increasing at distances closer to the neck centre. The evolution of $d_{\dot{\epsilon}_0}$ with deformation begins at the $d_{0.05}$ and does not vary as significantly as $d_{0.05}$ or $d_{0.10}$. At the limit of ϵ_D, $d_{\dot{\epsilon}_0}$ is almost equal to $d_{0.10}$ and actual becomes greater than $d_{0.10}$ at the point of localized necking. This shows a clear delineation where the effect of both m_{uc} and m_{dc} play a role on strain localization before the onset of a localized neck (by definition) but upon localized necking, only m_{uc} is important as all deformation contained within the neck interior is at a strain rate greater than $\dot{\epsilon}_0$. This may now be compared with the strain and strain rate distributions around the neck in Figures 8-16a and 8-16b, respectively.

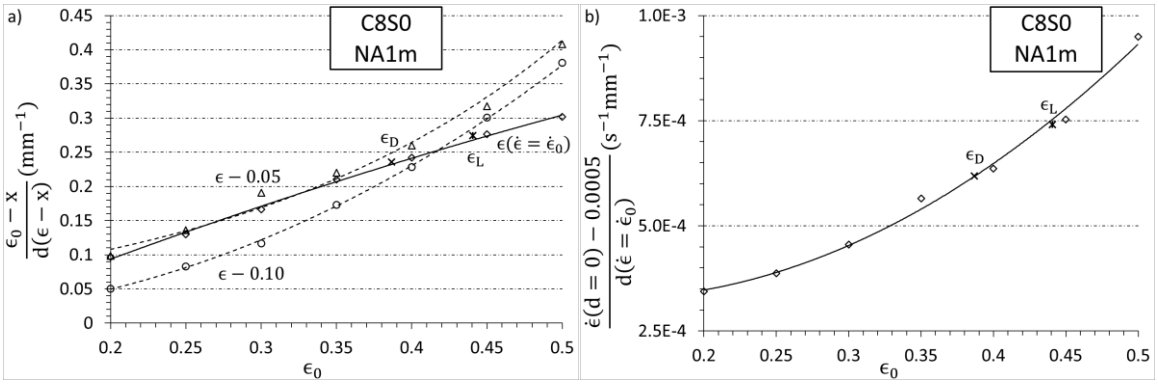

Figure 8-16: *The **a)** strain distribution for the $\epsilon_0 - 0.05$ (triangles), $\epsilon_0 - 0.10$ (circles), and $\epsilon(\dot{\epsilon} = \dot{\epsilon}_0)$ (diamonds) levels and **b)** the strain rate distribution for the base strain rate in the C8S0 sample in the NA1m condition.*

It is clear that for any means of measuring the strain distribution, it increases with deformation with the $d_{0.05}$ distribution always being greater than the $d_{0.10}$ distribution with this discrepancy decreasing during straining. Concerning the $d_{\dot{\epsilon}_0}$ strain distribution, the low-strain behaviour follows that of $d_{0.05}$ until the onset of diffuse necking, ϵ_D, when there is an apparent transition and it does not accelerate like $d_{0.05}$ but rather follows a linear evolution and actual becomes less than the $d_{0.10}$ strain distribution. There is clearly an interplay between the relevance of m_{uc} and m_{dc} in the strain distribution whereby additional hardening is occurring at distances less than $d_{\dot{\epsilon}_0}$ due to m_{uc} but the softening is exacerbated in the regions exterior of $d_{\dot{\epsilon}_0}$ due to m_{dc} being greater than m_{uc}. The evolution of the strain rate distribution with deformation follows the same exponentially increasing behaviour as the strain distributions of $d_{0.05}$ and $d_{0.10}$ which begins to change slowly at lower levels of deformation, accelerating until the diffuse neck and finally local neck are formed. During uniform elongation the strain rate heterogeneity should be zero (or very little if the presence of shear bands or Lüder's bands occur) such that $d_{\dot{\epsilon}_0}$ should be zero. The goal of preventing the formation and development of a local neck should be in terms of reducing the strain rate distribution as much as possible.

6.0 Discussion

The various deformation and necking parameters that have been explored in this work have been able to provide general information regarding neck localization, propagation and the influence of the strain rate sensitivity exponents on the accumulation of strain and strain rate in and around the neck. One of the complexities that was found was concerning the evolution of $d_{\dot{\epsilon}_0}$ with deformation. At low strains, $d_{\dot{\epsilon}_0}$ was shown to decrease with deformation until a critical strain was obtained and then it was found to increase with further deformation. Figure 8-17 shows the evolution of $d_{\dot{\epsilon}_0}$ with deformation (in terms of the strain at the centre of the neck, ϵ_0).

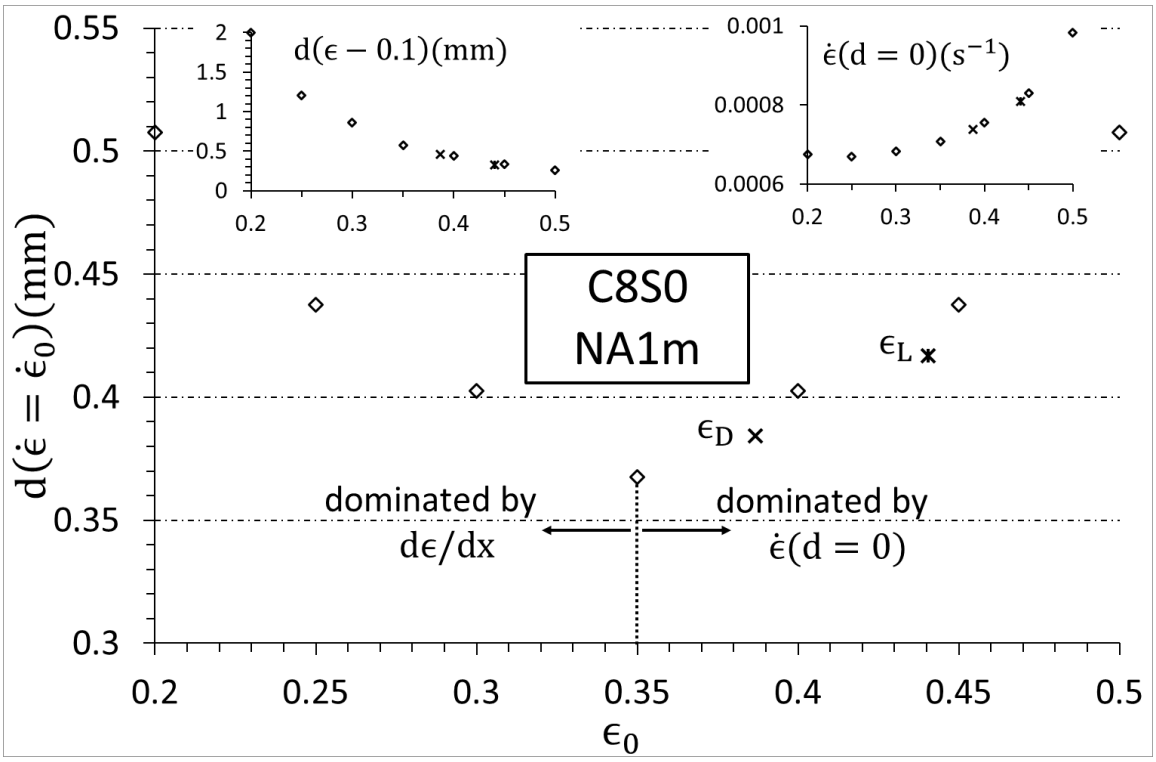

Figure 8-17: *The evolution of $d_{\dot{\epsilon}_0}$ with ϵ_0 determined between 0.20 and 0.50 for the FEM model using the constitutive parameters for the C8S0 sample in the NA1m. The top-left inset shows the evolution of $d_{0.10}$ with ϵ_0 and the top right shows the strain rate at the neck centre evolving with deformation. Note the values for the onset of diffuse necking, ϵ_D, and local necking, ϵ_L, at shown for the "X" and "*", respectively.*

Focusing specifically on how the distance to the base strain rate changes, Figure 8-17 it is clear that there are two regions located above and below ϵ_0 of 0.35 (although this may change if finer strain increments were used). In the first region, the decrease follows the trend of the distribution of strain (shown as the left inset for $d_{0.10}$) whereby the distances decreases rapidly with deformation. By having the rapid changing of deformation, the effect of the strain hardening exponent is able to dominate with the strain accumulation occurring rapidly near the centre of the neck via the strain distribution. Concerning the second half, or strains greater than 0.35, it appears that the strain rate at the centre of the neck plays a dominant role. The transition point is effectively a minimization problem whereby the strain distribution has almost settled to its maximum and the strain rate at the centre of the neck has not yet started to rapidly increase.

Now, attention should be turned towards two concepts: neck localization and neck stabilization/propagation. Neck localization will be used to refer to the extent of the strain accumulation around the neck centre and how the strain distribution changes during diffuse necking. Neck stabilization or propagation will be used to relate to the evolution of strain (strain

rate) and its distribution around the neck and if it changes with further deformation. These two ideas will be connected to the parametric studies.

6.1 Neck localization, stabilization, and propagation

The idea of neck localization is related directly to the distribution of strain around the neck $d\epsilon/dx$, where x is the distance away from the neck. Although this FEM simulation includes an artificial neck in order to induce a strain rate and strain variation during deformation, the effects of the strain rate sensitivity are clearly apparent. Since the FEM model is constantly searching for the Considère criterion for each element

$$\frac{d\sigma}{d\epsilon} = \frac{K\epsilon^n \dot{\epsilon}^m}{\epsilon}\left(n + m\frac{\partial \ln \dot{\epsilon}}{\partial \ln \epsilon}\right) = \sigma_0 + K\epsilon^n \dot{\epsilon}^m = \sigma$$

Two things can be seen; prior to the formation of a diffuse or local neck (uniform elongation) the term $\frac{\partial \ln \dot{\epsilon}}{\partial \ln \epsilon}$ is zero and thus the strain rate sensitivity does not have an effect on Considère and thus only by increasing n will Considère be delayed. However, upon the formation of a diffuse neck, the region within $d_{\dot{\epsilon}_0}$ will be affected by m_{uc}, the region exterior, by m_{dc}. We shall consider each of the parametric study cases; ULDL, UHDL, ULDH, and UHDH upon the formation of the diffuse neck.

6.2 ULDL: $m_{uc} = m_{dc} = 0$

When there is an absence of strain rate sensitivity, the Considère criterion is controlled strictly by the local strain state and $d\sigma/d\epsilon = nK\epsilon^{n-1}$ is the law controlling the onset of diffuse necking. In this case, the only method for delaying necking is through the increase of n, and upon the formation of a diffuse neck, local necking will inevitably proceed resulting in neck localization. This is clearly evident in Figure 8-6a and 8-6b whereby the ULDL parameters result in not only the largest strains and strain rates at the neck centre but also shows a very large variation in these properties moving away from the neck centre.

6.3 UHDL: m_{uc} 0.05; $m_{dc} = 0$

In the case where $m_{uc} > m_{dc}$ (UHDL), both $d\sigma/d\epsilon$ and σ are increased due to the increase in the local strain rate and depending on the magnitude of m_{uc} and the local strain rate, the Considère criterion can not be obtained. However the effect of softening due to $\frac{\partial \ln \dot{\epsilon}}{\partial \ln \epsilon}$ being negative at distances greater than $d_{\dot{\epsilon}_0}$ will not be as significant (or zero in the parametric study case) such that despite the drop in strain rate, the Considère criterion is still achieved resulting in the formation of a diffuse neck. Thus in order to balance these two regions, the additional hardening in the neck interior will require additional strain be located exterior to $d_{\dot{\epsilon}_0}$ but solely due to the enhanced hardening occurring at distances less than $d_{\dot{\epsilon}_0}$. This is the case that is conventionally studied (or considered) and has been shown to delay neck localization such that $d_{\dot{\epsilon}_0}$ should either increase or remain the same. As the strain increases and deformation occurs exterior to $d_{\dot{\epsilon}_0}$, it signifies that the neck is stable and does not increase in severity with further deformation. In Figure 8-6b, the strain rate begins to lower with increased distance from the neck centre until a certain distance is obtained at which point the local strain rate increases suggesting that there is a stabilization of the neck. Additionally, the strain gradient close to the neck centre is lower than the ULDL and ULDH samples. One of the interesting factors to consider is the ratio between n and m_{uc} and m_{dc} whereby the post-uniform deformation behaviour will change depending on the term in brackets, $\left(n + m\frac{\partial \ln \dot{\epsilon}}{\partial \ln \epsilon}\right)$, where in the event of a very large m, (or very small n), it is possible for

changes in the local strain rate to eventually become larger than the hardening component, n, such as the case of super-plastic materials where m is frequently greater than 0.6.

6.4 ULDH: $m_{uc} = 0$; $m_{dc} = 0.05$

When $m_{uc} < m_{dc}$ (ULDH), both $d\sigma/d\epsilon$ and σ are decreased due to the local decrease in the strain rate at distances greater than $d_{\dot{\epsilon}_0}$. This signifies that the region interior of the neck, upon formation of a diffuse neck will continue to match the Considère criterion and any strain rate effects on the local regions will not provide any additional hardening. However, in the regions outside $d_{\dot{\epsilon}_0}$, there will be a stress drop due to $\frac{\partial \ln \dot{\epsilon}}{\partial \ln \epsilon}$ being negative. In this case, the region greater than $d_{\dot{\epsilon}_0}$ will be in a state further along the Considère criterion (between diffuse and local necking) and as a result, deformation will be preferential to this region. The increased deformation in the neck exterior will result in an increase in the strain and strain rate distribution and will also yield neck stabilization. However, due to the fact that the decreased strain rate will take place over larger distances, the drop in the strain rate, $\frac{\partial \ln \dot{\epsilon}}{\partial \ln \epsilon}$, will almost always be lower than the corresponding increase in strain rate of the neck interior. The net result is that despite the neck being stabilized, the effect of m_{dc} on neck stabilization is less pronounced from local area softening that the effect of m_{uc} on neck stabilization due to local area hardening. This is clear with the fluctuations observed in Figure 8-6b with respect to the evolution of strain rate moving away from the neck centre, specifically at distances greater than $d_{\dot{\epsilon}_0}$whereby the strain rate does not monotonically decrease with increasing distance. Separately, the strain distribution near the neck centre is quite pronounced and greater than the UHDL parameters but decreases with increasing distance from the neck centre.

6.5 UHDH: $m_{uc} = m_{dc} = 0.05$

Finally, when both m_{uc} and m_{dc} are increased (UHDH) and greater than zero, a combined effect is resulted and the larger effect of local hardening inside the neck (due to m_{uc}) is coupled with the local softening outside the neck (due to m_{dc}) resulting in neck propagation. The strongest example of this is that both the strain, strain rate and their respectively evolutions with distance from the neck centre are the lowest amongst any of the samples showing only minor variations in Figures 8-6a and 8-6b.

7.0 Conclusions

- The definition of the size of the neck being based on the limiting width of the region retaining the nominal strain rate has been shown to be inadequate for real experimental properties rather than in parametric studies. It provides an important parameter for understanding the regions of the sample being influenced by the m_{uc} and m_{dc} strain rate sensitivity parameters. Its evolution with deformation may give insight into the neck formation and propagation.
- The distinction between the neck localization and neck propagation/stabilization were discussed and shown to be related to the distribution of strain and strain rate with distance, respectively.
- In order to delay and prevent the onset of local necking, having a high m_{uc} and m_{dc} are suggested with m_{uc} playing a larger role due to the larger concentrations of strain rate being located at distances less than $d_{\dot{\epsilon}_0}$ which m_{dc} acts on a larger area but at distances further away from the neck centre.
- The evolution of $d_{\dot{\epsilon}_0}$ with deformation has been shown to be related to not only the distribution of strain rate but also the magnitude of the strain rate at the neck centre being largely tied to the m_{uc} strain rate exponent.

8.0 References

[1] S. Saimoto and P. Van Houtte, “Constitutive relation based on Taylor slip analysis to replicate work-hardening evolution,” *Acta Mater.*, vol. 59, no. 2, pp. 602–612, Jan. 2011.

[2] E. W. Hart, “Theory of the tensile test,” *Acta Metall.*, vol. 15, no. 2, pp. 351–355, Feb. 1967.

[3] A. K. Ghosh, “Tensile instability and necking in materials with strain hardening and strain-rate hardening,” *Acta Metall.*, vol. 25, no. 12, pp. 1413–1424, Dec. 1977.

[4] A. K. Ghosh, “The Influence of Strain Hardening and Strain-Rate Sensitivity on Sheet Metal Forming,” *J. Eng. Mater. Technol.*, vol. 99, no. 3, p. 264, 1977.

[5] A. K. Ghosh, “A-physically-based-constitutive-model-for-metal-deformation,” *Acta Metall.*, vol. 28, pp. 1443–1465, 1980.

[6] S. Saimoto *et al.*, “Method to decode stress-strain diagrams to identify the structure-strength relationships in aged aluminum alloys,” *Mater. Sci. Eng. A*, vol. 709, pp. 9–16, Jan. 2018.

[7] M. Carlone and S. Saimoto, “Precision strain rate sensitivity measurement using the step-ramp method,” *Exp. Mech.*, vol. 36, no. 4, pp. 360–366, 1996.

9 Discussion, conclusions and perspectives

The work presented in this thesis permits to improve the understanding of the effect of additions of Si, Cu, and Mg to Al on the natural ageing and pre-ageing behaviours of Al-Mg-Si-Cu alloys commonly used in automotive applications. We have evaluated the effects of these various solutes and the corresponding microstructures formed during processing on the mechanical properties that control the formability of aluminium sheet alloys. The use of hardness testing and differential scanning calorimetry, complemented by the use of tensile testing and strain rate jump tests have been able to provide insight on the expression of formed clusters on the resulting mechanical properties. These mechanical properties were then implemented in finite element modelling to better understand their influence, specifically the asymmetry in increasing and decreasing strain rate sensitivity, on the overall onset and evolution of necking found in tensile testing.

This chapter contains three sections; a general discussion of the work, conclusions that can be made from this work, and finally perspectives and future work.

9.1 Discussion

To summarize and connect each of the parts of the thesis, the work will be summarized succinctly to aid in the understanding of the industrial processing route beginning with the given alloy composition, the common heat treatments performed, the methods of analysis and both the resulting direct, and indirect, mechanical properties. The largest impact this thesis may have is in terms of the full chain connection of alloy composition to mechanical properties and the different contributions of each solute species. This section will be separated into three parts. The first part will focus on the effects of solutes and processing on the mechanical properties with explanations given using supporting evidence from the thesis. The second part will focus on the strain rate sensitivity testing and the observation of the asymmetry between the up-change and down-change strain rate sensitivities. The third and final part will focus on the interplay of the mechanical properties and both the uniform and post-uniform elongation.

9.1.1 Solute additions and processing on the mechanical properties

To begin understanding the effects of both solutes and processing, it is easiest to recall the evolution of the artificial ageing behaviour of each of the alloy from the sNA1w, PB 20 min, and peak age states. The effects of specific solute additions for the three aged conditions are shown in Figure 9-1.

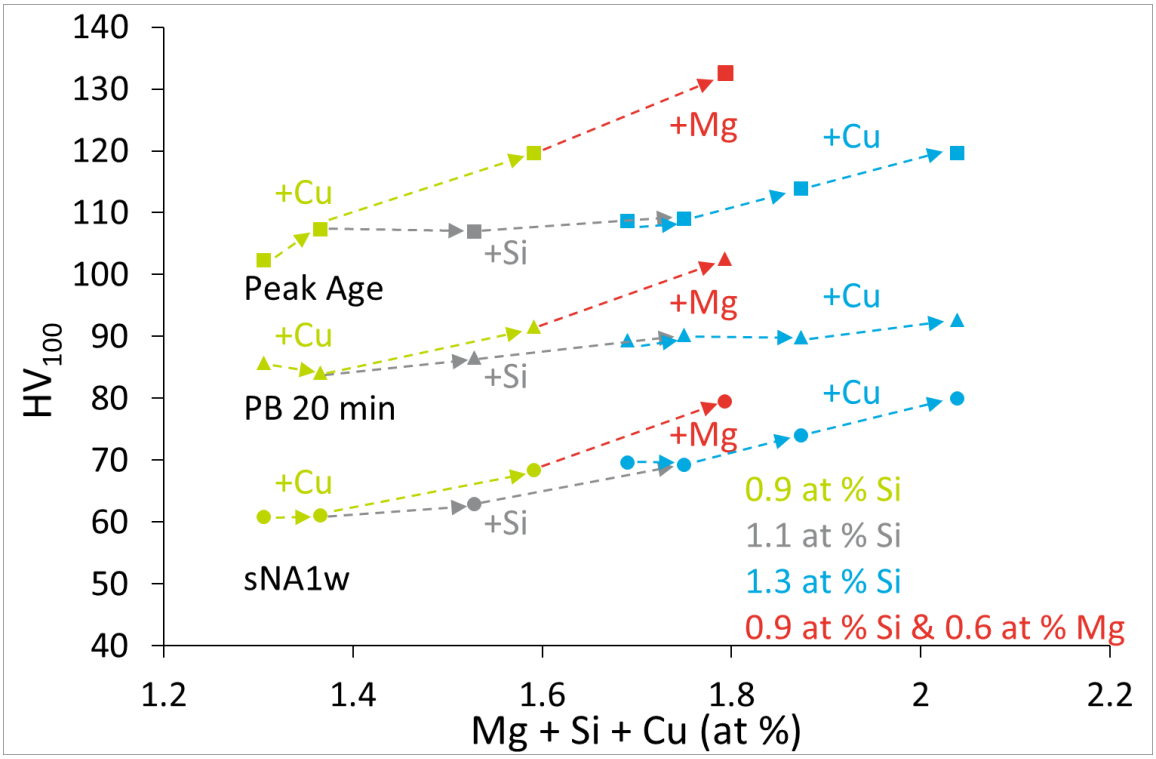

Figure 9-1: *The evolution of the HV_{sNA1w} (circles), HV_{PB} (triangles), and HV_{Peak} (squares) hardness properties with total solute content to illustrate the dependency of certain properties of the different solutes. For clarity, the effects of Cu additions at 0.9 and 1.3 at% Si, are connected in green and blue dashed arrows, respectively. The effects of Si additions at 0.2 at% Cu and 0.4 at% Mg are connected with the grey dashed arrows. The effects of Mg addition at 0.9 at% Si and 0.3 at% Cu are connected with red dashed arrows.*

It can be clearly observed that the sensitivity of the hardness with solute additions changes depending on the heat treatment performed. In the sNA1w condition, all solutes have a similar effect on increasing the hardness with Mg having a slightly increased sensitivity. After 20 minutes of ageing at 185 °C (PB 20 min), there is still a similar sensitivity of the hardness for all solute additions except for Mg which retains its sensitivity. This is suspected to be due to the retained effects of hardness from the sNA1w condition where there is little change in the cluster density and only minor precipitation occurring. At the peak age condition, the situation is completely changed whereby both Cu and Mg additions result in large increases in the hardness as compared to Si additions. Since the base composition of the alloys tested are Si heavy, the (Cu + Mg)/Si ratio being less than one, while the stoichiometry of the precipitates formed, β'' (Mg_5Si_6) and Q' (Cu + Mg)/Si of 1.36, the extra Si does not enable additional precipitation as is evident from no change in hardness detected from Si additions. This aids in explaining the effects of both Cu and Mg on providing a large increase in the hardness caused by the added precipitation in the peak age condition. This is further supported by the DSC experiments that were performed in this work. The effects of Cu additions at 0.9 at% Si on the DSC thermographs are shown below in Figures 9-2a-c for samples in WQ, NA1m, and as-PA conditions.

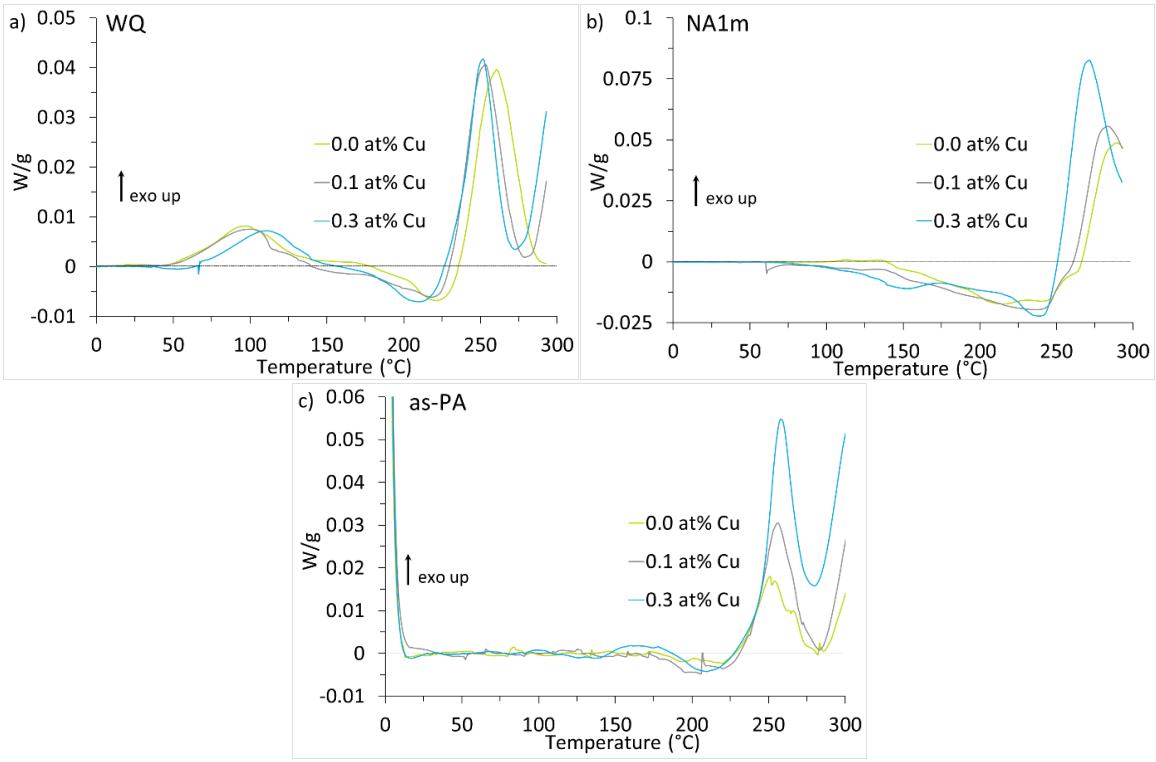

Figure 9-2: *The effects of Cu content at Si level of 0.9 at% on the DSC curves in the* ***a)*** *WQ,* ***b)*** *30 day NA, and* ***c)*** *as-PA conditions.*

The addition of Cu in the WQ condition has a small effect on increasing the cluster formation temperature to a slightly higher temperature, from 90 to 110 °C and decreases the onset of cluster dissolution from 175 to 150 °C, also acting to reduce the precipitation peak temperature from 255 to 235 °C but not changing the intensity. In the NA1m condition, there is an increase in the total cluster dissolution signal with increased Cu content and the appearance of two distinct cluster dissolution signals appear, the lower temperature, Cu-related peak occurring at 150 °C and the higher temperature, Cu-independent peak, occurring at 235 °C. The increased total dissolution signal with added Cu suggests that there is an increase in the total amount of solute taking place in clustering, increasing the strengthening of the alloy, as shown in Figure 9-3a. The Cu addition also yields both an increase in the precipitation intensity while simultaneously lowering its temperature of formation. These suggest that the addition of Cu both contribute to the increased precipitation hardening of the system and reduces the negative natural ageing effect by lowering the energy barrier for the formation of the precipitates during subsequent AA processes. In the as-PA condition, the addition of Cu appears to result in the small retention of Cu in solution evidenced by the small exothermic signal occurring at 150 °C. Conversely, there is no significant difference in the cluster dissolution signal with added Cu suggesting that a similar amount of solute and number of clusters have formed during the PA process. Only their growth during the sNA from the retained solutes would increase their size/number density yielding an increase in the hardness, as previously shown and in the yield strength of the alloys, shown below in Figure 9-3b. However, during the subsequent precipitation, the Cu additions increase both the precipitation peak intensity and peak temperature suggesting that their rate of formation is retarded but the total amount that may be formed increases. This would aid in explaining the fact that in the PB 20 min condition, the effects of Cu do not have a large effect on increasing the

hardness where the kinetics play a large role but in the peak age, when kinetics are of less importance, the total precipitation intensity results in a large increase in hardness, as observed.

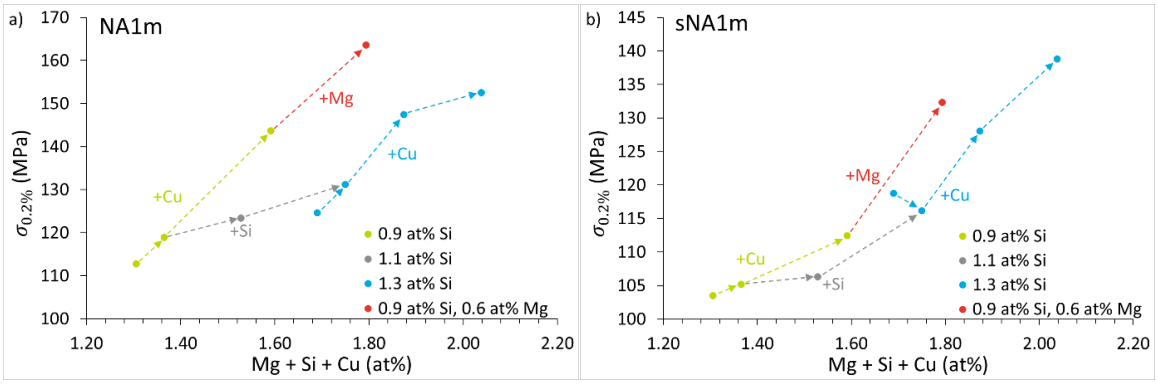

Figure 9-3: *The effects of alloy composition on the yield strength in the* ***a)*** *NA1m and* ***b)*** *sNA1m conditions. For clarity, the effects of Cu additions at 0.9 and 1.3 at% Si, are connected in green and blue dashed arrows, respectively. The effects of Si additions at 0.2 at% Cu and 0.4 at% Mg are connected with the grey dashed arrows. The effects of Mg addition at 0.9 at% Si and 0.3 at% Cu are connected with red dashed arrows.*

As explained using the results of the DSC thermographs, the sensitivity of the yield strength of the alloys with solute additions appear to relate directly to the dissolution intensities of the clusters formed during either NA or sNA. In Chapter 4, the effects of Cu, Si, and Mg additions were shown to have different effects on the clustering dissolution intensities and changed the number of dissolution peaks. In the NA1m condition, the appearance of two separate dissolution peaks were observed, the intensity of the lower temperature peak being most sensitive to Cu and Mg additions and the second peak being most sensitive to the total solute content. In the as-PA condition, the single dissolution peak increased in intensity by any solute addition, having a slightly stronger sensitivity to Mg additions. Both of these effects are reflected in the evolution of the yield strength in the NA1m condition, whereby Cu and Mg additions have a stronger effect as compared to Si, whereas in the sNA1m condition, Cu and Si have similar effects, with Mg having a stronger effect. The evolution of the strain hardening parameter at high strain with solute content are shown in Figures 9-4a and 9-4b for the two processing routes.

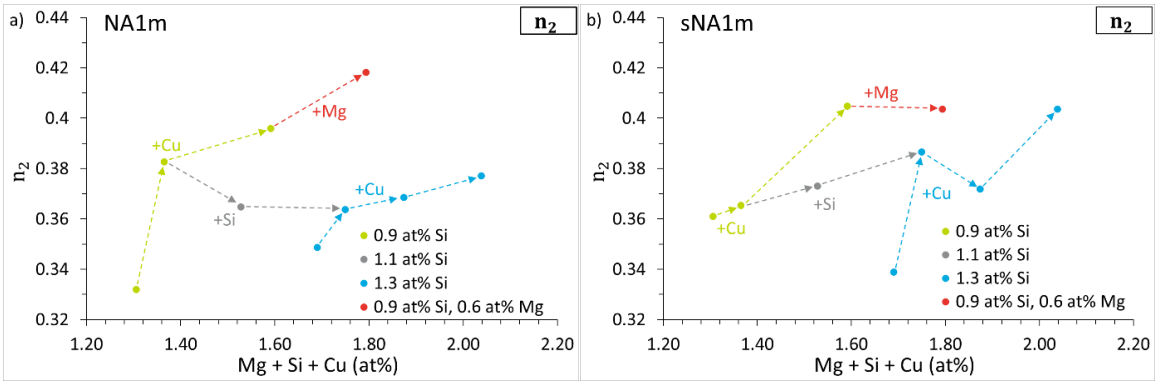

Figure 9-4: *The effects of alloy composition on the strain hardening exponent at high strain in the* ***a)*** *NA1m and* ***b)*** *sNA1m conditions. For clarity, the effects of Cu additions at 0.9 and 1.3 at% Si, are connected in green and blue dashed arrows, respectively. The effects of Si additions at 0.2 at% Cu and 0.4 at% Mg are connected with the grey dashed arrows. The effects of Mg addition at 0.9 at% Si and 0.3 at% Cu are connected with red dashed arrows.*

The possible rational for the observed effects of solute additions on the strain hardening may be explained using the amount of retained solute in solution and through the idea of dynamic strain ageing. As was demonstrated in Chapter 4 for the additions of solutes in the NA1m condition, Cu

additions were shown to increase the hardness and provide an increase in the low-temperature dissolution peak of the clusters that were formed. However, in the NA curves, at 0.9 at% Si, there was still sufficient hardening exhibited by the alloys even after reaching the NA1m condition whereas the samples with 1.3 at% Si did not show appreciable subsequent hardening suggesting that the maximum amount of solute has been incorporated into clusters reducing the total solute content within the matrix. As the presence of solute in solution have been shown to increase the strain hardening behaviour, the additions of Cu and Mg at 0.9 at% Si correlate with a large increase in the strain hardening behaviour. The increase in the total free solute will provide additional solute to the system increasing the likelihood of dynamic strain ageing shown to increase the strain hardening. Cu additions do still have a positive effect at 1.3 at% Si but this effect is mitigated due to the accelerated kinetics reducing the total solute in solution. The effects of Si additions show this clearly whereby they decrease the strain hardening behaviour in the NA1m condition which is suspected to be caused by the increased kinetics and net decrease of free solute in solution. In the sNA1m condition, the additions of solute were shown to provide an almost equal contribution to the dissolution peak of the clusters that were formed during the PA treatment. Comparing the levels of hardness in the NA1m and sNA1m condition, the additions of Cu were shown to increase the difference in hardness between these two conditions (NA1m – sNA1m hardness) such that the low-Cu samples had very similar levels of hardness while those with high Cu, had an NA1m hardness significantly greater than the respectively sNA1m hardness. The suspected cause is that there is a greater amount of retained solute in solution in the sNA1m condition yielding to a more pronounced effect of dynamic strain ageing and resulting in an enhanced strain hardening rate. This would aid in the explanation of the enhanced effects of Cu and the now positive effects of Si, both being due to the added retention of solute in solution. The corresponding effects of solute additions on the up-change and down-change strain rate sensitivities are shown in Figures 9-5a and 9-5b for the two processing routes, below.

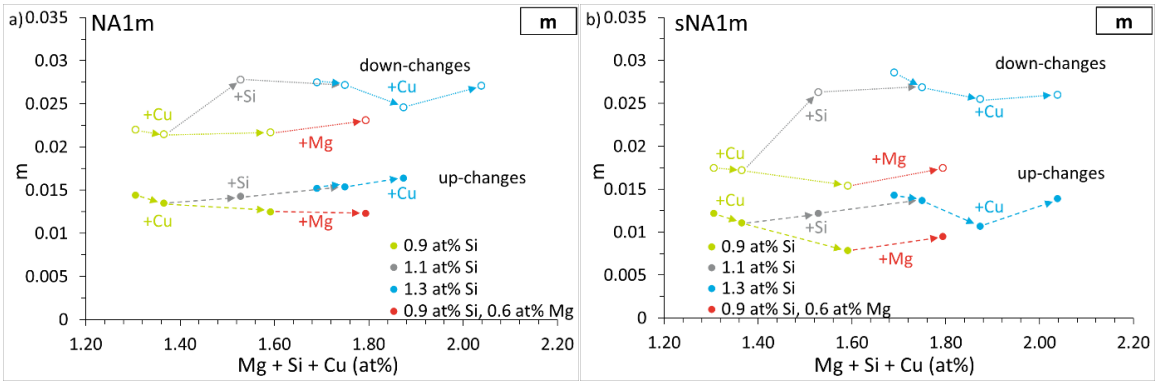

Figure 9-5: *The effects of alloy composition on the increasing (closed circles) and decreasing (open circles) engineering strain rate sensitivities in the* ***a)*** *NA1m and* ***b)*** *sNA1m conditions. For clarity, the effects of Cu additions at 0.9 and 1.3 at% Si, are connected in green and blue dashed arrows, respectively. The effects of Si additions at 0.2 at% Cu and 0.4 at% Mg are connected with the grey dashed arrows. The effects of Mg addition at 0.9 at% Si and 0.3 at% Cu are connected with red dashed arrows.*

Although not fully understood, the effects of solute additions on the up-change and down-change strain rate sensitivities can be explained using the ideas of dynamic strain ageing and the retention of solute in solution. Considering first the up-changes in the NA1m condition, the additions of Cu and Mg at 0.9 at% Si result in a decrease of the strain rate sensitivity speculated to be caused by the increase of solute retained in solution increasing the dynamic strain ageing aspect which is typically characterized by a decrease in the strain rate sensitivity. On the contrary, Si additions and

Cu additions at 1.3 at% Si yield an increase in the strain rate sensitivity as there is a more complete removal of solute from the matrix, as previously discussed. In the case of down-changes, the additions of Cu and Mg show a very little increase in the strain rate sensitivity while Si additions provide a strong increase. Again, these effects are postulated to be due to the effect of dynamic strain ageing whereby if a down-change takes place, there is additional time for the dynamic formation of clusters resulting in a greater number density of clusters yielding a decrease in the activation volume which results in an increase in the engineering strain rate sensitivity. Although speculative, these explanations will be elaborated when discussing the evolution of the inverse activation volumes with deformation, specifically concerning the effects of Si additions as studied in Chapter 5.

9.1.2 Strain rate sensitivity testing and asymmetry

As shown in Chapter 5, the experimental set-up to accurately perform strain rate sensitivity tests is not trivial and requires a deep comprehension of the interaction between tensile testing equipment and its influence on the sample being tested. The observations of an asymmetry in the inverse activation volume (Haasen plot) between up-changes and down-changes strongly suggests that there is an underlying mechanism that is not well understood whereby the thermal activation of obstacles are not the same at room temperature. The effects of Si additions were used as an example to show how this asymmetry evolves during plastic deformation and are recalled below in Figure 9-6.

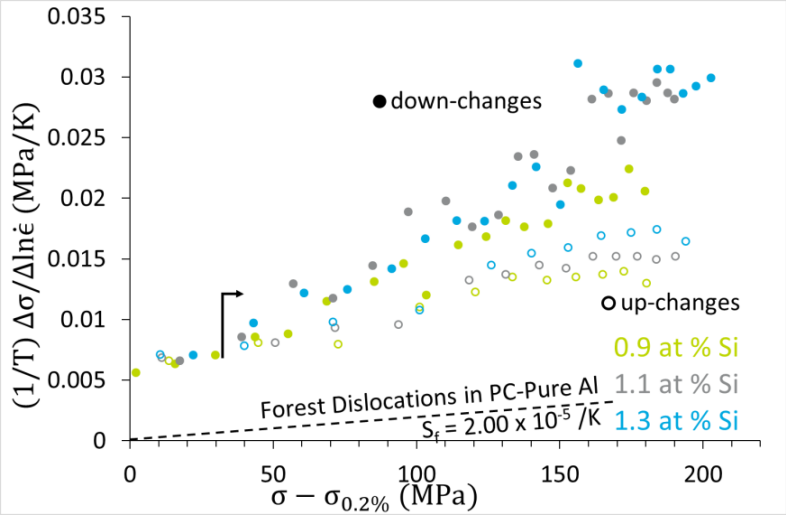

Figure 9-6: *The Haasen plot illustrating the effects of Si on the evolution of the inverse activation volume during strain hardening. The ¼ and 1/10 down-changes (closed symbols) are not identified separately in this plot but are differentiated from the up-change (open symbols). It is clear that the inverse activation volume from yield to about 40 MPa is similar for all alloys independent on the direction of the rate-change.*

Since the Haasen plot captures the evolution of the inverse activation volume during the production of dislocations (plastic deformation), three clear observations may be made:

i) The inverse activation volume is the same for both up-changes and down-changes at low levels of strain hardening and then deviate
ii) The inverse activation volume of down-change is larger than that of up-changes at larger levels of strain hardening
iii) Si additions increase the inverse activation volume during both up-changes and down-changes at equivalent levels of strain hardening

At early stages of deformation, the dislocation density of the materials is relatively low in comparison to the density of the clusters formed suggesting that the rate-controlling obstacles at the beginning of plastic flow are due to the clusters formed during NA. At room temperature, there is sufficient thermal energy so that there is not a significant difference between the strength

of the different clusters. Atom probe tomography (APT) experiments performed suggest that the number density and size of clusters do not change significantly with Si additions in the NA1m condition resulting in the inverse activation volume being similar for all alloys just after yielding since solute remains in solution are effectively invisible due to their low thermal activation barrier. Thus it is presumed that the mechanism controlling this part of the Haasen plot is the thermal activation of clusters by dislocations whereby the clusters are more thermal in nature than dislocations. However, the shearing of the material can cause both dissolution or dynamic formation of clusters as the movement of dislocations may shear a cluster and move it apart, but also bring solute together, this being a form of dynamic strain ageing. If this premise is followed, then the greater amount of solute in solution at greater levels of Si would decrease the spacing between solutes and result in an increase in the inverse activation volume, as shown for both up-changes and down-changes.

The differences between the up-changes and down-changes must now be addressed and two hypotheses are proposed; the first being related to the time component (deforming at a faster rate reduces the amount of time for diffusion, slower rate increases this time) and the second being related to the production of dislocations products during deformation and their recovery. In the first scenario, the up-changes reduces the time for diffusion to take place such that if there is a change in the dynamic equilibrium of cluster density, deforming the material at a faster rate should result in a decrease of the diffusion component of dynamic strain ageing resulting in a lower number density (greater spacing) between clusters resulting a smaller inverse activation volume. At a slower rate of deformation, the contrary would be true whereby there is additional time for the diffusion of solute to form additional clusters resulting in an increase in their equilibrium number density (smaller spacing) yielding an increase in the inverse activation volume; as observed. The effect of Si additions is in concurrence with this hypothesis as the additions of Si will yield an increase of the availability of solute able to contribute to cluster formation, resulting in a net increase of the dynamic cluster density and thus increasing the inverse activation volume, as observed for both up-changes and down-changes. In the second scenario, it has been shown that the interaction of dislocations with other dislocations, solutes, precipitates, or clusters, produces vacancies, small loops, and stacking faults (termed dislocation interaction products, DIPs) which are able to be recovered during deformation and reduce the flow stress. If additional time is permitted for the recovery of DIPs such as the case of down-changes, the stress drop due to the rate change will be larger resulting in a larger apparent inverse activation volume, as observed. In the case of up-changes, the opposite would be true where there is a reduced recovery of DIPs such that the stress change from the increased strain rate would be lower, as observed. The question now becomes the effect of Si on these two directions. The fact that the inverse activation volume increases with Si addition in the down-changes suggests that either additional DIPs are recovered or a greater amount of DIPs are produced. It is postulated that this effect would most likely be explained by the more efficient recovery of DIPs as in the NA1m condition, Si additions were shown to accelerate the NA kinetics resulting a smaller fraction of solute retained in solution. Solid solution additions have been shown to reduce dislocation recovery (see Al-Mg) via strain hardening but the addition of Si has been shown to decrease the strain hardening in the NA1m condition in this work, suggesting that there is a reduction of the solid solution component of Si thus facilitating recovery of both dislocations and DIPs. Alternatively, if the production rate of DIPs changes with Si content, it could be argued that having a greater number of clusters in the material results in an enhanced production of DIPs thus even if the recovery rate of DIPs does not change with added Si, the net result would be an enhanced

total stress drop. These ideas would correlate to the up-changes but in this scenario, the increased stress with added Si would be due to the thermal activation the centres producing the DIPs, the NA clusters.

9.1.3 Connection of the mechanical properties to failure properties

Finally, in order to combine all of the experiments performed in this work, the connection of the strain hardening, strain rate sensitivity and mechanical properties of the alloys are connected to the failure properties; the uniform and the post-uniform elongations. Figures 9-7a-f show effects of solute additions on the various mechanical and failure properties for samples in the sNA1m condition.

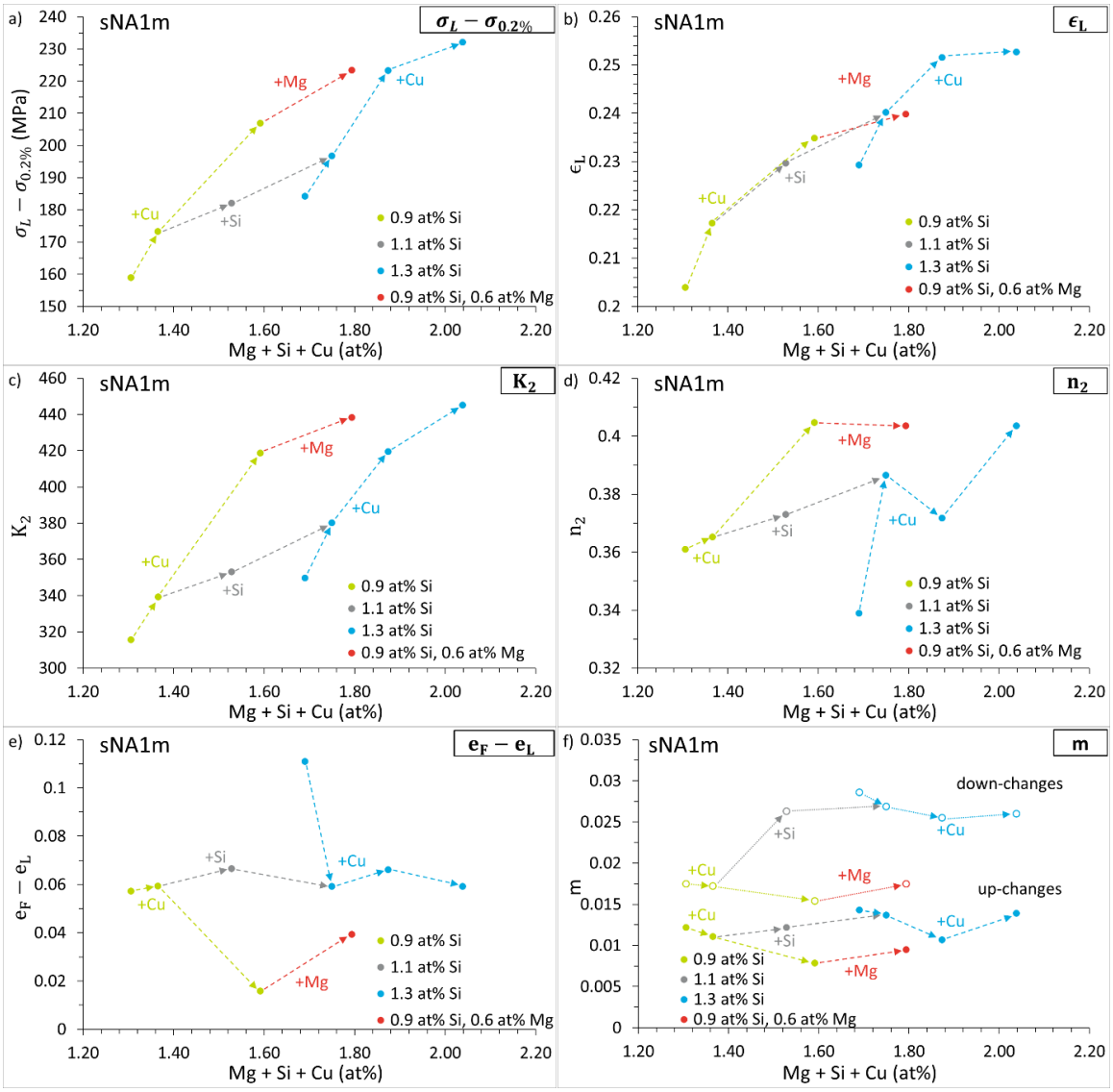

Figure 9-7: *The effects of total solute content on the* ***a)*** *strain hardening capacity,* ***b)*** *the uniform elongation,* ***c)*** *pre-exponential, K_2, for the second part of the constitutive relation,* ***d)*** *the strain hardening exponent, n_2,* ***e)*** *the post-uniform elongation, and* ***f)*** *the up-change (closed circles) and down-change (open circles) engineering SRS for the alloys tested in the sNA1m condition. For clarity, the effects of Cu additions at 0.9 and 1.3 at% Si, are connected in green and blue dashed arrows, respectively. The effects of Si additions at 0.2 at% Cu and 0.4 at% Mg are connected with the grey dashed arrows. The effects of Mg addition at 0.9 at% Si and 0.3 at% Cu are connected with red dashed arrows.*

The strain hardening capacity, $\sigma_L - \sigma_{0.2\%}$, represents the total dislocation storage capacity of the material, the strain hardening rate, n_2, the production rate, and pre-exponential factor, K_2, the

recovery rate, all increase with Cu and Mg (except for n_2), with Si having a smaller effect on all of these properties. Despite the differences in the specific mechanical properties, all of the solutes equally increase in the uniform elongation, ϵ_L. In the case of Cu additions, the increase in K_2 and n_2 suggest that the recovery of dislocations is reduced coupled with an increased dislocation production rate such that strengthening occurs at a faster rate. However, as there is also an increase in the strain hardening capacity allowing for more dislocations to be preserved in the material prior to failure and results in an increase in the uniform elongation. Similarly, the addition of Mg increases the storage rate and total storage capacity while not changing the dislocation production rate resulting in a total increase uniform elongation to a similar extent as Cu additions. Finally, despite the smaller increases in the dislocation production rate, total capacity and recovery rate, the compounded effects result in an identical increase in the uniform elongation. Concerning the post-uniform elongation, the strain rate sensitivity and total strength of the alloys seem to influence this post-necking behaviour. The addition of Cu increases the strength but does not cause a large effect on the strain rate sensitivity such that changes in the strength caused by the strain rate sensitivity from flow localization does not significantly affect the Considère criterion inside the neck interior such that the post-uniform elongation decreases with Cu additions. The opposite is true in the case of Si additions whereby there is not a significant effect on the strengthening component while the strain rate sensitivity has a large increase (both up-change and down-change) resulting in significant changes of the local Considère criterion during post-uniform elongation whereby the added strengthening reduces flow localization prolonging the elongation prior to failure, as-observed. Finally, with Mg additions, the story is similar to Cu additions where the relative strength of Mg is greater than Cu but also the strain rate sensitivity such that there is a sufficient contribution of the strain rate sensitivity to retarding flow localizations that the Mg addition yields a greater post-uniform elongation.

9.2 Conclusions

The complete work presented within this thesis leads to an improved understanding not only of the effects of alloy composition on the clusters formed during natural ageing and pre-ageing with secondary natural ageing, but also of the effects of the specific solute elements under each of the heat treatment condition on the specific mechanical properties and the resulting formability. The method of including compensation during strain rate sensitivity testing was also thoroughly discussed and the resulting asymmetry in the strain rate sensitivity was elucidated at room temperature. This allowed for the connection of the effects of strain hardening and strain rate sensitivity on the final necking formation and evolution during subsequent post-uniform elongation in order to serve as a framework for a better comprehension of formability. The following points derived from the work of this thesis are presented below:

- The types of clusters formed during NA and PA are not the same
    - During NA, Cu and Mg have a strong influence on the formation of the clusters able to dissolve at lower temperatures. Si additions do not significantly increase the formation of these clusters but causes a decrease of their dissolution temperature.
    - During PA, only a single cluster type appears to be formed being dissolved at temperatures greater than those formed during NA. Cu, Mg, and Si additions all appear to increase the cluster dissolution intensity. PA has been shown to reverse the negative natural ageing effect often observed in Al-Mg-Si-Cu alloys.

- There is a large difference between up-change (smaller) and down-change (larger) inverse activation volumes and strain rate sensitivities with the up-change strain rate sensitivities. The use of the compensation method during testing is necessary to obtain precise and reliable measurements, specifically during down-change tests.
    - Up-changes result in a relatively lower strain rate sensitivity and decrease the inverse activation volume. Down-changes result in a relatively larger strain rate sensitivity and increase the inverse activation volume.
- The expression of Cu, Mg, and Si additions on the resulting mechanical properties in the 6000-series depend directly on the heat treatment performed and the resulting cluster types.
    - During NA, Cu and Mg have a significantly larger influence on increasing the yield strength than Si.
    - During PA, all alloying elements contribute equally to increasing the yield strength of the alloys.
    - Si additions increases both the up-change and down-change strain rate sensitivities, independent of the heat treatment. Cu and Mg additions tend to not affect or decrease the up-change and down-change strain rate sensitivities.
- It is possible to determine the cluster-dislocation interaction profile by performing strain rate sensitivity measurements at various temperatures.
    - The activation distance of the alloys in the sNA1m condition are typically lower than those in the NA1m condition suggesting a more complete removal of solute from the matrix.
    - The addition of Si was shown to reduce the activation distance at room temperature supporting a more complete removal of solute from the matrix as supported by the NA and sNA hardness curves.
- Increasing the m_{uc} and m_{dc} together was shown to reduce the intensity of the strain rate at the centre of the neck in conjunction with both the strain rate and strain distribution along the length of the neck. The distance from the neck centre to the base strain rate was shown to be inadequate for defining the size of the neck but plays an important role on understanding the evolution of the neck.
    - The majority of the post-necking elongation is provided by m_{uc} due to the very localized effect of the increased strain rate interior of the neck.
    - The m_{dc} component acts only on the regions exterior to the neck, being much larger in size such that its effect is effectively “diluted”.
    - In the sample study, the distance to the base strain rate was shown to be controlled initially by the strain gradient and subsequently by the intensity of the strain rate at the neck centre.

9.3 Perspectives

After completing and understanding the main experiments contained within the thesis and the resulting potential for designing Al-Mg-Si-Cu alloys with specific properties with required mechanical properties, it is recommended that the following program be followed to enrich the current understanding of the influence of alloy composition on the formability of Al-Mg-Si-Cu alloys:

a) Perform digital image correlation testing in order to compare the evolution of the strain and strain rate distribution with the finite element modeling simulations performed in this work.

b) The completion of industrial formability tests such as Marciniak-Kuczynski and limiting dome height tests in order to generate the forming limit curve on samples having the highest and lowest m_{uc} and m_{dc} values. Samples with the largest discrepancy between m_{dc} and m_{uc} should also be tested to determine how large of a role the asymmetrical strain rate sensitivity plays on necking formation and propagation.
c) The completion of small angle X-ray scattering (SAXS) and further analysis of atom probe tomography (APT) experiments in order to elucidate the size, density and stoichiometry distribution of the clusters formed in the NA1m and sNA1m conditions to validate the observations made by DSC and hardness testing. SAXS measurements on 6000-series alloys will require specific development of low X-ray energy measurements at a synchrotron source so as to reach the Al K-edge (~1500 eV).
d) Additionally, the behaviour of clusters during plastic straining, such as dissolution or dynamic formation, are of significant interest as it is speculated that they will lead to contributions to both the strain hardening and strain rate sensitivity asymmetry. It is particularly challenging to evaluate this dynamic evolution, since all of the relevant experimental techniques (SAXS, DSC, APT) cannot be performed in-situ during a tensile test. Ex-situ measurements, minimizing the time between the end of the tensile test and the microstructure evaluation, should be carried out.

Appendices

Appendix 1 – Supplementary plots

The following sections contain the corresponding plots for each type of test not included in the main body of the work.

Appendix 1.1 – Hardness plots

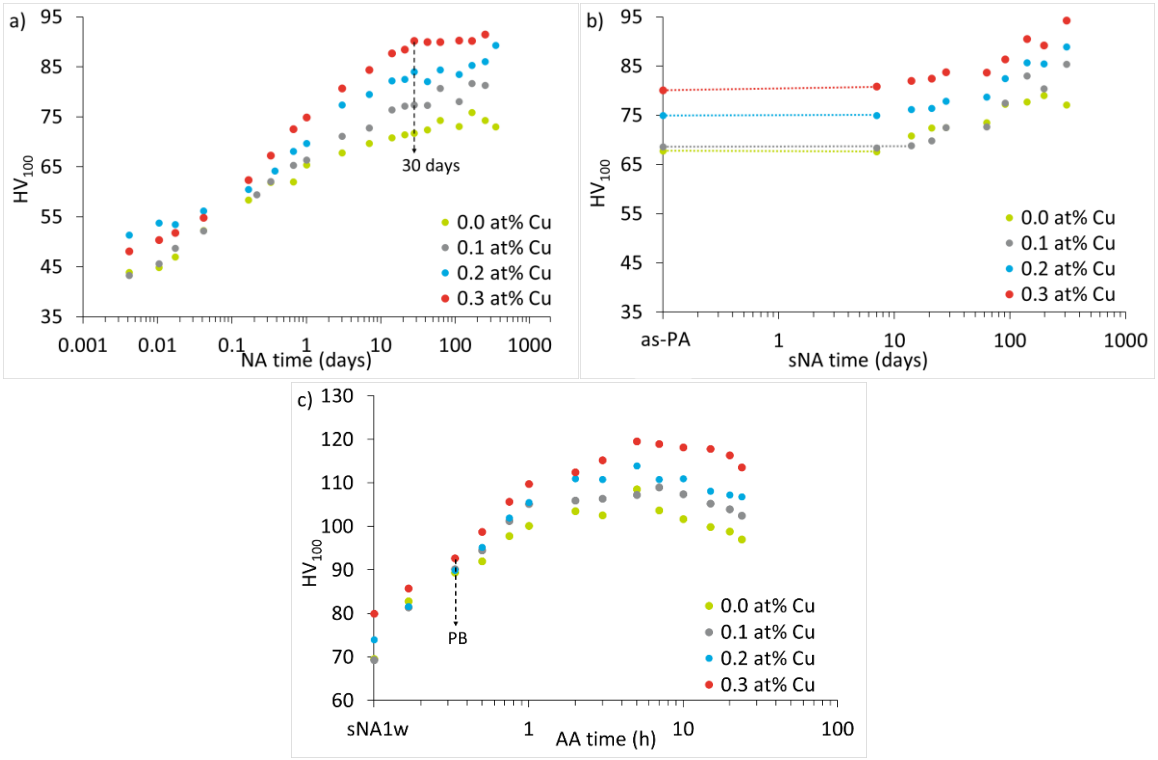

The effects of Cu content at Si level of 0.9 at% on the age hardening curves for **a)** NA, **b)** sNA, and **c)** AA after sNA1w. The incubation times prior to sNA are shown in dotted lines in b).

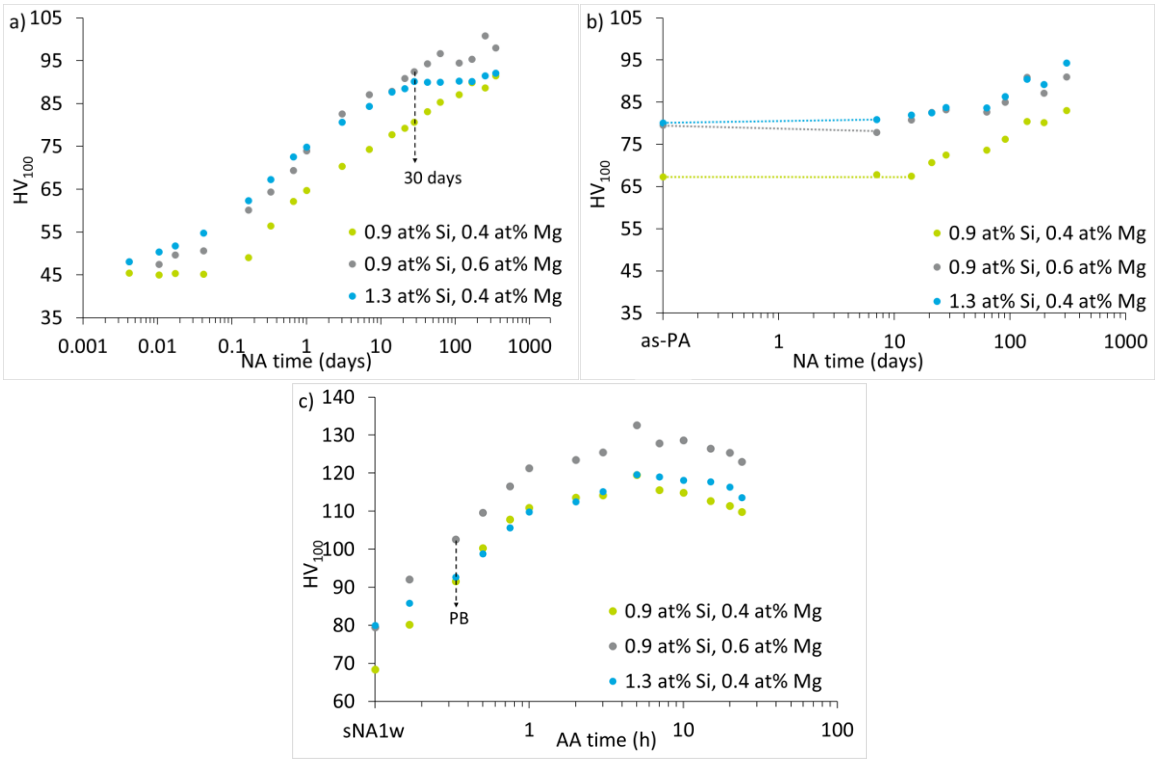

The effects of Cu content at Si level of 0.9 at% on the age hardening curves for **a)** NA, **b)** sNA, and **c)** AA after sNA1w. The incubation times prior to sNA are shown in dotted lines in b).

Appendix 1.2 – DSC thermographs

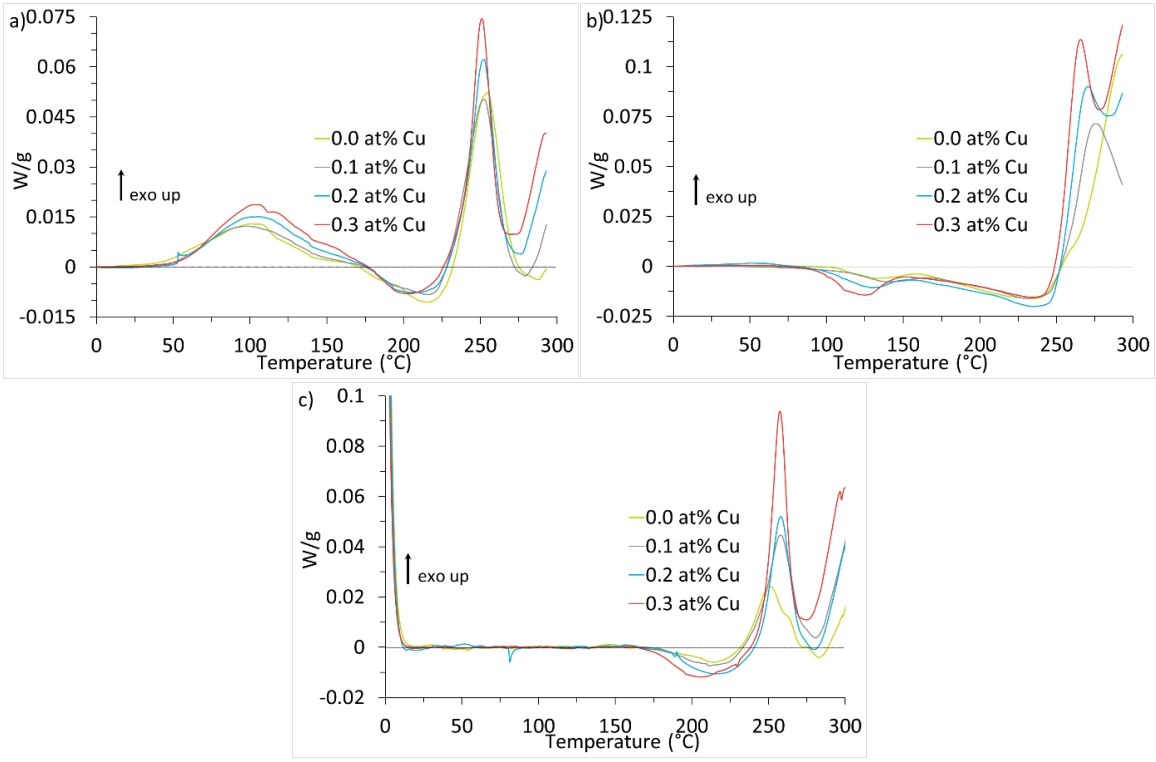

The effects of Cu content at Si level of 0.9 at% on the DSC curves in the **a)** WQ, **b)** 30 day NA, and **c)** as-PA conditions.

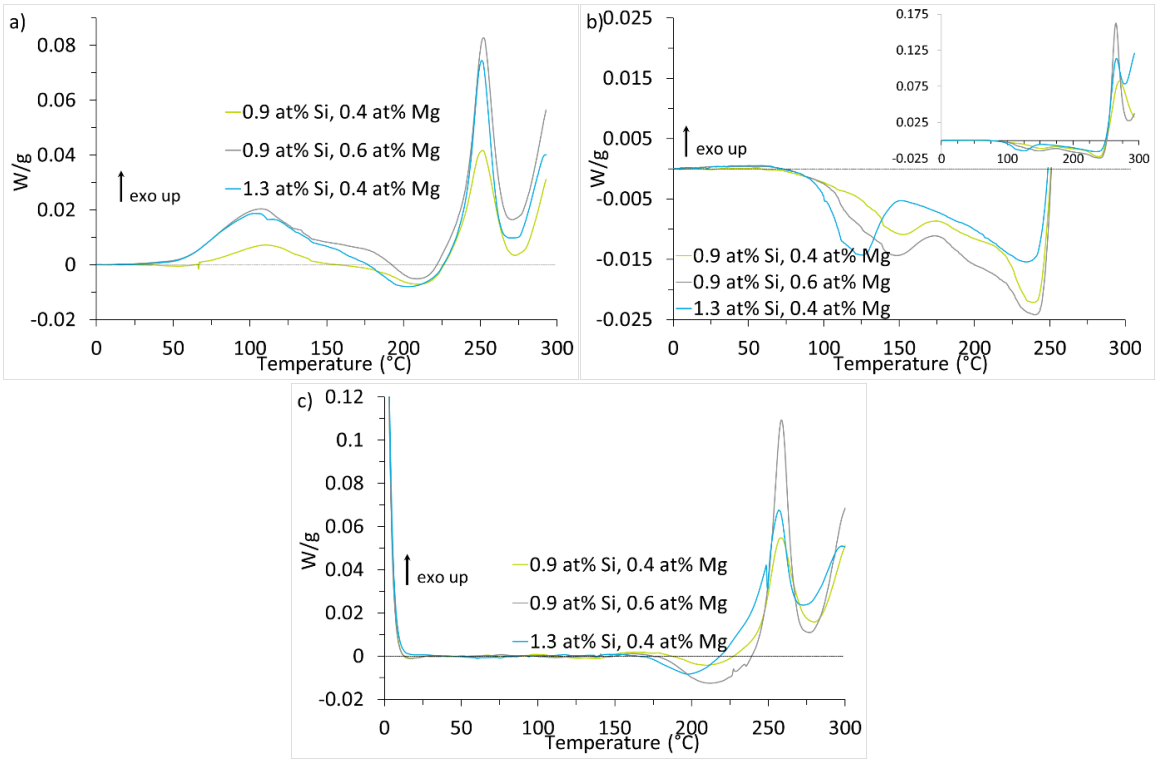

The effects of Cu content at Si level of 0.9 at% on the DSC curves in the **a)** WQ, **b)** 30 day NA, and **c)** as-PA conditions.

Appendix 1.3 – sNA1w mechanical data

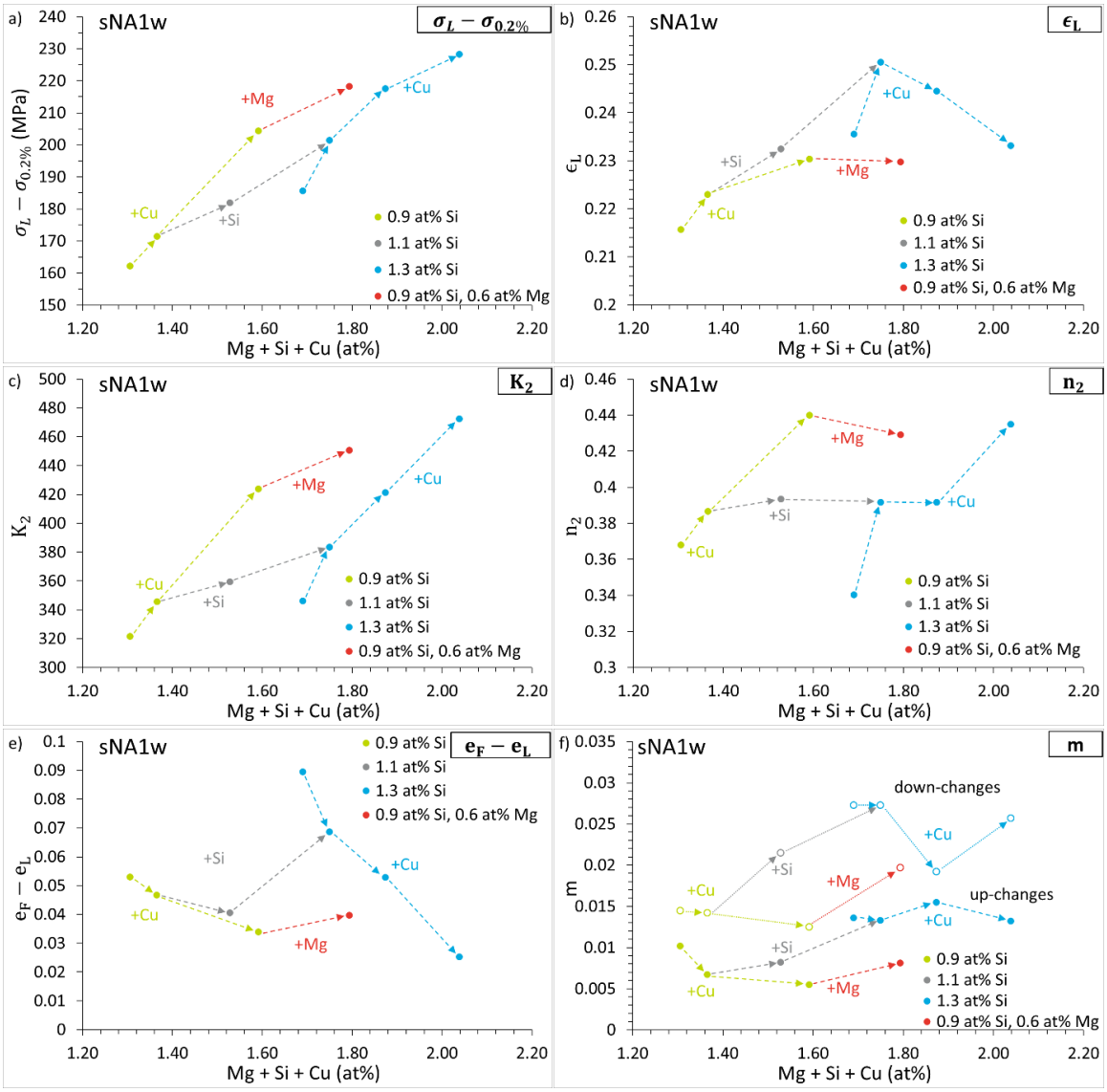

The effects of total solute content on the **a)** strain hardening capacity, **b)** the uniform elongation, **c)** pre-exponential, K_2, for the second part of the constitutive relation, **d)** the strain hardening exponent, n_2, **e)** the post-uniform elongation, and **f)** the up-change (closed circles) and down-change (open circles) engineering SRS for the alloys tested in the NA1m condition. For clarity, the effects of Cu additions at 0.9 and 1.3 at% Si, are connected in green and blue dashed arrows, respectively. The effects of Si additions at 0.2 at% Cu and 0.4 at% Mg are connected with the grey dashed arrows. The effects of Mg addition at 0.9 at% Si and 0.3 at% Cu are connected with red dashed arrows.

Appendix 1.4 – Haasen plot information

1.4.1 Haasen plots at the three tested temperatures

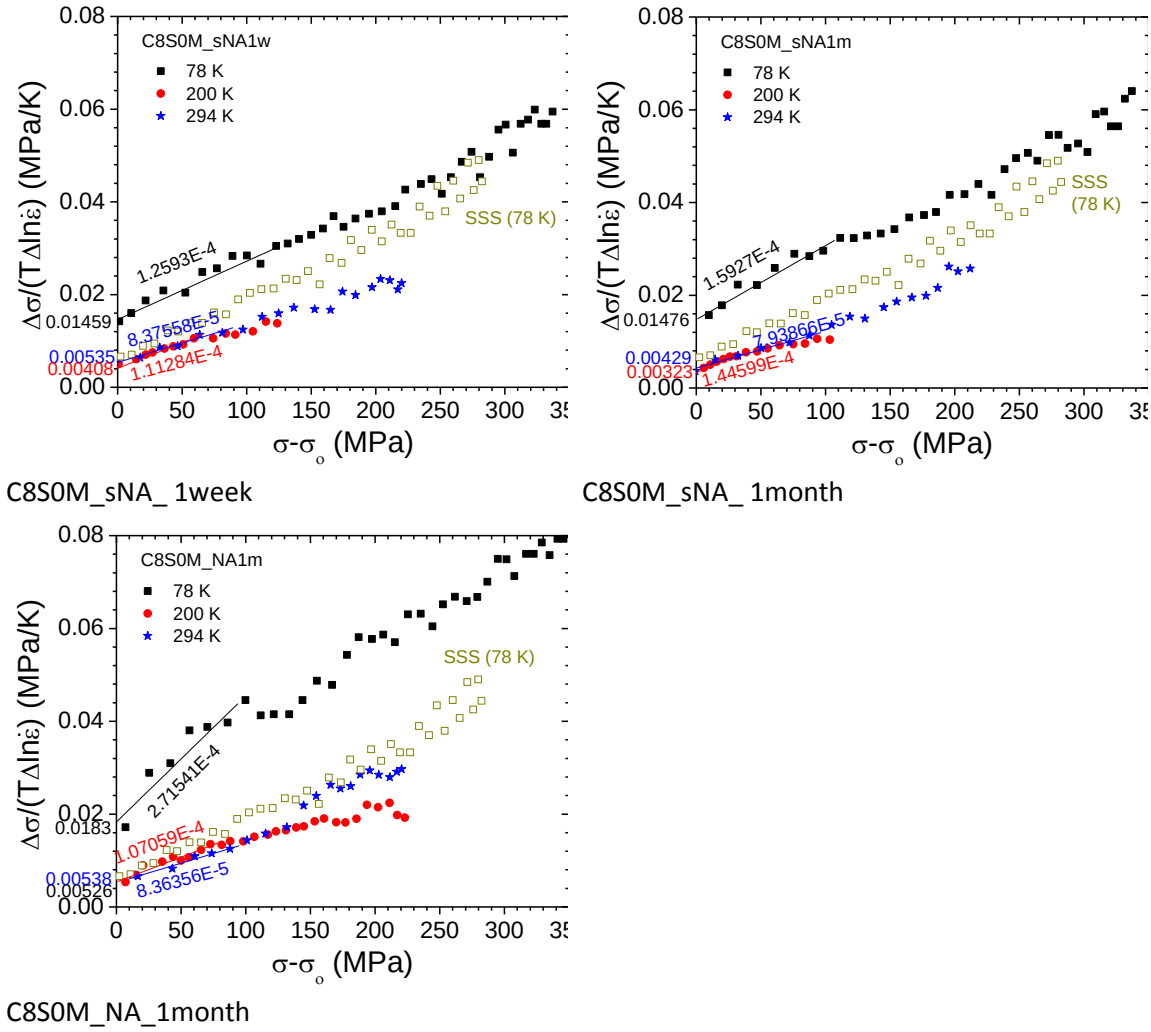

Figure C.1: C8S0M Haasen plots for the three ageing conditions and testing temperatures.

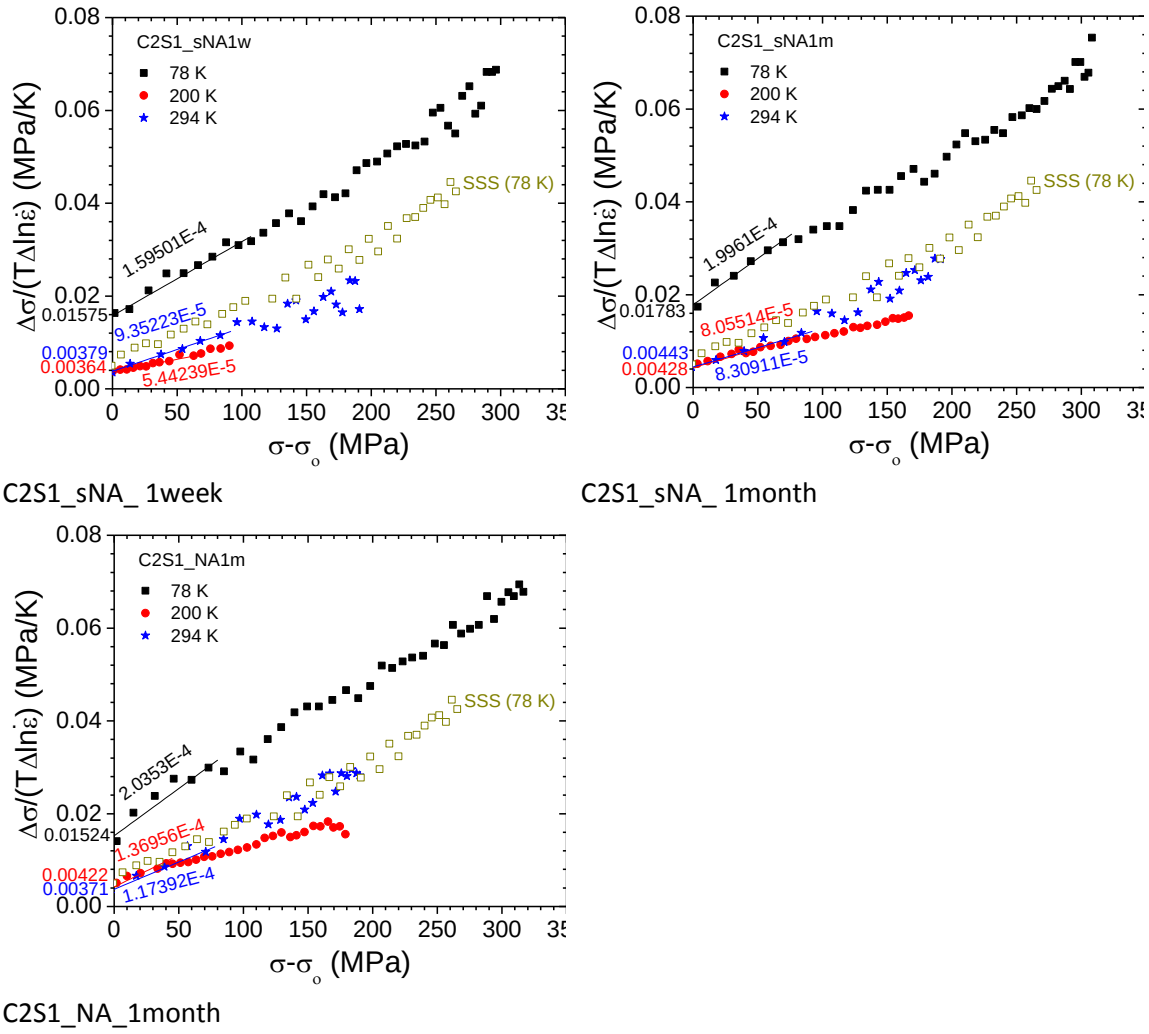

Figure C.2: C2S1 Haasen plots for the three ageing conditions and testing temperatures.

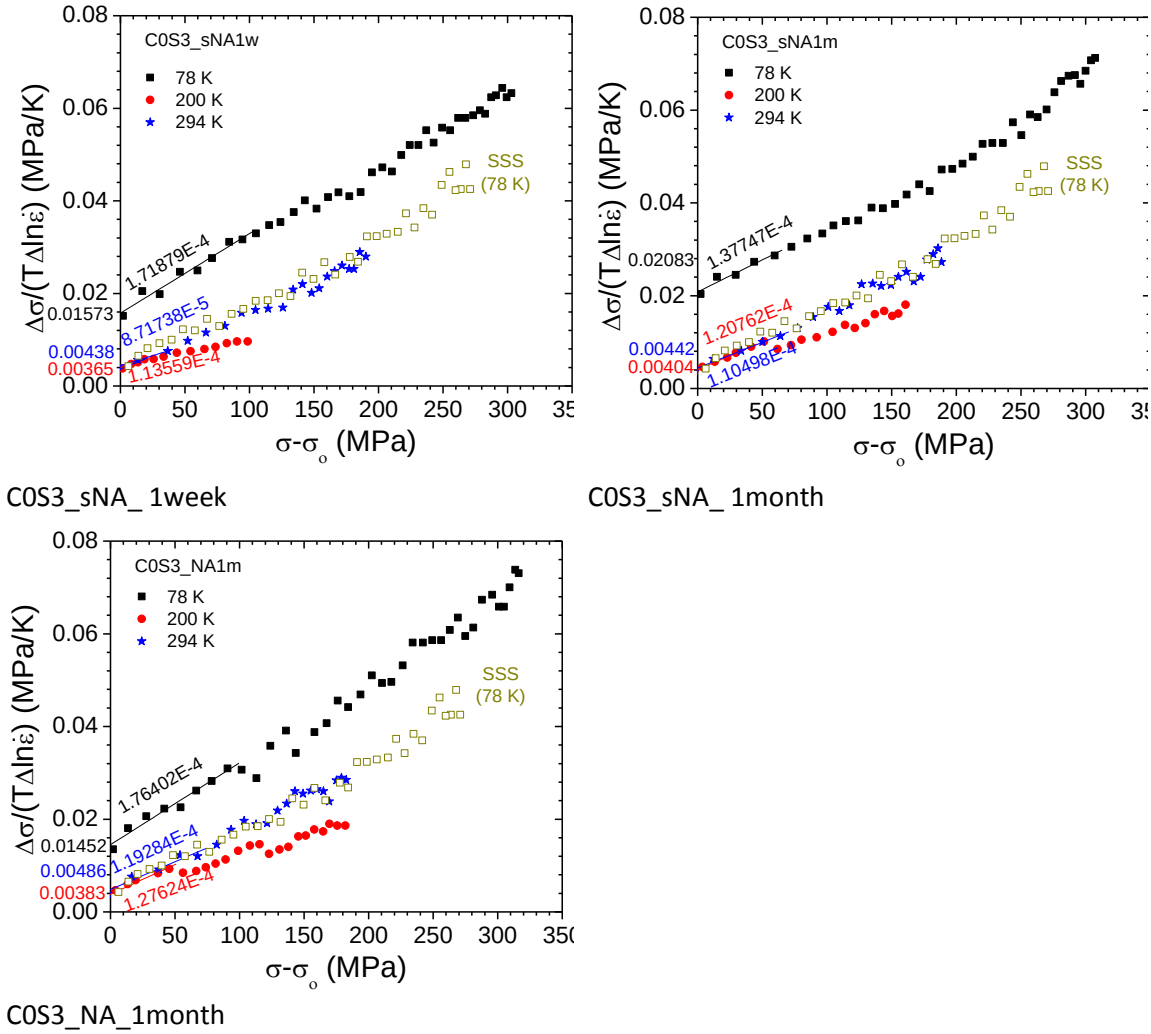

Figure C-3: C0S3 Haasen plots for the three ageing conditions and testing temperatures.

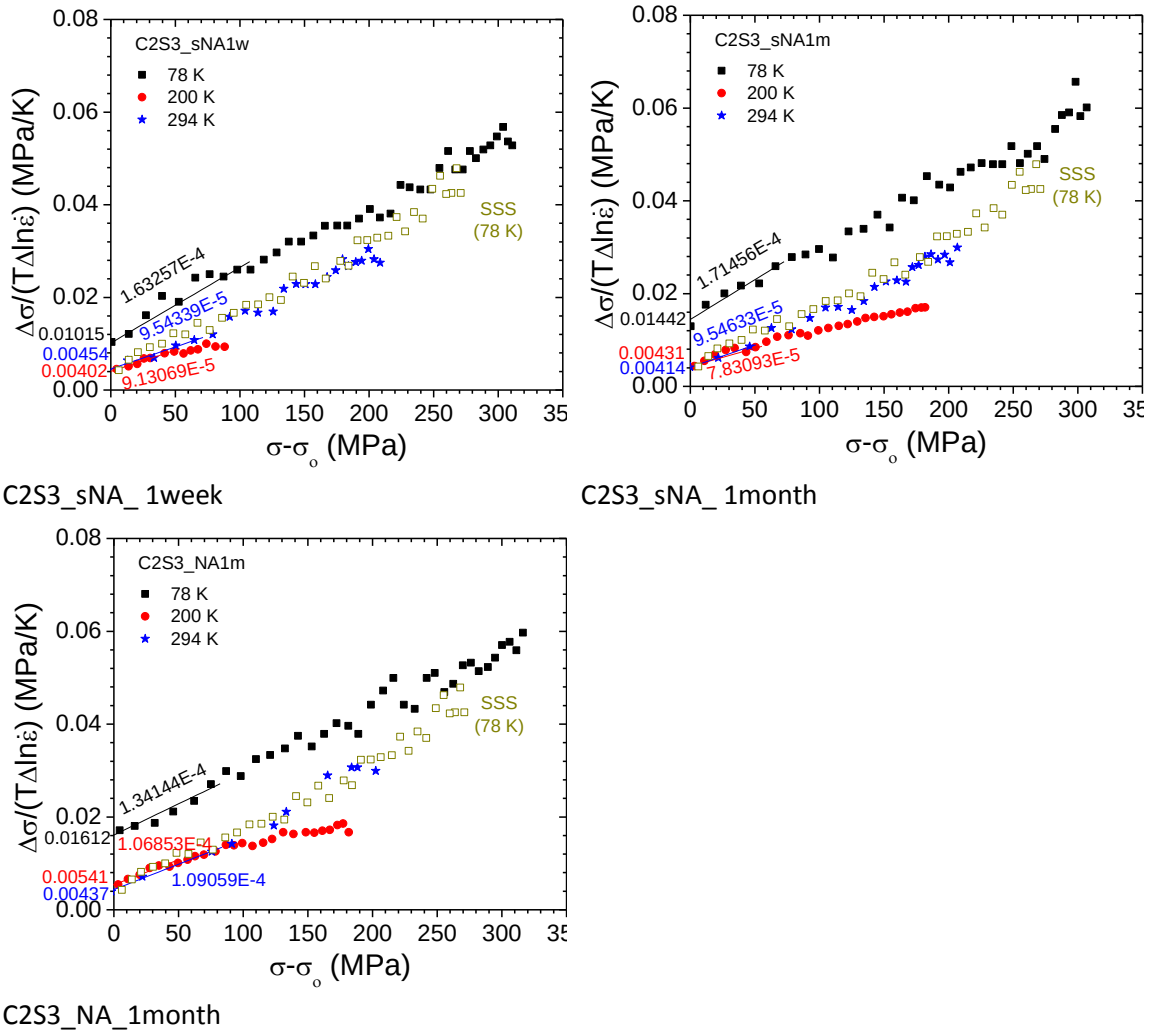

Figure C-4: C2S3 Haasen plots for the three ageing conditions and testing temperatures.

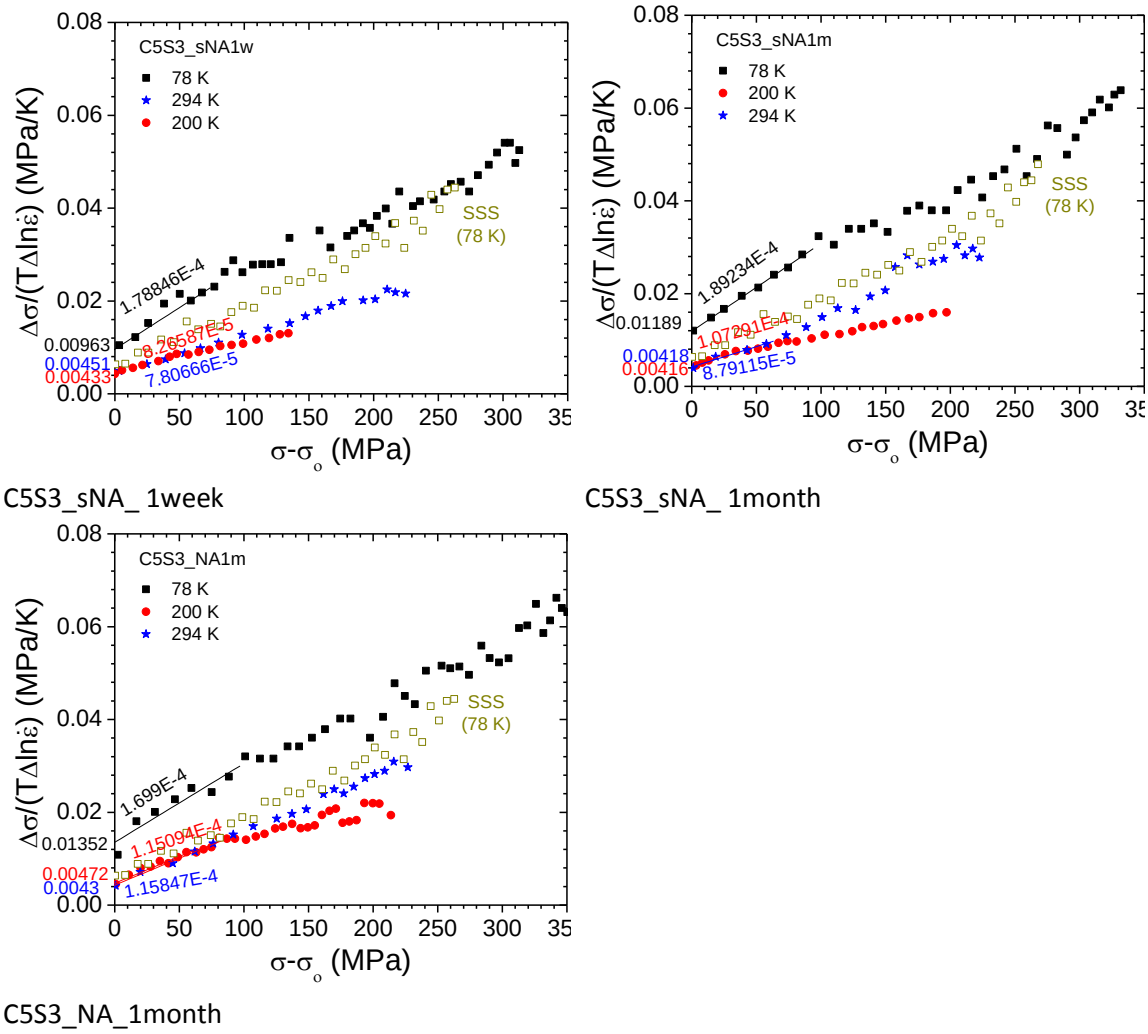

Figure C-5: C5S3 Haasen plots for the three ageing conditions and testing temperatures.

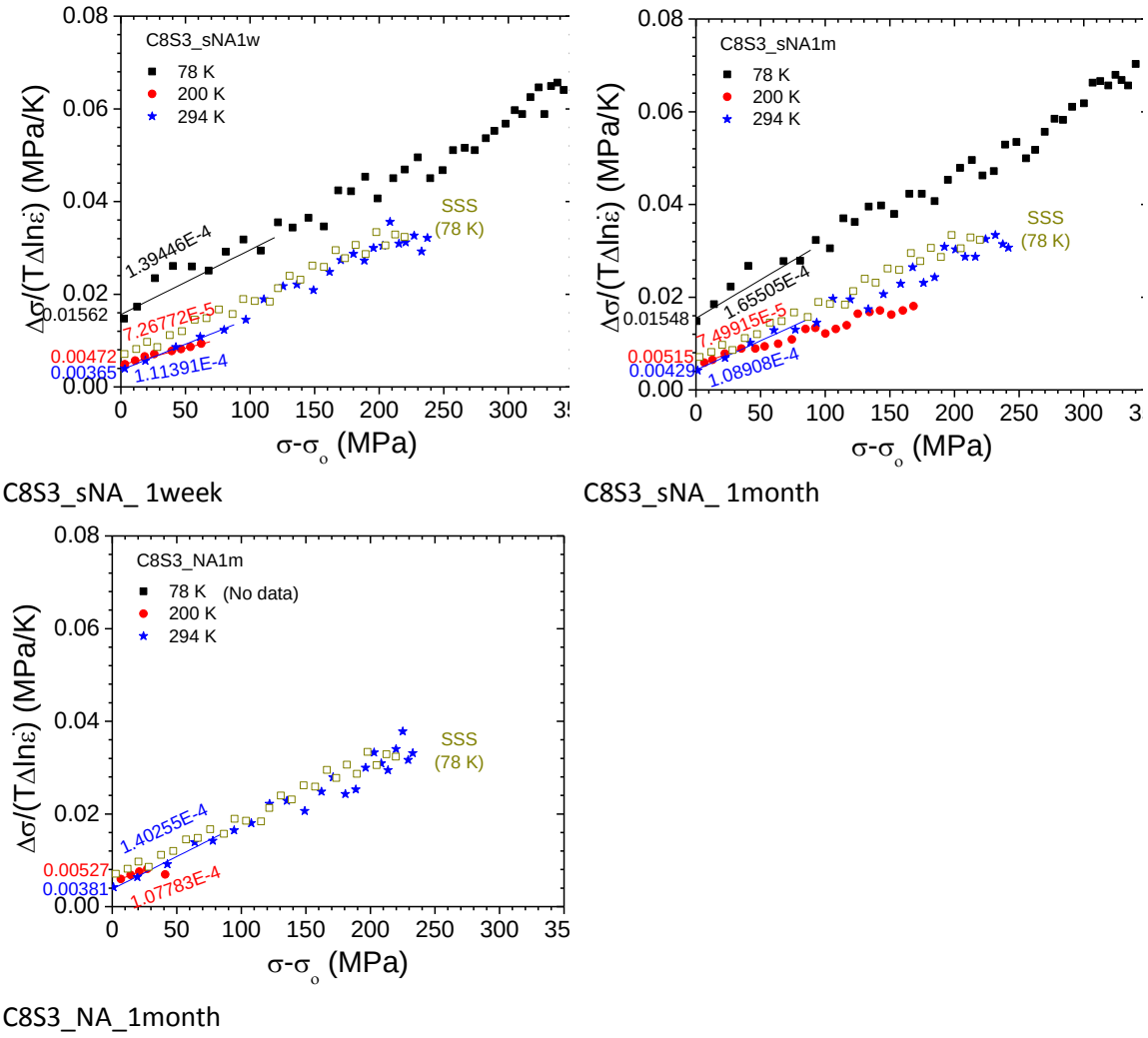

Figure C-6: C8S3 C5S3 Haasen plots for the three ageing conditions and testing temperatures. Note, not data was measured at 78 K for C8S3_NA1m.

Appendix 1.4.2 – Haasen plot data tables

Haasen plot intercept, k/V' (MPa K^{-1}), and initial slope, S1 (K^{-1}), values tabulated for **sNA1w**, **SNA1m** and **NA1m** at the three test temperatures.

Alloy		78 K			198 K			294 K		
		sNA1w	sNA1m	NA1m	sNA1w	sNA1m	NA1m	sNA1w	sNA1m	NA1m
C0S0	K/V′	1.45×10^{-2}	1.46×10^{-2}	1.44×10^{-2}	4.55×10^{-3}	4.63×10^{-3}	5.05×10^{-3}	3.15×10^{-3}	3.79×10^{-3}	3.73×10^{-3}
	S_1	1.41×10^{-4}	1.51×10^{-4}	1.49×10^{-4}	6.78×10^{-5}	6.66×10^{-5}	6.66×10^{-5}	7.90×10^{-5}	7.94×10^{-5}	1.39×10^{-4}
C2S0	K/V′	1.39×10^{-2}	1.84×10^{-2}	1.75×10^{-2}	5.88×10^{-3}	3.70×10^{-3}	5.14×10^{-3}	3.76×10^{-3}	3.49×10^{-3}	3.51×10^{-3}
	S_1	2.73×10^{-4}	2.39×10^{-4}	1.79×10^{-4}	2.78×10^{-5}	8.73×10^{-5}	7.32×10^{-5}	3.99×10^{-5}	7.92×10^{-5}	1.31×10^{-4}
C8S0	K/V′	1.57×10^{-2}	1.62×10^{-2}	1.98×10^{-2}	4.22×10^{-3}	4.08×10^{-3}	5.48×10^{-3}	4.22×10^{-3}	3.98×10^{-3}	5.53×10^{-3}
	S_1	1.62×10^{-4}	2.26×10^{-4}	1.47×10^{-4}	5.56×10^{-5}	7.52×10^{-5}	5.53×10^{-5}	6.85×10^{-5}	6.52×10^{-5}	9.01×10^{-5}
C8S0M	K/V′	1.46×10^{-2}	1.48×10^{-2}	1.83×10^{-2}	5.35×10^{-2}	4.29×10^{-3}	5.38×10^{-3}	4.08×10^{-2}	3.23×10^{-3}	5.53×10^{-3}
	S_1	1.26×10^{-4}	1.59×10^{-4}	2.72×10^{-4}	8.38×10^{-5}	7.94×10^{-5}	8.36×10^{-5}	1.11×10^{-4}	1.44×10^{-4}	9.01×10^{-5}
C2S1	K/V′	1.58×10^{-2}	1.78×10^{-2}	1.52×10^{-2}	3.79×10^{-2}	4.43×10^{-3}	3.71×10^{-3}	3.64×10^{-2}	4.28×10^{-3}	4.22×10^{-3}
	S_1	1.59×10^{-4}	2.00×10^{-4}	2.04×10^{-4}	9.35×10^{-5}	8.31×10^{-5}	1.17×10^{-4}	5.44×10^{-5}	8.06×10^{-5}	1.37×10^{-4}
C0S3	K/V′	1.57×10^{-2}	2.08×10^{-2}	1.45×10^{-2}	4.38×10^{-2}	4.42×10^{-3}	4.86×10^{-3}	3.65×10^{-2}	4.04×10^{-3}	3.83×10^{-3}
	S_1	1.72×10^{-4}	1.38×10^{-4}	1.76×10^{-4}	8.72×10^{-5}	1.10×10^{-4}	1.19×10^{-4}	1.14×10^{-5}	1.21×10^{-4}	1.28×10^{-4}
C2S3	K/V′	1.10×10^{-2}	1.44×10^{-2}	1.61×10^{-2}	4.54×10^{-2}	4.14×10^{-3}	4.37×10^{-3}	4.02×10^{-2}	4.31×10^{-3}	5.41×10^{-3}
	S_1	1.63×10^{-4}	1.71×10^{-4}	1.34×10^{-4}	9.54×10^{-5}	1.09×10^{-4}	1.19×10^{-4}	9.13×10^{-5}	7.86×10^{-5}	1.09×10^{-4}
C5S3	K/V′	9.63×10^{-3}	1.19×10^{-2}	1.35×10^{-2}	4.51×10^{-2}	4.18×10^{-3}	4.30×10^{-3}	4.33×10^{-2}	4.16×10^{-3}	4.72×10^{-3}
	S_1	1.79×10^{-4}	1.89×10^{-4}	1.70×10^{-4}	7.81×10^{-5}	8.79×10^{-5}	1.16×10^{-4}	8.27×10^{-5}	8.79×10^{-5}	1.15×10^{-4}
C8S3	K/V′	1.56×10^{-3}	1.55×10^{-2}	-	3.65×10^{-2}	4.29×10^{-3}	3.81×10^{-3}	4.82×10^{-2}	5.15×10^{-3}	5.72×10^{-3}
	S_1	1.39×10^{-4}	1.66×10^{-4}	-	1.11×10^{-4}	1.09×10^{-4}	1.40×10^{-4}	7.27×10^{-5}	7.50×10^{-5}	1.78×10^{-4}

1.5 The yield strength for the AQ samples at 78K in the three conditions

Sample	AQ	NA1m	sNA1m	sNA1w
C0S0	67.2	145.4	133.7	120.5
C2S0	50.6	153.9	138.8	115.5
C8S0	54.8	185.5	143.5	135.1
C8S0M	67.1	214.5	174.6	171.8
C2S1	62.2	160.6	137.2	123.1
C0S3	60.0	159.8	152.5	140.7
C2S3	67.6	178.9	154.5	148.6
C5S3	73.5	188.1	163.3	156.2
C8S3	70.2	184.6	182.4	184.6

Appendix 2 – Temperature dependent shear modulus of aluminium

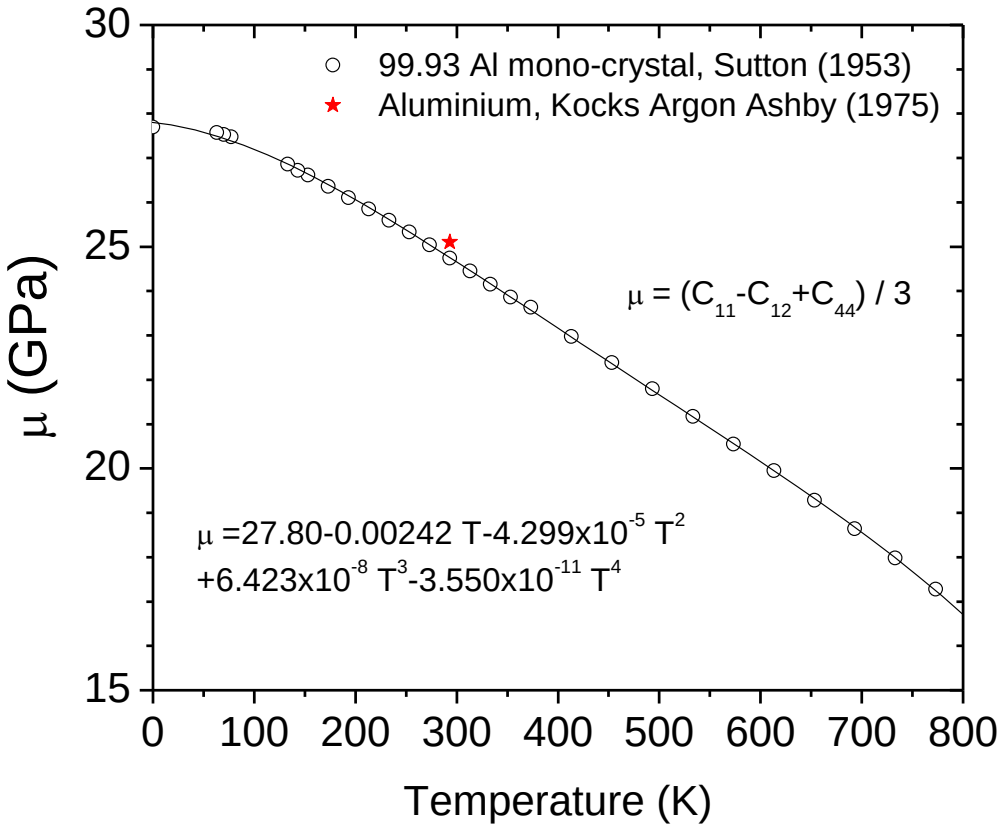

The temperature dependence of the elastic shear modulus for 99.93 purity aluminium single crystal calculated from the elastic constants measured by Sutton [Phys. Rev. 91(1953) 816-821.]. Also shown is a polynomial fit for the data and the room temperature data point tabulated by Kocks, Argon and Ashby [Prog. Matls. Sci. 19 (1975) 1-291.].

Influence des constituants microstructuraux sur la formabilité des tôles en alliages d'aluminium

Alors que les constructeurs automobiles cherchent à améliorer l'efficacité énergétique des voitures, ils cherchent à remplacer les composants actuels en acier par de nouveaux alliages d'aluminium (Al) plus légers et plus récents. Il a été démontré que les alliages d'aluminium à base de magnésium (Mg), de silicium (Si) et de cuivre (Cu) offrent une résistance suffisante pour remplacer ces composants en acier, mais ne possèdent pas la formabilité souhaitée. Ce travail vise à comprendre les effets des ajouts de Mg, Si et Cu sur la formabilité de ces alliages. Grâce à l'utilisation de la calorimétrie et des essais de dureté, l'état de la microstructure a été révélé. L'utilisation d'essais de traction a permis de déterminer les propriétés mécaniques en relation avec la microstructure. Les paramètres de propriétés mécaniques ont ensuite été inclus dans des simulations par éléments finis pour comprendre leurs effets sur la formabilité de l'alliage. Cette thèse a établi un lien entre la composition, les microstructures pour deux voies de traitement différentes, les propriétés mécaniques résultantes et leur influence sur la formabilité finale de ces alliages Al-Mg-Si-Cu.

The influence of microstructural components on the formability of aluminium alloy sheets

As automotive manufacturers seek to improve the fuel efficiency of passenger vehicles, they look to replace current, heavy steel components with newer, lightweight aluminium (Al) alloys. Al alloys based on addition of magnesium (Mg), silicon (Si), and copper (Cu), have been shown to provide adequate strength to replace these steel components but lack the desired formability. This work aims to understand the effects of Mg, Si, and Cu, additions on the overall formability of these alloys. Through the use of differential scanning calorimetry and hardness testing, the state of the microstructure has been indirectly revealed. The use of tensile testing has permitted to determine the mechanical properties in relation with the microstructure. The mechanical properties parameters have then been included into finite element modeling simulations to understand their effects on the overall alloy formability. This thesis has achieved a connection between the composition, the changes in microstructure for two different processing routes, the resulting mechanical properties and their influence on the ultimate formability of these Al-Mg-Si-Cu alloys.